ACS SYMPOSIUM SERIES [illegible]

Smart Coatings III

EDITED BY
Jamil Baghdachi
and Theodore Provder

Downloaded by 89.163.35.42 on June 22, 2012 | http://pubs.acs.org
Publication Date (Web): November 10, 2010 | doi: 10.1021/bk-2010-1050.fw001

Smart Coatings III

In Smart Coatings III; Baghdachi, J., et al.;
ACS Symposium Series; American Chemical Society: Washington, DC, 2010.

Downloaded by 89.163.35.42 on June 22, 2012 | http://pubs.acs.org
Publication Date (Web): November 10, 2010 | doi: 10.1021/bk-2010-1050.fw001

Downloaded by 89.163.35.42 on June 22, 2012 | http://pubs.acs.org
Publication Date (Web): November 10, 2010 | doi: 10.1021/bk-2010-1050.fw001

ACS SYMPOSIUM SERIES **1050**

Smart Coatings III

Jamil Baghdachi, Editor
Coatings Research Institute
Eastern Michigan University

Theodore Provder, Editor
Polymer & Coatings Consultants, LLC

American Chemical Society, Washington, DC

Downloaded by 89.163.35.42 on June 22, 2012 | http://pubs.acs.org
Publication Date (Web): November 10, 2010 | doi: 10.1021/bk-2010-1050.fw001

Library of Congress Cataloging-in-Publication Data

Library of Congress Control Number: 2006051208

ISBN 978-0-8412-2565-7

The paper used in this publication meets the minimum requirements of American National Standard for Information Sciences—Permanence of Paper for Printed Library Materials, ANSI Z39.48n1984.

Copyright © 2010 American Chemical Society

Distributed by Oxford University Press

All Rights Reserved. Reprographic copying beyond that permitted by Sections 107 or 108 of the U.S. Copyright Act is allowed for internal use only, provided that a per-chapter fee of $40.25 plus $0.75 per page is paid to the Copyright Clearance Center, Inc., 222 Rosewood Drive, Danvers, MA 01923, USA. Republication or reproduction for sale of pages in this book is permitted only under license from ACS. Direct these and other permission requests to ACS Copyright Office, Publications Division, 1155 16th Street, N.W., Washington, DC 20036.

The citation of trade names and/or names of manufacturers in this publication is not to be construed as an endorsement or as approval by ACS of the commercial products or services referenced herein; nor should the mere reference herein to any drawing, specification, chemical process, or other data be regarded as a license or as a conveyance of any right or permission to the holder, reader, or any other person or corporation, to manufacture, reproduce, use, or sell any patented invention or copyrighted work that may in any way be related thereto. Registered names, trademarks, etc., used in this publication, even without specific indication thereof, are not to be considered unprotected by law.

PRINTED IN THE UNITED STATES OF AMERICA

Foreword

The ACS Symposium Series was first published in 1974 to provide a mechanism for publishing symposia quickly in book form. The purpose of the series is to publish timely, comprehensive books developed from the ACS sponsored symposia based on current scientific research. Occasionally, books are developed from symposia sponsored by other organizations when the topic is of keen interest to the chemistry audience.

Before agreeing to publish a book, the proposed table of contents is reviewed for appropriate and comprehensive coverage and for interest to the audience. Some papers may be excluded to better focus the book; others may be added to provide comprehensiveness. When appropriate, overview or introductory chapters are added. Drafts of chapters are peer-reviewed prior to final acceptance or rejection, and manuscripts are prepared in camera-ready format.

As a rule, only original research papers and original review papers are included in the volumes. Verbatim reproductions of previous published papers are not accepted.

ACS Books Department

Downloaded by 89.163.35.42 on June 22, 2012 | http://pubs.acs.org
Publication Date (Web): November 10, 2010 | doi: 10.1021/bk-2010-1050.fw001

Downloaded by 89.163.35.42 on June 22, 2012 | http://pubs.acs.org
Publication Date (Web): November 10, 2010 | doi: 10.1021/bk-2010-1050.pr001

Preface

In the past few years, in part fueled by nano-science and nano-technology, coatings research has taken a new turn. The new direction has also been due to the development and availability of new raw materials, innovative particles, polyelectrolytes, liquid crystals, conductive polymers, as well as large families of stimuli responsive polymer systems. Other research and development contributions have been in raw material design, including polymers made through Atom Transfer Radical Polymerization (ATRP), layer-by layer, self-assembly, supramolecules and novel polymer bound additives. Along with the availability of new raw materials innovative technologies for design and formulating novel coatings have also be developed.

The survey of the literature in the coatings field indicates that the two areas of "Green Coatings" and "Multifunctional Responsive Coatings" are among the most researched topics the lead to commercial products. The Green Chemistry movement aims to produce coatings from renewable resources with the least "carbon foot print" and those products that can conveniently be recycled. The other challenge is to use coatings as materials of choice to respond to multitude of stimuli, while providing the traditional protective or decorative functions. Among technologies in this class include the broad fields of bioactive materials, drug delivery systems, self-healing, self-cleaning and self-stratifying and coatings that are used as sensors for use in all areas that need early detection and warning. These most intensely researched areas of material science, promise to deliver highly innovative functional and value-added coatings products. These coatings are often referred to as *smart coatings*. Previous Smart Coatings Symposia are embodied in two ACS Symposium Series volumes (*1*, *2*).

A major challenge today for material scientists is to develop technologies that can produce novel coating products with extended lifetime, increased safety and perhaps with little or no maintenance. Such an objective may be achieved by designing and developing coating systems that can self-repair. The first section of the *Smart Coatings III* begins with self-healing technology that is one of the most sought after areas of research world wide. The theme of stimuli responsive coatings continues with other three articles in this section. The second section deals with new platform technologies on smart coatings and their characterization. The last section of the book follows the theme of smart surfaces since the coatings modify the surface properties imparting them special characteristics while performing the traditional coating functions.

We expect that this book will encourage scientific and technological investigators to expand knowledge to commercially relevant coating systems.

We thank the authors for their effective oral and written communications and the reviewers for their helpful critiques and constructive comments.

References

1. *Smart Coatings*; Provder, T., Baghdachi, J., Eds.; ACS Symposium Series 957; American Chemical Society: Washington, DC, 2007.
2. *Smart Coatings II*; Provder, T., Baghdachi, J., Eds.; ACS Symposium Series 1002; American Chemical Society: Washington, DC, 2009.

Jamil Baghdachi

Coatings Research Institute
Eastern Michigan University
430 West Forest Avenue
Ypsilanti, Michigan 48197, USA

Theodore Provder

Polymer & Coatings Consultants, LLC
5645A Emerald Ridge Parkway
Solon, Ohio 44139

Downloaded by 89.163.35.42 on June 22, 2012 | http://pubs.acs.org
Publication Date (Web): November 10, 2010 | doi: 10.1021/bk-2010-1050.pr001

Downloaded by 89.163.35.42 on June 22, 2012 | http://pubs.acs.org
Publication Date (Web): November 10, 2010 | doi: 10.1021/bk-2010-1050.ch001

Chapter 1

Design and Development of Self-Healing Polymers and Coatings

Jamil Baghdachi,[*] Heidi Perez, and Amit Shah

Coatings Research Institute, Eastern Michigan University, Ypsilanti, MI, 48197 (USA)
[*]jbaghdach@emich.edu

In an effort to mimic self-healing functions in biological systems, we report here the development of polymeric coating systems that are stimuli responsive and possess the ability to self-heal when damaged. This work describes coatings that contain small amounts of healing agent in the form of microcapsule homogeneously dispersed in the coating medium. The most attractive feature of this system is that the factors that cause the most damage to the coating, such as humidity, mechanical compromise, exposure to high temperatures etc., are the same factors that initiate self-healing phenomenon. This property is unique since the extent of the healing is proportional to the magnitude of the damage, i.e., repair on demand. It was confirmed that the simulated natural aging or mechanical damage triggered the release of healing agents, repaired the damage, restored the integrity of the coating and enhanced overall coating properties. The self-healing performance was assessed through direct evaluation and observation of improved key coating properties such as, enhanced mechanical and surface properties. The self-healing samples showed several fold enhancements in corrosion resistance as well as reduced water vapor permeability as compared to standard polyurethane coatings. The development of self-healing materials has the potential to significantly impact the coatings and related industries by enhancing coatings' performance and service life.

Introduction

Surface coatings function to protect or improve the appearance of a substrate or both. Protective attributes of coatings, such as cracking, scratch resistance, corrosion protection, etc., are related to the coating integrity and thus to mechanical properties (*1*, *2*). Studies on coatings' protective properties and their durability have predominantly been concerned with ultraviolet light absorption, but moisture absorption and temperature variation can be very important also (*3*, *4*). In addition, decreasing gas and water vapor permeability with physical aging has been well documented in the literature (*5–8*).

No matter how carefully the coatings are designed, manufactured and applied, all will eventually fail through some type of force in excess of the tolerance level of the coating or its ingredients. Failure of coating systems occur by any number of failure modes (*9*) and can often be attributed to a number of root causes including coating degradation, mechanical damage, or polymer fatigue upon service and exposure to elements of weather.

Weather includes many elements, among which are sunlight, environmental or service heat, oxygen and ozone, humidity, precipitation, wind, and atmospheric contaminants. All these elements contribute individually and in combination to change the properties of the coating. Water or moisture can have a great affect on the degradation of coatings. Chemically, hydrolysis of the polymer can occur, which can result in microcracking, degradation, and physically, expansion/contraction, or a pigment-polymer bond can be attacked, which can result in premature chalking and a short coating life. The natural process of fatigue in coatings leads to microcracking and other forms of microdamage. Eventually these microcracks coalesce (*10–12*) to form cracks that propagate and lead to a large scale coating failure including delamination and corrosion of the substrate. Similarly, excessive heat build-up in the coating can result in migration of additives and stress build-up leading to crack formation and eventually loss of coating properties. In practice, certain additives are included in coating formulation that dissipate heat, absorb UV light, and capture free radicals generated during such exposure.

The durability of man-made materials and the products made thereof is often limited by the absence of built-in "self-healing" mechanisms. Polymers have a finite lifetime; their inherent properties degrade with age (*13*). The traditional approach for maintaining predefined properties of polymers and coatings has been to include certain additives in coating formulation that reduce the impact of environmental stress and natural fatigue. However, additives may also become fugitive materials, react or interact with other coating ingredients, migrate out or deplete over time and under adverse environmental service conditions.

Synthetic materials have a fixed property profile and are designed to behave statically and to deliver certain predefined functions. In contrast to synthetic materials, in an attempt to survive, many living biological systems react to external stresses and damage by providing an autonomic healing response at the site of injury (*14*) Often this occurs by the plant or animal secreting various agents when the integrity of the system is compromised, causing filling healing and/or regeneration at the damaged location (*15*). For example, the highly

Downloaded by 89.163.35.42 on June 22, 2012 | http://pubs.acs.org
Publication Date (Web): November 10, 2010 | doi: 10.1021/bk-2010-1050.ch001

hierarchical structures of skeletal bone (*16*) enables biological fluids containing clotting agents, nutrients, and stem cells to flow from the network of blood vessels into a fractured region upon injury, facilitating over time the development of fibrocartillage, which calcifies into fibrous bone (*14*, *16*). This process forms new bone that is essentially indistinguishable from uninjured bone tissue.

The surface oxides on aluminum and aluminum alloys can be called "self-healing" in that they quickly re-form after scratching. Self-healing has also been reported on various other metals and alloys such as steel (*17*), metal oxide composites and SiC and MoSi2 heating elements, which form a protective amorphous silica coating on their surfaces after being scratched (*18–21*).

Chromate-based self-healing paint systems have been used to provide corrosion protection to aluminum alloys for many decades. Chromate inhibits corrosion by leaching from the primer, migrating through condensed moisture on the surface and reacting with actively corroding sites, thereby resulting in passivation (*22–25*). In a recent work, Hikasa et al. (*26*) used the volume expansion of clays to create self-healing ceramic-type coatings while, Miccichè et al. (*27*) demonstrated the self-healing properties of montmorillonite clay in a two-layer coating system. In recent years, autonomic healing has also been studied within the context of concrete by various investigators (*28–30*).

The concept of healing polymers was established in the 1980's, but the presentation of self-healing polymer composites by Dry (*31*) in 1993 followed by the well-cited White (*32*) publication in 2001 inspired world wide interest in these materials (*33–42*). Self-healing and self-repair concepts, using both organic and inorganic materials have been applied to composites, plastics, concrete, adhesives, and artificial skin (*43–52*).

The method of thermally reversible crosslinking in composites was introduced in 2002 (*50*) using Diels-Alder based cycloaddition of polymer chains containing multi-furan and multi-maleimide functionalities. More recently, thermal repair of composites using epoxy compounds (*51*) was demonstrated.

Design, formulation and characterization of self-healing coatings would obviously be an advantage but it presents unique challenges to overcome. Compared to bulk materials, coatings challenge us even more as thin film layers limit, to some extent, the size and distribution of healing agents along the coating film. For a coating film to heal, the mobility or transport of healing agents to the damaged area is essential and a suitable transport mechanism under the condition imposed by the physical and chemical properties of coatings is of utmost importance. Self-healing is one of the most sought after topics in the family of "smart coatings (*53*)."

Most of the efforts in self-healing polymers, composites, metals, etc., have been concentrated on the repair caused by mechanical forces. In this work we focus on physiochemical stimuli that in general result in coating degradation and failure. Therefore in these systems, where the factors which cause the damage are the factors that contribute its repair, damage control can be much more effective to enhance the performance properties and increase functional life of the systems. In this work, we report on a unique extension of the self-healing concept as it is applied to ordinary coatings.

Downloaded by 89.163.35.42 on June 22, 2012 | http://pubs.acs.org
Publication Date (Web): November 10, 2010 | doi: 10.1021/bk-2010-1050.ch001

Downloaded by 89.163.35.42 on June 22, 2012 | http://pubs.acs.org
Publication Date (Web): November 10, 2010 | doi: 10.1021/bk-2010-1050.ch001

Experimental

Various poly-and diisocyanates including 1,6 hexamethylene diisocyanate (HDI), Isophorone diisocyanate (IPDI) and 4,4′-diphenylmethane diisocyanate (MDI) were obtained from Aldrich-Sigma or Bayer Material Sciences and were encapsulated by depositing thermoplastic polyalkyl acrylate resins over either liquid or solid di-and polyisocyanate particles to afford dry particles ranging from 5-100 micron in size. A typical polyalkyl acrylate, Intelimer IPA 13-1 having a sharp melting point of 45 °C was obtained from Landec Corporation (now Air Products & Chemicals). Other polyalkyl acrylates having sharp melting points of 58, 65 and 92 °C were synthesized according to established procedures. The particle size of microcapsules in general was observed to be the function of core size, type of surfactant, temperature and the rate of dispersion. Anionic surfactant sodium dodecylsulfate and non-ionic ethoxlated nonylphenol and Triton X-100 (Dow Chemical) were used as received. The encapsulation processes were carried out at temperatures ranging from 1-40 °C. The stirring rates ranged from 500-10,000 RPM at various stages of the encapsulation process. The microcapsules were analyzed by FTIR, ATIR, SEM/EDXA and optical microscopy. The dry microcapsules were stored at temperatures below 40 °C and under dry conditions up to 180 days without agglomeration or caking. The base polyurethane coating was prepared by reacting Desmodur Z4470 BA (Bayer Material Sciences) with high solid acrylic polyol resin Joncryl 910 (BASF Corp.). The samples of polyurethane coatings were cured at room for 72 hours. In general, ATIR and FTIR spectroscopy confirmed the absence of isocyanate bands after 72 hours at ambient temperature. The self-healing compositions were prepared by incorporating various types (shell temperature melting points) about 3-7% wt/wt microcapsules in a two-component polyurethane formulation. Polyurethane coatings were applied onto clean steel panels at a dry film thickness in the range of 35-60 microns and cured at room temperature for 72 hours before subjecting to various evaluations.

Exposure and Characterization

Accelerated weathering was performed in Xenon Q-Sun test chamber following ASTM G155-05a with 102 minutes light plus 18 minutes light plus sprays. Thermocouple measurements indicated the air temperature at 55 °C and the coating film temperature at 51 °C during the hot cycle. The samples were viewed and rated for general appearance, gloss and color every 250 hour. Stress-strain determination studies were conducted using an Instron 5545 tensile testing machine. Free films of sample coatings were made by applying the coatings onto DuPont Tedlar® film. Samples free of visible defects were cut with a die following ASTM 412 type C with a gauge length of 50.00 mm. The crosshead speed was 50.0 mm/min. Stress strain analysis was also conducted using a Dynamic Mechanical Analyzer.

Downloaded by 89.163.35.42 on June 22, 2012 | http://pubs.acs.org
Publication Date (Web): November 10, 2010 | doi: 10.1021/bk-2010-1050.ch001

Water Vapor Transmission and Corrosion Testing

The water permeability of test specimens was investigated according to ASTM Test Method D1653. Six samples each of the control and the self-healing coating, both exposed and unexposed free films were fixed in permeability cups filled (dia 0.018 m) with DI water in the cup and initial weights of each total assembly were recorded. The permeability cups were placed in a controlled environment in a desiccator.

The standard corrosion test of ASTM B117 was carried out. The distinct styles of exposure were as following:

> Scribed and then exposed, (XE)
> Scribed, heated (45 °C, 10 min.) and exposed, (XHE)
> Scribed, exposed to corrosion chamber for 100 hours, heated for 10 minutes and again exposed, (XEHE)
> Heated to 45 °C, scribed and exposed, (HXE)

Results and Discussion

In an effort to mimic self-healing functions in living systems, here we discuss the development of polymeric coating systems that are stimuli responsive. The most attractive feature of this system is that the factors that damage the coating the most, such as humidity, exposure to high temperatures etc., are the same factors that initiate self-healing phenomenon. This property is unique since the extent of the healing is proportional to the magnitude of the damage, i.e., repair on demand.

Such compositions contain micro capsules evenly dispersed in the coating systems. These capsules contain reactive polymers or un-reacted monomers and crosslinkers (mainly HDI). The outer shell of the capsules is made of a material with some distinctive property depending on the mechanism adopted for self-healing. In this investigation we have chosen a series of polyalkyl acrylate polymers with sharp melting points in the range of 45-92 °C. Representative chemical structure of a typical polyalkyl acrylate is shown in Fig. 1.

Upon exposure to temperatures above the melting point threshold, the shells soften or melt allowing the encapsulated healing agent to release into cracks and voids created by stress and water ingression due to natural aging. This gradual release of the healing agent and its mixing with water and other available reactive functional groups initiate and promote polymerization in the voids and cracks, thereby repairing the damage. Schematic representation of the concept is shown in Fig. 2.

The microcapsules were prepared using a modified procedure used by other investigators (*32–41*). The particle size in general was observed to be the function of core size, type of surfactant, temperature and the rate of dispersion. The quality as well as stability of dispersions were improved with the increase in amount of surfactant used. The best combination was found to be a 50/50 mixture of sodium dodecylsulfate and ethoxylate nonylphenol surfactants. In general, smaller particle size was achieved using higher amounts of surfactant. However, at higher levels

Downloaded by 89.163.35.42 on June 22, 2012 | http://pubs.acs.org
Publication Date (Web): November 10, 2010 | doi: 10.1021/bk-2010-1050.ch001

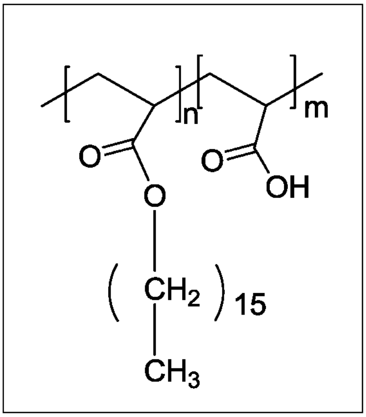

Figure 1. Representative chemical structure of polyalkyl acrylate.

of surfactant, intense foaming occurs that requires reduced dispersion speeds and the addition of a defoaming agent.

Since the core, either in liquid or in solid phase was selected from a group of di-and polyisocyanate materials, the exposure to water was minimized. It was observed that by maintaining water temperature close to 1°C urea formation was minimized and the activity of the healing agent was preserved. The stirring rates ranged from 500-10,000 RPM at various stages of the encapsulation process.

The particle size determination confirmed that the microcapsules were stable at 40% relative humidity and 25 °C for up to 180 days. Further confirmation of their stability to coating ingredients was verified by mixing the capsules with polyol and solvents under various mixing and dispersion shear forces. In all cases an IR spectrum was obtained which did not reveal an NCO band around 2260 cm^{-1}. The mixture was also titrated for NCO content.

The self-healing compositions were prepared by incorporating about 3-7% wt/wt microcapsules in two component polyurethane formulations. A typical formulation contained 2.5% each of microcapsules with melting points of 45 and 92 °C. The identity of the microcapsules were verified by first washing the dry capsules with acetone and toluene until the washings were free of any isocyanate functionality as indicated by ATIR. Following the removal of residual isocyanate, a small number of fine capsules were crushed by pressing against a clean glass slide. An immediate FTIR analysis indicated a sharp peak at 2260 cm^{-1} confirming the identity of the core material.

Characterization and Performance Evaluation

Characterization of capsules is carried out using SEM/EDXA. In order to identify the composition of the healing agent, fluorine or silicon labeled isocyanate was used as the core material. The washed microcapsules were then cooled in liquid nitrogen and were crushed immediately before placing onto SEM pad. Scanning Electron Microscopy images of various microcapsules with varied shell thicknesses and core sizes are shown in Fig. 3.

Downloaded by 89.163.35.42 on June 22, 2012 | http://pubs.acs.org
Publication Date (Web): November 10, 2010 | doi: 10.1021/bk-2010-1050.ch001

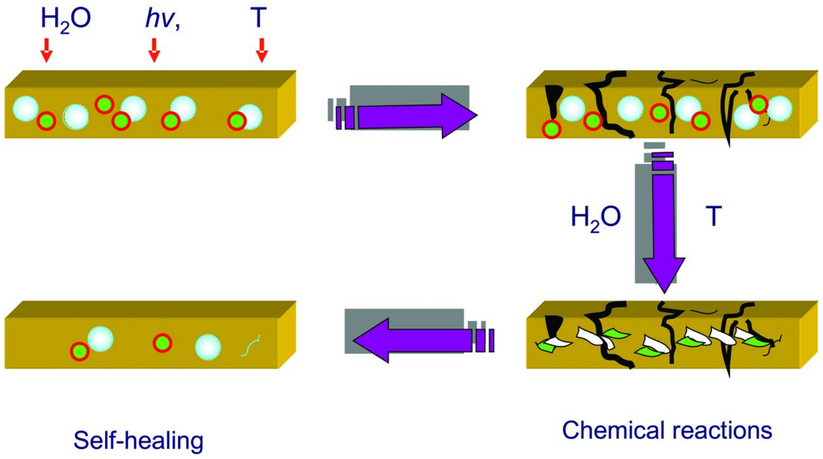

Figure 2. Schematic representation of self-healing concept.

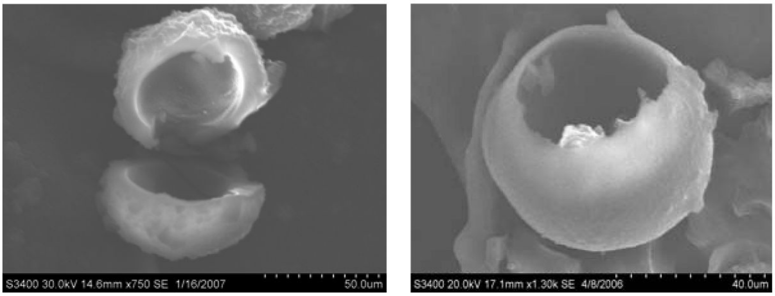
S3400 30.0kV 14.6mm x750 SE 1/16/2007
50.0um
S3400 20.0kV 17.1mm x1.30k SE 4/8/2006
40.0um

a

b

Figure 3. SEM images (a), a crushed and vacant capsule (b), an empty shell.

To further characterize the microcapsules, both shell (Intelimer) and poly/diisocyanate were separately observed using a DAPI filter and reflected light. As can be seen from Fig. 4a, the pure isocyanate material is fluorescent. In contrast, Fig. 4b, the shell containing mostly acrylic and alkyl moieties does not respond to fluorescent light. As can be seen in Fig. 4c, the crushed microcapsule shows the released isocyanate material as fluorescent compared to the shell material.

The healing performance was assessed by incorporating various amounts of the healing agent in a standard polyurethane coating formulation. The polyurethane coating was made by combining appropriate amounts of acrylic polyol, Joncryl 910, and various di-trimer and polyisocyanates such as HDI, IPDI, and HMDI, and necessary additives and pigments. The prototype self-healing formulation contained the same ingredients and ratios except that it contained 3-7% wt/wt of microcapsules with an average particle size of 20 microns. In general, the coatings were applied by a draw down technique and were allowed to cure at 40-50% humidity and 20-28 °C, for 72 hours. SEM images of cross sections of the self-healing coating are shown in Fig. 5.

Downloaded by 89.163.35.42 on June 22, 2012 | http://pubs.acs.org
Publication Date (Web): November 10, 2010 | doi: 10.1021/bk-2010-1050.ch001

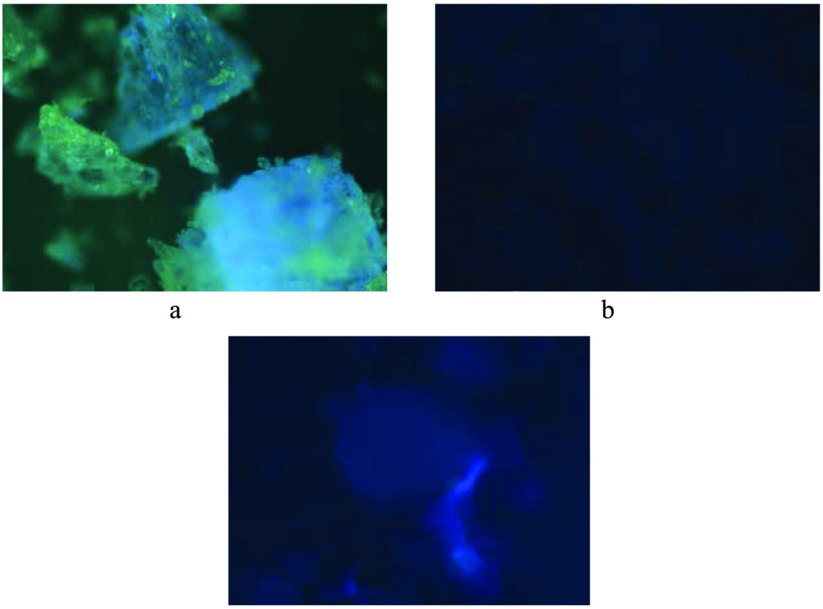

a b c

Figure 4. (a), Crushed piece of a solid isocyanate crosslinker observed under fluorescent light; (b), pure shell polymer (Intelimer®) observed under fluorescent light; (c), Crushed microcapsule observed under fluorescence and reflected light.

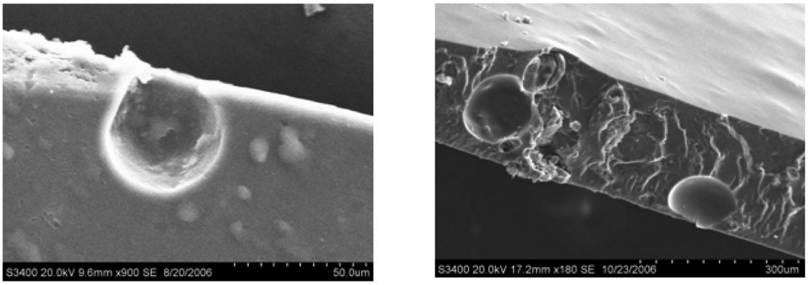
S3400 20.0kV 9.6mm x900 SE 8/20/2006 50.0um
S3400 20.0kV 17.2mm x180 SE 10/23/2006 300um

Figure 5. SEM images of a cross-section of self-healing coating.

Optical Microscopy and SEM Characterization

Inclusion and the dispersion of microcapsules in coating media and the release of the healing agent, their diffusion and their conversion to polymeric material were confirmed by SEM and EDXA images. As shown in Fig. 6, the microcapsules have uniformly been distributed in the coating media.

Similarly, the SEM images of the control polyurethane coating and the self-healing coatings along with various modes of embedded microcapsules in the media are shown in Fig. 7.

Downloaded by 89.163.35.42 on June 22, 2012 | http://pubs.acs.org
Publication Date (Web): November 10, 2010 | doi: 10.1021/bk-2010-1050.ch001

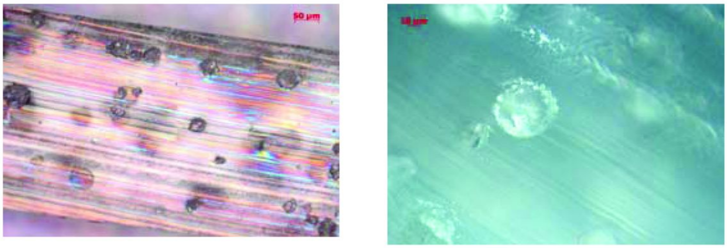

a b

Figure 6. Optical microscopy images of self-healing coating under BF transmitted light (a), viewed under BF fluorescence (b).

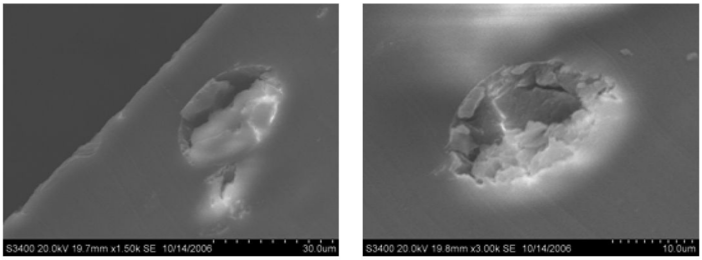
S3400 20.0kV 19.7mm x1.50k SE 10/14/2006
30.0um
S3400 20.0kV 19.8mm x3.00k SE 10/14/2006
10.0um

a b

Figure 7. SEM image of a Microcapsule embedded in self-healing coating (a); a broken microcapsule with healing agent (b).

In general, the self-healing properties were assessed by subjecting panels of both control and prototype self-healing coatings to various simulated environmental conditions through accelerated laboratory exposure testing such as high temperature and humidity, mechanical damage, water vapor transmission and salt spray, for specified periods.

Mechanical Properties

The healing of the coating is demonstrated by comparing the stress-strain behaviors of exposed and unexposed samples of the coatings. For this purpose, the free-film samples of controls and self-healing coatings (SH) were stored in controlled environmental conditions of 65-70% relative humidity and 45-50 °C temperature for 24 hours. As can be seen from the dynamic mechanical analysis (DMA) curves in Fig. 8 (a & b), the control sample (a), lost quite a bit of its initial strength accompanied by substantial gain in strain values presumably due to plasticization by water. In contrast, the sample containing the self-healing agent (b) responded favorably to exposure conditions by an increase in modulus and a negligible decrease in elongation. Such behavior may be explained by reduction in free volume, voids and cracks and the tighter packing of the already cured and adhered coating due to healing resulting in added crosslinking and repair.

Downloaded by 89.163.35.42 on June 22, 2012 | http://pubs.acs.org
Publication Date (Web): November 10, 2010 | doi: 10.1021/bk-2010-1050.ch001

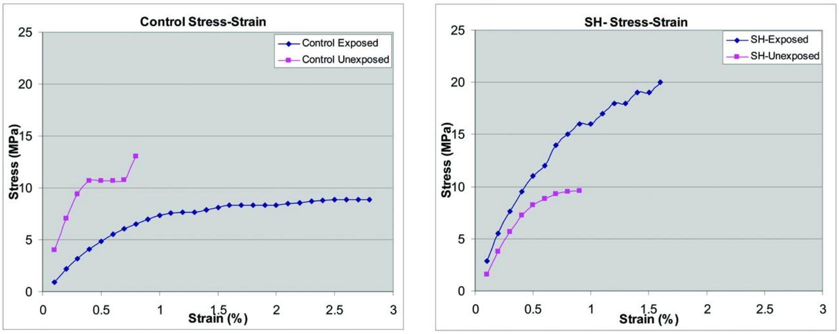

a

b

Figure 8. Control without healing agent (a), -■- Control unexposed, -◆- Control exposed at 65-70% RH, 45-50 °C; sample with healing agent (b), -■- SH-unexposed, -◆- SH-exposed.

Even though the most important feature of this self-healing composition is its stimuli responsive ability which allows healing to proceed on demand, it is interesting to investigate the coating properties if the healing agent was included without encapsulation in the original formula. Since gains in performance are presumed to be due to higher crosslinking, or reduction in void volumes, one may suspect that the addition of similar amounts of the healing agent to the formulation might produce similar performance. This hypothesis was put to test by formulating a coating with a pure (un-encapsulated) healing agent in addition to the base composition. First, due to imbalance of the ingredients, the coating required in excess of 140 hrs (twice as long as the self-healing composition of 72 hrs) to reach a tack-free stage. Second, the coating, after full cure, lost its flexibility and developed cracks once exposed to high temperature and humidity conditions.

Tensile Strength and Hardness

A similar trend is also observed when the free-film samples of a control and a self-healing coating are tested according to ASTM D638, Tensile Properties of Plastics; and ASTM D1474, Indentation Hardness Test methods. As can be seen from Table I, the average tensile value of the exposed (48 hr @ 45 °C and 65%RH) control polyurethane coating increased about 5%, presumably due to the reaction of unreacted isocyanate groups accompanied by an expected increase in elongation and reduction in coating hardness due to plasticization by water. On the other hand, exposure of the self-healing coating results in an increase of about 25%, accompanied by negligible increase in elongation and the fair amount of increase in surface hardness.

The coating hardness appears to follow the same trend. As can be seen from Table I, the exposed control sample has become slightly softer than the unexposed sample, presumably due to ingression of water and plasticization effect. Again, and in accordance with DMA results (Fig. 8), the self-healing sample has gained

Downloaded by 89.163.35.42 on June 22, 2012 | http://pubs.acs.org
Publication Date (Web): November 10, 2010 | doi: 10.1021/bk-2010-1050.ch001

Table I. Tensile, Elongation and Surface Hardness Comparison of Control and Self-healing Coating

Sample	Tensile (Psi)	Strain %	KHN, Hardness
Control. Unexposed	31.29	14.75	3.38
Control. Exposed*	33.05	16.91	3.32
SH55 Unexposed	32.12	13.77	3.56
SH55 Exposed	40.34	15.13	4.08

* 48 hours at 45 °C, 65% RH; SH, self-healing.

about 15% in hardness value which confirms the self-healing action. It is also interesting to note that the unexposed self-healing sample has also gained about 5% in hardness as compared with unexposed sample. Assuming that the baseline for both samples is the same, the gain in hardness may be due to the rupture of a small number of microcapsules during sample preparation followed by environmental condition prior to testing.

Water Vapor Permeability

The water vapor permeability of test specimens was investigated according to ASTM D1653. Two samples each of the control and the self-healing coating both exposed and unexposed free films, were fixed in permeability cups filled with DI water in the cup and initial weights of each total assembly were recorded. The permeability cups were placed in a controlled environment in a desiccator. The weights of the cups were monitored on a daily basis and change in weight was recorded. As can be seen from the charts in Figures 9 and 10, after 21 days of the water vapor permeability study, the exposed self-healing (ES) films showed the least change in weight. Both exposed and unexposed control films showed a significant amount of loss of water. The lower water vapor permeability of self-healing films presumably indicates lower porosity due to higher extent of cross linking. The unexposed self-healing films also showed less water vapor permeability toward water vapor as time proceeded, which might be attributed to reaction of isocyanate with water vapor as a result of rupture and healing agent release under mechanical forces during sample preparation.

Accelerated Exposure Effect

A decrease in coating mechanical and cohesive properties and possibly in crosslink density might reflect a loose and collapsed structure with exposure to accelerated weathering (*1*). As can be seen in Figs. 11a (control), and 11b (self-healing), the control sample after 369 hours severely cracked and lost coating integrity. In contrast, the self-healing coating sample under the same conditions,

Downloaded by 89.163.35.42 on June 22, 2012 | http://pubs.acs.org
Publication Date (Web): November 10, 2010 | doi: 10.1021/bk-2010-1050.ch001

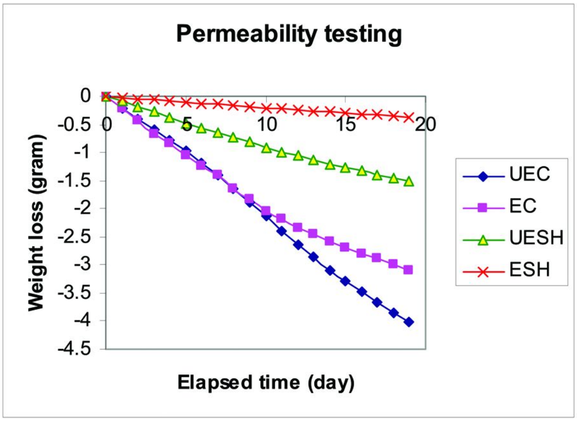

Figure 9. Water vapor permeability performance of control and self-healing coating films. U, unexposed; E, exposed; C, control; SH, self-healing.

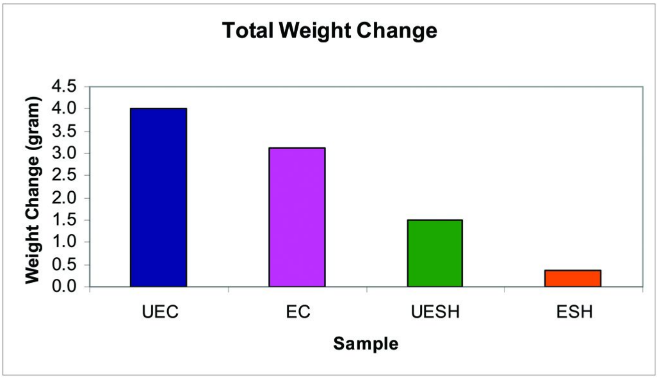

Figure 10. Comparative water vapor permeability of control and self-healing polyurethane coating. U, unexposed; E, exposed; C, control; SH, self-healing

while yellowed, retained its mechanical integrity. The decay of coatings without ultraviolet light and hindered amine light stabilizers is common and has been well-documented to be due to a wide variety of factors including molecular chain scission under the exposure condition. The increase weathering durability may be explained in terms of further fortification of the coating under the conditions of the exposure as a result of self-healing phenomenon which also correlated with the improved water vapor permeability discussed earlier.

Corrosion Testing

There were two objectives for corrosion testing; the first was to confirm self-healing function, and the second was to study if the self-healing feature would help to improve the corrosion resistance of prototype coatings during accelerated corrosion testing. The sample size was six panels each of the control and SH coatings. Half of the cured panels of each type were X scribed. Additionally, only half of the total panels of each type were X scribed. After that, certain panels were again put in an oven for 10 minutes at 45 °C. The idea was that the panels in which the capsules were embedded will have a self-healing effect around the X scribed area and it will act, at the least to partially heal the scratch. If healing occurs, the corrosion on that panel would be lower since lesser amount of salt water would penetrate inside. Other panels from each pair were only heated along with the X scribed panels and will be X scribed before putting them in the testing environment. In these panels, if the adhesion would have increased due to the cross-linking, we would observe less corrosion compared to the standard panels.

The distinct styles of exposure were as following: Scribed and then exposed, (XE), scribed, heated (45 °C, 15 min.) and exposed, (XHE), scribed, exposed to corrosion chamber for 100 hours, heated for 10 minutes and again exposed, (XEHE), heated to 45 °C, scribed and exposed, (HXE).

The self-healing and control panels for corrosion testing were observed every 100 hours and the change in appearance or development of corrosion on the panels was observed and rated according to ASTM/FSCT corrosion rating standard. The extent and progress of corrosion on control and self-healing panels are shown in Fig. 12.

The results of corrosion testing of the panels coated with control and self-healing polyurethane coatings confirmed the self-repair phenomenon triggered by the conditions of exposure and treatments. As can be seen in Fig. 12, all control panels corroded shortly after the exposure began. In contrast, all self-healing specimens resisted corrosion up to 400 hours of salt spray and when the corrosion began the progress and rate of corrosion was much slower than that of control panels. This trend indicates that the microcapsules' release of the healing agent, either during initial heat aging, or upon the mechanical forces of scribe or due to the diffusion of salt water during the exposure period.

The photographs of both the control and self-healing polyurethane panels with various treatments prior to and after exposure to salt spray, are shown in Fig. 13. As can be seen from these images, there is little or no presence of corrosion and creep in SH panels, which showed very good adhesion and lower voids presumably due to higher crosslinking and better polymer packing. Another positive observation was the partial healing of the scribe. In addition, it was observed that the depth of the scribe had significantly decreased after the exposure.

The corrosion resistance of the self-healing coating (Fig. 13b) is quite interesting. Even though the panels were not heat treated prior to salt spray testing, the self-healing sample still performed identical to those of heat treated specimens. This phenomenon may be explained by noting that during the salt spray some salt water may have diffused into the capsules resulting in increased osmotic pressure and ultimately leading to the rupture of the shell.

Thus, it is safe to conclude that the factors that damage the coating the most, such as humidity, exposure to high temperatures etc., are the same factors that initiate self-healing function in the above composition.

Downloaded by 89.163.35.42 on June 22, 2012 | http://pubs.acs.org
Publication Date (Web): November 10, 2010 | doi: 10.1021/bk-2010-1050.ch001

Downloaded by 89.163.35.42 on June 22, 2012 | http://pubs.acs.org
Publication Date (Web): November 10, 2010 | doi: 10.1021/bk-2010-1050.ch001

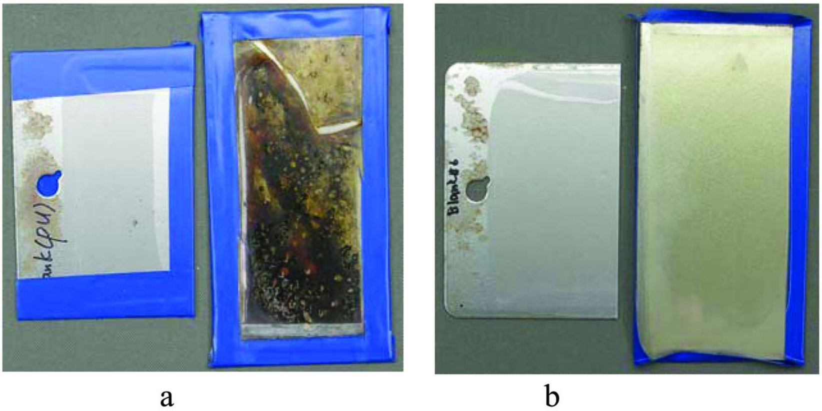
ank(PU)
Blank#6
a
b

Figure 11. Control polyurethane after 369 hours accelerated weathering (a, left unexposed), self-healing polyurethane (b, left unexposed).

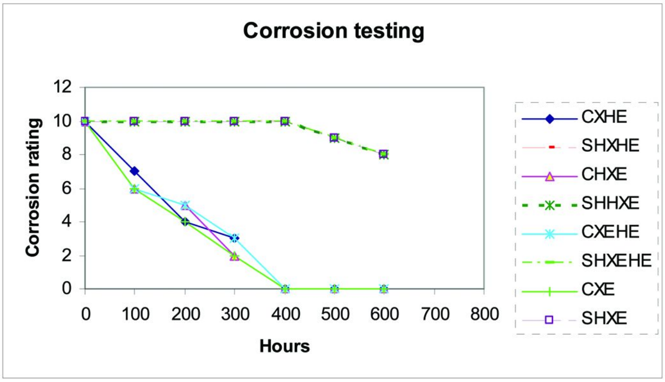

Figure 12. Corrosion testing of the control and self healing panels following the above protocol. C, control; SH, self-healing, X, scribed; H, heated; E, exposed.

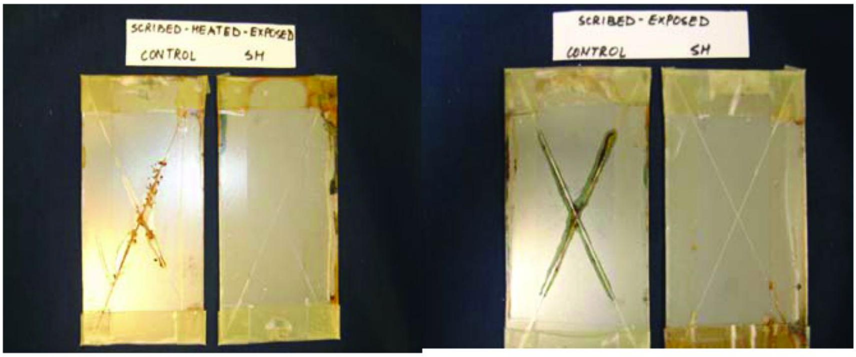
SCRIBED - HEATED - EXPOSED
CONTROL
SH
SCRIBED - EXPOSED
CONTROL
SH

Figure 13. Corrosion test panels: Control and SH- (a) scribed/heated/exposed; (b) scribed/exposed.

Downloaded by 89.163.35.42 on June 22, 2012 | http://pubs.acs.org
Publication Date (Web): November 10, 2010 | doi: 10.1021/bk-2010-1050.ch001

Conclusions

This research work investigated and applied the self-healing concept to ordinary thin film polyurethane coatings. Microcapsules with a shell composed of a thermoplastic polymer with a sharp melting point containing poly- and diisocyanate crosslinking agents were prepared. Observations and investigations indicated that the microcapsule size can be controlled by factors such as the chemical nature, ratios and the amount of surfactant used. In addition, it was found out that the particle sizes of the microcapsules were affected by the dispersion speed and the process temperature.

Prototype acrylic polyurethane coatings using commercial raw materials were made both as control and as self-healing coatings. The self-healing coatings contained an average of 3-7% of microcapsules on w/w basis. The best formulation for a two-part room temperature composition was determined to contain microcapsules with shell polymer melting temperatures of 45 and 65 °C, while forced air dry versions required microcapsules with 92 °C shell melting point. The two-part self-healing polyurethane composition was confirmed to be stable when stored at below the melting temperature of the shell polymer.

The release of the healing agent triggered by heat, excessive moisture and mechanical damage was confirmed through direct observation and characterization. It was confirmed that the natural aging, at least within the experimental time frame, resulted in self-healing as a response to environment stimuli, and rejuvenation and restoration or improvement of initial mechanical properties of the coating. In addition, accelerated exposure evaluation indicated that the self-healing feature can control or prevent coatings from premature crack propagation thereby improving coating durability and performance.

The self-healing performance was assessed through observation of improved key coating properties. The corrosion resistance of the self-healing coating proved to be significantly better than that of the control. In addition, the water vapor permeability of the self-healing coating was observed to be much less than that of the control samples which confirmed the self-healing process. Developments in self-healing technology have opened a new area of multifunctional coatings with the potential to increase the service of surface coatings.

References

1. Shi, X.; Fernando, B. M. D.; Croll, S. Concurrent Physical Aging and Degradation of Crosslinked Coating Systems in Accelerated Weathering. *J. Coat. Technol. Res.* **2008**, *5* (3), 299–309.
2. Nichols, M. E. Anticipating Paint Cracking: The Application of Fracture Mechanics to Paint Weathering. *J. Coat. Technol.* **2002**, *74*, 39.
3. Ochs, H.; Vogelsang, J.; Meyer, G. Enhanced Surface Roughness due to UV-Degradation: An Unknown Source of EIS-Artifacts. *Prog. Org. Coat* **2003**, *46*, 182–190.
4. Perera, D. Y. Physical Aging of Organic Coatings. *Prog. Org. Coat.* **2003**, *47*, 61–76.

5. Huang, Y.; Paul, D. R. Experimental Methods for Tracking Physical Aging of Thin Glassy Polymer Films by Gas Permeation. *J. Membr. Sci.* **2004**, *244*, 167–178.
6. Huang, Y.; Wang, X.; Paul, D. R. Physical Aging of Thin Glassy Polymer Films: Free Volume Interpretation. *J. Membr. Sci.* **2006**, *277*, 219–229.
7. Skaja, A.; Fernando, D.; Croll, S. G. Mechanical Property Changes and Degradation during Accelerated Weathering of Polyester-Urethane Coatings. *J. Coat. Technol.* **2006**, *3*, 41–51.
8. Perera, D. Y. Effect of Thermal and Hygroscopic History on Physical Ageing of Organic Coatings. *Prog. Org. Coat.* **2002**, *44*, 55–62.
9. Martin, J. W.; Saunders, S. C.; Floyd, E. L.; Wineburg, J. P. Methodologies for Predicting the Service Lives of Coating Systems. *Federation Series on Coatings Technology, FSCT*, 1996.
10. Nairn, J. A.; Kim, S. R. *Eng. Fract. Mech.* **1992**, *42*, 195.
11. Hsieh, A. J.; Huang, P.; Venkataraman, S. K.; Kohlstedt, D. L. *Mat. Res. Cos. Symp. Proc.* **1993**, *308*, 653.
12. Kim, S. R.; Nairn, J. A. *Eng. Fract. Mech.* **2000**, *65*, 595.
13. Wudl, F.; Bergman, S. Mendable Polymers. *J. Mater. Chem.* **2008**, *18*, 41–62.
14. Kessler, M. R. Self-Healing: A New Paradigm in Materials Design. *Proc. IMechE* **2007**, *221* (Part G).
15. Zhou, B. L. Some Progress in the Biomimetic Study of Composite Materials. *Mater. Chem. Phys.* **1996**, *45* (2), 114–119.
16. Weiner, S.; Wagner, H. D. The Material Bone: Structure-Mechanical Function Relations. *Annu. Rev. Mater. Sci.* **1998**, *28*, 271–298.
17. Shinya, N.; Kyono, J.; Laha, K. *J. Intell. Mater. Syst. Struct.* **2007**, *17*, 1127.
18. Files, B.; Olson, G. Terminator 3: Biomimetic Self-Healing Alloy Composite in SMST-97. *Proceedings of the Second International Conference on Shape Memory and Super elastic Technologies*; 1997.
19. Ando, K.; Houjyou, K.; Chu, M. C.; Kakeshita, S.; Takahashi, K.; Sakamoto, S.; Sato, S. *J. Eur. Ceram. Soc.* **2002**, *22*, 1339.
20. Callister, W. D. *Materials Science and Engineering: an Introduction*, 6th ed.; John Wiley & Sons: New York, 2003.
21. Govindarajan, S.; Mishra, B.; Olson, D. L.; Moore, J. J.; Disam, J. *Surf. Coat. Technol.* **1995**, *76*, 7.
22. Scholes, H.; Furman, S. A.; Hughes, A. E.; Nikpour, T.; Wright, N.; Curtis, P. R.; Macrae, C. M.; Intem, S.; Hill, A. J. *Prog. Org. Coat.* **2006**, *56*, 23–32.
23. Furman, S. A.; Scholes, F. H.; Hughes, A. E.; Lau, D. *Prog. Org. Coat.* **2006**, *56*, 33–38.
24. Scholes, F. H.; Furman, S. A.; Hughes, A. E.; Tuomisto, F.; Saarinen, K.; Pas, S. J.; Hill, A. J. *J. Coat. Technol. Res.* **2006**, *3*, 105–108.
25. Furman, S. A.; Scholes, F. H.; Hughes, A. E.; Jamieson, D. N.; Macrae, C. M. *Corros. Sci.* **2006**, *48*, 1827–1847.
26. Hisaka, T.; Sekino, Y.; Hayashi, R.; Rajagopalan, K.; Nikara *Mater. Res. Innovations* **2004**, *8*, 84–88.
27. Micciche, F.; Fischer, H.; Varley, R.; Zwaag, S. Self-Healing Barrier Coating Using an Expandable Phase. *Proc. Intl. Conference Self-healing*; 2007.

Downloaded by 89.163.35.42 on June 22, 2012 | http://pubs.acs.org
Publication Date (Web): November 10, 2010 | doi: 10.1021/bk-2010-1050.ch001

28. Dry, C. Matrix Cracking Repair and Filling Using Active and Passive Modes for Smart Timed Release of Chemicals from Fibres into Cement Matrices. *Smart Mater. Struct.* **1994**, *3* (2), 118–123.
29. Li, V. C.; Lim, Y. M.; Chan, Y. W. Feasibility Study of a Passive Smart Self-Healing Cementitious Composite. *Compos., Part B* **1998**, *29* (B), 819–827.
30. Mihashi, H.; Kaneko, Y.; Nishiwaki, T.; Otsuka, K. Fundamental Study on Development of Intelligent Concrete Characterized by Self-Healing Capability for Strength. *Transactions of the Japan Concrete Institute* **2000**, *22*, 441–450.
31. Dry, C. M.; Sattos, N. R. Passive Smart Repair in Polymer Matrix Composite Materials. *North American Conference on Smart Structures Materials*, Albuquerque, NM, Jan 31−Feb 4, 1993; pp 438−444.
32. White, S. R.; Sottos, N. R. Autonomic Healing of Polymer Composites. *Nature* **2001**, *409*, 794–797.
33. Meure, S.; Wu, D. Y. The Biomimetic Approach to Self-Healing Polymer Composite Development in the Aerospace Industry. *Self-healing Mater. Proc. 1st Intl. Conference*; 2007.
34. Rule, J. D.; Sottos, N. R.; White, S. R.; Moore, J. S. The Chemistry of Self Healing Polymers. *Educ. Chem.* **2005**, *42*, 130–132.
35. Wool, R. P. A Material Fix. *Nature* **2001**, *409*, 794–797.
36. Brown, E. N.; Kesslers, M. R.; Sottos, N. R.; White, S. R. In situ Poly(urea formaldehyde) Microencapsulation of Dicyclopentadiene. *J. Microencapsulation* **2003**, *20* (6), 719–730.
37. Brown, E. N.; Sottos, N. R.; White, S. R. Fracture Testing of a Self Healing Polymer Composite. *Exp. Mech.* **2002**, *42* (4), 372–379.
38. Kessler, M. R.; Sottos, N. R.; White, S. R. Self Healing Structural Composite Materials. *Compos., Part A* **2003**, *34*, 743–753.
39. Brown, E. N.; White, S. R.; Sottos, N. R. Retardation and Repair of Fatigue Cracks in a Microcapsule Toughned Epoxy Composite- Part I: Manual Infiltration. *Composite Sci. Technol.* **2005**, *65*, 2466–2473.
40. Brown, E. N.; White, S. R.; Sottos, N. R. Retardation and Repair of Fatigue Cracks in a Microcapsule Toughened Epoxy Composite- Part II: In situ Self Healing. *Composite Sci. Technol.* **2005**, *65*, 2474–2480.
41. Brown, E. N.; Jones, A. S.; White, S. R.; Sottos, N. R. Fracture and Fatigue Behavior of a Self Healing Polymer Composite. *Mater. Res. Soc. Symp. Proc.* **2003**, *735*, C11.22.1–c11.22.6.
42. Brown, E. N.; White, S. R.; Sottos, N. R. Microcapsule Induced Toughening in a Self Healing Polymer Composite. *J. Mater. Sci.* **2004**, *39*, 1703–1710.
43. Cho, S. H.; Andersson, H. M.; White, S. R.; Sottos, N. R.; Braun, P. V. Polydimethylsiloxane Based Self Healing Materials. *Adv. Mater.* **2006**, *18*, 997–1000.
44. Yin, T.; Rong, M. Z.; Zhang, M. Q.; Yang, G. C. Self Healing Epoxy Composites- Preparation and Effect of the Healant Consisting of Microencapsulated Epoxy and Latent Curing Agent. *Compos. Sci. Technol.* **2007**, *67*, 201–212.
45. Balkus, K. J.; Liu, H. A.; Gnade, B. E. A Delivery System for Self-Healing Inorganic Film. *Adv. Funct. Mater.* **2008**, *18*, 3620–3629.

Downloaded by 89.163.35.42 on June 22, 2012 | http://pubs.acs.org
Publication Date (Web): November 10, 2010 | doi: 10.1021/bk-2010-1050.ch001

46. Sugama, T.; Gawlik, K. Self Repairing Poly(phenylenesulfide) Coatings in Hydrothermal Environments at 200 deg C. *Mater. Lett.* **2003**, *57*, 4282–4290.
47. Ando, K.; Kim, B. S.; Chu, M. C.; Saito, S.; Takahashi, K. Crack Healing and Mechanical Behavior of Al_2O_3/SiC Composites at Elevated Temperature. *Fatigue Fract. Eng. Mater. Struct.* **2003**, *27*, 533–541.
48. Zako, M.; Takano, N. Intelligent Material Systems Using Epoxy Particles to Repair Microcracks and Delamination Damage in GFRP. *J. Intell. Mater. Syst. Struct.* **1999**, *10* (10), 836–841.
49. Carlson, J. A.; English, J. M.; Coe, D. J. A Flexible, Self Healing Sensor Skin. *Smart Mater. Struct.* **2006**, *15*, N129–N135.
50. Chen, X.; Dam, M. A.; Ono, K.; Mal, A.; Shen, H.; Nutt, S. R.; Sheran, K.; Wudl, F. A Thermally Re-mendable Cross-linked Polymeric Material. *Science* **2002**, *295*, 1698–1702.
51. Liu, Y. L.; Hsich, C. Y. Crosslinked Epoxy Materials Exhibiting Thermal Remendability and Removability from Multifunctional Maleimide and Furan Compounds. *J. Polym. Sci., Polym. Chem.* **2006**, *44* (2), 905–913.
52. Rule, J. D.; Sottos, N. R.; White, S. R.; Moore, J. S. The Chemistry of Self Healing Polymers. *Educ. Chem.* **2005**, *42*, 130–132.
53. Baghdachi, J. *Smart Coatings*; American Chemical Society Symposium Series 1002; American Chemical Society: Washington, DC, 2009.

Downloaded by 89.163.35.42 on June 22, 2012 | http://pubs.acs.org
Publication Date (Web): November 10, 2010 | doi: 10.1021/bk-2010-1050.ch001

Downloaded by UNIV OF DELAWARE MORRIS LIB on June 22, 2012 | http://pubs.acs.org
Publication Date (Web): November 10, 2010 | doi: 10.1021/bk-2010-1050.ch002

Chapter 2

Tethered Stimuli-Responsive Polymer Films

Keisha B. Walters*

Dave C. Swalm School of Chemical Engineering, Mississippi State University, Mississippi State, MS 39762-9595
***kwalters@che.msstate.edu**

Tethered (surface bound) polymer films have been synthesized using a 'grafting-to' (end-functionalized, preformed polymers) technique and the chemistry and pH-response of these layers characterized. Poly(tert-butyl acrylate) (PtBA) films are tethered to gold and silicon substrates via self-assembled monolayers (SAMs) and are characterized using FTIR spectroscopy, static water contact angle goniometry, and ellipsometry. The pendant groups were then converted to amide/amine functionalities using a novel diamine reaction. The synthesis, chemical characterization, and *in situ* pH response behavior of polyacids and polyamines is presented. The polyacids and polamines were found to expand and contract, respectively, with increasing pH.

As indicated by the literature, interest in stimuli responsive polymers, and resultant "smart" materials, has increased dramatically over the past 10 years. The ultimate goal of this work is the ability to design and synthesize materials on a molecular scale that subsequently determines the conformation and properties on a macromolecular scale, with a particular emphasis on charged polymer layers with well-defined, environmentally responsive structures. Presented here are efforts to synthesize and characterize dynamic polymer layers (i.e. significant changes in chemical functionalities and conformation at surfaces and interfaces) grafted to solid substrates. To achieve this goal, several different avenues have been explored including grafting-to versus grafting-from methods, gold, silicon, and polymer substrates, and acid, amine, and amide pendant groups to exact conformational changes in response to pH (and/or temperature). While this work presents the

In Smart Coatings III; Baghdachi, J., et al.;
ACS Symposium Series; American Chemical Society: Washington, DC, 2010.

Downloaded by UNIV OF DELAWARE MORRIS LIB on June 22, 2012 | http://pubs.acs.org
Publication Date (Web): November 10, 2010 | doi: 10.1021/bk-2010-1050.ch002

formation of responsive polymer films on Si substrates, the author has also formed responsive polymer films using a grafting-from approach (surface-confined living radical polymerizations, SC-LRP) on both Si and Au substrates (*1–4*) and both the grafting-from and grafting-to techniques have been reproduced on ethylene-based copolymers, specifically ethylene-acrylic acid (EAA) and ethylene-vinyl alcohol (EVOH) (*2–5*).

End-functionalized polymers have been grafted to a wide range of inorganic (*6–9*) and polymeric (*10–12*) substrates in the form of films, fibers, particles, or other geometries. As part of the work presented, a grafted polymer layer was formed from carboxyl-terminated poly(tert-butyl acrylate) (PtBA), which is commercially available in various molecular weights with a narrow molecular weight distribution. Selection of PtBA was primarily due to the ease of removing the pendant tert-butyl esters in order to replace them with other functional groups. Previously, Boyes et al. used atom transfer radical polymerization to form block copolymers from silicon wafers, with one block being PtBA (*13*). The tert-butyl esters of PtBA were subsequently converted to acids and then to silver salts. Azobenzene alkanethiol was attached to gold by Lee et al. to form a brush terminated with tert-butyl ester groups that were converted to acids using chemical and photochemical methods (*14*). In this work, the goal was to investigate a chemical scheme for converting the tert-butyl ester pendant groups of PtBA to tertiary amine pendant groups via reaction with diamines. The selection of diamine reactants was due to the ability of tertiary amines to become positively charged at low pH and the potential for reversible changes in polymer conformation, adhesion, separations, wettability, and even biocompatibility.

Materials and Methods

Materials

The substrate used in this study was silicon (Si) wafer purchased pre-diced from Silicon Quest International (N doped <1,0,0>). Carboxyl-terminated poly(tert-butyl acrylate) (PtBA-COOH) (M_n = 6500, M_w = 7000, M_w/M_n = 1.08) was purchased from Polymer Source, Inc. and used as received. The following chemicals were used as received: dichloromethane (Burdick and Jackson, 99.9+%), 3-aminopropyldimethylethoxysilane (3-APDMES, Gelest Inc., >95%), phosphorous pentachloride (Aldrich, 95%), $ZnBr_2$ (Alfa Aesar, 99.9%), sulphuric acid (EMD, ~91.5%), hydrogen peroxide (VWR, 30%), acetone (VWR, 99.5%), toluene (Fisher, HPLC grade), ethanol (EMD Chemicals, 92%), water (Burdick and Jackson, HPLC grade), and isopropyl alcohol (VWR, 70%). The diamine compounds were purchased from various vendors and were used as received: ethylenediamine (Aldrich, 99%), n,n-dimethylethylenediamine (TCI America, 99%), n,n-diethylethylenediamine (TCI America, 98%), n,n-diisopropylethylenediamine (TCI America, 97%), n-isopropylethylenediamine (Aldrich, 98%), and 7-(dimethylamino)heptylamine (Matrix Scientific, 97%).

Downloaded by UNIV OF DELAWARE MORRIS LIB on June 22, 2012 | http://pubs.acs.org
Publication Date (Web): November 10, 2010 | doi: 10.1021/bk-2010-1050.ch002

Grafting of PtBuA

Amine-terminated monolayers were prepared on the Si wafers using 3-aminopropyl dimethylethoxysilane. The deposition of the silane self-assembled monolayers (SAMs) has been described in detail previously (*15*). The carboxylic acid of the end-functionalized PtBA was converted to acid chloride in preparation for the grafting reaction. To a solution of PtBA-COOH in CH_2Cl_2, a stoichiometric excess of PCl_5 was added. This reaction proceeded with sonication to form the acid chloride end-functionalized PtBA [PtBA-COCl]. The amine-terminated monolayers on Si [Si-NH_2] were then placed into the PtBA-COCl/PCl_5/CH_2Cl_2 solution and allowed to react with sonication to graft the PtBA to the Si-NH_2 substrates [Si-g-PtBA]. After reaction, the samples were first washed and sonicated repeatedly in CH_2Cl_2. The samples were then rinsed with ethanol and dried with N_2.

Tert-Butyl Ester Substitution

Once a layer of PtBA was grafted to the Si surface [Si-g-PtBA] using the scheme described above, the pendant tert-butyl ester groups were replaced by amine functionalities. The diamines used have the general structure $NH_2(CH_2)_XNR_1R_2$. A previously reported reaction scheme for tert-butyl ester substitution was used (*5*, *15*).

Characterization

The deposition of the self-assembled monolayer (Si-NH_2), grafting of the PtBA (Si-g-PtBA), and conversion of the pendant tert-butyl ester groups were monitored using external reflectance (ER-FTIR) and transmission FTIR spectroscopy, ellipsometry, and static water contact angle goniometry. The ER-FTIR analysis was performed using a Nicolet Nexus 870 with an FT-80 horizontal grazing angle accessory with an 80° fixed incidence angle. Transmission FTIR spectra on the silicon wafer samples were obtained using a Thermo-Nicolet Magna 550 FTIR spectrometer equipped with a microscope accessory using a minimum of 32 scans and 4 cm^{-1} resolution. All FTIR characterization was conducted at 25 °C in dry air purged chambers. Peak assignments were referenced to literature values (*16–18*). Silane and polymer layer thicknesses were analyzed using a Beaglehole Picometer ellipsometer. A multi-layer model using appropriate n and k values was fit to variable-angle data to determine the layer thicknesses. To investigate the thickness changes of the grafted polymer layers *in situ*, a cylindrical glass cell was employed. This liquid cell has a stage with clamps that allowed the sample position to be maintained during solution transfer through the inlet and outlet ports via a peristaltic pump. Static water contact angle goniometry was used to assess changes in surface wettability. The sessile drop method was used with a Krüss DSA10-Mk2 with digital photo analysis software. The contact angle values reported are averages of a minimum of nine drops for each sample along with 95% confidence intervals.

Downloaded by UNIV OF DELAWARE MORRIS LIB on June 22, 2012 | http://pubs.acs.org
Publication Date (Web): November 10, 2010 | doi: 10.1021/bk-2010-1050.ch002

Results and Discussion

Amine-Terminated Self-Assembled Monolayers on Silicon Wafers and the Grafting of End-Functionalized PtBA

Alkylsilane monolayers, attached to oxide surfaces via covalent siloxane linkages, were used to give a robust substrate for polymer grafting and substitution reactions (*15*). The average layer thickness for each wafer was measured with ellipsometry and used later in the multi-layer model to find the grafted polymer thickness. ER-FTIR was used to confirm the deposition of the 3-APDMES layer on the silicon wafer (Figure 1a). Peaks were seen at 1445 and 1297 cm^{-1} corresponding to the propyl CH_2 bending and Si-CH_3 deformation, respectively (*17*, *18*). There are two 'typical' signature bands for siloxane, a weak absorbance at ~1870 cm^{-1} for the Si-O combination band and a strong absorbance at ~1000 cm^{-1} for the asymmetric Si-O-Si stretch (*19–21*). The weaker band at ~1870 cm^{-1} was not seen in our samples. However, the strong band at 1106 cm^{-1} was easily detected. Several bands for the Si-O stretch were also seen at 964, 891, 818, and 738 cm^{-1} (*17*, *19*, *20*). The higher wavenumber region containing the N-H and C-H stretches was not clear due to distortions in the baseline and difficulties in completely removing water from the purge air. These difficulties were increased for the PtBA grafted samples (Si-g-PtBA) since the films are anisotropic and non-metallic substrates (such as Si) reflect vibrations both parallel and perpendicular to the surface (but in opposite directions) so that the spectra are composed of superimposed upward- and downward-pointing absorptions. Due to this phenomenon, transmission FTIR was performed on the Si-g-PtBA samples. (Note that transmission FTIR could not be performed successfully on the Si-NH_2 samples due to low signal to noise ratio.)

A representative transmission FTIR spectrum for Si-g-PtBA is shown in Figure 1b. Compared to the ester carbonyl peak at ~1726 cm^{-1} seen in Figure 1c for neat PtBA, the carbonyl in the Si-g-PtBA was shifted slightly to a lower wavenumber (~1714 cm^{-1}) (*17*, *18*, *21*, *22*). The shift indicated that some of the tert-butyl esters had been converted to carboxylic acids. The carbonyl stretch was also fairly broad and encompassed the absorbance for the amide carbonyl (~1630-1800 cm^{-1}) that was formed from the grafting of the carboxylic acid end-functionalized PtBA to the amine terminated layer (*22*). The peaks that correspond to the $C(CH_3)$ asymmetric and symmetric stretches were seen at 1478 and 1370 cm^{-1}, respectively, in both the Si-g-PtBA and neat PtBA samples (*22*, *23*). The peak at ~1392 cm^{-1} in both the Si-g-PtBA and neat PtBA samples corresponds to $C(CH_3)_3$ bending deformations (*22*). There was evidence of a peak at ~1290 cm^{-1} in the Si-g-PtBA samples which was not present in neat PtBA. This peak corresponds to the amide III absorbance of secondary amides. Both Si-g-PtBA and neat PtBA showed fairly strong absorbances at ~1250 cm^{-1} from the skeletal vibration of the $(CH_3)_3CR$ functionality (*22*). The C-O asymmetric stretch for ester was found at ~1150 cm^{-1} for both the Si-g-PtBA and neat PtBA samples (*17*). As expected, this peak was both stronger and broader than the ester carbonyl peak in neat PtBA (*17*). Several of the peaks indicative of the silane monolayer were seen in the Si-g-PtBA sample including the Si-O-Si asymmetric stretch at ~1106 cm^{-1} and the Si-O stretches at

Downloaded by UNIV OF DELAWARE MORRIS LIB on June 22, 2012 | http://pubs.acs.org
Publication Date (Web): November 10, 2010 | doi: 10.1021/bk-2010-1050.ch002

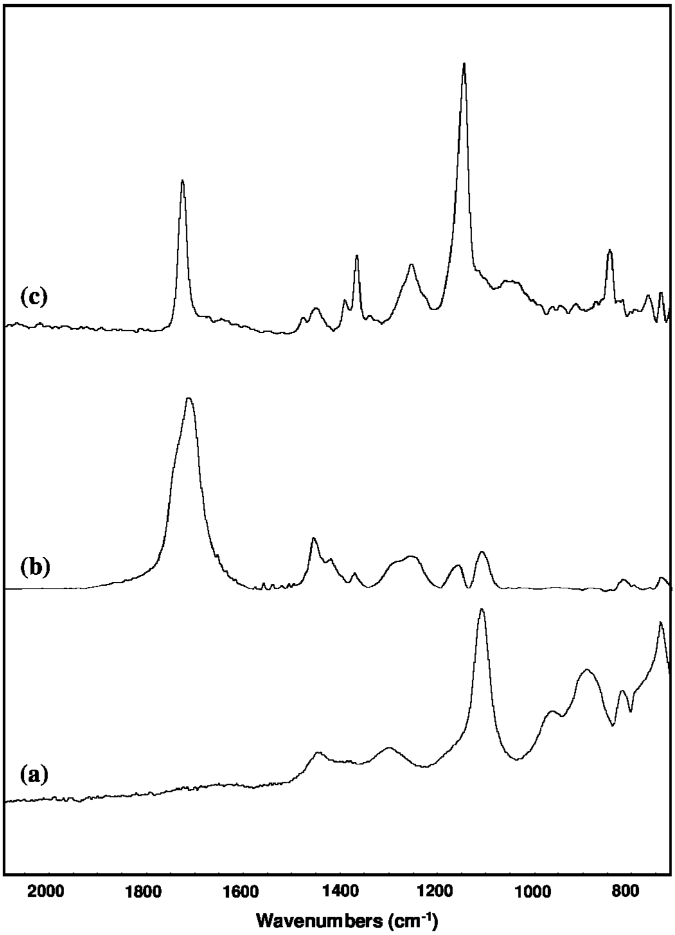

Figure 1. FTIR spectra of (a) Si-NH$_2$, (b) Si-g-PtBA, and (c) neat PtBA.

~818 and 738 cm^{-1}. From these FTIR results, we have been able to confirm qualitatively the deposition of the 3-APDMES layer, grafting reaction of the end-functionalized PtBA, and partial hydrolysis of the grafted PtBA layer. XPS has been performed to examine the grafting reactions more quantitatively (*15*).

The static water contact angle of piranha treated Si wafers was ~0° (the drop completely wets out). After deposition of the 3-APDMES layer, the static contact angle was 78° ± 0.8°. There is a very wide range of contact angles reported in the literature for amine-terminated monolayers (see Table 1) (*24–29*). This makes it difficult to evaluate the structure or density of our layer using contact angle. A change in the contact angle was seen after the grafting of the PtBA. The contact angle decreased to 62° ± 0.8°. This is lower than the literature value of 75° ± 2° for a grafted PtBA layer (*23*), but this was not unexpected since some of the tert-butyl ester groups were converted to carboxylic acid functionalities (which would lower the water contact angle).

Table 1. Static water contact angle values from the literature for amine-terminated monolayers

Measured Water Contact Angle (degrees)	*Reference*
28-40	(*24*)
52 ± 2	(*25*)
63 ± 2	(*26*, *27*)
83.5 ± 1.5	(*28*)
68-103	(*29*)

Downloaded by UNIV OF DELAWARE MORRIS LIB on June 22, 2012 | http://pubs.acs.org
Publication Date (Web): November 10, 2010 | doi: 10.1021/bk-2010-1050.ch002

Diamine Conversion Reactions

Prior to carrying out the diamine conversion reactions on the Si-g-PtBA samples, several reactions were carried out on PtBA homopolymer to confirm the potential hydrolysis and diamine conversion of the pendant tert-butyl groups (*5*, *15*), but will not be discussed here. Since the reactions on the homopolymer PtBA were successful, the diamine conversions were conducted on Si-g-PtBA. As was the case with the Si-g-PtBA samples, ER-FTIR spectra could not be successfully obtained on these specimens. The transmission-FTIR spectra shown below were obtained with a microscope ATR accessory as described previously. Even these transmission-FTIR spectra were difficult to obtain due to low signal-to-noise ratios, absorbance from Si (which necessitated baseline corrections), and small scan area of the microscope ATR accessory. While a total of five different amines were reacted with the surface-grafted PtBA (*15*), this paper will focus on dimethyethylendiamine ($NH_2CH_2CH_2N(CH_3)_2$). In Figure 2, the broad N-H stretch and Amide B band for the amide groups from reaction of Si-g-PtBA with dimethyethylendiamine (Si-g-PtBA→DMEDA) is centered at ~3300 cm^{-1}. The amide I and amide II bands can be seen at 1648 and 1542 cm^{-1}, respectively. Because of the difficulty with using FTIR to confirm the chemistry within our relatively thin films on Si substrates, survey and high-resolution X-ray photoelectron spectroscopy (XPS) was used (*15*).

pH Response

In situ ellipsometry was used to characterize the pH response of these tethered films. A sample was placed in the liquid cell and allowed to equilibrate at a given pH and a variable angle experiment was then performed after a discrete time interval of 30 min. (Note: An interval of 30 min was chosen after measuring the thickness of three samples at 5 min time intervals from 0 to 60 min. After 30 min there was no further significant thickness change in these polymer layers.) This procedure was repeated for a range of solution pH values. The grafted layer thickness was then determined by fitting the data with a multi-layer model that included the silicon substrate, silane monolayer, grafted polymer layer, and the surrounding aqueous medium.

Downloaded by UNIV OF DELAWARE MORRIS LIB on June 22, 2012 | http://pubs.acs.org
Publication Date (Web): November 10, 2010 | doi: 10.1021/bk-2010-1050.ch002

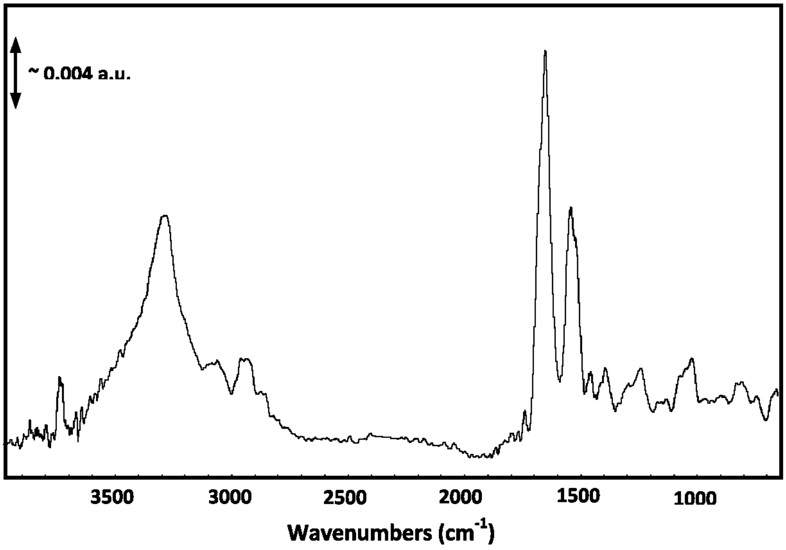

Figure 2. Transmission-FTIR of Si-g-PtBA conversion with dimethyethylenediamine (Si-g-PtBA→DMEDA).

Figure 3a shows a plot of grafted layer thickness versus pH for a Si-g-PtBA/PAA sample. For a sample with partial acrylic acid content such as Si-g-PtBA/PAA, the polymer will be compressed at low pH due to more of the acid groups being protonated. At high pH, more acid groups become deprotonated and the polymer expands as the negatively charge carboxylic anions repel one another. This general trend holds true for our partially hydrolyzed samples. As shown in Figure 3a, the grafted layer thickness increased with pH. The plot of polymer layer thickness as a function of pH shows a shape from pH 2 to 10 similar to those seen in other experimental and theoretical work for weak polyacids (*30*, *31*). The increase in the thickness between pH 10 and 11 may be due to the hydrolysis of the remaining tert-butyl ester groups at this high pH (*30*, *32*).

For polymers with weakly ionizable amine pendant groups, at low pH the amine groups become charged and the ionic repulsion between the charged pendant groups can dominate over the hydrophobic interaction between alkyl functionalities and their aqueous environment so that the polymer chains become expanded (Figure 3b). As the pH increases, the number of charged pendant groups decreases and the hydrophobic interactions begin to dominate causing the polymer chain to contract. *In situ* ellipsometry experiments were performed on Si-g-PtBA samples that had been reacted with diamines. The dry thickness of the PtBA layer for the Si-g-PtBA samples was 2.5 ± 0.12 nm (95% confidence interval). Changes measured in the dry layer thickness after reaction with the diamines was found to be statistically insignificant. Preliminary calculations show that the dry PtBA layer is in the transition region between mushroom and brush regimes and indicate that the grafted polymer layer is not densely packed, which is an advantage because it provides the surface-confined chains the ability to expand and contract.

Downloaded by UNIV OF DELAWARE MORRIS LIB on June 22, 2012 | http://pubs.acs.org
Publication Date (Web): November 10, 2010 | doi: 10.1021/bk-2010-1050.ch002

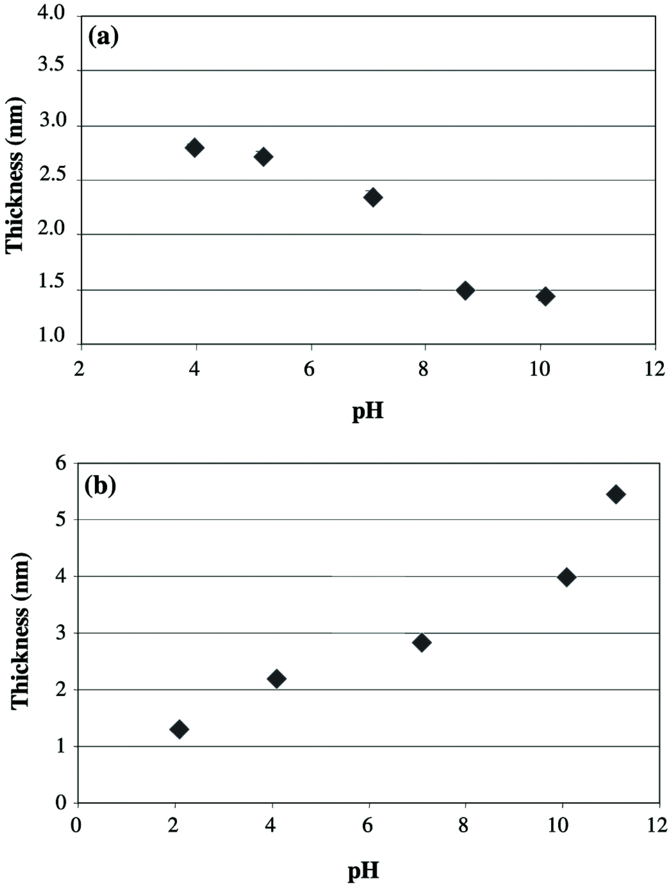

Figure 3. In situ grafted polymer layer thicknesses plotted as a function of pH for (a) a Si-g-PtBA/PAA sample and (b) a Si-g-PtBA→DMEDA sample. The standard deviation of these thickness measurements was ~ 0.03 nm.

The grafted layer thickness is plotted as a function of solution pH for Si-g-PtBA→DMEDA. Of the diamines studied, DMEDA showed the greatest thickness change over pH 4-10 (Figure 3b). There is an inflection at ~ pH 8 (near the pK_a) and a plateau in thickness at higher pH values. The plateau at higher pH values is reasonable since the chains can contract only up to a point due to steric hindrance. For these tethered polyamines, the layer response is due to several factors. The charge on the amine groups as a function of pH can control the chain extension/contraction, and there may also be the effect of hydrophobic aggregation promoting contraction at higher pH. The hydrophobic effect is governed largely by the aliphatic content of the amine pendant groups, but, as stated above, the contraction is limited by steric hindrance. Therefore, a large aliphatic content may aid in responsiveness, but the overall extent of response may be hindered. Of the polyamines investigated, Si-g-PtBA→DMEDA showed the most promise as a responsive layer.

Downloaded by UNIV OF DELAWARE MORRIS LIB on June 22, 2012 | http://pubs.acs.org
Publication Date (Web): November 10, 2010 | doi: 10.1021/bk-2010-1050.ch002

Conclusions

Amine-terminated silane SAMs were deposited onto silicon (Si) wafers. The terminal amine reaction sites were used to graft end-functionalized PtBA. During the grafting reactions, some tert-butyl ester groups were hydrolyzed. In fact, the polymer can be converted to hydrolyzed poly(acrylate) (polyacrylic acid, PAA). The pendant groups, whether acid, tert-butyl ester, or a mixture, were then converted to amide/amine functionalities using a novel diamine reaction. Each reaction step and the changes in surface properties were monitored with external-reflectance-FTIR, ellipsometry, and static water contact angle goniometry.

Partially hydrolyzed Si-g-PtBA (Si-g-PtBA/PAA) was found to expand with increasing pH due to deprotonation and charge repulsion between neighboring carboxylic anion groups. The polyamines were found to contract with increasing pH due to less charge of the amine pendant groups (and therefore less ionic repulsion) and segregation of the hydrophobic content of the polymers. However, the response was not consistent in a well-defined trend within the series of polyamines studied. Of the pendant diamine functionalities investigated, PDMEDA was the most responsive showing approximately a 50% change in layer thickness over the pH range of 4 to 10.

Acknowledgments

This work was supported by the ERC Program of the National Science Foundation under Award Number EEC-9731680 and by the Department of Education GAANN fellowship program. The author offers sincere thanks to Dr. Doug Hirt (Clemson University, Department of Chemical and Biomolecular Engineering and Center for Advanced Engineering Fibers and Films) for enlightening discussions and access to equipment. Appreciation is also expressed to the following Clemson University researchers: Dr. Amol Janorkar (currently at the University of Mississippi Medical Center, Department of Biomedical Materials Science) and Dr. JoAn Hudson for XPS measurements, and Kim Ivey for transmission-FTIR spectra.

References

1. Ding, S.; Floyd, A.; Walters, K.B. *J. Polym. Sci., Part A: Polym. Chem.* **2009**, *47*, 6522–6560.
2. Walters, K. B.; Hirt, D. E. *Proceedings of the ACS Division of Polymeric Materials, Science and Engineering* **2003**, *89*, 159–161.
3. Walters, K. B.; Wang, W.; Harris, R. P.; Hirt, D. E. *Proceedings of ANTEC – Society of Plastics Engineers* **2004**, 3859–3864.
4. Walters, K. B.; Hirt, D. E. *Proceedings of ANTEC – Society of Plastics Engineers* **2003**, 2793–2797.
5. Walters, K. B.; Hirt, D. E. *Polymer* **2006**, *47*, 6567–6574.
6. Jones, R. A. L.; Lehnert, R. J.; Schonherr, H.; Vancso, J. *Polymer* **1999**, *40*, 525–530.

7. Karim, A.; Satija, S. K.; Orts, W.; Ankner, J. F.; Majkraz, C. F.; Fetters, L. J. *Materials Research Society Symposium Proceedings, Polymer/Inorganic Interfaces* **1993**, *304*, 149–154.
8. Penn, L. S.; Hunter, T. F.; Lee, Y.; Quirk, R. P. *Macromolecules* **2000**, *33*, 1105–1107.
9. Koutsos, V.; van der Vegte, E. W.; Hadziioannou, G. *Macromolecules* **1999**, *32*, 1233–1236.
10. Takei, Y. G.; Aoki, T.; Sanui, K.; Ogata, N.; Sakurai, Y.; Okano, T. *Macromolecules* **1994**, *27*, 6163–6166.
11. Karavia, V.; Deimede, V.; Kallitsis, J. K. *J. Macromol. Sci., Pure Appl. Chem.* **2004**, *41*, 115–131.
12. Zdyrko, B.; Varshney, S. K.; Luzinov, I. *Langmuir* **2004**, *20*, 6727–6735.
13. Boyes, S. G.; Mirous, B. K.; Brittain, W. J. *Polym. Prepr.* **2003**, *44*, 552−553. Boyes, S. G.; Akgun, B.; Brittain, W. J.; Foster, M. D. *Macromolecules* **2003**, *36*, 9539−9548.
14. Lee, K.; Pan, F.; Carroll, G. T.; Turro, N. J.; Koberstein, J. T. *Langmuir* **2004**, *20*, 1812–1818.
15. Walters, K. B.; Hirt, D. E. *Macromolecules* **2007**, *40* (14), 4829–4838.
16. Urban, M. W. *Attenuated Total Reflectance Spectroscopy of Polymers: Theory and Practice*; American Chemical Society: Washington, DC, 1996.
17. Silverstein, R. M.; Bassler, G. C.; Morrill, T. C. *Spectrometric Identification of Organic Compounds*; John Wiley & Sons: New York, 1991.
18. Kuptsov, A. H.; Zhizhin, G. N. *Handbook of Fourier Transform Raman and Infrared Spectra of Polymers*; Elsevier: Amsterdam, 1998.
19. Shreedhara Murthy, S.; Blitz, J. P.; Leyden, D. E. *Anal. Chem.* **1986**, *58*, 3167–3172.
20. Shreedhara, R. S.; Leyden, D. E. *Anal. Chem.* **1986**, *58*, 1228–1233.
21. Coates, J. Interpretation of Infrared Spectra, A Practical Approach. In *Encyclopedia of Analytical Chemistry*; Meyers, R. A., Ed.; John Wiley and Sons, Ltd., 2000.
22. Bellamy, L. J. *The Infra-red Spectra of Complex Molecules*; Methuen & Co., Ltd.: London 1958.
23. Mengel, C.; Esker, A. R.; Meyer, W. H.; Wegner, G. *Langmuir* **2002**, *18*, 6365–6372.
24. Heiney, P. A.; Grüneburg, K.; Fang, J. *Langmuir* **2000**, *16*, 2651–2657.
25. Kurth, D. G.; Bein, T. *Langmuir* **1993**, *9*, 2965–2973.
26. Balachander, N.; Sukenik, C. *Langmuir* **1990**, *6*, 1621–1627.
27. Kong, X.; Kawai, T.; Abe, J.; Iyoda, T. *Macromolecules* **2001**, *34*, 1837–1844.
28. Lee, I.; Wool, R. P. *Thin Solid Films* **2000**, *379*, 94–100.
29. Heise, A.; Stamm, M.; Rauscher, M.; Duschner, H.; Menzel, H. *Thin Solid Films* **1998**, *327-329*, 199–203.
30. Biesalski, M.; Johannsmann, D.; Rühe, J. *J. Chem. Phys.* **2002**, *117*, 4988–4994.
31. Biesheuvel, P. M. *J. Colloid Interface Sci.* **2004**, *275*, 97–106.
32. Carlise, J. R.; Kriegel, R. M.; Rees, W. S.; Weck, M. *J. Org. Chem.* **2005**, *70*, 5550–5560.

Downloaded by UNIV OF DELAWARE MORRIS LIB on June 22, 2012 | http://pubs.acs.org
Publication Date (Web): November 10, 2010 | doi: 10.1021/bk-2010-1050.ch002

Downloaded by PENNSYLVANIA STATE UNIV on June 22, 2012 | http://pubs.acs.org
Publication Date (Web): November 10, 2010 | doi: 10.1021/bk-2010-1050.ch003

Chapter 3

Preparation of a Delivery System for Smart Coatings by Electrostatic Deposition

Harvey A. Liu,[1] Bruce E. Gnade,[1,2] and Kenneth J. Balkus, Jr.[1,*]

[1]The University of Texas at Dallas, Department of Chemistry and the Alan MacDiarmid NanoTech Institute, 800 West Campbell Rd, Richardson, TX 75080-3021
[2]The University of Texas at Dallas, Department of Electrical Engineering, 800 West Campbell Rd, Richardson, TX 75080-2021
[*]balkus@utdallas.edu

Multilayer composites that utilize polymer and metal oxide thin films are the enabling technology for many flexible electronic devices. However, crack formation within the brittle inorganic layers that arise from defects as well as the flexing of these multilayer composite materials allow the influx of atmospheric water, a major source of device degradation. Thus, a composite material that can initiate self-healing upon the influx of environmental water through defects or stress induced cracks would find potential applications in permeation barriers. In the present study, reactive metal oxide precursors such as titanium(IV) chloride ($TiCl_4$) or trimethylaluminum ($AlMe_3$) were encapsulated within the pores of a degradable polymer such as polylactic acid (PLA). The PLA polymer containing metal oxide healing agent were prepared as spheres or fibers. The PLA spheres or fibers were reactive under controlled humidity resulting in hydrolysis of the degradable polymer shell and subsequent release of the reactive metal oxide precursor. Hydrolysis of the metal oxide precursors results in formation of solid titanium oxides or aluminum oxides at the surface of the delivery vehicle. The efficacy of this self-healing delivery system was further demonstrated by the integration of these reactive fibers or spheres in a polymer planarization layer (PMMA) of a multilayer barrier film. The introduction of nanocracks in the barrier film led to the release

In Smart Coatings III; Baghdachi, J., et al.;
ACS Symposium Series; American Chemical Society: Washington, DC, 2010.

of the metal oxide precursor and the formation of titanium oxide or aluminium oxide nanoparticles in the cracks. In this study we have established the first site-specific, smart, self-healing system for multilayer barrier films through the delivery of metal oxide nanoparticles by reactive composite fibers or spheres.

Downloaded by PENNSYLVANIA STATE UNIV on June 22, 2012 | http://pubs.acs.org
Publication Date (Web): November 10, 2010 | doi: 10.1021/bk-2010-1050.ch003

Introduction

The field of smart coatings continues to grow in terms of public interest and awareness. This is due impart to the development of products such as the *Scratch Guard Coat*, a self-healing paint coating for cars introduced by the Nissan Motor Co. (*1*) The coating is a clear paint, made from a synthetic resin that will provide resistance to scratches as well as “heal” light scratches. While this technology demonstrates a remarkable feat it is the product of many recent advances in smart coatings. The efforts in smart coatings over the past few years has resulted in the development of anticorrosive composites (*2*), self-cleaning coatings (*3–6*), coatings for the detection of heavy metals to poisonous gases, as well as many others (*7*). Many of the current approaches to developing smart coatings for self-healing or crack detection have been centered on encapsulating materials within a microcapsule or the core of a fiber that ruptures upon a mechanical action (*8–11*). While this approach works well it becomes more difficult to break open nanoscale containers. In contrast, many drug delivery systems are based on biodegradable particles that release their contents upon dissolution. Such a delivery system might be exploited in the design of smart coatings to prevent the permeation of moisture. The goal of this study was to develop a new delivery system that is sensitive to not only the physical breaking of the encapsulating shell or film, but also to the environmental conditions surrounding the coating. Of particular interest is the delivery of healing agents for inorganic films, which is far more challenging than polymers.

The use of biodegradable polymers as a vehicle for drug delivery has been demonstrated well (*12–15*). The preferred method of encapsulation is the fabrication of polymer capsules through an emulsion, a technique that is often used in smart coatings (*16–18*). This method is simple and adaptable for the encapsulation of many materials and can produce capsules of varying sizes. In addition to the relatively easy method of fabrication this procedure also presents other advantages including the ability to produce encapsulations in the nanometer range. Though, with microcapsules the issue of attaining a uniform dispersion as well as the delivery of a sufficient amount of material to the targeted site is an underlying factor that limits its utility in smart coatings (fig. 1). To address this issue, efforts have been made to produce fibers with core-shell structures to mimic the vascular system and provide a better response (*19–21*). While this method allows for better coverage of the targeted coating the size of these functional fibers that can be produced is limited. These two approaches both share the same disadvantage in that they are limited in the types of materials that can be encapsulated.

Downloaded by PENNSYLVANIA STATE UNIV on June 22, 2012 | http://pubs.acs.org
Publication Date (Web): November 10, 2010 | doi: 10.1021/bk-2010-1050.ch003

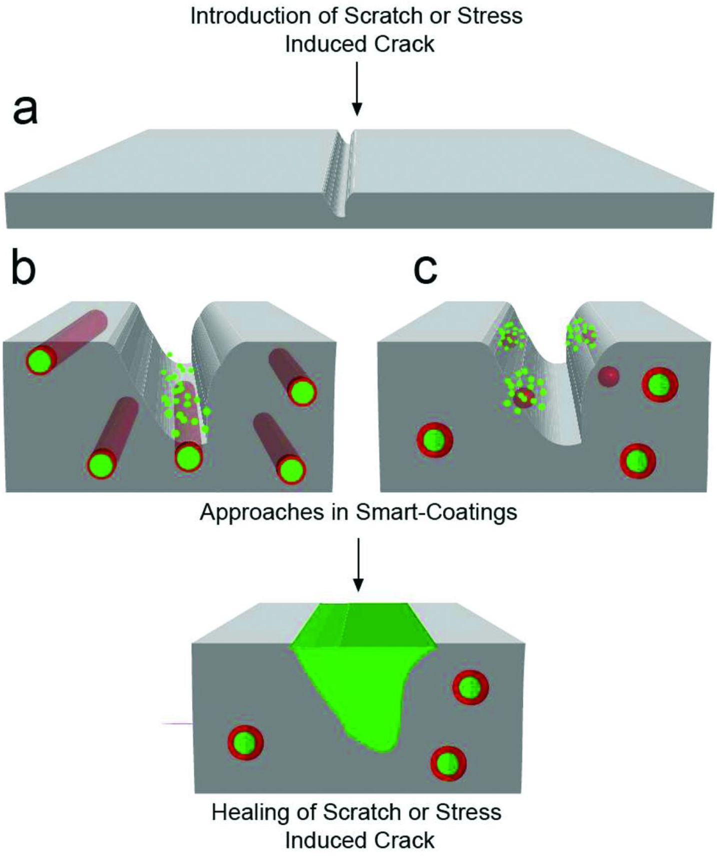
Introduction of Scratch or Stress Induced Crack
a
b
c
Approaches in Smart-Coatings
Healing of Scratch or Stress Induced Crack

Figure 1. Schematic of smart coatings for self-healing delivery systems

In this study we demonstrate the capability of our system to deliver a healing agent in a smart coating that is not only responsive to physical stimuli, but a chemical one as well. Through the technique of electrostatic deposition we have prepared hollow spheres and porous fibers that can encapsulate highly air-sensitive and moisture reactive materials, such as the reactive metal oxide precursors $TiCl_4$ and $Al(CH_3)_3$. The water degradable polymer polylactic acid was used to form the microcapsules as well as porous fibers in a free-standing paper that approaches the nanoscale. The method of encapsulation demonstrated here can also be applied to the encapsulation of other materials that are highly reactive, moisture sensitive, or are not easily encapsulated through an emulsion. To date, the encapsulation of such reactive materials in a degradable polymer has not yet been explored. The facile integration of our system within a thin film will be discussed and its ability to fill cracks in both polymer and alumina films will be presented.

Downloaded by PENNSYLVANIA STATE UNIV on June 22, 2012 | http://pubs.acs.org
Publication Date (Web): November 10, 2010 | doi: 10.1021/bk-2010-1050.ch003

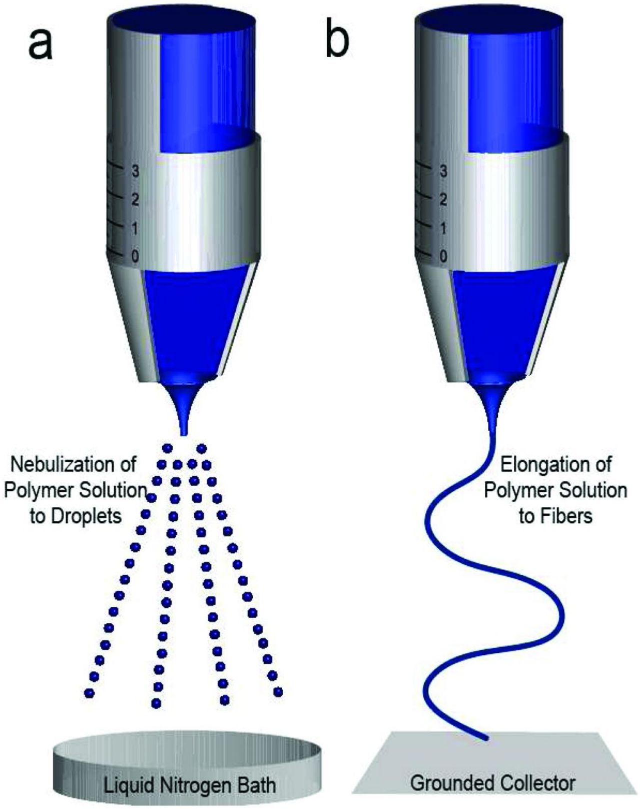
a
b
3
2
1
0
3
2
1
0
Nebulization of Polymer Solution to Droplets
Elongation of Polymer Solution to Fibers
Liquid Nitrogen Bath
Grounded Collector

Figure 2. Electrostatic deposition methods

Experimental

Materials

All chemicals were used as received. Titanium (IV) chloride ReagentPlus 99.9% ($TiCl_4$), 2.0 M Trimethylaluminum solution in heptane (75-24-1) (TMA), and poly(methylmethacrylate) (PMMA) (M_r~120 kDa) were obtained from Sigma Aldrich. Anhydrous DriSolv ® toluene and chloroform was obtained from EMD Chemicals Inc. Polylactic acid (M_r~100 kDa) was obtained from Monomer-Polymer & Dajac Laboratories Inc.

Preparation of Hollow Polymer Shells and Porous Polymer Fibers

Polymer shells of high molecular weight lactic acid polymer were prepared by integrating the technique of electrospraying with a freeze drying method for generating core shell structures reported by Hyuk et al. (*22*) In a typical preparation, high molecular weight polylactic acid was dissolved in chloroform at room temperature in the range of 1-3% w/w. From the polymer solution, 2 mL were drawn into a 5 ml plastic syringe, which was controlled by a syringe pump

(7802CO, KD Scientific Inc., USA) feeding at a rate of 0.1 ml/min to a flat tip 20-G needle. The distance between the needle tip and the grounded collector, an aluminum target, was adjusted to 20-25 cm. The electrosprayed PLA was collected in a 100 ml Petri dish containing liquid nitrogen placed directly above the grounded collector place. Electrospraying was initiated when 15 kV was applied to the needle from a variable high voltage power supply (ES50P-5W, Gamma High Voltage Research) nebulizing the polymer solution into a fine mist (fig. 2a). The resulting frozen droplets of the polymer solution dispersed in liquid nitrogen were placed in a vacuum less than 225 torr for at least 5 h. The spheres were allowed to warm up to room temperature and the chloroform then allowed to evaporate; the hollow polymer shells were then collected and characterized by scanning electron microscopy (SEM).

Electrostatic deposition was also utilized to form porous PLA fibers by using a solution of higher viscosity was used through the dissolution of PLA in chloroform (7-10% w/w). Aligned fibers were obtained by using a grounded rotating drum positioned a distance of 25 cm from the needle tip (fig. 2b). It is also possible to prepare hollow fibers by using concentric needles, where the PLA is passed through the outer needle and the encapsulating agent is fed through the core.

Downloaded by PENNSYLVANIA STATE UNIV on June 22, 2012 | http://pubs.acs.org
Publication Date (Web): November 10, 2010 | doi: 10.1021/bk-2010-1050.ch003

Filling and Sealing of Hollow Polymer Shells and Porous Fibers

The filling and sealing of both the polymer shell and porous fibers were achieved by similar methods. The polymer shells or porous fibers were transferred to a 40 mL glass reactor equipped with a vacuum stopcock, then transferred to a vacuum line and pumped on for approximately one hour under heating at ~40°C. After evacuation, either titanium (IV) chloride or trimethylaluminum was introduced by vacuum transfer to sufficiently fill the fibers or hollow polymer shells (~1 ml). This process was followed by the vacuum transfer of dry toluene (~2 ml) to seal the polymer shells and porous fibers. The toluene was allowed to react with the beads and fibers for approximately 20-30 minutes to allow proper sealing of the polymer holes and pores. The remaining toluene-titanium (IV) chloride/trimethylaluminum was then removed by vacuum transfer and the beads and fibers stored under a vacuum at room temperature.

Characterization of Polymer Microspheres and Fibers

The morphologies of the fibers and spheres were evaluated by scanning electron microscopy using a Leo 1530 VP field emission electron microscope from Au/Pd coated samples. The PLA fibers and capsules were characterized by elemental mapping via energy dispersive X-ray (EDX) analysis.

Results/Discussion

Polymer Microspheres

Figure 3 shows an SEM image of a typical hollow PLA polymer shell formed from electrospraying the polymer solution into liquid nitrogen. The size of the

Downloaded by PENNSYLVANIA STATE UNIV on June 22, 2012 | http://pubs.acs.org
Publication Date (Web): November 10, 2010 | doi: 10.1021/bk-2010-1050.ch003

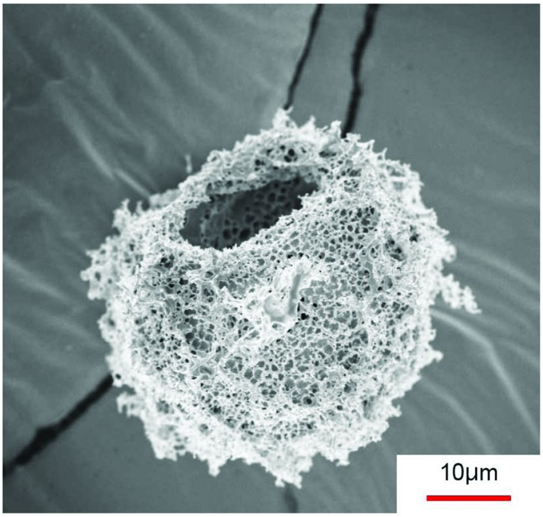

Figure 3. Hollow PLA polymer shell

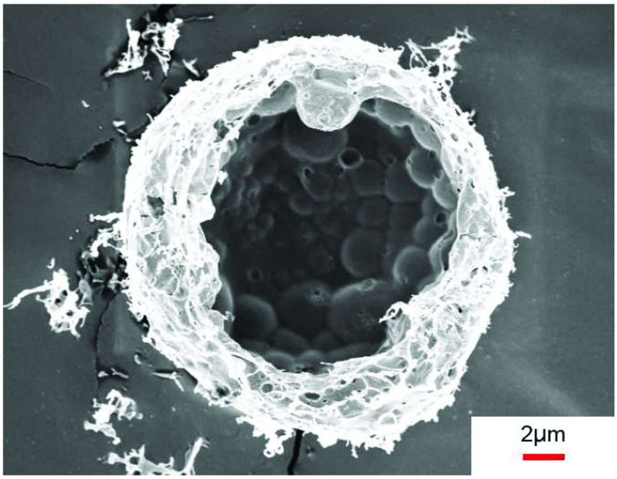

Figure 4. Interior of hollow polymer shell

polymer shells range from 15-40 μm in diameter and the size of the holes on the surface ranged from 5-10 μm in diameter. The size of the hollow polymer shells were shown to be dictated by the size of the droplets, which could be controlled by the electrospraying parameters, while the size of the holes on the polymer shell can be attributed to the chloroform used and the condition at which the solvent was evaporated such as the rate of evaporation.

Downloaded by PENNSYLVANIA STATE UNIV on June 22, 2012 | http://pubs.acs.org
Publication Date (Web): November 10, 2010 | doi: 10.1021/bk-2010-1050.ch003

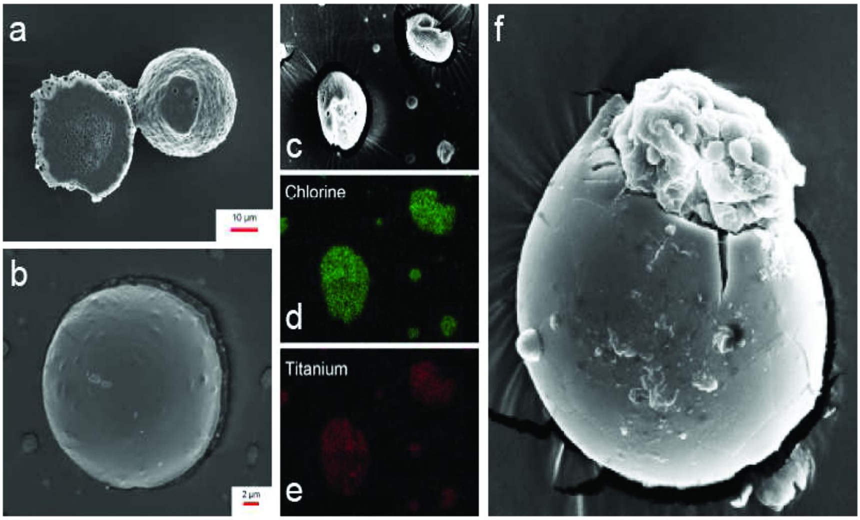

Figure 5. Encapsulation and release of reactive metal oxide precursors from microcapsules

Hyuk Im et al. first demonstrated the method of producing hollow polymer shells using polystyrene beads as the starting material. In our study, we eliminated the step of forming the polymer beads by directly nebulizing the polymer solution into fine droplets and collecting the droplets directly in liquid nitrogen through electrospraying. The step involves nubulizing the polymer solution and collecting the fine droplets in liquid nitrogen. Due to the poor thermal conductivity of polylactic acid, a temperature gradient is generated in the radial direction and solidification of the chloroform begins from the surface. As the droplets freeze, then density of the chloroform at the surface of the droplets increases, driving the chloroform from the center of the droplet toward the surface and creating the initial void in the center. When theses droplets are allowed to warm up under vacuum, the polylactic acid chains migrate from the center to the surface of the droplets due to the flux of the evaporating chloroform creating the hollow polymer shells of PLA. In the case of polystyrene conducted by Hyuk et al. the whole process must be carried out below 0°C or the hollow particles compress back into the solid beads by the surrounding water. This condition is not necessary in our method since the suspension of the polymer beads in an aqueous media is eliminated (*22*). Further investigation of the interior and exterior surface morphology of the hollow polymer shell structures in Figure 4, suggest the walls are composed of not a continuous polymer matrix, but a porous network. This type of morphology suggests a thermally induced phase separation (TIPS) process, which was induced by the freeze-drying of the polylactic acid solution in liquid nitrogen. The solid-liquid phase separation occurs during the cooling of the polymer, when the droplets of the polymer melt are electrosprayed into the liquid nitrogen, completely freezing the chloroform, producing polymer rich regions and polymer poor regions. This phase separation is stabilized by the polymer crystallization and the high glass transition temperature of the polymer-rich phase, resulting in a porous structure after removing the solvent.

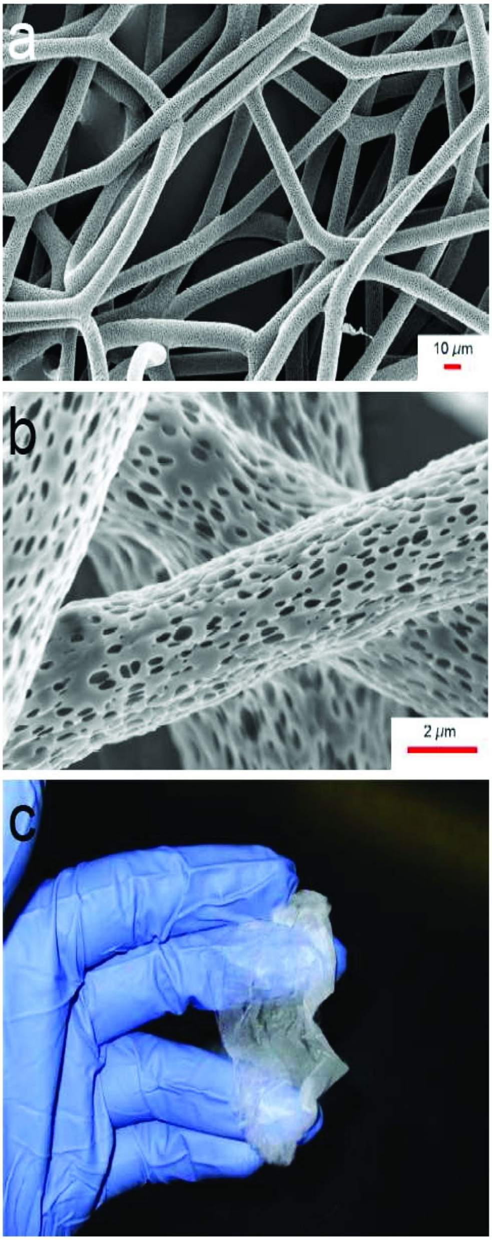

Figure 6. Electrospun porous fibers

Downloaded by PENNSYLVANIA STATE UNIV on June 22, 2012 | http://pubs.acs.org
Publication Date (Web): November 10, 2010 | doi: 10.1021/bk-2010-1050.ch003

Downloaded by PENNSYLVANIA STATE UNIV on June 22, 2012 | http://pubs.acs.org
Publication Date (Web): November 10, 2010 | doi: 10.1021/bk-2010-1050.ch003

Figure 5a depicts the result of the toluene solvent treatment on the hollow polymer shells. While polylactic acid has been shown to be readily soluble in many solvents such as chlorinated or fluorinated organic solvents, dioxane, and furan, in the presence of solvents such as toluene, xylene, and tetrohydrofuran the polymer undergoes a swelling process in which the rigid structure and integrity of the polymer melts and softens. The result is the sealing of the hole on the surface of the polymer shells, producing hollow polymer beads approximately 15 μm in diameter. The change in the surface morphology of the polymer shell due to the toluene treatment is clearly seen (fig. 5a). The rigid porous morphology previously seen (fig. 3-4) is no longer present and is replaced by a smooth nonporous capsule. Figure 5a also shows a sealed microcapsule attached to the remnants of a fractured hollow polymer bead exposing the interior wall morphology. It can be seen from this image that softening also occurred in the interior, which is attributed to the encapsulation of the toluene solvent within the capsules.

After demonstrating the ability to seal theses hollow polymer shells the introduction of titanium (IV) chloride was performed. Figure 5b shows the resulting microcapsules after filling with titanium (IV) chloride and the subsequent sealing with toluene. The size of the sealed microcapsules ranged from ~10-25 μm in diameter, slightly smaller than the diameter of the hollow polymer shells. The discrepancy in size was attributed to the softening and subsequent closing of the hollow sphere. Elemental mapping of the sealed microcapsules in Figure 5c-d indicates the presence of a high concentration of chlorine (fig. 5d) and titanium (fig. 5d) in the polymer spheres, thus presenting preliminary evidence for the presence of titanium (IV) chloride. The response of these microcapsules to a moisture rich environment is depicted in figure 5f where the encapsulating shell is ruptured not physically, but from partial dissolution of the PLA and hydrolysis of the $TiCl_4$ agent from the capsule. Upon exposure of these microcapsules to a moisture rich environment the ester bonds of the PLA begin to hydrolyze creating pinholes in the surface of the outer shell, which ultimately provide access to the encapsulated material. Upon the exposure of the core to moisture, hydrolysis of the metal oxide precursor occurs resulting in the formation and delivery of titanium dioxide. Thus, electrospray can be used to produce microcapsules that are effective at encapsulating moisture reactive species, a limitation of other encapsulating methods, and an ability that has not been demonstrated in previous studies. The encapsulation of these reactive species in a degradable polymer produces a microcapsule that is responsive to environmental moisture as well as physical rupture of the encapsulating shell. This method of encapsulation and delivery also expands the range of materials that can be encapsulated. The ability to integrate these microcapsules within a suitable material expands the responsiveness of the target smart coating. The only challenge with the hollow spheres is the manipulation and transfer to composite films. Hollow fibers in the form of paper are far easier to handle.

Downloaded by PENNSYLVANIA STATE UNIV on June 22, 2012 | http://pubs.acs.org
Publication Date (Web): November 10, 2010 | doi: 10.1021/bk-2010-1050.ch003

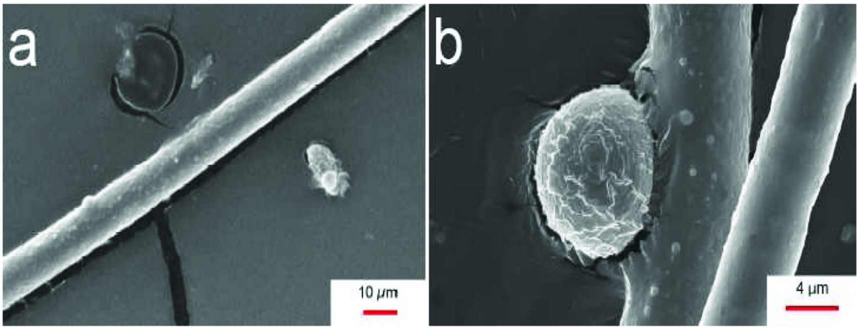

Figure 7. Encapsulation and release $TiCl_4$ and formation of TiO_2

Porous Fiber: Encapsulation of Reactive Metal Oxide Precursors

Figure 6a-b shows SEM images of porous PLA fibers ranging in diameter from 10-12 μm formed from electrospinning a 10% w/w polymer solution. The pores were oval shaped with the average pore size on the order of 150 nm in width and 300 nm in length with the long axis oriented along the fiber axis (fig 6b). The formation of these porous fibers was attributed to the rapid phase separation between polymer rich and polymer poor regions during the electrospinning process followed by a rapid solidification of the polymer caused by the evaporation of the solvent. The elongation of the pores on the fiber developed from the whipping action of the fibers between the spinneret and the grounded target in the electrospinning process.

These porous PLA fibers were collected on a grounded rotating drum, resulting in a flexible free-standing paper material consisting of aligned fibers that are easily physically manipulated without compromising the structural integrity (fig. 6c). The fabrication of these fibers as a paper provided a means of easily transferring them from the electrospinning apparatus to the vacuum line for the encapsulation process and then the subsequent transferring from the vacuum line to characterization. The ease of manipulating these fibers as a paper also introduces the potential for the facile integration into inorganic composite materials.

Titanium (IV) Chloride

Figure 7a shows a fiber after filling the pores with $TiCl_4$ and the subsequent treatment with toluene. The size of the polymer fibers fabricated ranged in diameter from 8-10 μm. The surface morphology of theses fibers showing the sealed pores is similar to the sealing of the hollow polymer shells, the introduction of toluene softens the polymer and encapsulates the titanium (IV) chloride.

Before encapsulating the $TiCl_4$ within the pores, the fibers exhibit a semi-transparent white color. Upon introduction of toluene into the system, the titanium (IV) chloride immediately formed a yellow-orange solution, which was consequently encapsulated within the pores of the fiber, causing the fibers to also take on this yellow-orange color. Upon exposing the titanium (IV) chloride treated fibers to 80% RH for an extended period of time, the majority of the yellow-orange color dissipated. This change in color was due to the formation of a charge transfer complex between the aromatic toluene and the titanium (IV) chloride (*23*).

Upon exposure of the fibers to 80% relative humidity oxide growths begin to appear on the surface of the fiber. As the exposure of these fibers to the humid environment increases the size of the nodules also increase. Within 15-20 days the size of these growths near the diameter of the fibers and begin to penetrate the encapsulating polylactic acid (fig. 7b). It is proposed that these growths or nodules are initiated by the influx of moisture through the introduction of a pinhole in the membrane of the fibers due to hydrolysis of the ester bonds in the polylactic acid shell, similar to the process seen in the microcapsules previously discussed. The appearance of these pinholes exposes the titanium (IV) chloride to the moist environment resulting in the initiation of hydrolysis. Further hydrolysis of the polymer shell leads to an increased pinhole size and thus an increased influx of moisture into the pore and thus an increased size in the growths. Micro-Raman spectroscopic as well as X-ray diffraction studies of these fibers throughout its exposure to the moisture rich atmosphere indicates the depletion of titanium (IV) chloride and formation of titanium oxychlorides, an intermediate hydrolysis product, and ultimately titanium dioxide nanoparticles (*23*).

Downloaded by PENNSYLVANIA STATE UNIV on June 22, 2012 | http://pubs.acs.org
Publication Date (Web): November 10, 2010 | doi: 10.1021/bk-2010-1050.ch003

Trimethylaluminum

Figure 8a shows the porous fibers after filling the pores with TMA and the subsequent treatment with toluene. Similar to the fibers with the titanium (IV) chloride, the fibers exhibit a continuous morphology with the pores sealed from the toluene treatment. The morphological changes of the fibers upon exposure to 80% relative humidity do not parallel that of the $TiCl_4$. While the titanium (IV) chloride treated fibers showed the slow growth of nodules on the fiber surface, the reaction of the TMA treated fibers was much more rapid. The exposure of the TMA through hydrolysis and physical stress of the encapsulation resulted in the formation of amorphous alumina, which can be seen in figure 8b. The frequency of these formations was directly related to the length of time at which these fibers were exposed to the humid environment. A digital image of the fibers after the encapsulation of TMA is shown in figure 8c.

The contrast in the release characteristics of the trimethylaluminum to the titanium (IV) chloride is attributed to the difference in reactivity of these two precursors. The pyrophoric trimethylaluminum reacts much more violently upon the influx of moisture forming amorphous alumina while in the case of titanium (IV) chloride intermediate hydrolysis products such as titanium oxychlorides are formed, which eventually leads to the formation of titanium dioxide. The encapsulation of these two reactive precursors demonstrates the versatility of this approach to producing a delivery system for smart coatings.

Downloaded by PENNSYLVANIA STATE UNIV on June 22, 2012 | http://pubs.acs.org
Publication Date (Web): November 10, 2010 | doi: 10.1021/bk-2010-1050.ch003

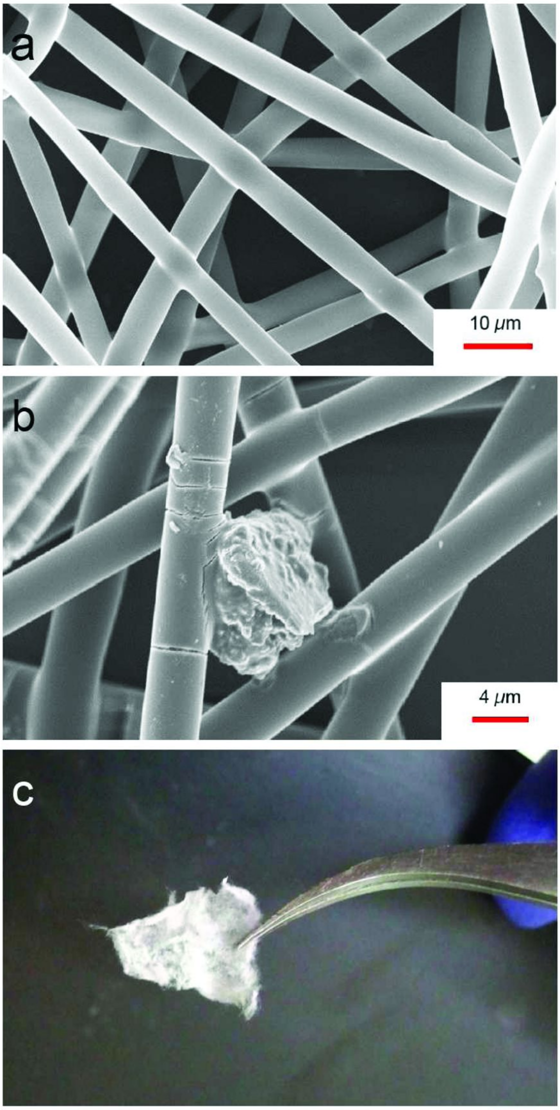

Figure 8. Encapsulation and release of Trimethylaluminum in fibers

Smart Coatings with Fibers

The ability to encapsulate these reactive species into fibrous free-standing papers provides many benefits. The easy fabrication and manipulation of these fibers as a free-standing paper allows for the integration into a thin film by the method of spin coating, resulting in a thin film that could be used as a smart coating. In order to test its efficacy as a smart coating a sheet of the treated fibers were integrated into a thin film of PMMA and cracks were introduced on the thin film surface by flexing the thin film around a known radius of curvature. These films were then allowed to rest for a predetermined amount of time. The results

Downloaded by PENNSYLVANIA STATE UNIV on June 22, 2012 | http://pubs.acs.org
Publication Date (Web): November 10, 2010 | doi: 10.1021/bk-2010-1050.ch003

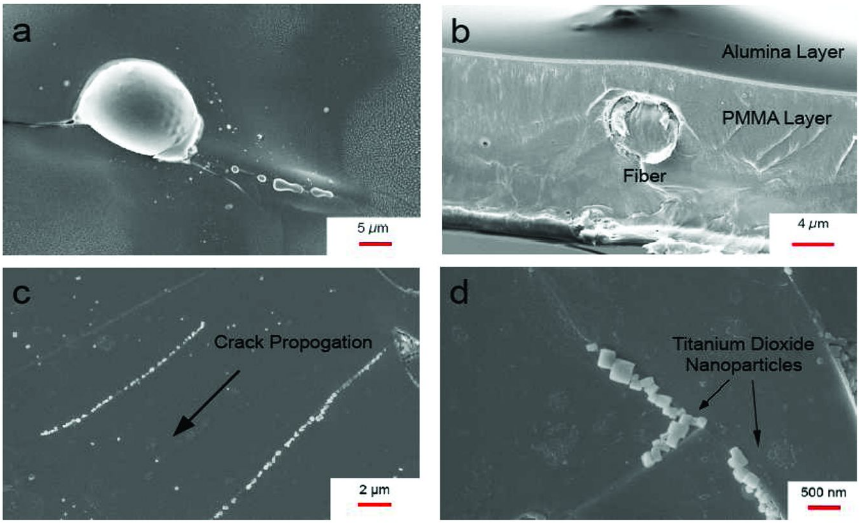

Figure 9. Integrated fibers in smart-coating and response to stress induced cracks

of these studies showed growths protruding from the induced cracks, which are depicted in the electron micrographs of figure 9a. After observing the appearance of growths on the PMMA surface, a new film was fabricated and a thin layer of alumina was deposited upon the surface through atomic layer deposition (ALD) (fig. 9b). Theses films were then exposed to the same treatment as the PMMA films and cracks were induced. Scanning electron micrographs of the surface of the film revealed the formation of titanium dioxide nanoparticles along the cracks of the fractured surfaces (fig. 9c). To further demonstrate the ability of this delivery system, an electron micrograph showing the delivery of titanium dioxide nanoparticles to the convergence of two cracks forming a perpendicular fissure is shown in figure 9d. EDAX images (not shown) confirm these crystals are TiO_2. The results shown in this smart-coating system suggest the ability of these fibers to release the encapsulated metal oxide precursor resulting in the delivery/formation of metal oxide nanoparticles to a site-specific location. These results also suggest that the initiation of this system is not only reactive to the physical fracture of these fibers, but also to the influx of moisture in the crack.

Conclusion

A technique for the electrostatic fabrication of a delivery system composed of microcapsules and fibers for smart coatings was demonstrated in this study. The ability to encapsulate highly reactive precursors in the fibers of a free-standing paper as well as capsules that are easily integrated in a thin film for a smart coating was also proven. The efficacy of this delivery system for the delivery of metal oxide nanoparticles was also shown. While this specific study focuses on the encapsulation of highly reactive metal oxide precursors, other applications for this delivery system have been explored by our group including: the encapsulation of nitric oxide releasing materials for donor organs as well as the encapsulation of zeolitic materials for the facile collection of heavy metals in the environment.

Acknowledgments

We would like to recognize Srinivas Gowrisanker for help in the ALD of alumina and financial support from the Robert A. Welch Foundation (AT-1153).

References

1. "Scratch Guard Coat." Nissan Motor Company. 15 Jan. 2008. http://www.nissan-global.com/EN/TECHNOLOGY/INTRODUCTION/DETAILS/SGC/index.html.
2. Zafar, S.; Riaz, U.; Ahmad, S. *J. Appl. Polym. Sci.* **2008**, *107*, 215–222.
3. Guan, K. *Surf. Coat. Technol.* **2005**, *191*, 155–160.
4. Nakajima, A.; Hashimoto, K.; Watanabe, T.; Takai, K.; Yamauchi, G.; Fujishima, A. *Langmuir* **2000**, *16*, 7044–7047.
5. Parkin, I. P.; Palgrave, R. G. *J. Mater. Chem.* **2005**, *15*, 1689–1695.
6. Zhang, X. T.; Sato, O.; Taguchi, M.; Einaga, Y.; Murakami, T.; Fujishima, A. *Chem. Mater.* **2005**, *17*, 696–700.
7. Feng, W.; Patel, S. H.; Young, M. Y.; Zunino, J. L.; Xanthos, M. *Adv. Polym. Technol.* **2007**, *26*, 1–13.
8. Brown, E.; Sottos, N.; White, S. *Exp. Mech.* **2002**, *42*, 372–379.
9. Brown, E. N.; White, S. R.; Sottos, N. R. *J. Mater. Sci.* **2004**, *39*, 1703–1710.
10. Kessler, M. R.; Sottos, N. R.; White, S. R. *Composites, Part A* **2003**, *34*, 743–753.
11. White, S. R.; Sottos, N. R.; Geubelle, P. H.; Moore, J. S.; Kessler, M. R.; Sriram, S. R.; Brown, E. N.; Viswanathan, S. *Nature* **2002**, *415*, 817.
12. Jalil, R.; Nixon, J. R. *J. Microencapsulation* **1990**, *7*, 53–66.
13. Leelarasamee, N.; Howard, S. A.; Malanga, C. J.; Ma, J. K. H. *J. Microencapsulation* **1988**, *5*, 147–157.
14. Freitas, S.; Merkle, H. P.; Gander, B. *J. Controlled Release* **2005**, *102*, 313–332.
15. Hyon, S. H. *Yonsei Med. J.* **2000**, *41*, 720–734.
16. Dalpiaz, A.; Scatturin, A.; Pavan, B.; Biondi, C.; Vandelli, M. A.; Forni, F. *Int. J. Pharm.* **2002**, *242*, 115–120.
17. Nakashima, T.; Shimizu, M.; Kukizaki, M. *Adv. Drug Delivery Rev.* **2000**, *45*, 47–56.
18. Van der Graaf, S.; Schroen, C. G. P. H.; Boom, R. M. *J. Membr. Sci.* **2005**, *251*, 7–15.
19. Qi, H.; Hu, P.; Xu, J.; Wang, A. *Biomacromolecules* **2006**, *7*, 2327–2330.
20. Xie, J.; Wang, C. H. *Pharm. Res.* **2006**, *23*, 1817–1826.
21. Vaseashta, A.; Erdem, A.; Stamatin, I. *MRS Symp. Proc.* **2006**, *920*, 143–148.
22. Hyuk Im, S.; Jeong, U.; Xia, Y. *Nat. Mater.* **2005**, *4*, 671–675.
23. Liu, H.; Gnade, B. E.; Balkus, K. J., Jr. *Adv. Funct. Mater.* **2008**, *18*, 1–10.

Downloaded by PENNSYLVANIA STATE UNIV on June 22, 2012 | http://pubs.acs.org
Publication Date (Web): November 10, 2010 | doi: 10.1021/bk-2010-1050.ch003

Downloaded by PENNSYLVANIA STATE UNIV on June 22, 2012 | http://pubs.acs.org
Publication Date (Web): November 10, 2010 | doi: 10.1021/bk-2010-1050.ch004

Chapter 4

Smart Self-Healing Material Systems Using Inductive and Resistive Heating

**Terrisa Duenas,[*,a] Andrew Enke,[a] Karen Chai,[a] Matt Castellucci,[b]
Vishnu Baba Sundaresan,[b] Fred Wudl,[c] Erin B. Murphy,[c] Ajit Mal,[d]
James R. Alexandar,[e] Aaron Corder,[f] and Teng K. Ooi[f,g]**

**[a]NextGen Aeronautics Inc., Torrance, CA
[b]Virginia Polytechnic Institute and State University, Blacksburg, VA
[c]University of California, Santa Barbara, CA
[d]University of California, Los Angeles, CA
[e]US Army Aviation and Missile Research, Development and Engineering Center, Redstone Arsenal, AL
[f]Missile Defense Agency, Pentagon Defense, Washington, DC
[g]Office of Naval Research, Washington, DC
[*]tduenas@nextgenaero.com**

Based on the metric of “healing window”, the ionomer composite containing 2-3% nano iron oxide particles and heated at induction frequencies between 250 and 300 kHz yields the most favorable results. The metric of healing window is defined as the time difference between initiation of healing (melting) and onset of deformation. At this aforementioned ideal volume fraction, composition and induction frequency range, healing of a damaged thick film of ionomeric polymer occurs between 5 and 10 seconds. In this study, both compliant and structural remendable polymers are combined with a small amount of heating material (<5% volume fraction) to facilitate site-specific healing and facilitate future active self-healing. The compliant remenable polymer is an ionomer. The structural remendable polymer is a highly cross-linked polymers called “Mendomer.” The heating materials include nanoscale and microscale magnetic particles used with induction heating and carbon fibers used with resistive heating. The inductive heating approach compared to the resistive heating approach has the advantage of being non-contact. Current approaches describe in-situ healing where external power is delivered to generate heating. Active self-healing will be made possible by coupling the healing mechanism with a damage event. Remending polymers can be layered or combined with conventional materials to yield a multifunctional solution offering both a conventional function plus the added remendable feature. One application combines ionomeric remendable polymers layered with polyimide and polytetrafluoroethylene to form remendable wire insulation multilayer composites. Another application uses the Mendomer as the matrix for conventional carbon-fiber composite fabrication to mitigate damage from matrix cracking and subsequent delamination. Preliminary and quantitative results are given and discussed for ionomers, ionomers combined with magnetic particles, ionomers combined with carbon fiber, Mendomers, and Mendomers combined with magnetic particles. For the case of magnetic particles used with induction heating, optimal volume fractions are between 2 and 3%.

Downloaded by PENNSYLVANIA STATE UNIV on June 22, 2012 | http://pubs.acs.org
Publication Date (Web): November 10, 2010 | doi: 10.1021/bk-2010-1050.ch004

Introduction

Self-healing is the ability of a material to inherently sense damage and respond in a way that results in self-repair from incurred damages. An ideal example of a self-healing material is human skin. Although the self-healing mechanism in remendable materials is not passive as in the case of human skin, it can be mimicked when applied along with damage-detection methods such as Nondestructive Evaluation (NDE). A multifunctional actively self-healing material results when the damage-detection methods are used to trigger the initiation of a healing mechanism. In this paper, the healing mechanisms of two remendable polymers are combined with conventional materials to address two aerospace applications--wire insulation and structural carbon-fiber composites. Coupling of damage events with self-healing via damage-detection methods will be addressed in the future.

The two remendable materials that are investigated are Surlyn® 8940 and Mendomer. Surlyn® 8940 is a commercially available material sold by Dupont™ with a Young's Modulus of approximately 200 MPa. This poly(ethylene-co-methacrylic acid) (EMAA) ionomer-based material was investigated by Fall (2001) (*1*) and Kalista (2003) (*2*) to demonstrate self-healing after bullet penetration. Surlyn® 8940 has been chosen to address the wire insulation application due to its compliant modulus and self-healing properties. The structural remendable polymer presented in this paper is a highly cross-linked, Furan-Maleimide-based polymer developed by the University of California (UCLA) (*3*) and subsequently named "Mendomer" (*4*). This remendable structural polymer with a Young's Modulus between 2 and 3 GPa has shown 80% recovery of initial strength after repeated fracture and subsequent healing cycles. The Mendomer has been chosen to address carbon-fiber composite matrix failure.

Downloaded by PENNSYLVANIA STATE UNIV on June 22, 2012 | http://pubs.acs.org
Publication Date (Web): November 10, 2010 | doi: 10.1021/bk-2010-1050.ch004

To enable remending, <5% volume fraction of heating material are incorporated into the polymer composites. The healing process in these remendable polymers is performed by induction and resistive heating. Using a current-conducting coil, induction heating directs a high-frequency alternating magnetic field at an electromagnetic-energy-absorbing material (susceptor). The degree of heating from resistive heating (eddy current loss) or hysteresis loss (changes in the material as it is magnetized and demagnetized) depends on the susceptor material. The size and shape of the coil also determine the location and area of heating. In 2000, Wetzel began using magnetic particles in induction heating of thermoplastics as a novel bonding method over traditional techniques (*5*); he continued his investigation using magnetic particles for "Curie Temperature-Controlled Processing of Composite Materials" (*6*). In 2005, researchers D. Leo and T. E. Long from Virginia Polytechnic Institute and State University (Virginia Tech) proposed working with NextGen Aeronautics to use magnetic particles as a means to deliver heat and subsequent healing to their Virginia Tech developed ionomers (*1*, *2*). This work resulted in the novel combination of ionomers containing magnetic particles (gamma-Fe_2O_3, alpha-Fe_2O_3, and a ferrite compound) to fabricate remendable compliant polymer composites for the potential use as self-healing wire insulation materials (*7*). The current work continues this previous research by investigating an alternate magnetic material (nickel), the effects of induction frequency, and the effects of particle-size distribution to ionomeric polymer healing. This work also reviews a similar induction heating approach to Mendomer materials and introduces a resistive approach to healing ionomers. Resistive heating can also be used to heal Mendomer materials (*8*, *9*). Detailed discussions of these remendable materials, resistive heating, and related topics can be found in "Self Healing Materials" (*10*).

NextGen has fabricated both the ionomeric and Mendomer remendable material composites as well as combined them with conventional materials to create multifunctional materials. The solutions presented in this paper suggest that in-situ healing is performed on the damage site instead of replacing entire parts of failed wire insulation and carbon-fiber composites. The suggested in-situ healing can be accomplished either by manual intervention or by an automated response. To facilitate healing in a carbon-fiber panel, an inductive field is applied to the damaged area. The polymer begins to heat due to the embedded magnetic particles, which is followed by healing of the carbon-fiber matrix. In the wire-insulation case, external power is used to generate either induction heating or resistive heating to facilitate healing. Implementation of an automated response to a damage event constitutes active self-healing as opposed to just remending. The metric of "healing window" is introduced to facilitate the understanding and applicability of these remendable materials to commercial applications. The healing window is defined as the time difference (heating time) between initiation of healing (melting) and onset of deformation. This metric is important to application developers to facilitate the understanding of those parameters related to heating and control of healing. This paper presents new results and reviews previous results for induction heating of Surlyn® 8940 as well as presents results for resistive heating of Surlyn® 8940 using carbon fibers. Previous results of heating Mendomer polymers with an induction heater are also

Downloaded by PENNSYLVANIA STATE UNIV on June 22, 2012 | http://pubs.acs.org
Publication Date (Web): November 10, 2010 | doi: 10.1021/bk-2010-1050.ch004

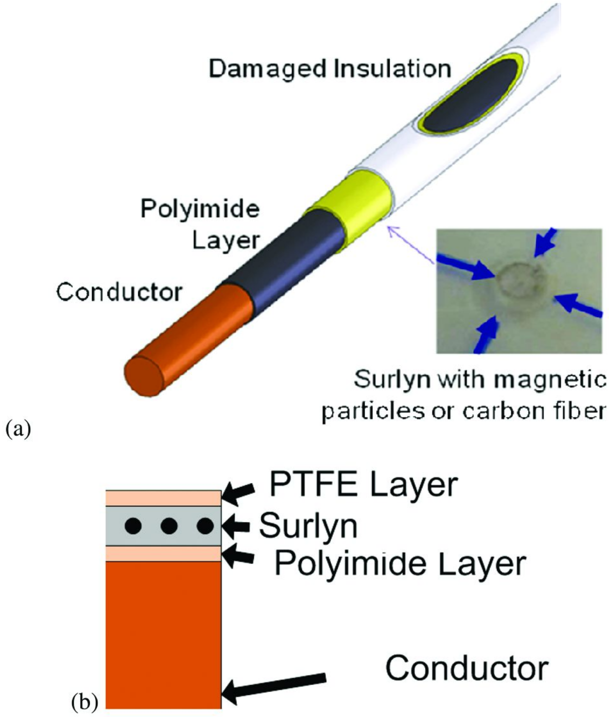

Figure 1. Schematic of (a) the wire insulation solution as applied to a cylindrical wire geometry and (b) the layer setup as used for testing and characterization of wire insulation solution of ionomer/magnetic-particle composite layered with conventional insulation materials. (Adapted with permission from reference (16). Copyright 2009 Matt Castellucci.)

reviewed to provide a complete summary of the current work with remendable materials in aerospace applications.

Wire Insulation Failure

There have been at least 10 space missions which have experienced wire system failures. Several appear linked to the failure of wire insulation which is the common mode of failure for wiring systems. For example, Gemini 8 experienced an electrical wiring short and near loss of crew. In Apollo 204, damaged insulation caused an electrical spark, fire and loss of astronauts. Damaged wire insulation was also documented as a part of Apollo 13's aborted mission. STS-6 experienced insulation abrasion and subsequent arc tracking causing insulation pyrolysis and melted conductors. Spacelab experienced a similar event resulting in damage during maintenance (*11*). While specific numbers for their prevalence and rate of occurrence is not readily available, the loss of lives and equipment is prohibitively costly and warrants the study of self-healing wire insulation materials. Where damage is manually identified as during maintenance, repairing damaged wire insulation may introduce susceptibility to failure. This can be caused by splicing or creating stress concentrations with post-applied shrink-wrapping. Manual in-situ healing of damaged wire insulation prevents splicing and secondary shrink-wrapping; instead insulation material is healed in place without the need for material replacement and/or addition. Active (or autonomous) self-healing would enable automatic healing of failed wire insulation which would be critical during flight and certain ground operations where immediate repair is prohibitive.

Carbon-Fiber Composite Failure

In the mid-1980s, civilian and military aircraft manufacturers began fabricating structural components using fiber-reinforced polymer composites, such as carbon-fiber composites, rather than metals. This change brought about great benefits to the structural design of aircraft due to the material's high-strength and light-weight characteristics. However, these new materials demonstrated unique damage characteristics when compared with their metal counterparts. Specifically, carbon-fiber composite materials are threatened by three failure modes: (1) matrix cracking, (2) internal, interlayer delamination and (3) fiber breakage. This work aims to address cracking which will mitigate delamination. Advanced composites are usually incorporated into structures in the form of laminates. Delamination is an intrinsic and severe problem of these materials (*12*, *13*). Interlaminar stresses due to mismatch of anisotropic mechanical and thermal properties of plies occur at free edges, joints, matrix cracks, and under out-of-plane loadings. Delamination is a dominant failure mode for laminates subjected to impact and fatigue loadings that are typical for military applications. High interlaminar stresses occur in the vicinity of cracks in the primary reinforcing plies (*14*, *15*). As more vehicles are fabricated using fiber-reinforced polymer composites, greater control of damage must also be investigated and addressed.

Wire Insulation Composite - Experimental

Materials Used in the Wire Insulation Composite

As previously mentioned, Surlyn® 8940 is combined with a magnetic particle constituent. This combination is then multilayered with the conventional wire insulation materials of Teflon® (polytetrafluoroethylene (PTFE)) and of Kapton® (polyimide) (also products of DuPont). The resultant composite is a remendable wire insulation assembly which can serve the basis for a self-healing wire insulation material if damage can be coupled with the healing response. The solution to damaged wire insulation combines ionomers with magnetic particles or carbon-fiber to then be layered with traditional insulation materials to result in a remendable wire insulation assembly. When damage has occurred which causes an unwanted opening or crack in the insulation, heating can be applied to the area to flow the ionomer material into the damaged area and as a result, heal the insulation assembly. The layering order of these samples is depicted below in Figure 1. The ferrite particles were obtained from Powder Processing & Technology, LLC. The nickel and iron oxide particles were purchased from Sigma-Aldrich. The nano-sized iron oxide (Fe_2O_3) particles used were sized 50

Downloaded by PENNSYLVANIA STATE UNIV on June 22, 2012 | http://pubs.acs.org
Publication Date (Web): November 10, 2010 | doi: 10.1021/bk-2010-1050.ch004

Downloaded by PENNSYLVANIA STATE UNIV on June 22, 2012 | http://pubs.acs.org
Publication Date (Web): November 10, 2010 | doi: 10.1021/bk-2010-1050.ch004

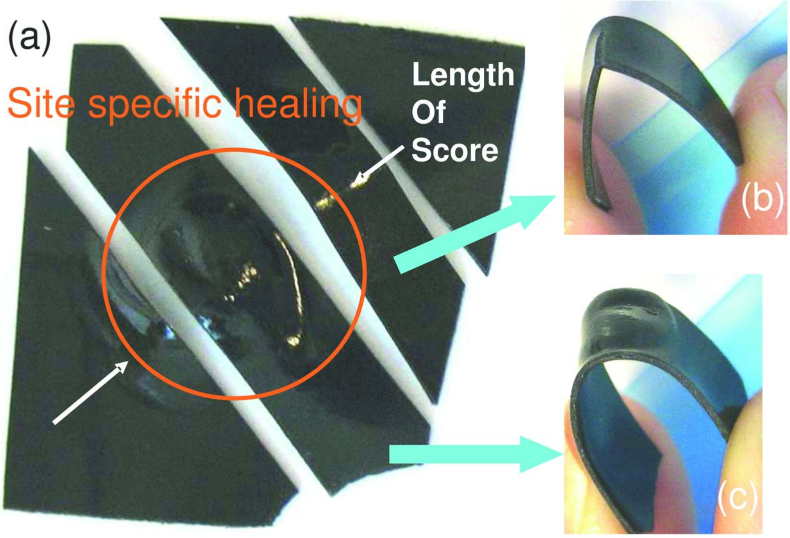

Figure 2. Bending tests on an ionomer/6% volume fraction ferrite sample (a) the area of site-specific healing (circle) is shown. (b) This is a strip of sample outside the focused area of healing and (c) shows a strip of sample where the site-specific healing occurred. (Adapted from (4).)

nm or less in particle diameter. The micro-sized nickel particles were under 3 µm in diameter, and nano-sized nickel particles were under 100 nm in diameter.

Ionomer/Magnetic-Particle Composite Manufacturing

Ionomer material with imbedded magnetic particles was manufactured using a melt-press technique. A sheet of pure ionomer (DuPont Surlyn® 8940) was first fabricated using the raw material in pellet form. The pressing technique involved heating steel press plates to 160°C, and then applying the appropriate pressure. Polyimide (DuPont Kapton®) film was used as a release agent for the plates. Magnetic particles were intermixed with the ionomer also using the melt-press method. A fixed amount of the pressed ionomer was measured, and the appropriate amount of magnetic particles was weighed, using densities to achieve the desired volume fraction. The magnetic particles, in dry powder form, were placed in between layers of the pressed ionomer. Due to the high viscosity of the ionomer (even in melted form), multiple pressings (typically 8-10 or more) were required to achieve uniform particle distribution within the ionomer. The pressing cycle involved cutting the partially-mixed ionomer/particle material into smaller pieces, stacking these pieces, re-pressing the material, and then allowing the material to cool. Homogeneous magnetic particle distribution was verified visually using a microscope. For the results other than the sample using a 6% volume fraction of ferrite magnetic, the volume fraction is given with the data.

Downloaded by PENNSYLVANIA STATE UNIV on June 22, 2012 | http://pubs.acs.org
Publication Date (Web): November 10, 2010 | doi: 10.1021/bk-2010-1050.ch004

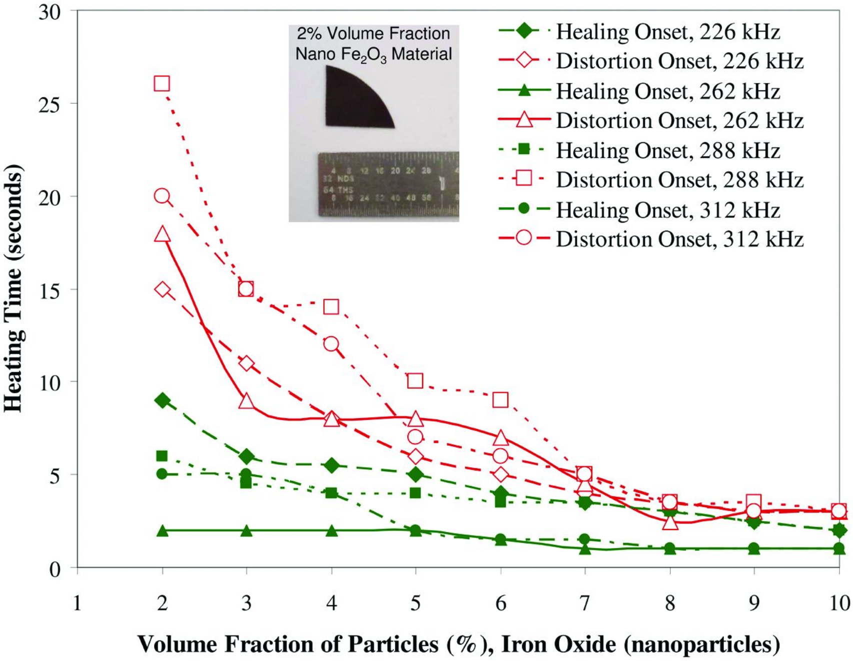

Figure 3. Graphical display of the onset of healing and distortion of ionomer/iron oxide (nanoparticle) composite coupons of varying volume fraction which experienced varying induction heating frequencies. A portion of 2% volume fraction material is shown in the inset.

Ionomer/Magnetic-Particle Composite Characterization and Results

The sample is first scored with a razor blade (not completely cutting through the material). The material is then healed in a local site using an induction heater (Figure 2(a)). The induction heating takes place in a localized area where the induction coil is placed; the heating size and location can be tailored by the size and position of the coil used, as the electromagnetic field is limited in range. For example, a small coil will heat a small area, and a large coil will heat a larger area. Therefore, site-specific healing refers to healing that can be localized to a specific area based on the location and size of the inductive coil used. The heated region of the sample has shown to have the razor damage healed, no longer displaying the cut (Figure 2(b)), whereas the unheated portion remains damaged (Figure 2(c)). Further details of the procedures to manufacture and test this sample are provided in (*4*).

Downloaded by PENNSYLVANIA STATE UNIV on June 22, 2012 | http://pubs.acs.org
Publication Date (Web): November 10, 2010 | doi: 10.1021/bk-2010-1050.ch004

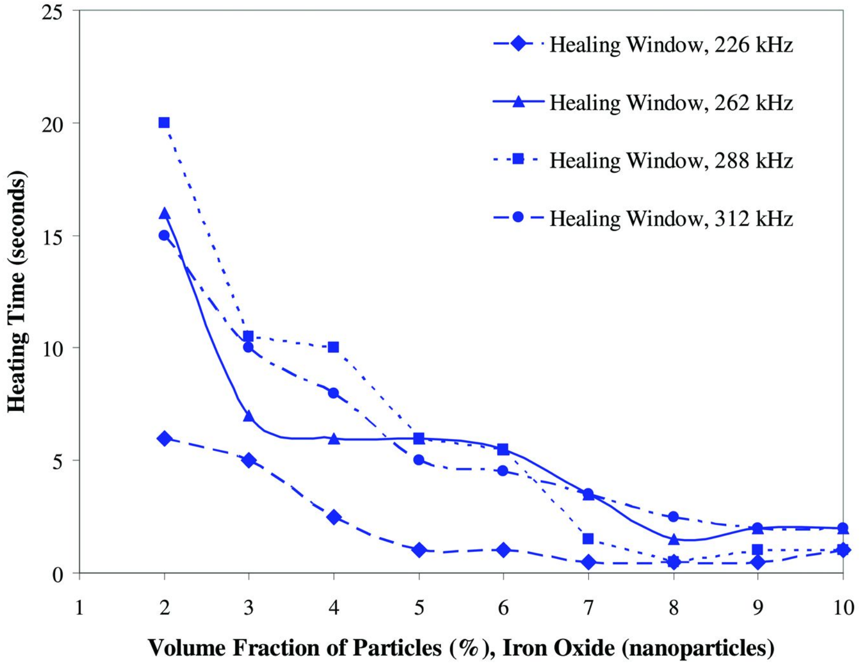

Figure 4. Graphical display of the healing window (between the onset of healing and distortion) of ionomer/iron oxide (nanoparticle) composite coupons of varying volume fraction which experienced varying induction heating frequencies.

In addition to this simple qualitative bending test, a parametric study was performed analyzing the sample healing response to different magnetic particle/ionomeric polymer samples. An induction heater was used to output a high-frequency electromagnetic field that resulted in heating the coupon in the area where the field was applied. Testing variables included volume fraction, induction heater frequency, particle composition, and particle size. The ionomer samples were fabricated with volume fractions from 1% to 10% in 1% increments. Samples with 1% volume fractions showed insufficient heating, thus data plots start with 2% volume fraction. The characterization frequency output was dependent on the coil connected to the heater.

The healing window is the heating time that is calculated from the duration of time between the initial heating of the sample to its melting point where healing is first possible, and the deformation time where changes in shape of the sample due to overheating could degrade the insulation integrity. This collection of data relies on a human observation of both the onset of healing and the recognition of deformation. Preliminary results of the induction heating tests are shown in Figures 3 and 4. Here, coupons of varying volume fraction experienced varying induction frequencies of 226, 262, 288, and 312 kHz.

The time was recorded when the material initiated healing (as indicated by the with solid data markers) and also when the sample started to deform (as shown by

Downloaded by PENNSYLVANIA STATE UNIV on June 22, 2012 | http://pubs.acs.org
Publication Date (Web): November 10, 2010 | doi: 10.1021/bk-2010-1050.ch004

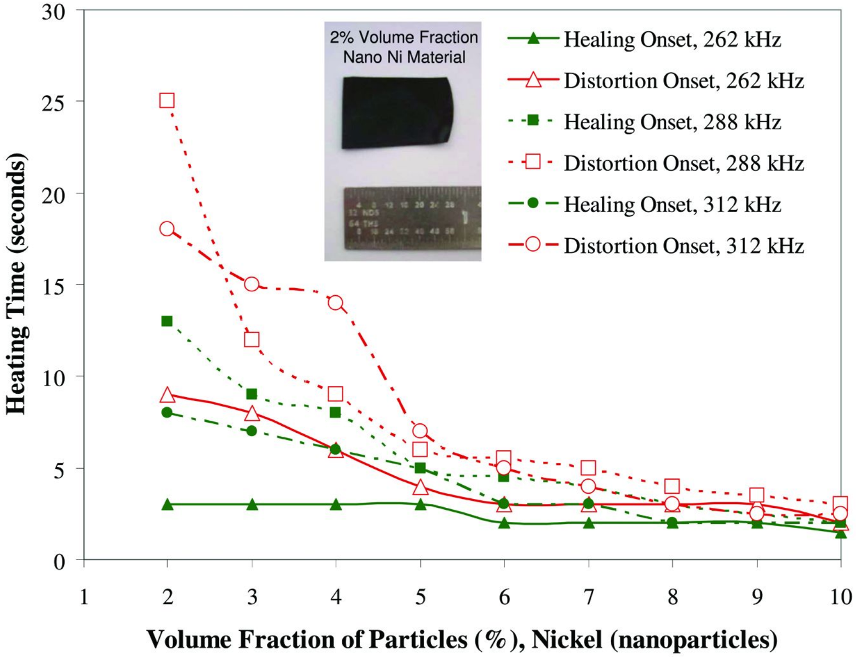

Figure 5. Graphical display of the onset of healing and distortion of ionomer/nickel magnetic nanoparticles with volume fraction varying from 2-10% and induction frequencies 262, 288, and 312 kHz. A portion of 2% volume fraction material is shown in the inset.

the unfilled data markers). Data was collected by visual inspection, with samples held in position 3 to 5 mm over the induction coil with nonmagnetic tweezers. Healing initiation was visually determined when the material would lose stiffness. This transition coincides with the point where the material begins to soften on the surface and it is able to mend with itself. Deformation or degradation of the material covered several characteristics that would not be favorable to a wire insulation. The time was noted when the first of these characteristics was apparent. Modes of deformation included various physical signs of overheating, typically including warping of shape and blistering. Either deformation mode would imply that the material was overheated to a point where it may no longer be viable as wire insulation. Warping would expose the conductor within, as could any blistering. As possible wire insulation damage varies, the healing window does not necessarily correlate to a specific wire healing cycle; for example, an incurred damage could be so severe that no amount of heating could allow the insulation to heal properly. Conversely, a very small damage could be healed in a short amount of time. In general, however, the larger the healing window is, the longer a sample could be heated. This would allow more time for healing, increasing the likelihood of the insulation to mend any damage without overheating to the point where the heat adds the possibility of wire insulation degradation. An observed trend was that a larger healing window was possible at higher applied frequencies.

Downloaded by PENNSYLVANIA STATE UNIV on June 22, 2012 | http://pubs.acs.org
Publication Date (Web): November 10, 2010 | doi: 10.1021/bk-2010-1050.ch004

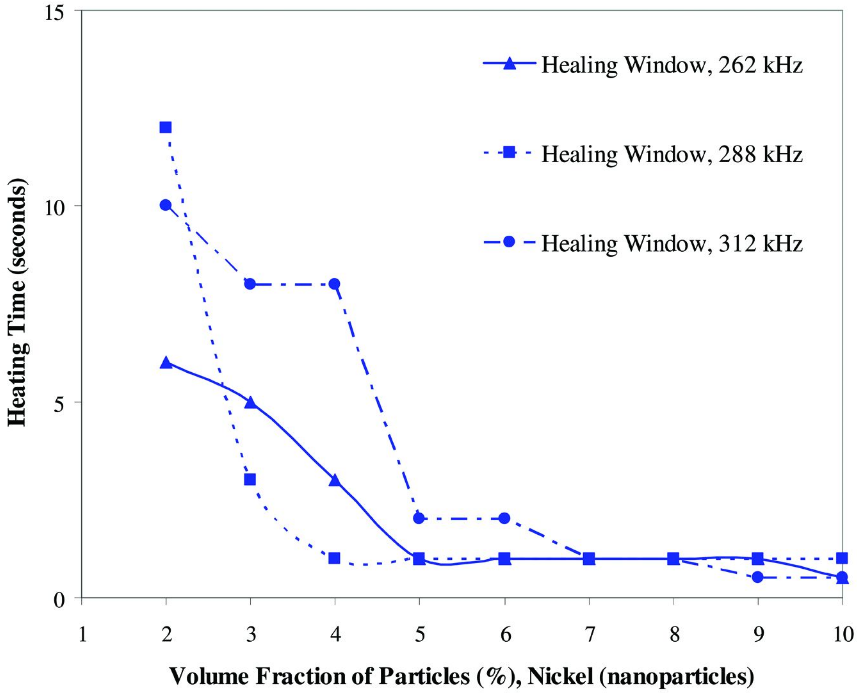

Figure 6. Graphical display of the healing window (between the onset of healing and distortion) of ionomer/nickel magnetic nanoparticles with volume fraction varying from 2-10% and induction frequencies 262, 288, and 312 kHz.

In addition to iron oxide magnetic particles, nickel particles were also evaluated at the nano- and the micro-scale. In addition to composition dependency of the healing response, mean particle size dependency was also investigated. The results of these tests are shown below, with heating and distortion times shown in Figure 5 and Figure 7 and healing window times plotted in Figure 6 and Figure 8.

From the results of the ionomer/magnetic particle composites with nano- and micro-scale nickel magnetic particles, it was observed that the samples with nanoparticles heated at a faster rate than those with microparticles, but also deformed at a faster rate. After conducting the ionomer/magnetic particle healing window tests, it was concluded that high volume fractions (6-10%) tended to have a significantly briefer healing window, hence would be more likely to overheat. Lower induction heater frequencies tended to have a briefer healing window than higher frequencies. Generally speaking, the material with the nano iron oxide particles as well as the two sizes of nickel particles performed similarly, however the nickel particles tended to exhibit shorter healing windows at lower frequency. For example, at 2% volume fraction and at 262 kHz, the heating time (healing window), is approximately 16 seconds for the nano iron oxide particle composites and only approximately 6 seconds for the nano- and micro-scale nickel particles. Based on these testing results, an ideal material would be composed of approximately 2-3% nano iron oxide particles, and heated with a higher induction heater frequency in the 250-300 kHz range. This would allow

Downloaded by PENNSYLVANIA STATE UNIV on June 22, 2012 | http://pubs.acs.org
Publication Date (Web): November 10, 2010 | doi: 10.1021/bk-2010-1050.ch004

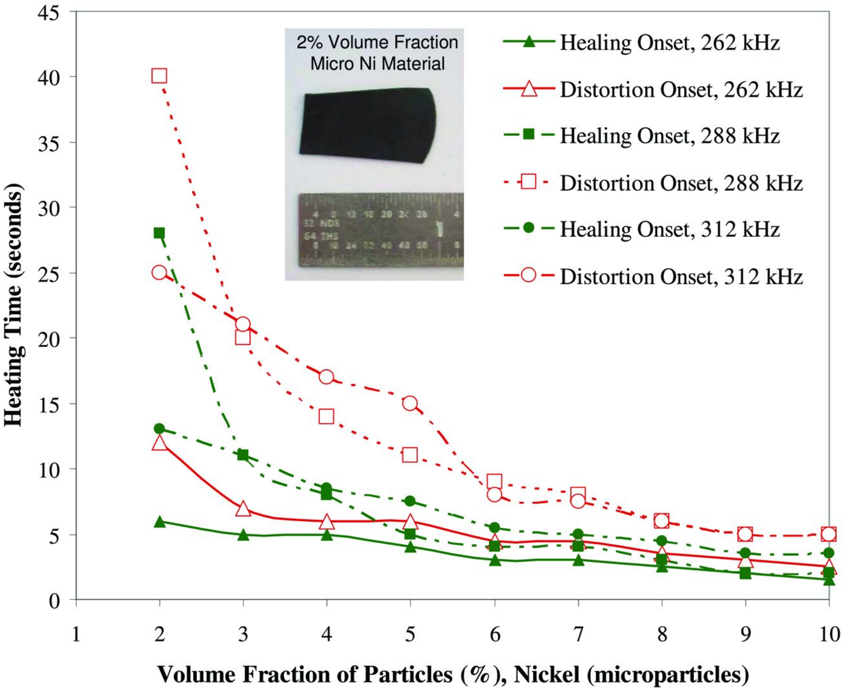

Figure 7. Graphical display of the onset of healing and distortion) of ionomer/nickel magnetic microparticles with volume fraction of the magnetic microparticle varying between 2-10% and induction heater frequencies of 262, 288, and 312 kHz. A portion of 2% volume fraction material is shown in the inset.

for the insulation material to reach a healing temperature in a reasonable amount of time (5-10 seconds), but allow for it to be heated for 10 or more seconds, giving the material the largest opportunity to most effectively heal damage. Low volume fractions would have the advantage of adding less weight to the insulation in addition to having a smaller effect on the dielectric breakdown strength of the layer. It also is apparent that for the same volume fraction of nickel nanoparticles as microparticles (for a given induction frequency), considerably less time is required for the onset of healing. The work by Müller 2004 suggests that at least for nanoparticles, there is a strong dependency on mean particle size and the type of loss processes (example, hysteresis loss) produced during remagnetization of nanoparticles in an AC-field (*17*). While the results in the current work suggest a particle-size dependency on healing onset time, further quantitative investigation is warranted before drawing this conclusion. This investigation will determine the minimum volume fraction below 2% of nanoparticles (or microparticles) for the onset of healing. The use of nanoparticles as opposed to microparticles may offer other benefits in terms of material properties.

Downloaded by PENNSYLVANIA STATE UNIV on June 22, 2012 | http://pubs.acs.org
Publication Date (Web): November 10, 2010 | doi: 10.1021/bk-2010-1050.ch004

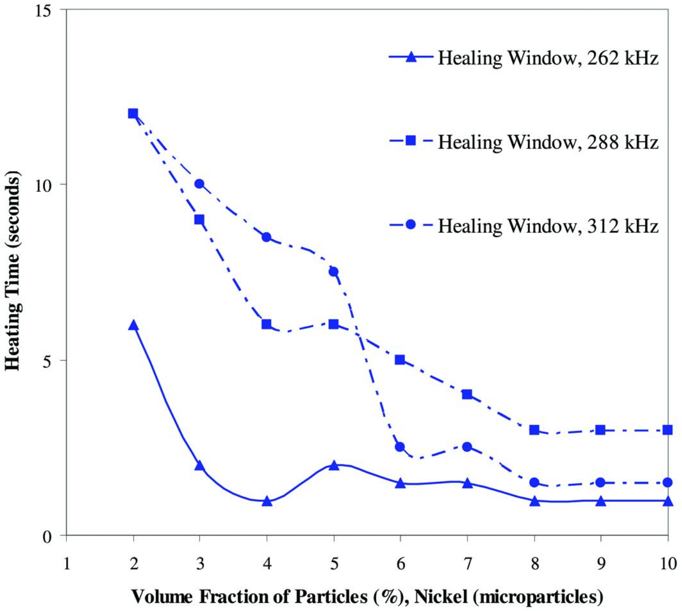

Figure 8. Graphical display of the healing window (between the onset of healing and distortion) of ionomer/nickel magnetic microparticles with volume fraction of the magnetic microparticle varying between 2-10% and induction heater frequencies of 262, 288, and 312 kHz.

Ionomer/Carbon-Fiber Composite and Resistive Heating

Ionomer/carbon-fiber composite material consists of an ionomeric polymer matrix with embedded carbon fibers. To demonstrate the healing mechanism, a voltage of 3 Volts is applied to the ionomer/carbon-fiber composite, as shown below in Figure 9. As the current passes through the carbon fibers, the fibers are resistively heated. As this heats the composite to a temperature above its melting point, the ionomer can flow sufficiently to heal the damaged portion. The test results below show a coupon scored with a razor and subsequently heated. The cut damage is healed sufficiently to restore its electrically-insulating properties (although with some residual surface scarring).

Carbon-Fiber Composite - Review

To address matrix cracking and potential subsequent failure of carbon-fiber ply skins, the Mendomer is combined with magnetic particles and used as the matrix component in the carbon-fiber composite. Instead of replacing the failed carbon-fiber part or area, the matrix cracking can be healed in-situ. The resultant composite is a remendable carbon-fiber composite skin which can serve as the basis for a self-healing carbon-fiber composite if damage can be coupled with the healing response. As previously mentioned, Mendomer polymers have also been shown to heal using the resistive properties of carbon-fiber (*8*, *9*). The Mendomer

Downloaded by PENNSYLVANIA STATE UNIV on June 22, 2012 | http://pubs.acs.org
Publication Date (Web): November 10, 2010 | doi: 10.1021/bk-2010-1050.ch004

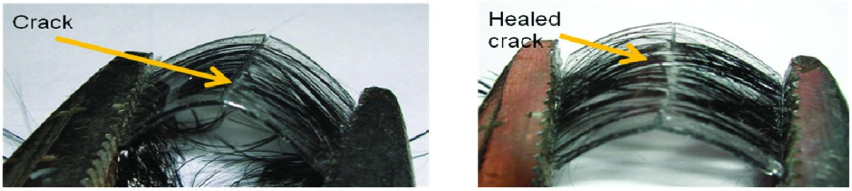

Figure 9. Images of a damaged ionomer/carbon-fiber composite (a) before resistive heating and (b) after resistive heating consisting of 3 Volts, 0.54 Amp current draw applied for 10 minutes. (Adapted with permission from reference (16) Copyright 2009 Matt Castellucci.)

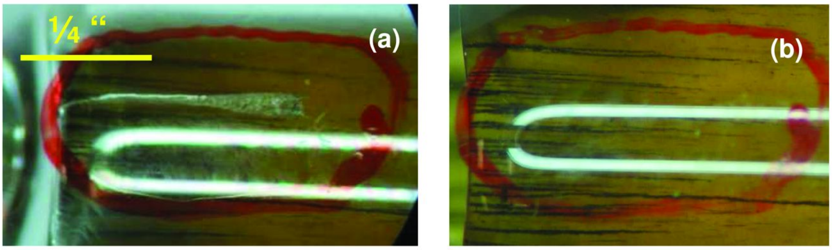

Figure 10. Mendomer combined with a low-volume fraction of aligned magnetic particles with the damage site is circled in red. The first image (a) is of the sample with a crack (horizontal in the picture and near the middle of the picture) prior to remending and the second (b) is of the sample after remending. (Adapted from (4).)

has also been combined with the same ferrite particles used in the ionomer/6% magnetic particle sample shown in Figure 2.

Figure 10 shows Mendomer-401 combined with ferrite magnetic particles that have been aligned in a magnetic field. Figure 10a shows this Mendomer-401/ferrite coupon with a 360x5000 micron crack (at largest width). Figure 10b shows the same composite after healing. The circular markings are to identify the location of the crack. The white line features are artifacts of the fluorescent lighting that were present during the micrograph picture collection (*4*). The crack that formed was likely a result of uneven cooling of the material inside the test tube. Healing was performed using a Superior Induction SI-7kW HF system and a flat "pancake" coil. Details about the healing process are provided in a previous publication (*4*). This is a proof-of-concept showing remending of the Mendomer using a low-volume fraction of aligned magnetic particles.

A favorable characteristic of Mendomer polymers is that this material can be molecularly tailored. Two Mendomers, Mendomer-400 and Mendomer-401, were investigated to validate theory supporting the control of glass transition (Tg) temperatures and mechanical properties where the Tg of Mendomer-401 was verified to be lower than Mendomer-400 whose Tg is 150°C. The mechanical properties of Mendomer-400 and Mendomer-401 are enumerated in Table 1.

Table 1. Mechanical properties of Mendomer-400 and Mendomer-401. (SOURCE: Reproduced from (*4*))

Polymer	*Compressive Modulus GPa*	*Compressive Strength MPa*	*Flexural Modulus GPa*	*Maximum Fiber Stress MPa*
Mendomer-401	1.95	104	3.26	116.8
Mendomer-400	1.65	83.5	2.63	109.3

Conclusions and Future Work

Ionomeric and Mendomer polymer composite multifunctional material structures provide a potential means of addressing aerospace problems in the areas of failed wire insulation and carbon-fiber composite damage. These structures include remendable polymer composites combined with conventional materials to serve dual purposes. As a potential solution for wire insulation failure, ionomeric polymers are layered with conventional wire insulation materials to provide insulation and on-site remending properties. As a potential solution for carbon-fiber composite failure, Mendomer is used as the matrix in conventional carbon-fiber composite fabrication thus rendering the composite remendable. In the work that was presented, magnetic particles were combined with the remendable polymers, Surlyn® 8940 and Mendomer-400, to enable non-contact healing using inductive heating. Healing through resistive heating was also discussed with proof-of-concept preliminary results demonstrating this method with Surlyn® 8940. References for resistive healing of Mendomer materials performed by others was mentioned. Through the use of a remendable-polymer/magnetic-particle matrix and a portable inductive heater, mitigation of matrix cracking and propagation can be addressed. In the case of wire-insulation failure, if any of the insulation layers fail by cracking, the ionomer material flows into the exposed crack and prevents unwanted wire exposure. Matrix cracking is the first mode of failure in composites and it can lead to delamination as it propagates; therefore, this remending may also indirectly mitigate delamination.

This technology offers benefits in terms of reduced maintenance costs and long-term survivability. To be sure, the cost benefit and feasibility of replacing conventional materials with the proposed multifunctional remendable material systems is of central concern. Accordingly, complexity and increased weight must be balanced with the overall cost of providing damage mitigation in the form remendable properties. While the magnetic particle parametric study was conducted with the ionomeric polymer, the results can be readily applied to the Mendomer/magnetic-particle composites. The term "healing window" was introduced and defined to provide guiding data to application developers of these materials for aerospace applications. A low-volume fraction of magnetic material between 2 and 3% is sufficient to cause remending of these materials as well as provides the operator ample control as a function of healing window. As previously mentioned, healing window is defined as the time difference

Downloaded by PENNSYLVANIA STATE UNIV on June 22, 2012 | http://pubs.acs.org
Publication Date (Web): November 10, 2010 | doi: 10.1021/bk-2010-1050.ch004

between initiation of healing (melting) and onset of deformation. A longer healing window is attributed to ample operator control where in our judgment, a 5 to 10 second healing time is ideal for material remending maintenance. If the healing window is used as the guiding metric, then approximately 2-3% nano iron oxide particles at induction frequencies between 250 and 300 kHz is the ideal volume fraction, composition and induction frequency range. For the ionomer coupons using nickel nanoparticles, healing is observed at a significantly faster rate than the coupons with nickel microscale particles for the same volume fraction and induction frequency. This is a contrived healing situation and must be investigated for other damage modes--including where one of the conventional layers has been cracked and healing entails flow of the ionomer into the cracked area. The optimal volume fraction, composition, and frequency range must also be verified with the Mendomer material. The healing window was not applied in the carbon-fiber used with resistive healing for the ionomer material.

The goal of future research is to provide a multifunctional solution for aerospace applications through "active self-healing" or true self-healing. This is being accomplished through the coupling of damage detection and associated self-healing. A proprietary capacitive damage sensing method for the wire insulation solution has been developed and continues to be investigated. Also, an acoustic wave propagation method (*18*) is under investigation for damage detection in the carbon-fiber composites. In both cases, the solution first entails passive detection of an onset of damage followed by autonomous implementation of healing in response to the detected damage. Synthesis of new Mendomer materials also continues for different application requirements.

Downloaded by PENNSYLVANIA STATE UNIV on June 22, 2012 | http://pubs.acs.org
Publication Date (Web): November 10, 2010 | doi: 10.1021/bk-2010-1050.ch004

Acknowledgments

The authors gratefully acknowledge the support NASA Kennedy Space Center (NASA KSC) contract numbers NNK05OA32C and NNK06MB01C. The authors thank Drs Orlando Melendez and Luke Roberson for their technical guidance on applying this technology to damaged wire insulation as well as Dr. Eric D. Wetzel for his technical advice on induction heating use and applications. The authors also thank Powder Processing & Technology, LLC for the ferrite particles associated with Figure 2 and Figure 10. The authors thank former deceased co-author, Mr. Matt Smith, for his significant contributions.

References

1. Fall, R. Master's thesis. Virginia Polytechnic Institute and State University, Blacksburg, VA, 2001.
2. Kalista, S. J. Master's thesis. Virginia Polytechnic Institute and State University, Blacksburg, VA, 2003.
3. Chen, X.; et al. New Thermally Remendable Highly Cross-Linked Polymeric Materials. *Macromolecules* **2003**, *36*, 1802–1807.

4. Duenas, T.; et al. Multifunctional Self-healing Morphing Composites. *Proceedings for the 25th Army Science Conference*; Orlando, FL, November 27−30, 2006; Paper No. GP-03.
5. Wetzel, E. D.; Fink, B. K.; Li, Y. F.; Xiao, J. Q. Advanced magnetic materials for Curie temperature–controlled bonding. *Proceedings for the 22nd Army Science Conference*, Baltimore, MD, Dec. 11−13, 2000.
6. Wetzel, E. D.; Fink, B. K. *Feasibility of magnetic particle films for Curie temperature controlled processing of composite materials*; Army Research Laboratory Technical Report; ARL-TR-2431; March 2001.
7. Owen, C. C. Master's thesis. Virginia Polytechnic Institute and State University, Blacksburg, VA, 2006.
8. Park, J. S.; Takahashi, K.; Zhanhu, G.; Wang, Y.; Bolanos, E.; Hamann-Schaffner, C.; Murphy, E.; Wudl, F.; Hahn, H. T. *J. Compos. Mater.* **2008**, *42*, 2869–2881.
9. Park, S. P.; Kim, H. S.; Hahn, H. T. Healing behavior of a matrix crack on a carbon fiber/mendomer composite. *Compos. Sci. Technol.* **2009**, *69*, 1082–1087.
10. *Self Healing Materials: An Alternative Approach to 20 Centuries of Materials Science*; van der Zwaag, S.; Springer Series in Materials Science 100; Springer: Dordrecht, The Netherlands, 2007.
11. Stavnes, M. W.; Hammoud, A. N.; Bercaw, R. W. *Operational Environments for Electrical Power Wiring on NASA Space Systems*; NASA Technical Memorandum 106655; Lewis Research Center, June 1994.
12. Dry, C. M.; et al. In *Smart Structures and Materials 1993: Smart Materials*; Varadan, V. K., Ed.; SPIE Proceedings; SPIE: Bellingham, WA, 1993; Vol. 1916, p 438.
13. Herakovich, C. T. Failure Modes and Damage Accumulation in Laminated Composites with Free Edges. *Compos. Sci. Technol* **1989**, *36*, 105–119.
14. Hibbs, M. I.; et al. Correlations Between Micromechanical Failure Processes and Delamination Toughness of Graphite/Epoxy Systems. In *Fractography of Modern Engineering Materials, Composites and Metals*; Masters, J. E., Au, J. J., Eds.; ASTM STP 948, American Society for Testing and Materials: Philadelphia, 1988; pp 68−97.
15. Nairn, J. A. *Microcracking, Microcrack-Induced Delamination, and Longitudinal Splitting of Advanced Composite Structures*; NASA CR-4472; 1992.
16. Castellucci, M. Master's thesis. Virginia Polytechnic Institute and State University, Blacksburg, VA, 2009.
17. Möller, R.; Hergt, R.; Zeisberger, M.; Gawalek, W. Preparation of magnetic nanoparticles with large specific loss power for heating applications. *J. Magn. Magn. Mater.* **2005**, *289*, 13–16.
18. Banerjee, S.; Ricci, F.; Monaco, E.; Mal, A. A wave propagation and vibration-based approach for damage identification in structural components. *J. Sound Vibration* **2009**, *322*, 167–183.

Downloaded by PENNSYLVANIA STATE UNIV on June 22, 2012 | http://pubs.acs.org
Publication Date (Web): November 10, 2010 | doi: 10.1021/bk-2010-1050.ch004

Downloaded by UNIV OF GUELPH LIBRARY on June 22, 2012 | http://pubs.acs.org
Publication Date (Web): November 10, 2010 | doi: 10.1021/bk-2010-1050.ch005

Chapter 5

Design and Synthesis of Living-Free Electroactive Dendron End-Functionalized Macromolecules: Surface Grafting Studies

Rigoberto C. Advincula* **and Maria Celeste Tria**

University of Houston, Department of Chemistry, Houston, TX 77204
***radvincula@uh.edu**

Grafting of polymer brushes if of high interest towards intelligent materials systems with stimuli response. While there has been a lot of interest on chemically modified attachment of initiators towards surfaces for surface initiated polymerization (SIP), very little work has been done on modifying electrode surfaces via electrochemical methods. To address this issue, we have proposed to use a preformed RAFT agent with an electrochemically active moiety to mediate SI-RAFT polymerization as well as grafting of CTA's on electrode surfaces to promote RAFT-SIP. In particular, we have used the first generation CTA (G1-CTA), which had been reported to facilitate RAFT polymerization in solution. The presence of the electro-active carbazole group in this RAFT agent enables its immobilization on the electrode surface through electro-grafting.

Introduction

Tailored macromolecular architectures end-grafted on a solid substrate, known as polymer brushes, play an important role in controlling surface properties of relevance to fundamental science and technological applications. Such areas include biomaterials (*1*), drug delivery (*2*), adhesion and wettability (*3*), lubrication (*4*), and tribology (*5*). Indeed, there is a valuable need in developing a facile, controlled and versatile methodology for grafting functional polymer brushes on a variety of solid support substrates. This paper therefore aims to

Downloaded by UNIV OF GUELPH LIBRARY on June 22, 2012 | http://pubs.acs.org
Publication Date (Web): November 10, 2010 | doi: 10.1021/bk-2010-1050.ch005

provide a complimentary strategy to fabricating polymer brushes primarily on electrode surfaces.

Polymer brushes can be tethered onto a surface either by “grafting to” (GT) or “grafting from” (GF) (also called as surface-initiated polymerization (SIP)) methods. GT approach involves pre-forming of the polymer with an “anchor” group, which is either an end-group or a pendant group, and is subsequently attached to complementary reactive groups on the surface. This process is generally straightforward and experimentally simple, but it poses some limitations: (1) it is difficult to obtain high grafting densities due to the sterically-hindered reactive sites occupied by the “already” adsorbed polymers; (2) the film thickness is limited by the molecular weight of the polymer in solution, thus formation of thick films is generally unattainable; and (3) the functional groups of the preformed polymer can compete with the anchor moieties for surface sites, hence limiting the choice of polymer type that can be attached on the surface (*6*). These drawbacks can be circumvented by employing the GF technique where the polymer chains are directly grown from the surface using surface-bound initiators (*7*). In this method, the functionality, density and thickness of the polymer brushes can be easily controlled. Also, higher grafting densities are obtained because no significant diffusion barrier exists, as only the monomers in solution have to reach the reactive site of the interface.

Over the past decade, the combination of SIP and controlled living radical polymerization (CLRP) has been widely explored due to its applicability in preparing polymer brushes with controlled brush density, polydispersity, and composition. Furthermore, the living character of the process enables the formation of block copolymers on the surface. The most recently developed CLRP technique is the reversible addition-fragmentation chain transfer (RAFT) polymerization (*8*). It relies on the degenerative transfer mechanism, which involves the use of dithioester compounds, known as the chain transfer agent (CTA) or the RAFT agent. The transfer of the dithioester moiety between active and dormant species maintains the controlled character of the polymerization (Scheme 1) (*9*). RAFT has emerged as a promising CLRP technique due to its versatility over a wide range of functional monomers amenable to radical polymerization and reaction conditions. In addition, the polymers formed are free from contamination of metal catalyst (*8*).

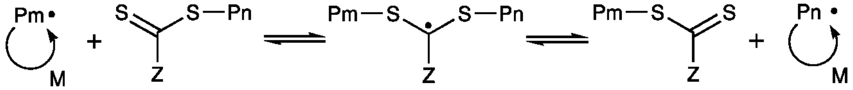

Scheme 1. General Representation of RAFT Polymerization Mechanism

Surface-initiated RAFT (SI-RAFT) polymerization can be performed by the immobilization of the initiator onto the surface with the RAFT agent in solution (*9a*, *10*). This approach requires the use of unbound initiator to act as a scavenger for the impurities that can terminate the active initiating sites on the surface (*9a*). The consequence for this is the production of excess amounts of ungrafted polymer (*11*). To eliminate this possibility, another method involves

Downloaded by UNIV OF GUELPH LIBRARY on June 22, 2012 | http://pubs.acs.org
Publication Date (Web): November 10, 2010 | doi: 10.1021/bk-2010-1050.ch005

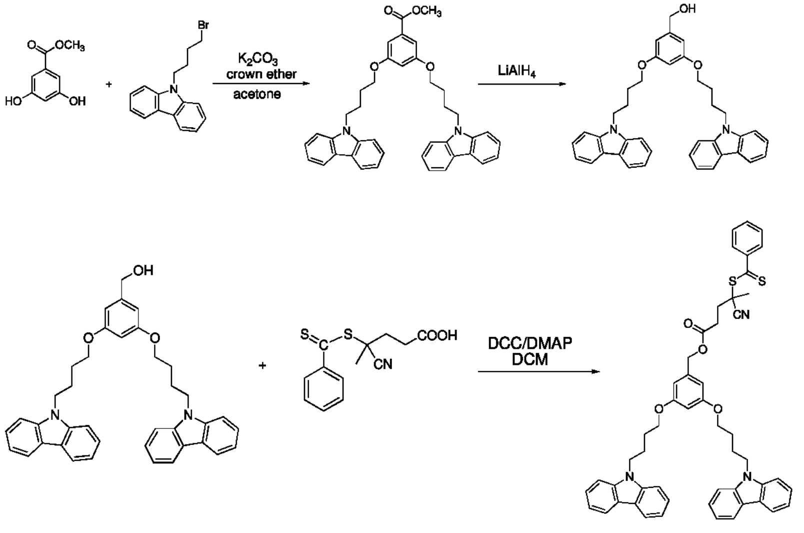

G1-CTA

Scheme 2. Synthetic Route for the Preparation of the G1-CTA

anchoring the CTA directly onto the surface. Immobilization of the CTA on the substrate can be accomplished by chemical modification of a functionalized surface (*12*). For example, modifying the surface with an active halogen group followed by substitution reaction with the dithio moiety leads to the generation of a surface RAFT agent (*12a–12f*). This method is inconvenient because it necessitates careful handling techniques on the solid support in solution during the synthesis. An alternative way is to pre-form the RAFT agent followed by subsequent attachment onto the surface (*13*). However, in both cases, most of the reported surface-bound RAFT agents are silane-coupled and consequently can only be grafted on hydroxyl-terminated substrates such as silicon wafers and silica particles (*12a–12e*, *13a*, *13b*). Therefore, such methods are not applicable for other metal or metal oxide surfaces that are useful as metal or electrically conducting electrodes. Such surfaces are of high industrial importance as well as for biomedical applications.

To address this issue, we have proposed to use a preformed RAFT agent with an electrochemically active moiety to mediate SI-RAFT polymerization from electrode surfaces. In particular, we have used the first generation CTA (G1-CTA), which had been reported to facilitate RAFT polymerization in solution (*14*). The presence of the electro-active carbazole group in this RAFT agent enables its immobilization on the electrode surface through electro-grafting (Scheme 2). This method extends the scope of application of SI-RAFT polymerization on any conducting substrates (*e.g.* gold, ITO-coated surface, platinum, carbon felt, glassy carbon, and steel). Because polymer brushes are used to improve the performance and properties of many devices (*e.g.* implants (*1*), biosensors (*15*), microelectromechanical systems (MEMS) (*16*)), a practical way of preparing polymer brushes on electrically conducting surfaces is valuable. To the best of

Downloaded by UNIV OF GUELPH LIBRARY on June 22, 2012 | http://pubs.acs.org
Publication Date (Web): November 10, 2010 | doi: 10.1021/bk-2010-1050.ch005

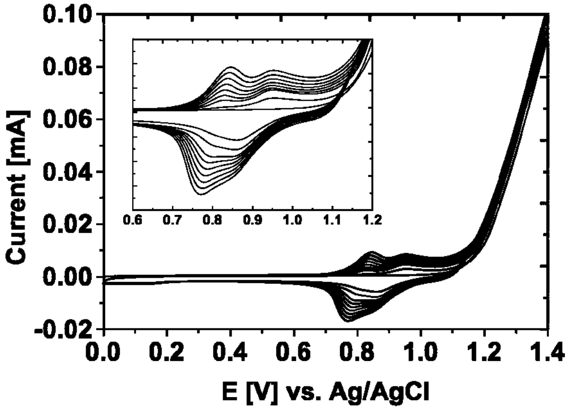

Figure 1. CV curve for the electro-grafted G1-CTA on the gold substrate. Inset: Enlarged portion of the cyclic voltammogram.

our knowledge, the use of SI-RAFT in combination with electro-grafting has never been previously reported. In this study, we have developed an efficient method of preparing poly(methyl methacrylate) (PMMA) and poly(poly(ethylene glycol) methyl ether methacrylate) (PPEGMA) polymer brushes onto gold surface through electro-grafting followed by SI-RAFT polymerization.

Results and Discussion

Electro-Grafting of G1-CTA

The mechanism of the anodic oxidation of carbazole and *N*-substituted carbazoles were studied previously (*17*). During the anodic oxidation process, the carbazole monomer was first oxidized to form a very unstable cation radical, which readily couples with another cation radical to form the 3,3′-bicarbazyl species. This ring-ring coupling is suggested to be the major decay pathway, especially for the *N*-substituted derivatives where the 9- position is blocked. On the other hand, several groups reported the formation of longer chains of carbazole under appropriate conditions (*18*).

In this study, the presence of the carbazole moieties in the G1-CTA was exploited to deposit this RAFT agent on the gold substrate electrochemically. Cyclic voltammetry (CV) was particularly employed as an electrochemical method to anodically oxidize the carbazole moieties onto the gold surface. CV experiments were carried out using a three-electrode set-up where gold substrate was used as the working electrode, Pt wire as the counter electrode and Ag/AgCl as the reference electrode. A solution of G1-CTA (0.5 mM) and the supporting electrolyte, tetrabutylammonium hexafluorophosphate (TBAH) (0.1 M) in THF was used for preparing the electro-generated CTA film. A scan rate of 50 mV/s was employed for the 10-cycle CV run of the sample in a potential window of 0 - 1.4 V.

Downloaded by UNIV OF GUELPH LIBRARY on June 22, 2012 | http://pubs.acs.org
Publication Date (Web): November 10, 2010 | doi: 10.1021/bk-2010-1050.ch005

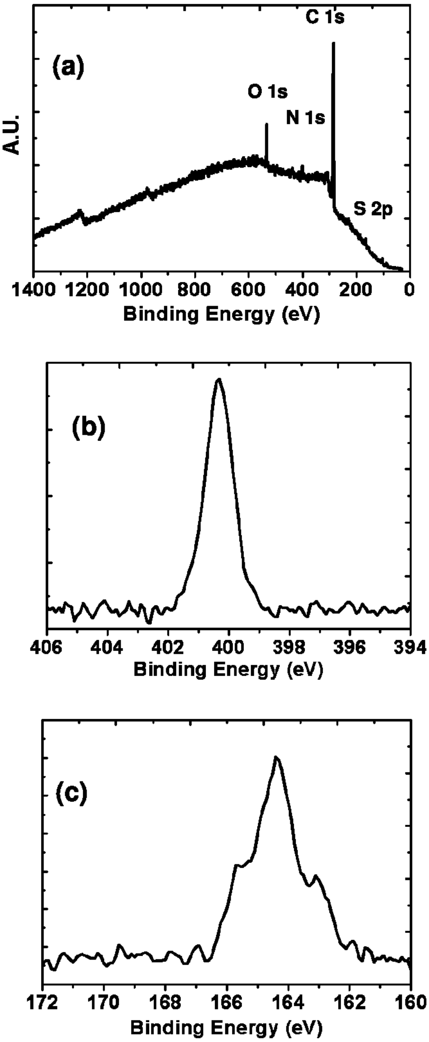

Figure 2. XPS data for the electro-grafted G1-CTA. (a) Survey and high resolution scan in the (b) N 1s (c) S 2p regions.

Figure 1 shows the cyclic voltammogram of the electrodeposited G1-CTA. Two peaks were observed for both the anodic (oxidation) and cathodic (reduction) scans, which can be attributed to the two redox processes that is typical for electrochemically reversible *N*-substituted carbazoles (*17*). The oxidation peaks observed at ~0.88 - 0.95 V and the reduction peaks at ~0.78 – 0.85 V are attributed to the redox couples of the 3,6-bicarbazyl species. The two oxidation peaks observed in the CV curve represent the loss of the two electrons of the 3,6-bicarbazyl in a two reversible one-electron steps to yield a moderately stable dication with extensive conjugation (*17*). In addition, it is observed that the peak current

Table 1. Experimental Atomic Percentages on Surface and Expected Atomic Percentages of the Elements in G1-CTA

Element	*Atomic percentage on surface*	*Expected atomic percentage*
C	78.11	78.59
O	5.40	5.29
N	8.85	8.05
S	7.64	8.07

increases as the number of cycles increases. This increase in current indicates the formation of the electro-generated film on the electrode (*19*).

The thickness and contact angle of the electro-grafted film were obtained. Ellipsometric measurements showed an average thickness of 5.10 ± 0.12 nm, measured at 3 different areas of the sample. A static water contact angle value of 72.50 ± 2.23° was obtained, indicating the presence of a more hydrophobic film compared to the starting material.

XPS analysis was also performed to further confirm the deposition of the G1-CTA on the gold substrate. XPS data of the electro-grafted film is shown in Figure 2. XPS survey scan shows the presence of the expected C, N, O, and S signals. High-resolution N 1s data reveal an intense peak at 400.4 eV due to the nitrogen contributions from the carbazole ring (*20*) and the cyano nitrogen (*21*). The appearance of a broad signal at 164.4 eV in the S 2p region was attributed to the dithio moiety of the G1-CTA (*22*). The relative atomic concentration of C, N, O and S obtained from the XPS were in close agreement with the expected atomic percentage of the electro-grafted RAFT agent (Table 1).

SI-RAFT Polymerization

To check for the ability of the CTA-modified gold surface to facilitate surface-initiated RAFT polymerization, the standard monomer methyl methacrylate (MMA), was used to grow the polymer from the surface. The CTA-modified gold slide was immersed in a degassed solution of the monomer, "free" CTA, and the AIBN initiator in THF for 24 hours at 60 °C. Polymerization of MMA was initiated from the surface-bound CTA to generate a surface-grafted PMMA homopolymer brush. After polymerization, the PMMA-modified gold surface was subjected to Soxhlet extraction in THF for 24 hours to ensure the removal of any unbound polymers. On the other hand, the solution was precipitated in excess amount of hexanes to obtain the free polymer formed in the solution.

The molecular weight and polydispersity of the free polymer can be used for the estimation of the molecular weight and polydispersity of the grafted PMMA film as reported in literatures (*23*). GPC analysis of the solution-formed polymer measured a number-average molecular weight (M_n) of 10,637 and a weight–average molecular weight (M_w) of 12,300. From these values, a molecular weight distribution (M_w/M_n) of 1.16 was obtained. This "very narrow" polydispersity value (<1.2) is expected for a controlled polymerization process.

Downloaded by UNIV OF GUELPH LIBRARY on June 22, 2012 | http://pubs.acs.org
Publication Date (Web): November 10, 2010 | doi: 10.1021/bk-2010-1050.ch005

Downloaded by UNIV OF GUELPH LIBRARY on June 22, 2012 | http://pubs.acs.org
Publication Date (Web): November 10, 2010 | doi: 10.1021/bk-2010-1050.ch005

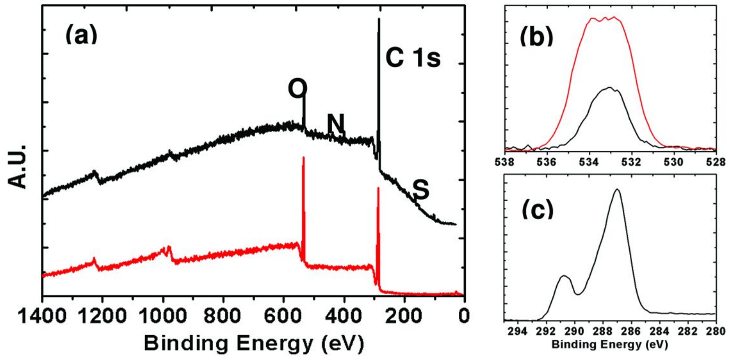

Figure 3. (a) Survey spectra of the SI-RAFT polymerization of PMMA on gold. (black) Electro-grafted G1-CTA on gold prior to SI-RAFT of PMMA and (gray) after the growth of the PMMA homopolymer brush on the G1-CTA-modified gold. (b) O 1s data of (black) the electro-grafted G1-CTA and (gray) the PMMA brush after SI-RAFT. (c) C 1s data of the PMMA brush after SI-RAFT.

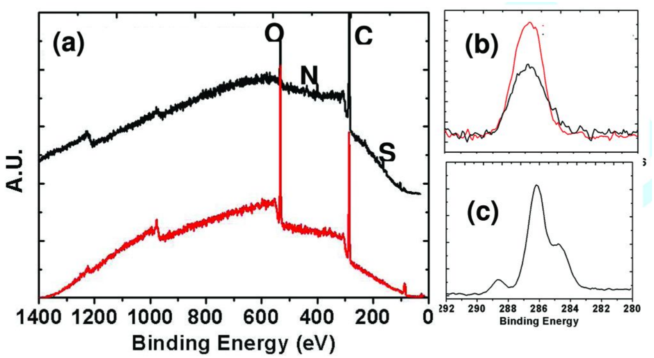

Figure 4. (a) Survey spectra of the SI-RAFT polymerization of PEGMA on gold. (black) Electro-grafted G1-CTA on gold prior to SI-RAFT of PEGMA and (gray) after the growth of the PPEGMA homopolymer brush on the G1-CTA-modified gold. (b) O 1s data of (black) the electro-grafted G1-CTA and (gray) the PPEGMA brush after SI-RAFT. (c) C 1s data of the PPEGMA brush after SI-RAFT.

Ellipsometric measurements of the resulting film after polymerization showed a significant change in thickness. The thickness of the film increased from 5.10 ± 0.12 nm (initial G1-CTA film) to 15.88 ± 1.37 nm, (resulting film after polymerization), signifying the growth of the PMMA brush on the surface. In addition, the static contact angle in water of the resulting PMMA brush was found to be 66.16 ± 0.98°. This value is close to the reported contact angle value (61°) for PMMA on gold (*24*). The slight discrepancy between the experimental and the literature values is possibly due to the incorporation of the hydrophobic G1-CTA to the PMMA. In comparison to the electro-grafted CTA film, the contact angle shifted to lower value after MMA polymerization, which is possibly due to the presence of more oxygen on the surface, rendering the film more polar after polymerization.

XPS analysis of the PMMA film showed a significant increase in the intensity of the O signal after the surface-initiated MMA polymerization, as compared to the electro-grafted RAFT agent (Figure 3a and 3b). This increase was expected due to the polymerization of the MMA, thus increasing the number of oxygen present on the surface. The observed O/C ratio after polymerization (29:70) correlates well with PMMA composition that is 2 O atoms to 5 C atoms.

After examining the capability of the CTA-modified gold substrate to mediate a RAFT surface-initiated polymerization through grafting PMMA film from the surface, the method was applied to prepare a potential non-specific protein-resistant surface. Poly(ethylene glycol) methyl ether methacrylate (PEGMA) contains the poly(ethylene glycol) (PEG) moiety, which is well-known to be a protein-resistant molecule (*25*), and the methacrylate unit that is similar to the model monomer used, MMA. Similar processes were carried out for the SIP of the PEGMA on the gold surface. The polymerization time, however, was shorter than that of MMA as PPEGMA gels out rapidly with the same conditions employed with the MMA polymerization. GPC measurements rendered values of 11,062 and 12,968 for M_n and M_w, respectively. A narrow molecular weight distribution of 1.17, similar to PMMA, was obtained, indicating a well-controlled polymerization process. Similar surface characterizations were performed on the film after PEGMA polymerization. A thickness of 22.52 ± 1.17 nm and a static water contact angle of 58.05 ± 0.74° were recorded after the polymerization. The lower value of contact angle as compared to the film before the RAFT-mediated polymerization is due to the contribution of the hydrophilic PEG chains. XPS results show the comparison of the survey scans before and after SI-RAFT polymerization of PEGMA on the surface (Figure 4). An increase in the O peak intensity was observed due to the growth of the PPEGMA brush on the surface. In addition, the O/C ratio after polymerization of PEGMA was 30:68 (0.44), close to the expected value for the PEGMA, that is 7 O atoms and 15 C atoms (0.47).

Downloaded by UNIV OF GUELPH LIBRARY on June 22, 2012 | http://pubs.acs.org
Publication Date (Web): November 10, 2010 | doi: 10.1021/bk-2010-1050.ch005

Conclusions and Future Works

A new approach for preparing polymer brushes via combination of SI-RAFT and electro-grafting of CTA was demonstrated. The RAFT agent with an electro-active moiety was successfully grafted onto gold substrates using CV as observed from the XPS, ellipsometry and contact angle results of the electro-generated film. The stability and activity of the RAFT agent were confirmed by its ability to generate PMMA and PPEGMA brushes on the surface. The growth of the brushes was verified by the significant increase in thickness (*i.e.* from 5.10 ± 0.12 nm to 15.88 ± 1.37 nm for PMMA and from 5.10 ± 0.12 to 22.52 ± 1.17 nm for PPEGMA), accompanied by the change in contact angle and topography. Furthermore, the calculated O/C ratio from the XPS after the polymerization (0.41 for PMMA and 0.44 for PPEGMA) showed a strong correlation with the expected value for the PMMA (0.40) and PPEGMA (0.46) brushes. The authors believe that the simplicity and efficiency of this approach will be a useful strategy in preparing various functional polymer brushes on electrode surfaces. Future works on this project include protein adsorption measurements of the obtained PPEGMA films, preparation of stimuli-responsive block copolymers on the substrate and generation of polymer brushes on other conducting substrates. Given that these applications work, the method presented in this paper will be a very promising tool in creating well-designed polymer architectures on conducting surfaces.

Acknowledgments

Support for this work from NSF CHE-03-04807, DMR-03-15565, ACS-PRF-45853-AC7 Grant. The authors also thank Agilent Technologies Inc., Optrel GmBH, and Varian Inc. for technical assistance.

References

1. (a) Tirrell, M.; Kokkoli, E.; Biesalski, M. *Surf. Sci.* **2002**, *500*, 61−83. (b) Elbert, D.; Hubbell, J. *Annu. Rev. Mater. Sci.* **1996**, *26*, 365−394. (c) Griffith, L. *Acta Mater.* **2000**, *48*, 263−277. (d) Klee, D.; Höcker, H. *Adv. Polym. Sci.* **1999**, *149*, 1−57.
2. (a) Langer, R. *Acc. Chem. Res.* **2000**, *33*, 94−101. (b) Santini, J., Jr.; Richards, A.; Scheidt, R.; Cima, M.; Langer, R. *Angew. Chem., Int. Ed.* **2000**, *39*, 94−101.
3. (a) Lenz, P. *Adv. Mater.* **1999**, *11*, 1531−1534. (b) Raphaël, E.; de Gennes, P. *J. Phys. Chem.* **1992**, *96*, 4002−4007.
4. Klein, J. *Annu. Rev. Mater. Sci.* **1996**, *26*, 581–612.
5. Klein, J.; Kumacheva, E. *Science* **1995**, *269*, 816–819.
6. Rühe, J.; Knoll, W. *J. Macromol. Sci., Polym. Rev.* **2002**, *C42*, 91–138.
7. (a) Prucker, O.; Rühe, J. *Macromolecules* **1998**, *31*, 592−601. (b) Prucker, O.; Rühe, J. *Macromolecules* **1998**, *31*, 602−613. (c) Prucker, O.; Rühe, J. *Langmuir* **1998**, *14*, 6893−6898.
8. Chiefari, J.; Chong, Y.; Ercole, F.; Krstina, J.; Jeffrey, J.; Le, T.; Mayadunne, R.; Meijs, G.; Moad, C.; Moad, G.; Rizzardo, E.; Thang, S. *Macromolecules* **1998**, *31*, 5559–5562.
9. (a) Baum, M.; Brittain, W. *Macromolecules* **2002**, *35*, 610−615. (b) Moad, G.; Rizzardo, E.; Thang, S. *Aust. J. Chem.* **2006**, *59*, 669−692.
10. (a) Yu, W.; Kang, E.; Neoh, K. *Ind. Eng. Chem. Res.* **2004**, *43*, 5194−5202. (b) Yu, W.; Kang, E.; Neoh, K. *Ind. Eng. Chem. Res.* **2004**, *43*, 1673−1680. (c) Chen, Y.; Sun, W.; Chen, L. *J. Polym. Sci., Part A: Polym. Chem.* **2006**, *44*, 3071−3082.
11. Edmondson, S.; Osborne, V.; Huck, W. *Chem. Soc. Rev.* **2004**, *33*, 14–22.
12. (a) Tsujii, Y.; Ejaz, M.; Sato, K.; Goto, A.; Fukuda, T. *Macromolecules* **2001**, *34*, 8872−8878. (b) Ranjan, R.; Brittain, W. *Macromol. Rapid Commun.* **2008**, *29*, 1104−1110. (c) Peng, Q.; Lai, D.; Kang, E.; Neoh, K. *Macromolecules* **2006**, *39*, 5577−5582. (d) Lu, C.; Zhou, W.; Han, B.; Yang, H.; Chen, X.; Wang, X. *Anal. Chem.* **2007**, *79*, 5457−5461. (e) Konopacki,

Downloaded by UNIV OF GUELPH LIBRARY on June 22, 2012 | http://pubs.acs.org
Publication Date (Web): November 10, 2010 | doi: 10.1021/bk-2010-1050.ch005

M.; Boyes, S. *Macromolecules* **2007**, *40*, 879−888. (f) Hong, C.; You, Y.; Pan, C. *Chem. Mater.* **2005**, *17*, 2247−2254. (g) Hong, C.; Li, X.; Pan, C. *J. Phys. Chem. C* **2008**, *112*, 15320−15324. (h) Chung, P.; Kumar, R.; Pruski, M.; Lin, V. *Adv. Funct. Mater.* **2008**,*18*, 1390−1398.

13. (a) Li, C.; Benicewicz, B. *Macromolecules* **2005**, *38*, 5929−5936. (b) Li, C.; Han, J.; Ryu, C.; Benicewicz, B. *Macromolecules* **2006**, *39*, 3175−3183. (c) Zhang, B.; Pan, C.; Hong, C.; Luan, B.; Shi, P. *Macromol. Rapid Commun.* **2006**, *27*, 97−102.
14. Patton, D.; Taranekar, P.; Fulghum, T.; Advincula, R. *Macromolecules* **2008**, *41*, 6703–6713.
15. Sackmann, E. *Science* **1996**, *271*, 43–48.
16. (a) Zhu, X. *Acta Phys. Chim. Sin.* **2002**, *18*, 855. (b) Bumbu, G.; Kircher, G.; Wolkenhauer, M.; Berger, R.; Gutmann, J. *Macromol. Chem. Phys.* **2004**, *205*, 1713−1720.
17. (a) Ambrose, J.; Nelson, R. *J. Electrochem. Soc.* **1968**, *115*, 1159−1164. (b) Ambrose, J.; Carpenter, L.; Nelson, R. *J. Electrochem. Soc.* **1975**, *122*, 876−894.
18. (a) Mengoli, G.; Musiani, M.; Schreck, B. *J. Electroanal. Chem.* **1988**, *246*, 73−76. (b) Macit, H.; Sen, S.; Sacak, M. *J. Appl. Polym. Sci.* **2005**, *96*, 894−898. (c) Inzelt, G. *J. Solid State Electrochem.* **2003**, *7*, 503−510. (d) Abe, S.; Ugalde, L.; del Valle, M.; Tregouet, Y.; Bernede, J. *J. Braz. Chem. Soc.* **2007**, *18*, 601−606.
19. Taranekar, P.; Fulghum, T.; Patton, D.; Ponnapati, R.; Clyde, G.; Advincula, R. *J. Am. Chem. Soc.* **1975**, *122*, 876–894.
20. (a) Taoudi, H.; Bernède, J.; Bonnet, A.; Morsli, M.; Godoy, A. *Thin Solid Films* **1997**, *304*, 48−55. (b) Taoudi, H.; Bernède, J.; del Valle, M.; Bonnet, A.; Molinie, P.; Morsli, M.; Diaz, F.; Trégouët, Y.; Bareau, A. *J. Appl. Polym. Sci.* **2000**, *75*, 1561−1568. (c) Abé, S.; Bernède, J.; Ugalde, L.; Trégouët, Y.; del Valle, M. *J. Appl. Polym. Sci.* **2007**, *106*, 1568−1575.
21. (a) McCoy, K.; Hess, D.; Henderson, C.; Tolbert, L. *J. Vac. Sci. Technol., B* **2004**, *22*, 3503−3508. (b) Tao, F.; Sim, W.; Xu, G.; Qiao, M. *J. Am. Chem. Soc.* **2001**, *123*, 9397−9403.
22. Morf, P.; Raimondi, F.; Nothofer, H.; Schnyder, B.; Yasuda, A.; Wessels, J.; Jung, T. *Langmuir* **2006**, *22*, 658–663.
23. (a) Pirri, G.; Chiari, M.; Damin, F.; Meo, A. *Anal. Chem.* **2006**, *78*, 3118−3124. (b) Rowe, M.; Hammer, B.; Boyes, S. *Macromolecules* **2008**, *41*, 4147−4157. (c) Matyjaszewski, K.; Miller, P.; Shukla, N.; Immaraporn, B.; Gelman, A.; Luokala, B.; Siclovan, T.; Kickelcik, G.; Vallant, T.; Hoffman, H.; Pakula, T. *Macromolecules* **1999**, *32*, 8716−8724.
24. Feng, J.; Haasch, R.; Dyer, D. *Macromolecules* **2004**, *37*, 9525–9537.
25. (a) McPherson, T.; Kidane, A.; Szleifer, R.; Park, K. *Langmuir* **1998**, *14*, 176−186. (b) Harris, J.; Chess, R. *Nat. Rev. Drug Discovery* **2003**, *2*, 214−341. (c) Harder, P.; Grunze, M.; Dahint, R. *J. Phys. Chem. B* **1998**, *102*, 426−436.

Downloaded by UNIV OF GUELPH LIBRARY on June 22, 2012 | http://pubs.acs.org
Publication Date (Web): November 10, 2010 | doi: 10.1021/bk-2010-1050.ch005

Downloaded by UNIV OF DELAWARE MORRIS LIB on June 22, 2012 | http://pubs.acs.org
Publication Date (Web): November 10, 2010 | doi: 10.1021/bk-2010-1050.ch006

Chapter 6

Formation of Photo-Responsive Surfaces by Surface-Initiated Ring Opening Metathesis Polymerization and Atom Transfer Radical Polymerization: Reversible Optodes for Metal Ion Sensors

Satyabrata Samanta, Kristen Fries, Sara Orski, and Jason Locklin*

Department of Chemistry and Faculty of Engineering, University of Georgia, Athens, GA 30602
***jlocklin@chem.uga.edu**

In this work, we report on the grafting of photochromic polymer brushes from oxide surfaces using surface-initiated ring-opening metathesis polymerization (ROMP) and atom transfer radical polymerization (ATRP). The spiropyran-based homopolymers were synthesized from norbornyl derivatives of spiropyran using ROMP in the presence of Grubbs Generation II catalyst, whereas copolymers of methacrylate based spiropyran (SPMA) and different methacrylate derivatives were synthesized using surface-initiated ATRP. In both cases, polymer growth was monitored by ellipsometry and atomic force microscopy (AFM). For polymer brushes prepared by ROMP, the growth of the polymer film is strongly influenced by the monomer: catalyst ratio as well as reaction time. Reaction conditions were optimized to provide brushes with controllable thickness up to 120 nm. For copolymers prepared by ATRP, the polymerization proceeds in a living fashion, and copolymer brushes with thickness up to 80 nm were prepared. These densely packed and highly smooth polymer films were successfully used as surfaces with switchable wettability. Also, these films were used as reversible, photoswitchable optical sensors that show selectivity for different metal ions. Covalently bound polymer chains allow for an increase in

In Smart Coatings III; Baghdachi, J., et al.;
ACS Symposium Series; American Chemical Society: Washington, DC, 2010.

sensor stability, impart a rapid response to analyte, and provide reversible, switchable sensor surfaces with longer lifetimes.

Designing functional surfaces using stimuli responsive polymeric materials is currently the subject of a wide variety of research. Various types of stimuli, e.g., temperature (*1*), pH (*2*), ionic strength, solvent vapors (*3–5*), light, or an electrical field (*6*), can affect properties and the conformation of polymer chains. Applications that utilize stimuli-responsive surfaces are diverse, ranging from nanolithography to biomedical applications (*7–9*). In this article, we focus on photochromic polymer brushes that have the ability to elicit changes in wettability upon irradiation of light, as well as the ability to reversibly complex metal ions, which make them excellent candidates for light-activated sensors.

It is well known that photo-responsive materials undergo changes in molecular conformation which correspond to a change in their physical properties such as dipole moment or refractive index by exposure with the appropriate wavelength of light (*10*, *11*). Spiropyrans comprise a group of the most extensively studied organic photochromic compounds, and their reversible photochromic process is shown in Scheme 1. Upon UV irradiation, spiropyran converts to its colored merocyanine form by cleavage of the C-O bond (*10*, *12*). This process is reversible with either heat or irradiation of visible light. The photoinduced geometry change between the ring closed spiropyran (SP) and the ring-opened merocyanine (MC) form is accompanied by a large change in dipole moment (Figure 1). If confined to an interface, the change in dipole moment affects the surface free energy, which in turn, gives rise to a switching of wettability. It is also known that MC can bind metal ions through complexation with the phenolate anion. This interaction is weak enough, however, that upon irradiation with visible light the ion will dissociate and ring closure can occur, allowing for a system capable of reversible binding.

Herein we report the development of smart surfaces that utilize the photochromic behavior of spiropyran. We have investigated an approach for the preparation of photochromic polymer brushes containing spiropyran moieties using surface-initiated ring-opening metathesis polymerization (SI-ROMP) and atom transfer radical polymerization (ATRP). Using SI-ROMP, three different photoresponsive homopolymer brushes were synthesized by varying the alkyl chain length between a ring-strained norbornyl moiety and pendant spiropyran units. These polymer brushes exhibit reversible photocontrol of surface properties and show large changes in surface morphology when irradiated in polar solvents.

We have also synthesized polymer brushes containing spiropyran moieties for colorimetric chemical sensor applications. These brushes were used as reversible, photoswitchable optical sensors that show selectivity for different metal ions. Different metal complexations were also used to create surfaces with drastic changes in wettability. Covalently bound polymer chains allow for an increase in sensor stability, impart a rapid response to analyte, and provide reversible, switchable sensor surfaces with longer lifetimes.

Downloaded by UNIV OF DELAWARE MORRIS LIB on June 22, 2012 | http://pubs.acs.org
Publication Date (Web): November 10, 2010 | doi: 10.1021/bk-2010-1050.ch006

Downloaded by UNIV OF DELAWARE MORRIS LIB on June 22, 2012 | http://pubs.acs.org
Publication Date (Web): November 10, 2010 | doi: 10.1021/bk-2010-1050.ch006

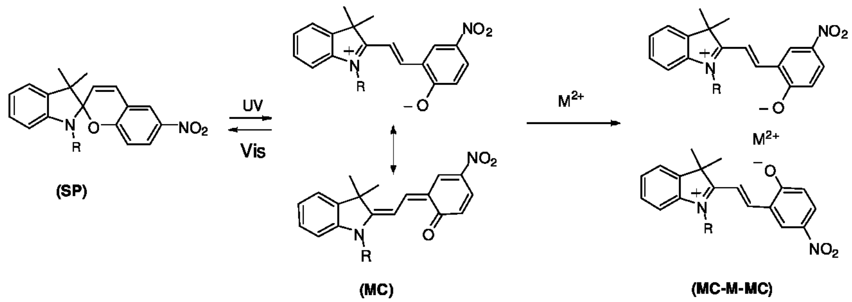

*Scheme 1. Isomeric molecular structure of the spiropyran moiety in the ring closed spiropyran (**SP**, left) and ring opened merocyanine (**MC**, middle) form. The dimeric complex of MC that forms upon metal ion complexation is also shown (right).*

Experimental Section

Materials

Silicon wafers (Universitywafer.com) with native oxide (cut into 2 × 1 cm pieces) were used as substrates for polymerization. 7-Octenyltrichlorosilane (Gelest), 5-norbornene-2-carboxylic acid (Alfa Aesar) and Grubbs Generation-II catalyst (Aldrich) were used as received. CuBr, ethyl-2-bromoisobutyrate (Et_2BrIB), $CuCl_2$, $NiCl_2$, $FeCl_2$, $MgCl_2$, $ZnCl_2$, $CoCl_2$, $HgCl_2$, and ethanol were purchased from either TCI or Alfa Aesar and used as received. Methyl methacrylate (MMA) was passed through a column of neutral alumina to remove inhibitor before polymerization. Acetonitrile, tetrahydrofuran (THF) and dichloromethane (CH_2Cl_2) solvents were dried prior to use. 1′-(2-Hydroxyethyl)-3′,3′-dimethyl-6-nitrospiro(2*H*-1-benzopyran-2,2′-indole) (SP alcohol), 1′-(6-hydroxhexyl)-3′,3′-dimethyl-6-nitrospiro(2*H*-1-benzopyran-2,2′-indole) and 1′-(10-hydroxydecyl)-3′,3′-dimethyl-6-nitrospiro(2*H*-1-benzopyran-2,2′-indole) (**1a-1c**) were synthesized according to literature procedures (*13*, *14*). 10-undecen-1-yl 2-bromo-2-methylpropionate and (11-(2-bromo-2methyl)propionyloxy)undecyltrichlorosilane were synthesized according to published procedure (*15*). (1/-(2-Hydroxyethyl)-3/-dimethyl-6-nitrospiro(2H-1-benzopyran-2,2/-indole (SP alcohol) (*12*) was subsequently coupled to the methacrylic acid chloride following standard procedures (*16*).

Synthesis

Synthesis of 5-Norbornyl Acid Chloride: 1.38 g (10 mmol) of 5-norbornyl acid and 15 mL of thionyl chloride were heated at 70 °C for 1 h under nitrogen atmosphere. The reaction mixture was cooled to room temperature and then the excess thionyl chloride was distilled under reduced pressure at room temperature. The colorless liquid obtained was used immediately without further purification. Yield: 1.4 g (87%) (exo/endo) ^1H NMR (300 MHz, $CDCl_3$) δ (ppm): 6.26 (m, 1H); 6.21 (m, 0.5H); 6.13 (m, 0.5H); 6.03, (1H); 3.43 (m, 2H); 3.29 (bs, 0.5); 2.96 (bs, 1.5H); 2.74 (m, 0.5H); 1.95 (m, 2H); 1.53 (m, 1.5H); 1.34 (m, 1H).

General Synthetic Procedure for Norbornyl Functionalized Spiropyran Monomers (2a-2c): Spiropyran alcohols (**1a**-**1c**) (5 mmol) and pyridine (0.475 g, 6 mmol) were dissolved in freshly distilled THF (25 mL) under a nitrogen atmosphere. To this solution, 5-norbornyl acid chloride (0.783 g, 5 mmol) in 10 mL of dry THF was added drop-wise at room temperature. The deep orange color of the SP alcohols gradually changed to light yellow. The reaction mixture was stirred at room temperature for 24 h, filtered, and concentrated to dryness using a rotary evaporator. An off-white solid was isolated by column chromatography on silica gel using hexane /ethyl acetate (10: 1 v/v) as the eluent.

2a: Yield: 1.6 g (68%). ^{1}H NMR (300 MHz, $CDCl_3$) δ (ppm): 8.03 (d, 2.1 Hz, 1H); 8.00 (s, 1H); 7.20 (t, 6.6 Hz, 1H); 7.08 (d, 6.0 Hz, 1H); 6.93 - 6.87 (m, 2H); 6.76 - 6.68 (m, 2H); 6.20 - 6.11 (m, 1H); 5.91 - 5.86 (m, 2H); 4.17 - 4.06 (m, 2H); 3.45 - 3.40 (m, 2H); 2.90 - 2.86 (m, 3H); 1.90 - 1.85 (m, 1H); 1.47 - 1.35 (m, 2H); 1.25 - 1.23 (m, 4H); 1.17 (s, 3H). ^{13}C NMR (300 MHz, $CDCl_3$) δ (ppm): 182.62, 141.10, 137.70, 135.65, 133.86, 133.67, 132.26, 128.30, 128.28, 127.83, 125.96, 122.75, 121.90, 121.86, 121.78, 115.56, 106.86, 106.54, 62.36, 52.85, 49.66, 45.65, 43.28, 42.51, 29.33, 25.86, 24.59, 19.86. MS (MALDI) *m/z* 473. Anal. Calcd for $C_{28}H_{28}N_2O_5$: C, 71.17; H, 5.97; N, 5.93. Found: C, 70.93; H, 6.07; N, 5.78.

2b: Yield: 1.6 g (61%). ^{1}H NMR (300 MHz, $CDCl_3$) δ (ppm): 8.02 (d, 2.7 Hz, 1H); 7.99 (s, 1H); 7.18 (t, 7.8 Hz, 1H); 7.09 (d, 7.2 Hz, 1H); 6.92 - 6.83 (m, 2H); 6.75 (d, 9.9 Hz, 1H); 6.58 (d, 7.8 Hz, 1H); 6.17 - 6.12 (m, 1H); 5.89 - 5.82 (m, 2H); 4.05 - 3.95 (m, 2H); 3.19 - 3.12 (m, 3H); 2.94 - 2.89 (m, 2H); 1.66 - 1.49 (m, 5H); 1.43 - 1.26 (m, 7H); 1.28 (s, 3H); 1.18 (s, 3H). ^{13}C NMR (300 MHz, $CDCl_3$) δ (ppm): 174.99, 159.88, 147.33, 141.12, 137.99, 136.14, 132.51, 128.33, 127.96, 126.09, 122.92, 122.24, 121.91, 119.55, 118.69, 115.74, 106.97, 106.85, 64.30, 52.78, 49.48, 45.94, 43.90, 43.57, 42.76, 29.41, 29.16, 28.84, 27.18, 26.25, 26.04, 20.08. MS (MALDI) *m/z* 529. Anal. Calcd for $C_{32}H_{36}N_2O_5$: C, 72.70; H, 6.86; N, 5.30. Found: C, 72.57; H, 7.06; N, 5.09.

2c: Yield: 1.71 g (59%). ^{1}H NMR (300 MHz, CDCl3) δ (ppm): 8.01 (d, 2.6 Hz, 1H); 7.99 (s, 1H); 7.18 (t, 7.8 Hz, 1H); 7.09 (d, 6.9 Hz, 1H); 6.91 - 6.83 (m, 2H); 6.75 (d, 8.4 Hz, 1H); 6.57 (d, 7.5 Hz, 1H); 6.18 - 6.12 (m, 1H); 5.92 - 583 (m, 2H); 4.06 - 3.99 (m, 2H); 3.19 - 3.10 (m, 3H); 2.95 - 2.90 (m, 2H); 1.60 - 1.58 (m, 5H); 1.43 - 1.25 (m, 18H); 1.18 (s, 3H). ^{13}C NMR (300 MHz, $CDCl_3$) δ (ppm): 174.82, 159.70, 147.14, 140.86, 137.72, 135.91, 132.35, 128.02, 127.70, 125.83, 122.67, 122.07, 121.63, 119.23, 118.84, 115.52, 106.74, 106.63, 64.28, 52.62, 49.61, 46.35, 45.72, 43.74, 43.36, 43.22, 42.35, 29.47, 29.37, 29.17, 28.95, 28.65, 27.30, 26.03, 25.90, 19.84.MS(MALDI) *m/z* 582. Anal. Calcd for$C_{36}H_{42}N_2O_5$: C, 73.94; H, 7.58; N, 4.79. Found: C, 72.95; H, 7.73; N, 4.27.

Surface-Initiated Polymerization Conditions for (3a-3c): Silicon wafers and glass slides were cut into rectangles. The substrates were sonicated with Fisherbrand sonicating soap, 18.2 MΩ deionized water, isopropanol, and acetone for 10 min each and finally dried in an oven for 1 h. After cleaning, a self-assembled monolayer of 7-octenyl trichlorosilane was formed from the vapor phase by suspending the substrates in a vacuum dessicator and placing two drops of silane on a glass substrate at the bottom. The substrates were kept in a vacuum flux with constant pressure (100 millitorr) for 20 min. After venting with

Downloaded by UNIV OF DELAWARE MORRIS LIB on June 22, 2012 | http://pubs.acs.org
Publication Date (Web): November 10, 2010 | doi: 10.1021/bk-2010-1050.ch006

nitrogen, the substrates were sonicated with acetone and dried under a stream of argon. The SAM coated silicon substrate was immersed in a degassed CH_2Cl_2 solution of Grubbs generation (II) catalyst (0.02 M in CH_2Cl_2) under argon at 45 °C for 1 h. After the catalyst-attached substrate was thoroughly washed with degassed CH_2Cl_2, it was exposed to the monomers (**2a**-**2c**) (0.5 M, in 1 mL degassed CH_2Cl_2) at 50 °C for 4 h. The polymerization was terminated by the addition of several drops of ethyl vinyl ether. Finally substrates were sonicated with acetone for 30 min to remove any physisorbed materials. The thickness of the polymer layers was measured using ellipsometry.

Synthesis of p(SPMA-co-MMA) Brush (4): SPMA (0.381g, 0.906 mmol), MMA (0.816 g, 8.15mmol), and CuBr (0.005 g, 0.0349 mmol) were added to a Schlenk flask under Ar, containing a Si wafer and glass slide with initiator. 5 mL of anhydrous THF was then added and the reaction mixture was degassed under Ar for 1h. To this was added PMDETA (0.060 g, 0.346 mmol), which was also degassed under Ar for 1 hour. The rubber septum on the Schlenk flask was then replaced with a glass stopper while the reaction was still under Ar to avoid any possible oxygen poisoning. The reaction was then placed in a 65 °C oil bath for 16-18 h. The reactions were quenched by exposing the flask to ambient temperature. Upon removal from the solution, the samples were immediately washed thoroughly with THF and DMF. The samples were stored in the dark when not in use. The Si wafer was used for thickness characterization by ellipsometry, while the glass substrate was used for UV-vis spectroscopy.

Downloaded by UNIV OF DELAWARE MORRIS LIB on June 22, 2012 | http://pubs.acs.org
Publication Date (Web): November 10, 2010 | doi: 10.1021/bk-2010-1050.ch006

Measurements

UV-vis spectra of polymer films were obtained on a Cary 50 (Varian). AFM experiments for spiropyran based polymer films were performed using a Multimode Nanoscope IIIa (Veeco Metrology Group). All measurements were performed using tapping mode. Null ellipsometry was performed on a Multiskop (Optrel GbR) with a 632.8 nm He-Ne laser beam as the light source. Both δ and ψ value thickness data were measured and calculated by integrated specialized software. At least three measurements were taken for every layer, and the average thickness was calculated. Contact angles of water drops were measured with the same Multiskop system by using a white light source and replacing the photodiode with a CCD camera. The syringe was fixed on top of the goniometer and the substrate moved in x, y and z directions. The contour of a sessile drop was analyzed and fitted to the Young-Laplace equation using a contour tracing algorithm that distinguishes the drop from its mirror image. For statistical purposes, at least three drops were measured on each sample. The reported contact angles are the average of these measurements. For photoswitching, the surface was dried with a flow of argon and illuminated with light of appropriate wavelength for the next sequence of contact angle measurements.

Light Source

An OmniCure, series 1000 with 365nm wavelength light was used as the UV light source. The substrates were held 2 cm from the source and irradiated at a

Downloaded by UNIV OF DELAWARE MORRIS LIB on June 22, 2012 | http://pubs.acs.org
Publication Date (Web): November 10, 2010 | doi: 10.1021/bk-2010-1050.ch006

power of 30 mW/cm^2. The visible light source was a Fiber-Lite, Model with 30W quartz-halogen fiber optic illuminator.

Water Contact-Angle Experiments

Contact angle measurements were taken on the sample before irradiating with UV light. The sample was then irradiated with 365 nm light while immersed in a 10 mM solution of metal salt in ethanol for 2 minutes. The sample was blown dry with air and contact angle measurements were taken. To show reversibility, the sample was irradiated for 10 minutes with visible light while immersed in toluene. For samples irradiated in DMF, the same procedure was followed with the exception that the sample was irradiated with UV light while immersed in DMF instead of the metal salt solution.

Solvent-Dependent Changes in Surface Morphology

The silicon substrate functionalized with a spiropyran polymer brush was irradiated with 365 nm light for two minutes in air or while immersed in solvents of different polarity. The substrates were then dried under a flow of argon. The change in surface morphology was characterized with AFM.

Results and Discussion

Synthesis

The synthetic strategy for polymer brushes **3a**-**3b** is outlined in Scheme 2. The spiropyran functionalized norbornyl derivatives (**2a** – **2c**) were isolated as colorless to light-yellow solids, in moderate yields (59% - 68%) by condensation reactions involving stoichiometric amounts of spiropyran alcohols (**1a** – **1c**) and norbornyl acid chloride in THF at room temperature. We incorporated the spiropyran moiety into the side chain of polymer brushes by using different alkyl spacer lengths (C_2, C_6 and C_{10}) to study the influence of spacer length on the surface morphology changes induced by UV irradiation. SI-ROMP reactions of norbornyl substituted spiropyrans (**2a** – **2c**) were carried out from oxide surfaces as described in the experimental section. For the attachment of Ru catalyst onto the substrate, we formed vinyl-terminated SAMs of 7-octenyl trichlorosilane. The vinyl group of the monolayer provides an alkylidene ligands for the attachment of ruthenium catalyst for ROMP (*17*, *18*). We investigated the optimal surface density of vinyl-terminated SAMs with Grubbs Generation II catalyst for the formation of thicker polymer brushes and better control over the grafting density. After the functionalization of Grubbs catalyst onto the vinyl-terminated monolayer, the catalyst-attached substrate was immersed in the degassed dichloromethane solutions of spiropyran substituted norbornyl derivatives (**2a**-**2c**) (0.5 M) for 4 h at 50 °C. Varying the monomer concentration from 0.05 M to 0.5 M, we are able to control the polymer thickness from 10 nm to 120 nm.

Downloaded by UNIV OF DELAWARE MORRIS LIB on June 22, 2012 | http://pubs.acs.org
Publication Date (Web): November 10, 2010 | doi: 10.1021/bk-2010-1050.ch006

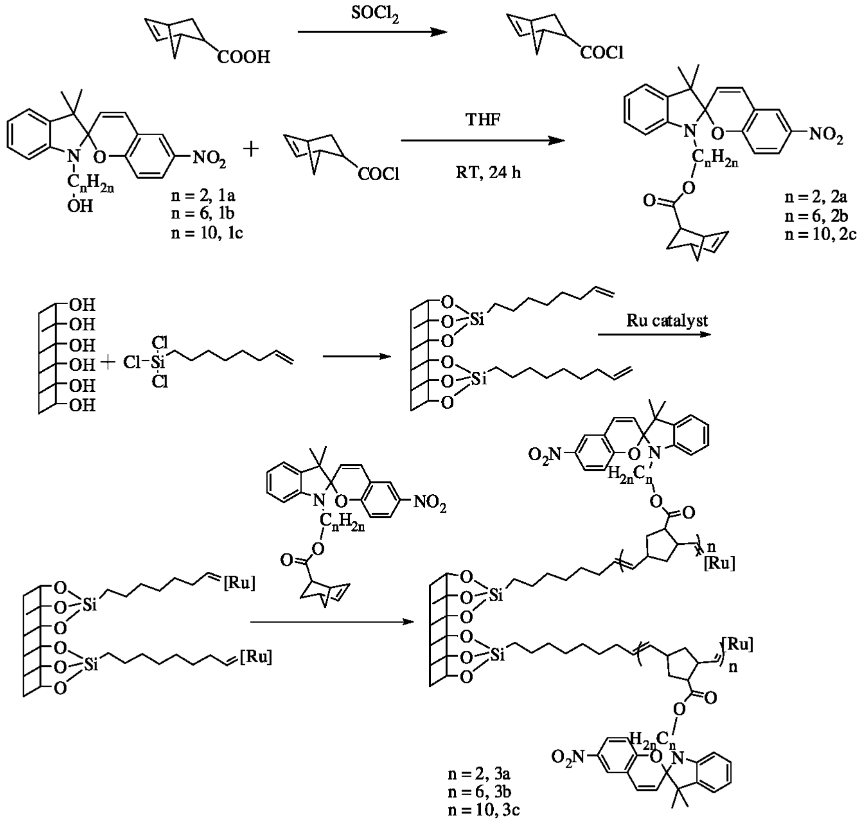

*Scheme 2. Synthetic pathway used to make spiropyran functionalized norbornyl derivatives (**2a-c**) and polymer brushes (**3a-c**) using SI-ROMP.*

The polymer brush **4** was synthesized from glass substrates using a surface bound bromoisobutyryl initiator by the reaction between SPMA monomer and MMA (Scheme 3). When homopolymerization was attempted, no brushes with a thickness larger than 4 nm were possible under different catalyst/ligand/solvent combinations, presumably due to the steric bulk of the SPMA monomer. Under conditions similar to those reported by Piech and Bell (*19*, *20*), we attempted to copolymerize SPMA with different methacrylates in varying ratios, and thicknesses up to 80 nm were possible under controlled conditions with high graft density. The final film thickness decreased with increasing mol% SPMA, and for the rest of this work, a copolymer with 10 mol% SPMA–90 mol% MMA was used.

Polymer Brushes as Metal Ion Sensors

The spiropyran-merocyanine optical switch has some interesting characteristics that can be exploited in optical sensing applications (*26*). It is well known that the colored merocyanine (MC) zwitterionic form can bind metal ions through a negatively charge phenolate group (*27*). Recently, Byrne showed that

Downloaded by UNIV OF DELAWARE MORRIS LIB on June 22, 2012 | http://pubs.acs.org
Publication Date (Web): November 10, 2010 | doi: 10.1021/bk-2010-1050.ch006

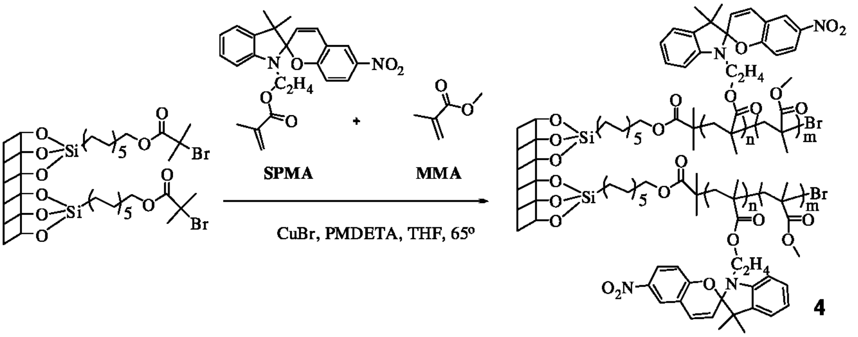

4

Scheme 3. Surface initiated copolymerization of a spiropyran methacrylate derivative (SPMA) and methyl methacrylate (MMA).

Co(II) ion can bind to the MC form and that this complexation is reversible (*26*). In this respect, we have synthesized polymer and copolymer brushes containing spiropyran moieties that can be used for reversible, photo-switchable optical sensors that are selective to different metal ions. All polymer brushes developed by both ROMP and ATRP were used as metal ion sensors. Figure 1 shows the UV-visible absorption spectrum of a 25 nm thick polymer brush **4** (copolymer of SPMA and MMA) in the presence of different metal ions. The colorless SP form has no characteristic absorbance in the visible region, whereas the zwitterionic form displays an intense electronic spectral band around 580 nm with a low intensity band centered at 374 nm. Upon irradiation with UV light in the presence of different metal ions, there is a decrease in absorbance at 580 nm, along with a significant blue shift in absorption maxima. The magnitude of the blue shift is largely influenced by the metal ion present on the surface. The group VIII metal ions, like Fe or Pd, has more influence on the magnitude of the blue shift, compared to alkali metal ions. The ion selectivity can easily be discriminated with the naked eye for most metal ions, as shown in the polymer coated film in Figure 1. The metal decomplexation is reversible when irradiated with visible light and is very slow in the solid state or in polar solvents. Using toluene, a better solvent to stabilize the non-polar SP forms, the reverse reaction occurs in minutes. The colorimetric response of the film is identical after repeating several cycles (at least five) of complexation/decomplexation.

Light-Induced Contact Angle Changes

The goal of this work is to develop a photoresponsive surface, which can change the surface energy upon irradiation of light, as measured by water contact angle experiments. We chose the spiropyran-coated surface because it was expected that the large change in dipole moment between the two isomeric states of the spiropyran would lead to measurable changes of surface energy. After irradiation with UV light, hydrophilicity of the surface is increased, resulting in a decrease of water contact angle. After subsequent irradiation with visible light, the surface recovers its initial hydrophobicity. Contact angles of surfaces, before and after irradiation, for all three polymer brushes synthesized using SI-ROMP

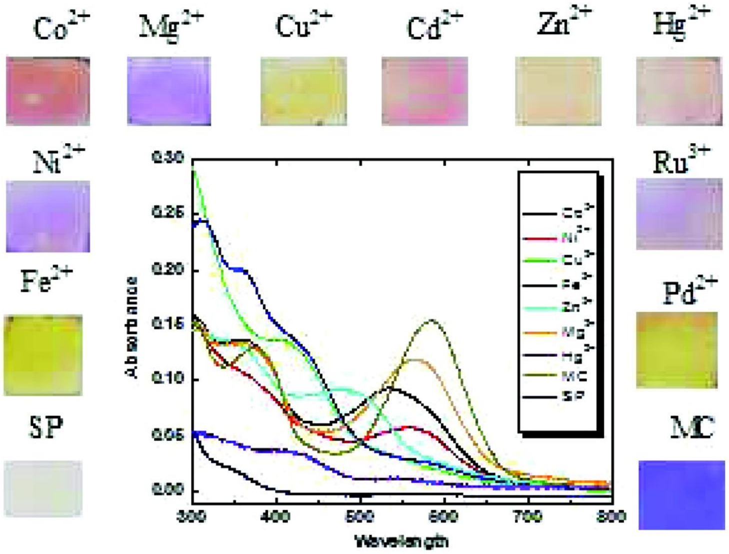

Figure 1. UV-visible spectra of copolymer brush (4) in presence of different metal ions.

(**3a**-**3b**) are given in Table 1. The initial contact angle of each sample increases with increasing spacer length (from 79° to 90°). Table 1 also shows the contact angle for each film after irradiation. Contact angle changes of 5-15° (5° for **3a**, 15° for **3b**, 13° for **3c)** were observed with each surface. The switching is reversible and no signs of degradation were observed in our system after at least 5 switching cycle.

The magnitude of the light-induced water contact angle change for our polymer brush system is greater than other systems reported (10° (*21*), 9° (*22*), 8° (*23*, *24*)) using functionalization by self-assembled monolayers of spiropyrans (or azobenzenes) or cast copolymer films on flat surfaces. It should be noted that Rosario et al. observed comparable changes in contact angle (11-14°) with diluted spiropyran monolayers and water of pH 5.5 (*25*). It is also important to note that the contact angle changes for hexyl (**3b**) and decyl (**3c)** substituted SPs are comparable (15° and 13°), where as ethyl (**3a**) substituted has much less contact angle change (5°). This is because the bulky spiropyran groups located close to the backbone limit the available free volume and restrict the conformational freedom of the spiropyran moieties. With hexyl and decyl spacers, the pendant side-chains have more available space to undergo ring opening/ closing reactions.

The metal ion bonding also enhances wettability. The open merocyanine (MC) form exists as a resonance hybrid between two forms, a charged zwitterion or a neutral quinoidal structure (Scheme 1). The zwitterion represents the major contribution to the MC isomer because aromaticity of the oxygen-bearing ring is lost in the neutral quinoidal structure. So it is expected that metal/phenolate anion interaction stabilizes the zwitterionic form, as well as enhances the hydrophilic

Downloaded by UNIV OF DELAWARE MORRIS LIB on June 22, 2012 | http://pubs.acs.org
Publication Date (Web): November 10, 2010 | doi: 10.1021/bk-2010-1050.ch006

Downloaded by UNIV OF DELAWARE MORRIS LIB on June 22, 2012 | http://pubs.acs.org
Publication Date (Web): November 10, 2010 | doi: 10.1021/bk-2010-1050.ch006

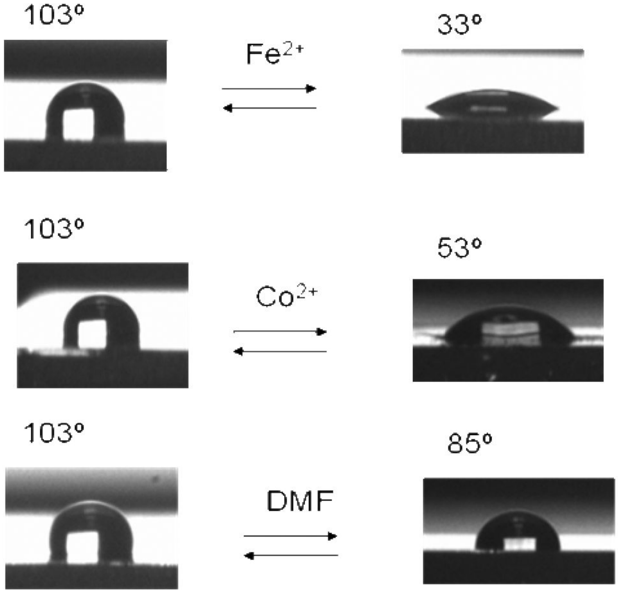

Figure 2. Reversible contact angle changes of film 4 with and without metal ion complexation.

character of the surface. On the other hand, the metal/phenolate anion interaction is weak enough to allow for the ring closing to occur after exposure to visible light.

In this study we also investigated the wettability change of the spiropyran polymer brushes by irradiating in the presence of various metal ions. The reversible switching of a water droplet on polymer brush **4** (60 nm thick brush) in the presence of metal ions (Co and Fe) is shown in Figure 2. The films were submerged in an ethanolic solution (10 mM) of metal salt and irradiated for two minutes. Static contact angle changes as large as 70 °, were observed when the films were irradiated in the presence of Fe (II). The contact angle change was completely reversible (at least 5 times) when the substrate was irradiated with visible light in non-polar solvents. To the best of our knowledge, this is the largest reported contact angle change on a flat surface. The degree of contact angle change in the presence of different metal ions correlates well with the blue shift in absorption spectra shown in Figure 1. Table 1 summarizes the contact angles taken for all polymer brushes that were synthesized by both ROMP and ATRP.

Observation of Morphology Changes Using AFM

We used AFM to observe the surface morphology before and after UV radiation, as well as the morphological changes in polar or non-polar solvents. Films with high grafting density and smooth morphologies were obtained for each monomer, with an RMS value of less than 2 nm. We also expected morphological changes during photoisomerization. Surprisingly, when irradiated with UV light, the image showed no strong evidence for a significant change in structure in the solid states or non-polar solvents. Although large changes in

Downloaded by UNIV OF DELAWARE MORRIS LIB on June 22, 2012 | http://pubs.acs.org
Publication Date (Web): November 10, 2010 | doi: 10.1021/bk-2010-1050.ch006

Table 1. Water Contact Angle Measurements of Polymer Brushes Before and After UV Irradiation

Polymer brush	*CA before UV*	*CA after visible*	*CA change*
3a	79°	74°	5°
3b	82°	67°	15°
3c	90°	77°	13°
3b with $CoCl_2$	80°	45°	35°
4 with DMF	103°	85°	17°
4 with $CoCl_2$	103°	53°	50°
4 with $FeCl_2$	103°	33°	70°

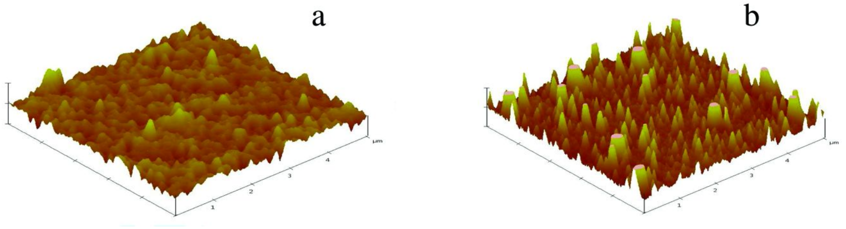

Figure 3. AFM images of polymer brush 3b before (a) and after (b) the radiation of UV light in DMF solvent.

wettability were observed for polymer brushes **3b**, **3c** and **4**, we observed no structural reorganization of the thin film morphology by AFM after irradiation. We did observe significant morphological changes, however, when the films were irradiated in DMF, a better solvent for the MC form. Figure 3 shows 3D AFM images of polymer film **3b** before and after UV radiation in DMF. Before irradiation, films were very smooth with a roughness of 2 nm. After irradiation with DMF, however, the brushes were more stretched and had formed sharp structures within the film. The RMS roughness also increased to 7 nm, a signature of huge morphology change.

Conclusions

In this work, we synthesized photochromic homopolymers and copolymers with pendant spiropyran groups covalently attached to the surface by ROMP and ATRP techniques. Manipulations of the reaction conditions allowed reproducible formation of polymer brushes of up to 120 nm thickness for **3a**-**3c** and 80 nm for **4**, with high grafting density. We have successfully used these polymer brushes as reversible ion sensors, where the confined microenvironment provides a colorimetric response that is selective for different metal ion complexation. Also, these films were successfully used as surfaces with photo-switchable wettability, and the metal ion complexation drastically amplifies this wettability change. Reversible contact angle changes of up to 70° were observed for films grown from flat substrates, which can be amplified further by growing polymers from rough surfaces. Lastly, morphological changes accompanying photochromism were investigated using AFM. Significant morphological changes can only be induced in the films by irradiating in polar solvents that help to stabilize the merocyanine ring open form. The sensor response to different chemical microenvironments, detection limits and fluorescence sensitivity are currently under investigation in our laboratory.

References

1. Xia, Y.; Yin, X.; Burke, N. A. D.; Stoever, H. D. H. *Macromolecules* **2005**, *38*, 5937–5943.
2. Zhang, H.; Ruehe, J. *Macromolecules* **2005**, *38*, 4855–4860.
3. Gallyamov, M. O.; Tartsch, B.; Khokhlov, A. R.; Sheiko, S. S.; Boerner, H. G.; Matyjaszewski, K.; Moeller, M. *Macromol. Rapid Commun.* **2004**, *25*, 1703–1707.
4. Gallyamov, M. O.; Tartsch, B.; Khokhlov, A. R.; Sheiko, S. S.; Boerner, H. G.; Matyjaszewski, K.; Moeller, M. *J. Microsc.* **2004**, *215*, 245–256.
5. Gallyamov, M. O.; Tartsch, B.; Khokhlov, A. R.; Sheiko, S. S.; Boerner, H. G.; Matyjaszewski, K.; Moeller, M. *Chem. Eur. J.* **2004**, *10*.
6. Lokuge, I. S.; Bohn, P. W. *Langmuir* **2005**, *21*, 1979–1985.
7. Ionov, L.; Minko, S.; Stamm, M.; Gohy, J. F.; Jerome, R.; Scholl, A. *J. Am. Chem. Soc.* **2003**, *125*, 8302–8306.
8. Fu, Q.; Rao, G. V. R.; Ista, L. K.; Wu, Y.; Andrzejewski, B. P.; Sklar, L. A.; Ward, T. L.; Lopez, G. P. *Adv. Mater.* **2003**, *15*, 1262–1266.
9. Stayton, P. S.; Shimoboji, T.; Long, C.; Chilkoti, A.; Chen, G.; Harris, J. M.; Hoffman, A. S. *Nature* **1995**, *378*, 472–474.
10. Saragi, T. P. I.; Spehr, T.; Siebert, A.; Fuhrmann-Lieker, T.; Salbeck, J. *Chem. Rev.* **2007**, *107*, 1011–1065.
11. Yokoyama, Y. *Chem. Rev.* **2000**, *100*, 1717–1740.
12. Hirshberg, Y. J. *J. Am. Chem. Soc.* **1956**, *78*, 2304–2312.
13. Raymo, F. M.; Giordani, S. *J. Am. Chem. Soc.* **2001**, *123*, 4651–4652.
14. Galvin, J. M.; Schuster, G. B. *Supramol. Sci.* **1998**, *5*, 89–100.
15. Matyjaszewski, K.; Miller, P. J.; Shukla, N.; Immaraporn, B.; Gelman, A.; Luokala, B. B.; Siclovan, T. M.; Kickelbick, G.; Vallant, T.; Hoffmann, H.; Pakula, T. *Macromolecules* **1999**, *32*, 8716–8724.
16. Little, J. C. *J. Am. Chem. Soc.* **1965**, *87*, 4020–4022.
17. Harada, Y.; Girolami, G. S.; Nuzzo, R. G. *Langmuir* **2003**, *19*, 5104–5114.
18. Kong, B.; Lee, J. K.; Choi, I. S. *Langmuir* **2007**, *23*, 6761–6765.
19. Piech, M.; Bell, N. S. *Macromolecules* **2006**, *39*, 915–922.
20. Bell, N. S.; Piech, M. *Langmuir* **2006**, *22*, 1420–1427.
21. Dattilo, D.; Armelao, L.; Fois, G.; Mistura, G.; Maggini, M. *Langmuir* **2007**, *23*, 12945–12950.
22. Siewierski, L. M.; Brittain, W. J.; Petrash, S.; Foster, M. D. *Langmuir* **1996**, *12*, 5838–5844.
23. Ichimura, K.; Oh, S.-K.; Nakagawa, M. *Science* **200**, *288*, 1624–1626.

Downloaded by UNIV OF DELAWARE MORRIS LIB on June 22, 2012 | http://pubs.acs.org
Publication Date (Web): November 10, 2010 | doi: 10.1021/bk-2010-1050.ch006

24. Oh, S.; Nakagawa, M.; Ichimura, K. *Chem. Lett.* **1999**, *4*, 349–350.
25. Rosario, R.; Gust, D.; Hayes, M.; Jahnke, F.; Springer, J.; Garcia, A. A. *Langmuir* **2002**, *18*, 8062–8069.
26. Byrne, R. J.; Stitzel, S. E.; Diamond, D. *J. Mater. Chem.* **2006**, *16*, 1332–1337.
27. Phillips, J. P.; Mueller, A.; Przystal, F. *J. Am. Chem. Soc.* **1965**, *87*, 4020–4020.

Downloaded by UNIV OF DELAWARE MORRIS LIB on June 22, 2012 | http://pubs.acs.org
Publication Date (Web): November 10, 2010 | doi: 10.1021/bk-2010-1050.ch006

Chapter 7

Smart Polyurethane Surfaces from Tethered Dendritic Polyols

Ravi G. Joshi,[1,2] Achin Goel,[1] and Vijay M. Mannari*[,1]

[1]Coatings Research Institute, School of Engineering Technology, Eastern Michigan University, Ypsilanti, MI 48197, USA
[2]Munzing Additives North America, Bloomfield, NJ 07003, USA
***Author for Correspondence: vijay.mannari@emich.edu**

Recently, stimuli-responsive surfaces have gained considerable interest among coatings researchers in industry as well as in academe. To date, many switchable surfaces based on such external stimuli as temperature, electricity, pH, and many others have been designed and developed. Environmentally switchable surfaces have been among the most widely studied surfaces since they are known to exhibit *smart* behavior under external influence. In the present work, we report the synthesis of hydrophobic, hydrophilic, and amphiphilic polyurethane coatings with tethered hydrophilic and/or hydrophobic moieties. The polyurethane networks were built using dendritic polyols (soft segments) and Isophorone Diisocyanate (IPDI) as primary components. These coatings have been characterized and tested for surface characteristics using such advanced instruments as the Scanning Probe Microscope (SPM) and Dynamic Contact Angle Analyzer (DCA). The surfaces with tethered hydrophobic or hydrophilic moieties, when immersed in water, showed remarkable changes in the surface topography, hence, their dynamic surface characteristics. The amphiphilic surfaces, containing both hydrophobic and hydrophilic moieties, showed *smart* behavior in response to the external environment. The ability to tailor surfaces with predictable behavior upon exposure to the external environment opens up enormous opportunities for their potential end-use applications.

In Smart Coatings III; Baghdachi, J., et al.;
ACS Symposium Series; American Chemical Society: Washington, DC, 2010.

Introduction

Marine biofouling, *the colonization of microorganisms, plants and animals on submerged aquatic surfaces*, of underwater structures particularly, ships' hulls, is commonly known to increase operational and maintenance costs (*1–4*). Marine biofouling has been successfully controlled using self-polishing marine coatings that release active compounds such as organotin and cuprous oxide which are toxic to the settling stages of fouling organisms (*5*) but many compositions have also been found to have negative effects on non-target aquatic organisms (*1–3*, *6*). Thus, the use of organotin compounds in marine coatings is now prohibited worldwide and coatings incorporating cuprous oxide and other biocides are under scrutiny because of the environmental concerns (*1–3*, *7–9*). An acute need has, therefore, been generated demanding major advances in coatings efficacy and robustness. To decrease the toxic effects on the marine environment is also a significant challenge because of the diverse range of biofouling organisms, associated fouling mechanisms and environmental conditions worldwide. A requirement also exists to develop effective marine coatings that have either greatly reduced or no toxicity. This need is being driven by extended service requirements and environmental regulations (*2*). A great number of innovations in surface chemistry, biocide development, and coating designs are being studied for developing alternatives to biocidal antifouling coating formulations (*2*). A distillation of formulation and design disclosures to date suggest that amongst the various approaches used to develop eco-friendly marine coatings, those based on controlled surface morphology to enhance self-cleaning or fouling resistance have attracted more attention by researchers (*2*, *8*, *10–31*).

For successful development of such marine coatings, it is critical to understand the basic adhesion mechanisms of marine organisms. An extensive literature search (*2*, *32–34*) of the current state-of-art indicates that due to the diverse adhesion mechanisms of marine organisms (*35*) and other numerous factors such as environment, material surface and bulk characteristics- chemical and physical configuration, the range of characteristics of secreted adhesives and their complex interactions with the contacting surface make it difficult to deduce a specific adhesion mechanism(s). The literature (*2*, *3*, *7*, *14*, *32–37*) reveals that many of the fouling organisms primarily use protein-based adhesives to attach themselves to the contacting surfaces.

Among the various possible approaches to combat the problem of marine fouling, we selected designing non-toxic environmental responsive surfaces, which can switch their surface property from hydrophobic to hydrophilic and vice-versa according to the external environment, for example, air or water. In the past, Anastasiadis et al. (*11*) explored and demonstrated the preparation of such stimuli responsive or "smart" surfaces. Also, Koberstein (*38*) defined and described "reorganization of functional polymer surface" as one of the significant strategies of surface modification to decrease surface interaction with the external materials. Two critical aspects while designing such surfaces are - (1) the extent to which they respond to the external environment and, (2) that this response should be two-way, in other words, coatings should revert to the original configuration when the trigger is removed. Thus, these coatings should be "Switchable" and flip back and forth under the influence of a trigger throughout their lifetimes. The driving force for such surface reorganization is the thermodynamic minima or minimum surface energy configuration attained by the surface under the influence of external environment. Such "*smart"* polymeric surfaces that can reorganize or re-orient themselves repetitively under the influence of such external stimuli as temperature (*16*, *28*), pH (*18*, *21*, *31*), light (*17*, *29*), electricity (*39*), environment (*10*), and many more are of great interest for developing potential coatings in many areas.

Literature review reveals that in the past and also recently, many attempts have been made to impart hydrophobic (*14*, *19*, *23*, *25*, *40–44*) or hydrophilic (*19*, *23*, *24*, *30*, *41*, *42*) functional groups to the bulk polymer either by grafting functional moieties or by incorporating functional segments. Previous work and experimental data revealed in earlier literature claim that hydrophilic surfaces such as, Polyethylene oxide (PEO)/Polyethylene Glycol (PEG) (commonly used in drug delivery, bio-medical, and pharmaceutical applications) due to their low-protein adsorption, good stability and low toxicity - are found to be more resistant to the adhesion (attachment) of marine organisms (*2*, *8*, *14*, *19*, *24*, *25*, *36*, *37*, *45*, *46*). Hydrophobic surfaces, for example silicone and fluorine based elastomers, are commonly employed as marine fouling release coatings due to their low surface energy and interesting mechanical properties (*2*, *10*, *12–14*, *24*, *31*, *36*, *37*, *39*, *45–47*). Commercial fouling release coatings based on silicone elastomers "release" accumulated biofouling either through the action of hydrodynamic forces generated as a vessel moves through water or through direct cleaning by hand or using robots, and have been researched widely (*2*, *8*, *20*, *39*, *47*). However, the present generations of fouling release coatings based on siloxane elastomers have a number of shortcomings and are unsuitable for use on the majority of vessels (*2*, *8*, *20*, *39*, *47*). Therefore, neither of the approaches seems effective and economical as one still needs re-painting and frequent dry-docking of marine vessels. Here we propose combining both non-toxic combat mechanisms in a single coating by grafting both hydrophilic and hydrophobic moieties in a bulk polymer. Such an approach will make the surface behave like an amphiphilic brush, which can switch its wettability behavior under the influence of such an external environment as water or air. In other words, in water the surface will become hydrophilic, which would resist the adhesion of bio-organisms for longer times, and in air, it would become hydrophobic, which would provide easy release of attached bio-organisms. This novel approach of designing and developing a *smart* amphiphilic brush would produce potential coatings not only for marine applications but also for biological, pharmaceutical, and many more application areas.

In the present study, we prepared isocyanate (-NCO) terminated pre-polymers using an isophorone diisocyanate (IPDI) and dendritic polyol (soft segment). The pre-polymers were further modified to prepare polyurethane surfaces with (a) tethered hydrophilic (Polyethylene oxide chains) moieties, (b) tethered hydrophobic (perfluoroalkyl chains) moieties and (c) tethered amphiphilic chains containing both hydrophobic and hydrophilic moieties. These surfaces were evaluated for wetting behavior using a Dynamic Contact Angle Analyzer (DCA) and for roughness behavior using a Scanning Probe Microscope (SPM). The coated surfaces were characterized initially in air (after allowing sufficient time for cure), then after immersing them in water for a sufficient period of time, (allowing the surfaces to undergo desirable topographical changes to acclimate to new environment) and finally after post drying in air so as to study the recovery of surface characteristic after the trigger (hydrophilic environment) was removed. Their wetting behavior and surface topography demonstrated interesting results as a function of the external environment. The surfaces of such polymeric assemblies are expected to show interesting characteristics in different contact environments, such as in air and in water. The choice of a polyurethane backbone provides superior mechanical properties such as high modulus and toughness, compared to currently used siloxane elastomers, which have low modulus and are susceptible to damage (*2*, *8*, *13*, *20*, *36*, *37*, *39*, *45*, *47*). These studies postulate potential characteristics of the amphiphilic surfaces and provide an insight into their scope for development of smart marine coatings with dual (fouling resistance and fouling release) properties.

Experimental Details

Materials and Methods

Materials with sources of supply utilized in this study are listed below: Boltorn H2004 (Dendritic polyol polymer - Certified) from Perstorp Specialty Chemicals (Sweden), Isophorone diisocyanate (IPDI) (98%, purchased from Aldrich Chemicals), dibutyltindilaurate (DBDTL) (95%, purchased from Aldrich), Methoxy polyethylene glycol (Mw= 750 g/mole) (Clariant Specialty Chemicals, North America Region),1H,1H,2H,2H- perfluoro octanol (97%, purchased from Alfa Aesar), ethoxylated fluoroalkyl surfactant, Zonyl FSO-100 obtained from Sigma-Aldrich, tetrahydrofuran (THF) (anhydrous 99% inhibitor free, purchased from Aldrich), acrylic polyol – Joncryl 920 (obtained from Johnson Polymers), petroleum ether (Anhydrous, purchased from Aldrich), plain glass microscope slides (75 mm X 25mm, purchased from Fisher Scientific), ACT phosphated cold roll steel panels (6 inch X 4 inch, purchased from ACT Test Panels, Inc.). All the reagents and materials were certified and used without further purification unless otherwise mentioned.

The final products were characterized for FT-IR and %NCO content as per ASTM D 5155-91, Test Method A. Methods used for surface analysis (contact angle measurement, micro/nano-roughness) are described in the *characterization* section of this paper.

Experimental

Synthesis of IPDI- Based Pre-Polymer

NCO-functional pre-polymers, with predetermined %NCO content were synthesized by reaction of molar excess of IPDI with dendritic polyol (Boltorn H2004), using THF as a solvent (Fig. 1a). The generic structure of Boltorn H2004 dendritic polyol (*48*) is shown in figure 1b. For conditions of this synthesis, the guidelines reported in the literature (*22*, *37*, *49*) were followed. The detailed procedure is shown below.

Into a 3-necked 250 mL flask equipped with a magnetic stirrer, a temperature control system, a reflux condenser, and an inlet for inert nitrogen, calculated amounts of isocyanate oligomer IPDI (NCO: OH = 8:1, excess NCO) and 5% solution in THF of dibutyl tin dilaurate catalyst (DBTDL) [0.01% of the total formulation weight] were placed. All necessary precautions were taken to prevent entry of moisture into the system. Under inert nitrogen atmosphere, the reaction mixture was stirred at reflux temperature of the solvent at approximately 50°C using a water bath. In another beaker, an 80% solution of Boltorn H2004 was made in THF. After thoroughly mixing, the solution was transferred into a dropping funnel. The polyol was added drop wise to the isocyanate oligomer for about 30 min. at the constant rate of 360 drops/hour (to maintain –OH starved condition) and to obtain desired NCO terminated pre-polymer as shown in figure 1a. The reaction temperature was kept constant at 50°C +/- 3° during the addition of the polyol. The completion of the reaction was monitored by determining % -NCO content (titration method). The previous literature also showed that good control of chain extension can be achieved by using large excess of isocyanate, or by addition of DBDTL as a catalyst (*22*, *37*, *49*). It should also be noted that in addition of monofunctional compound (predominant product), other compounds (di- & tri- functional) would also be present in the product.

Functionalization of Prepolymer with Amphiphilic Side Chains, Perfluoro Octanol and Polyethylene Glycol

In the second step, the prepolymer was reacted, separately, with calculated amounts of A: perfluoro octanol (PFO), B: methoxy terminated PEG with mol. wt. 750 gm/mole) (MPEG), and C: fluoro surfactants FSO-100, with NCO/OH ratio of 2:1 as represented in figure 2. These reactions were carried out for 6-12 hours at 50°C in presence of DBTDL catalyst.

Preparation of Films

Joncryl-920 (acrylic polyol) was mixed with tethered -NCO pre-polymers using a magnetic stirrer for 5 min in presence of 5% solution in THF of dibutyl tin dilaurate catalyst (DBTDL) [0.01% of the total formulation weight]. For all samples NCO/OH ratio was kept at 1.1/1. The resulting coating liquid films were applied on to cleaned glass plates (for contact angle measurements) and on phosphated MS panels (for roughness measurements) to yield dry film thickness of about 25 microns. After 30 minutes of ambient cure, samples were cured at 100-120°C for 2 hours, in an air-oven. Control film samples, without any hydrophobic or hydrophilic modifications were also prepared in the identical manner for comparative study. The resultant coatings are coded as shown in table 1. Nicolet 510P FT-IR spectrophotometer was used to monitor urethane formation reaction. The absorption peaks at 1532 cm^{-1}, 1763 cm^{-1} and 3352 cm^{-1}

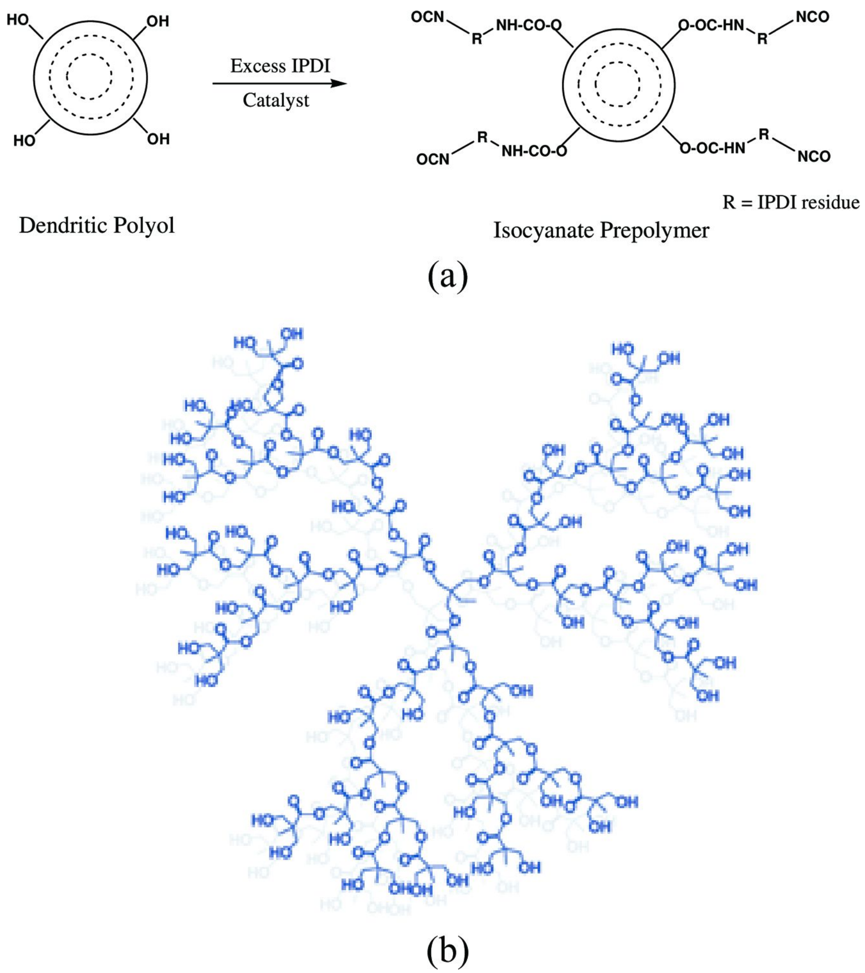
HO
OH
HO
OH
Excess IPDI
Catalyst
OCN
R
NH-CO-O
O-OC-HN
R
NCO
OCN
R
NH-CO-O
O-OC-HN
R
NCO
R = IPDI residue
Dendritic Polyol
Isocyanate Prepolymer
(a)
(b)

Figure 1. a: Schematic representation of preparation of isocyanate prepolymer, b: Generic structure of Boltorn H2004 dendritic polyol (45)

confirm urethane formation. Also, no appreciable absorption at around 2270 cm^{-1} (-NCO) and 3400 cm^{-1} (-OH) is indicative of quantitative consumption of isocyanate and hydroxyl groups.

Characterization

Contact Angle Measurement

This procedure was essentially published previously but is included here for completeness (*36*, *37*). A First Ten Angstrom, FTA-200, Dynamic Contact Angle Analyzer was used for contact angle determination. We used two test liquids, water (hydrophilic and capable of forming hydrogen bond with the substrate) and Hexadecane (non-polar, oleophilic liquid). Two spots were marked on the film

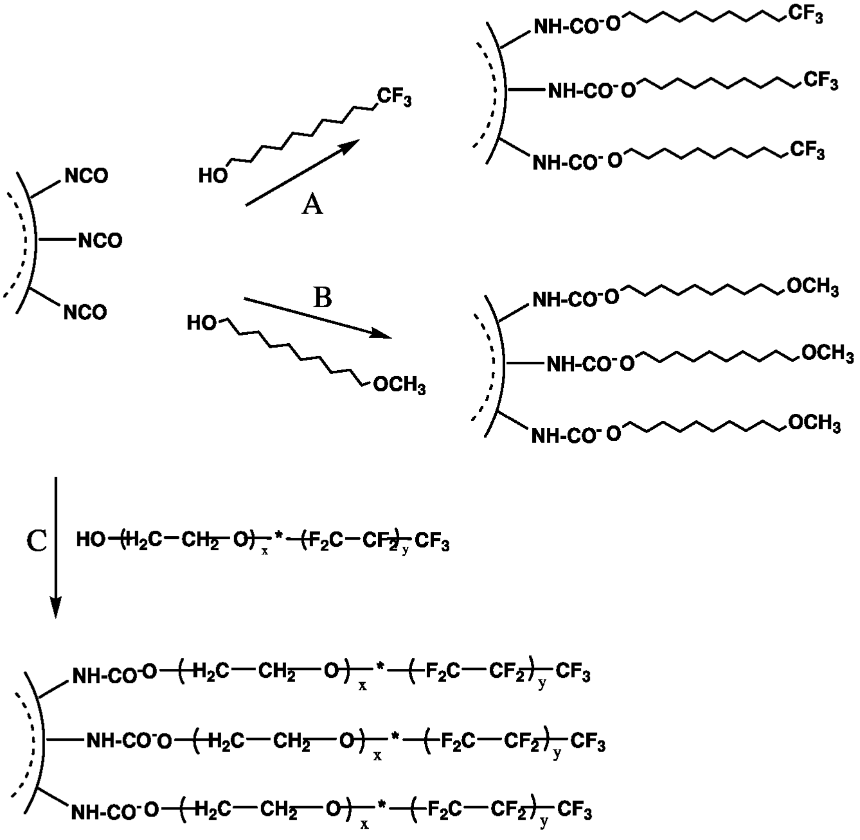
NCO
NCO
NCO
HO
CF3
A
B
HO
OCH3
C
HO-(H2C-CH2-O)x*-(F2C-CF2)y-CF3
NH-CO-O
CF3
OCH3
NH-CO-O-(H2C-CH2-O)x*-(F2C-CF2)y-CF3

Figure 2. Tethering of isocyanate terminated prepolymer with functional moieties A, B and C

surface of roughly 0.5 cm diameter. One slide was used for Contact Angle (CA) determination with each test liquid. The 10 µl of test liquid (water or hexadecane) droplet was allowed to fall on the surface at the rate of 1 µl/ sec within the marked spot. The movie was captured at the rate of 1 frame /sec and contact angle reading was noted after 15 sec (after allowing for the liquid droplet to equilibrate with the surface). The readings obtained at two different spots for the same test liquid were averaged and reported. Once the CA was determined in air, the samples were immersed in Deionized water for 12 hours. The samples were then taken out from water and excess water was wiped off. The contact angles on these surfaces were then instantaneously determined using the same test liquids, at the same spot to minimize the error due to heterogeneity of the surface. After determining the CA of the wet surfaces, these surfaces were dried at ambient temperature for at least 12 hours, and the CA was measured again to study the change in wetting behavior of the surfaces (post drying stage).

Table 1. List of Films

Composition	*Sample Code for DCA and AFM Measurements*	*Sample Code for Bioassays with Green fouling alga Ulva*
Dendritic polyol, diisocyanate, acrylic polyol	Control PU	MRC
Dendritic polyol, diisocyanate, hydrophilic (MPEG derivative) compound, acrylic polyol	MPEG-PU	MRPE
Dendritic polyol, diisocyanate, hydrophobic (PFO derivative) compound, acrylic polyol	PFO-PU	MRF
Dendritic polyol, diisocyanate, amphiphilic compound, acrylic polyol	Zonyl FSO-PU	MRZ100

AFM Roughness Measurements

Sample Preparation

Liquid coatings were applied on the 1 cm x 1 cm phosphated mild steel panels to achieve 25 microns dry film thickness. The samples were cured as described in the experimental section. For AFM imaging, the edges of the samples were sealed using marine epoxy to avoid permeation of water during immersion in water. The samples were first fixed firmly to the AFM mounting disk using ethyl cyanoacrylate adhesive.

Procedure

This procedure was essentially published previously but is included here for completeness (*36*, *37*). The samples were imaged using a Digital Instruments Multimode Atomic Force Microscope with a NanoScope 3a controller and an E-scanner (X-Y scanning limit of 15um and a Z limit of 2um) in the tapping mode. Both height and phase were captured at an image size of 5um x 5um. Each sample was thus imaged under three different conditions:

1. Pre scan: samples were imaged dry without any treatment other than mounting.
2. Wet: Samples were imaged in DI water after soaking in DI water for at least 12 hours, not more than 24 hours.

3. Post scan: samples were again imaged after drying for at least 12 hours

Two sets of images were captured for each sample under each of the conditions. Each captured image was flattened using a binomial flattening algorithm (a best-fit second degree polynomial is subtracted from each scan line). This allows for correction of error in the image introduced by hysteresis in the piezoelectric scanner. Roughness data was then calculated from each of the flattened images and an average of the roughness data was also calculated. In the present study, we considered Root Mean Square (RMS) roughness, average of height deviations taken from the mean data plot.

Results and Discussion

Design and Synthesis of Smart Polyurethane Surfaces

The synthesis of IPDI based prepolymer and its functionalization with different active compounds were carried out using the guidelines for the optimal conditions for similar reactions reported in the literature (*37*, *49*). The formation of intermediate and final products were confirmed by the % NCO contents of the products and that this reaction was monitored by FT-IR spectroscopy using disappearance of absorption peak corresponding to -OH group (~3400 cm^{-1}).

One of the critical requirements in designing such *smart* surfaces is to have a very flexible polymer backbone that facilitates ‘switching’ of tethered moieties, in response to external stimuli (*38*). The polyurethane networks were built using dendritic polyol, isophorone diisocyanate (IPDI), hydroxyl functional acrylic polyol, and different functional moieties (fig. 1a and 2). For functionalization of prepolymer (as described in fig. 2), dendritic polymers substituted by hydroxyl groups are particularly suitable. These dendritic polymers are of polyester type consisting of a multifunctional core, from which branches extend to give highly branched inherent structure with a large number of terminal hydroxyl groups. The core consists of a specific polyalcohol. The hyperbranced structure is generally built from 2, 2-dimethylol propionic acid (Bis-MPA) (*48*). We used Boltorn H2004, commercially available certified dendritic polyol from Perstorp Specialty Chemicals (Sweden) (*48*), which is reported to have 6 terminal hydroxyl groups, hydroxyl value: 105-125 mg KOH/g, acid value: 7 (max.) mg KOH/g., average molecular weight (Mw): 3200 g/mol, T_g: -35°C, viscosity: 15 Pa.s at 23°C (*48*). The generic structure of Boltorn dendritic polyol (*48*) is shown in fig. 1b. The Dendritic polyol serves as soft segment and also provides sites for tethering amphiphilic moieties. We believe, such a structure would provide the necessary backbone flexibility and hence facilitates orientation (‘switching’) of the tethered structures. Also, it has been reported that small amounts (5 wt. %) of an amphiphilic moiety is sufficient to give amphiphilic character to their surfaces with unaltered bulk properties (*45*, *50*).

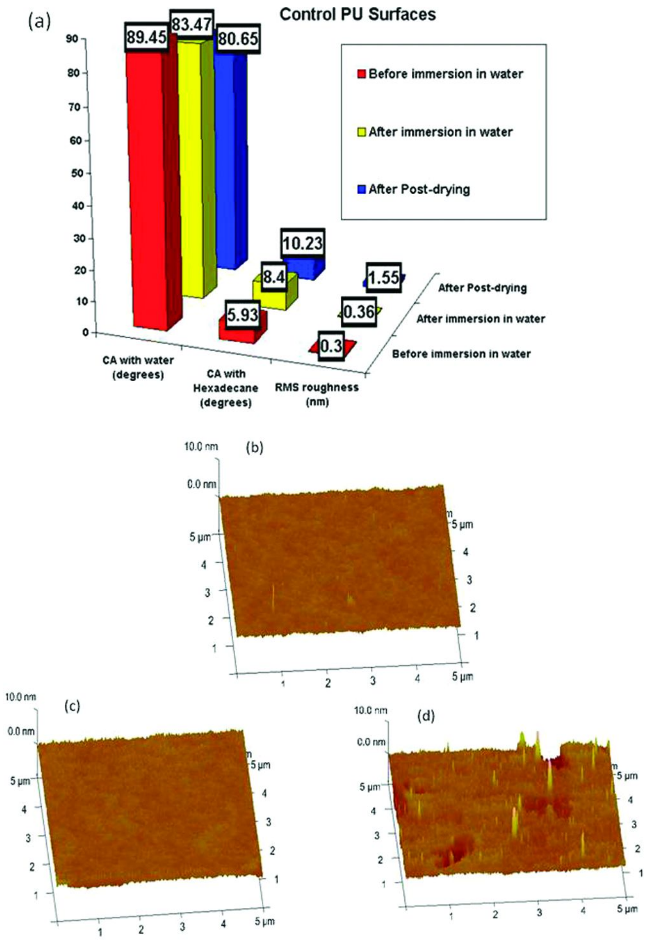

Figure 3. a: Control PU surfaces CA & RMS roughness, b: AFM image before water immersion, c: AFM image after water immersion, and d: AFM image for post-drying

Corroboration of DCA and AFM Analysis Results

The DCA results, in conjunction with the AFM analysis of the smart polyurethane coatings with different surface modifications gave meaningful information about their wetting behavior and surface topography in different contact environments. The analysis gave promising results, building a strong foundation for our current and future efforts to develop a potential amphiphilic marine coating that can combat diverse adhesion mechanisms of the marine organisms. Here, we explained the water and hexadecane wetting behavior of smart polyurethane coatings by taking RMS surface roughness into account. The standard deviation in all contact angle experiments is ± 2°-3°.

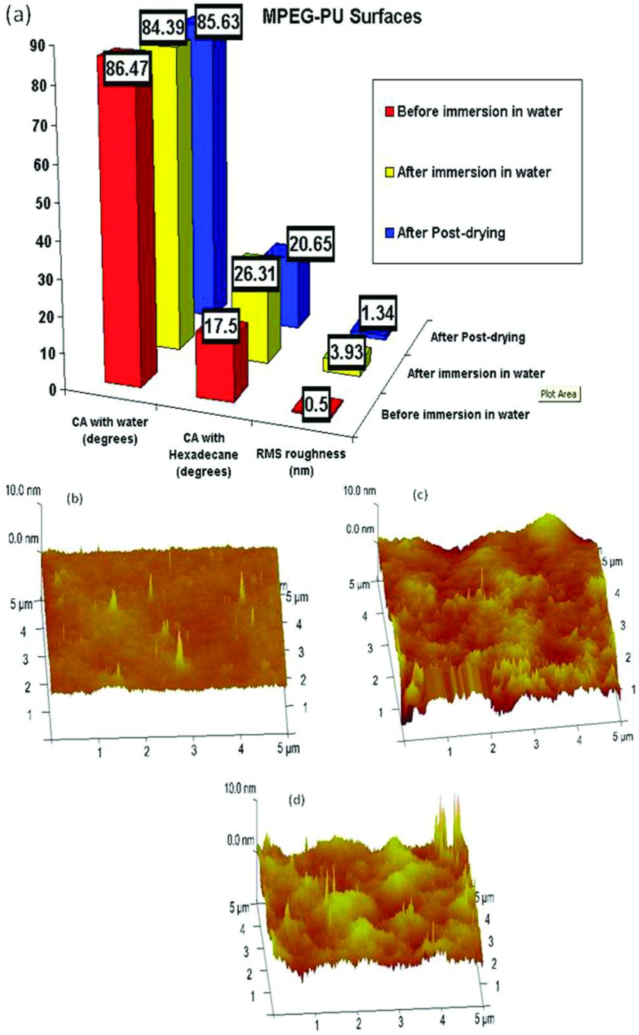

Figure 4. a: MPEG-PU surfaces CA & RMS roughness, b: AFM image before water immersion, c: AFM image after water immersion, and d: AFM image for post-drying

Control PU Surfaces

Figure 3a shows graphical representation of roughness data, contact angle results with water and hexadecane in three different conditions – before water immersion, immediately after water immersion, and post-drying. The control Polyurethane samples are smooth and do not undergo any noticeable change in surface topography after immersion in water. The CA with water and hexadecane and surface roughness remains nearly constant indicating no surface reorganization. Post-drying samples shows increased roughness indicating some ordered orientation in air.

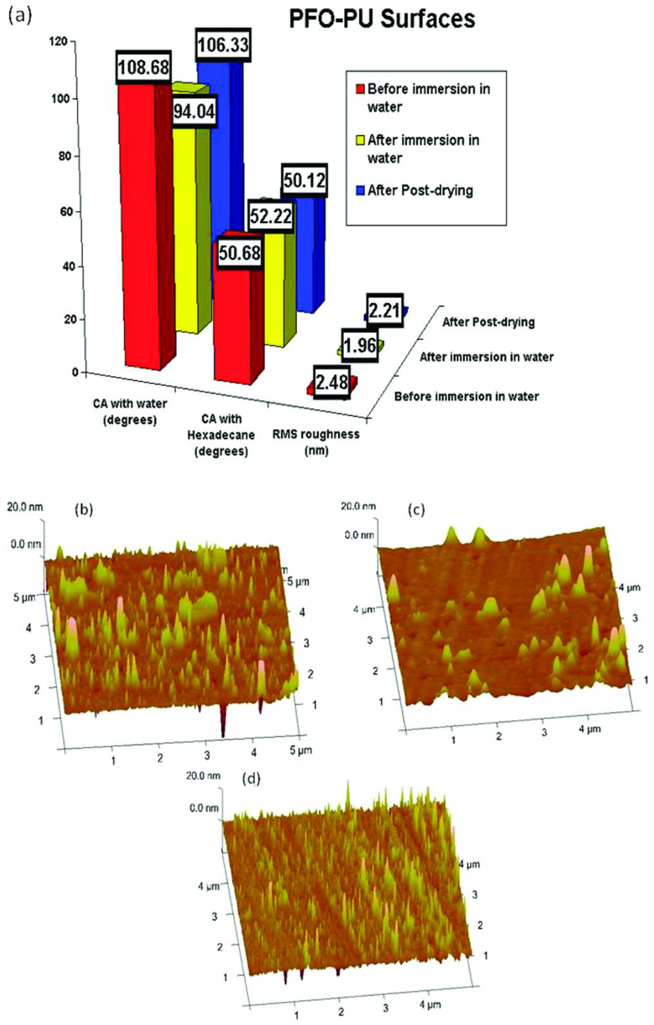

Figure 5. a: PFO-PU surfaces CA & RMS roughness, b: AFM image before water immersion, c: AFM image after water immersion, and d: AFM image for post-drying

Hydrophilic Surfaces Containing MPEG

Figure 4a shows results for hydrophilic surfaces under different conditions. Hydrophilic surfaces containing MPEG shows no difference in water CA after immersion in water and is comparable to control. But higher CA with Hexadecane compared to control PU is indicative of the fact that surface chemical composition of hydrophilic surfaces is different than that of the control since Hexadecane is non-polar. The increase in surface roughness when immersed in water, from 0.5 nm to 3.93 nm is believed to be the result of the perpendicular orientation of MPEG chains (see fig. 4c). We attribute higher CA for these surfaces despite the increase in surface free energy (due to the migration of polar groups at surface) to the surface roughness, which is known to reduce the effective contact area and hence higher CA. For post-drying samples, the surface roughness decreases probably due to the collapse of straightened MPEG chains in the hydrophobic air environment.

Hydrophobic Surfaces Containing PFO

Figure 5a shows results of hydrophobic surfaces in different environment. The surface topography (Fig. 5b) and roughness results (Fig. 5a) indicate the orientation of hydrophobic PFO chains in air. When these surfaces are immersed in water (Fig. 5c) the hydrophobic PFO chains bend towards the hydrophobic PU-surface or cluster together thereby decreasing the RMS roughness. Thus, drop in water CA after immersion in water can be attributed entirely to the decrease in surface roughness. After post-drying (Fig, 5c), the hydrophobic PFO chains again reorient perpendicular to the surface in more organized fashion thereby increasing surface roughness and decreasing surface energy.

Amphiphilic Surfaces Containing Zonyl FSO-100 Surfactant

Results of surface analysis of amphiphilic surfaces under different conditions are shown in Figure 6. Fig. 6a and the AFM images in Fig. 6 (b-d) show an interesting behavior of the surfaces containing amphiphilic moieties. These surfaces, like hydrophobic surfaces, become smoother when exposed to water. Decrease in water CA shows that surfaces become less hydrophobic in water (than when in air) which can be due to the orientation of the hydrphobes (perfluoro groups) of the amphiphilic moiety towards PU surface. This is thought to result in the greater exposure of the hydrophiles (PEO groups) at the surface. Observed increase in Hexadecane CA here is comparable to that for hydrophilic surfaces. For post-drying samples, the surface topography changes drastically and it becomes more hydrophobic which, possibly can be due to significant increase in surface roughness and more uniform reorientation of amphiphilic chains.

Overall, both hydrophobic and amphiphilic polyurethane surfaces are found to become somewhat hydrophilic when immersed in water, while in the former this behavior is associated with surface topography (decrease in surface roughness), in the later, it is due to the orientation of hydrophilic moieties at the surface. We characterize such dynamic behavior of amphiphilic surfaces as *"smart"* - because of their capability to respond to the external environment, in a predictable manner.

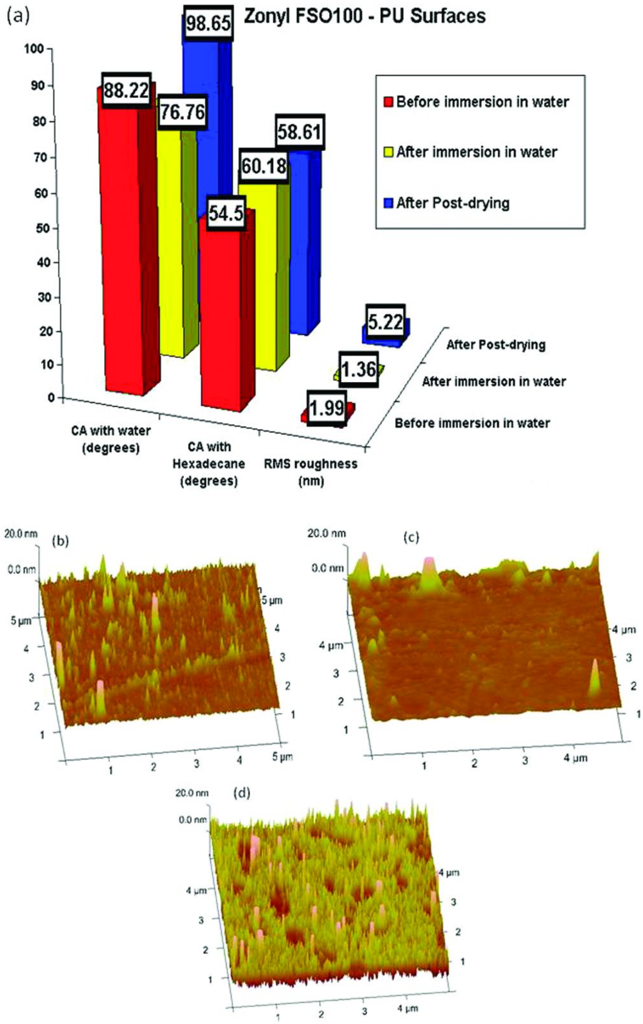

Figure 6. a: Zonyl-FSO PU surfaces CA & RMS roughness, b: AFM image before water immersion, c: AFM image after water immersion, and d: AFM image for post-drying

Conclusion

We report a novel design strategy to fabricate polymeric surfaces with hydrophilic, hydrophobic and amphiphilic characters. Their dynamic surface characteristics are primarily governed by chemical composition and surface topography of the films. The study of dynamic characteristics of such surfaces provides fundamental understanding of the mechanism underlying their dynamic surface behavior, under different external environments.

We characterized these polymeric surfaces for wetting and roughness behavior using DCA and SPM. Our results clearly showed that the control PU surfaces showed no noticeable change in surface topography after immersion in water and post-drying clearly indicating no surface reorientation or reorganization. The surfaces modified using MPEG (hydrophilic surfaces) showed no difference in water CA when immersed in water, however showed increase in roughness. This clearly indicated perpendicular orientation of MPEG chains in water due to migration of polar groups at the surface in water. For post-drying samples the decrease in roughness clearly showed collapse of MPEG chains in air (hydrophobic) environment. The PU surfaces modified using PFO (hydrophobic) surfaces showed increased roughness in air due to orientation of the PFO chains. In water, the drop in contact angle and decreased surface roughness showed that the hydrophobic chains oriented away from the surface. Upon post-drying the chains again re-oriented themselves showing increased roughness. The polyurethane surfaces with amphiphilic moieties showed combination of hydrophobic and hydrophilic behavior when in air and in water respectively. In water, the amphiphilic surfaces showed similar increase in contact angle to the hydrophilic surfaces and when in air (post-drying) showed similar surface topography to the hydrophobic surfaces. . We characterize such dynamic behavior of amphiphilic surfaces as *"smart"* - because of their capability to respond to the external environment, in a predictable manner. Their hydrophilic nature in hydrophilic environment and hydrophobic nature in hydrophobic environment open up enormous opportunities for potential application of such "*smart"* coatings in the arena of foul-release coatings, drug delivery, and hygienic coatings, to name a few.

Acknowledgments

The authors greatly appreciate support from Office of Naval Research (ONR) [Grant # N00014-04-1-0763 to VM]. The authors would especially like to thank Rene Crombez (Research Associate, Surface Science Center at Eastern Michigan University) for his help with AFM analysis, and Chirag Patel (Graduate Student) for assistance in synthetic experimental set-ups.

References

1. Anderson, C.; Atlar, M.; Callow, M.; Candries, M.; Milne, A.; Townsin, R. L. The development of Foul-release coatings for seagoing vessels. *Journal of Marine Design and Operations* **2003**, *B4*, 11–23.
2. Kiil, S.; Yebra, D. M.; Dam-Johansen, K. Antifouling technology- past, present and future steps towards efficient and environmentally friendly antifouling coatings. *Prog. Org. Coatings* **2004**, *50*, 75–104.
3. Nartensoon, L. Marine Biofouling: a sticky problem or gluing in seawater. *BioScience-Explained* **2005**, *2* (2), 1–9.
4. Schultz, M. P. Effects of Coating Roughness and Biofouling on Ship Resistance and Powering. *Biofouling* **2007**, *23*, 331–341.

5. Jelic-Mrcelic, G.; Sliskovic, M.; Antolic, B. Biofouling communities on test panels coated with TBT and TBT-free copper-based antifouling paints. *Biofouling* **2006**, *22*, 293–302.
6. Evans, S. M.; Leksono, T.; Mc Kinnell, P. D. Tributyltin Pollution: A Diminishing Problem Following Legislation Limiting the Use of TBT-Based Anti-fouling Paints. *Marine Pollut. Bull.* **1995**, *30*, 14–21.
7. Callow, M.; Callow, J. Marine Biofouling: a sticky problem. *Biologist* **2002**, *49*, 1–5.
8. Gudipati, C. S.; Finlay, J. A.; Callow, J. A.; Callow, M. E.; Wooley, K. L. The Antifouling and Fouling-Release Perfomance of Hyperbranched Fluoropolymer (HBFP)-Poly(ethyleneglycol) (PEG) Composite Coatings Evaluated by Adsorption of Biomacromolecules and the Green Fouling Alga Ulva. *Langmuir* **2005**, *21* (7), 3044–3053.
9. Sweeney, A.; Sanudo-Wilhelmy, S. A. Dissolved metal contamination in the East River–Long Island sound system: potential biological effects. *Marine Pollut. Bull.* **2004**, *48*, 663–670.
10. Adkins, J.; Mera, A.; Roe-Short, M. A.; Pawlikowski, G. T.; Brady, R. F. Novel non-toxic coatings designed to resist marine fouling. *Prog. Org. Coat.* **1996**, *29*, 1–5.
11. Anastasiadis, S. H.; Restos, H.; Pispas, S.; Hadjichristidis, N. Smart polymer surfaces. *Macromolecules* **2003**, *36* (6), 1994–1999.
12. Chaudhury, M. K.; Thanawala, S. K. Surface modification of silicone Elastomer using per fluorinated ether. *Langmuir* **2000**, *16*, 1256–1260.
13. Chaudhury, M. K.; Vaidya, A. Synthesis and surface properties of environmentally responsive segmented polyurethanes. *J. Colloid Interface Sci.* **2002**, *249*, 235–245.
14. Cunliffe, D.; Smart, C. A.; Alexander, C.; Vulfson, E. N. Bacterial adhesion at synthetic surfaces. *Appl. Environ. Microbiol.* **1999**, *65* (11), 4995–5002.
15. Genzer, J. A.; Efimenko, K. Recent Developments in Superhydrophobic Surfaces and Their Relevance to Marine Fouling: A Review. *Biofouling* **2006**, *22*, 339–360.
16. Gilcreest, V. P.; Carroll, W. M.; Rochev, Y. A.; Blute, I.; Dawson, K. A.; Gorelov, A. V. Thermoresponsive Poly(N- isopropylacrylamide) Copolymers: Contact Angles and Surface Energies of Polymer Films. *Langmuir* **2004**, *20*, 10138–10145.
17. Halabieh, R.; Mermut, O.; Barrett, C. Using light to control physical properties of polymers and surfaces with azobenzene chromophores. *Pure Appl. Chem.* **2004**, *76*, 1445–1465.
18. Houbenov, N.; Minko, S.; Stamm, M. Mixed Polyelectrolyte Brush from Oppositely Charged Polymers for Switching of Surface Charge and Composition in Aqueous Environment. *Macromolecules* **2003**, *36*, 5897–5901.
19. Jin, L.; Young, M. J.; Lee, W. K.; Park, D. K.; Young, K. H. Platelet adhesion onto segmented polyurethane surfaces modified by PEO- and sulfonated PEO-containing block copolymer additives. *J. Biomed. Mater. Res.* **1998**, *40*, 314–323.

20. Kohl, J. G.; Singer, I. L. Pull-off behavior of epoxy bonded to silicone duplex coating. *Prog. Org. Coat.* **1999**, *36*, 15–20.
21. Leonid, I.; Nikolay, H.; Sidorenko, A.; Manfred Stamm, M. Inverse and Reversible Switching Gradient Surfaces from Mixed Polyelectrolyte Brushes. *Langmuir* **2004**, *20*, 9916–9919.
22. Lundberg, D. J.; Brown, R. G.; Glass, J. E.; Eley, R. R. Synthesis, Characterization, and Solution Rheology of Model Hydrophobically-Modified, Water-Soluble Ethoxylated Urethanes. *Langmuir* **1994**, *10*, 3027–3034.
23. Minko, S.; Usov, D.; Goreshnik, E.; Stamm, M. Environment-Adopting Surfaces with Reversibly Switchable Morphology. *Macromol. Rapid Commun.* **2001**, *22*, 206–211.
24. Ober, C. K.; Youngblood, J. P.; Hexemer, A.; Callow, M. E. Coatings based on side chain ether linked poly (ethylene glycol) and fluorocarbon polymers for the control of marine Biofouling. *Biofouling* **2003**, *19*, 91–98.
25. Roosjen, A.; Vries, J.; van der Mei, H. C.; Norde, W.; Busscher, H. J. Stability and Effectiveness against Bacterial Adhesion of Poly(ethylene oxide) Coatings in Biological fluids. *J. Biomed. Mater. Res., Part B: Appl. Biomater.* **2005**, *73B*, 347–354.
26. Schumacher, J. F.; Aldred, N.; Callow, M. E.; Finlay, J. A.; Callow, J. A.; Clare, A. S.; Brennan, A. B. Species-specific engineered antifouling topographies: correlations between the settlement of algal zoospores and barnacle cyprids. *Biofouling* **2007**, *23*, 307–317.
27. Schumacher, J. F.; Carman, M. L.; Estes, T. G.; Feinberg, A. W.; Wilson, L. H.; Callow, M. E.; Callow, J. A.; Finlay, J. A.; Brennan, A. B. Engineered antifouling microtopographies – effect of feature size, geometry, and roughness on settlement of zoospores of the green alga Ulva. *Biofouling* **2006**, *23*, 55–62.
28. Taolei, S.; Guojie, W.; Lin, F.; Liu, B.; Ma, Y.; Lei, J.; Zhu, D. Reversible Switching between Superhydrophilicity and Superhydrophobicity. *Angew. Chem., Int. Ed.* **2004**, *43*, 357–360.
29. Wang, Y.; Zheng, J.; Brittain, W. J.; Cheng, S. Switchable Thin-Film Surface Prepared via a Simple Grafting-To Method Using a Polystyrene-b-Poly(2-vinylpyridine) Copolymer. *J. Polym. Sci., Part A: Polym. Chem.* **2006**, *44*, 5608–5617.
30. Yong, P.; Jing, M. Electric Field Induced Switching Behaviors of Monolayer-Modified Silicon Surfaces: Surface Designs and Molecular Dynamics Simulations. *J. Am. Chem. Soc.* **2005**, *127*, 6802–6813.
31. Zhiguang, G.; Feng, Z.; Jingcheng, H.; Weimin, L. Stable Biomimetic Super-hydrophobic Engineering Materials. *J. Am. Chem. Soc.* **2005**, *127*, 15670–15671.
32. Katsikogianni, M.; Missirlis, Y. F. Concise review of Mechanisms of Bacterial Adhesion to Biomaterials and of Techniques Used in Estimating Bacteria-Material Interactions. *Eur. Cells Mater.* **2004**, *8*, 37–57.
33. Yuehuei, H.; Friedman, R. J. Concise review of Mechanisms of Bacterial Adhesion to Biomaterial Surfaces. *J. Biomed. Mater. Res. (Applied Biomaterials)* **1998**, *43*, 338–348.

34. Cassé, F.; Stafslien, S. J.; Bahr, J. A.; Daniels, J.; Finlay, J. A.; Callow, J. A.; Callow, M. E. Combinatorial materials research applied to the development of new surfaces coatings V. Application of a spinning water-jet for the semi-high throughput assessment of the attachment strength of marine fouling algae. *Biofouling* **2007**, *23*, 121–130.
35. Callow, J. A.; Callow, M. E. The Ulva spore adhesive system. In *Biological Adhesives*; Smith, A. M., Callow, J. A. E., Eds.; Springer-Verlag: Berlin, Heidleberg, 2006; pp 63−78.
36. Goel, A.; Joshi, R. G.; Mannari, V. Intelligent Polymeric Surfaces Through Molecular Self-assembly. *J. Coat. Technol. Res.* **2009**, *6* (1), 123–133.
37. Joshi, R. G.; Goel, A.; Mannari, V. M.; Finlay, J. A.; Callow, M. E.; Callow, J. A. Evaluating Fouling-Resistance and Fouling-Release Performance of Smart Polyurethane Surfaces: An Outlook for Efficient and Environmentally Benign Marine Coatings. *J. Appl. Polym. Sci.* **2009**, *114*, 3693–3703.
38. Koberstein, J. T. Molecular Design of Functional Polymer Surfaces. *J. Polym. Sci., Part B: Polym. Phys.* **2004**, *42*, 2942–2956.
39. Brady, R. F. J. Properties which influence marine fouling resistance in polymers containing silicone and fluorine. *Prog. Org. Coat.* **1999**, *35*, 31–35.
40. Majumdar, P.; Lee, E.; Patel, N.; Ward, K.; Stafslien, S. J.; Daniels, J.; Boudjouk, P.; Callow, M. E.; Callow, J. A.; Thompson, S. E. M. Combinatorial materials research applied to the development of new surface coatings IX: An investigation of novel anti-fouling/fouling-release coatings containing quaternary ammonium salt groups. *Biofouling* **2008**, *24*, 185–200.
41. Martinelli, E.; Agostini, S.; Galli, G.; Chiellini, E.; Glisenti, A.; Pettitt, M. E.; Callow, M. E.; Callow, J. A.; Graf, K.; Bartels, F. W. Nanostructured films of amphiphilic fluorinated block copolymers for fouling release application. *Langmuir* **2008**, *24*, 13138–13147.
42. Krishnan, S.; Ayothi, R.; Hexemer, A.; Finlay, J. A.; Sohn, K. E.; Perry, R.; Ober, C. K.; Kramer, E. J.; Callow, M. E.; Callow, J. A.; Fischer, D. A. Anti-biofouling properties of comb-like block copolymer with amphiphilic side-chains. *Langmuir* **2006**, *22*, 5075–5086.
43. Ekin, A.; Webster, D. C.; Daniels, J. W.; Stafslien, S. J.; Cassé, F.; Callow, J. A.; Callow, M. E. Synthesis, formulation and characterization of siloxane-polyurethane coatings for underwater marine applications using combinatorial high-throughput experimentation. *J. Coat. Technol. Res.* **2007**, *4*, 435–451.
44. Beigbeder, A.; Degee, P.; Conlan, S.; Mutton, R.; Clare, A. S.; Pettitt, M. E.; Callow, M. E.; Callow, J. A.; Dubois, P. Preparation and characterization of silicone based coatings filled with carbon nanotubes and natural sepiolite and their application as antifouling materials. *Biofouling* **2008**, *24*, 291–302.
45. Wouters, M.; Zanten, J. V.; Hujis, F.; Vereijken, T. Surface rearrangement of tailored polyurethane-based coatings. *JCT Res.* **2005**, *1* (6), 435–443.
46. Statz, A.; Finlay, J.; Dalsin, J.; Callow, M.; Calllow, J. A.; Messersmith, P. B. Algal antifouling and fouling-release properties of metal surfaces coated with a polymer inspired by marine mussels. *Biofouling* **2006**, *22*, 391–399.

47. Brady, R. F. J., Assessing the Future of Coating Work: Composition and Performance of Fouling Release Coatings. *PCE*; Genoa, Italy, 2000; pp 7−15.
48. *Boltorn® Technical Information Brochure - "Boltorn® H2004"*; Perstorp Specialty Chemicals AB: Sweden, 2009; p 7.
49. Götz, H.; Beginn, U.; Bartelink, C. F.; Grünbauer, H. J. M.; Möller, M. Preparation of Isophorone Diisocyanate terminated star polyethers. *Macromol. Mater. Eng.* **2002**, *287* (4), 223–230.
50. Kober, M.; Wesslén, B. Surface properties of a segmented polyurethane containing amphiphilic polymers as additives. *J. Appl. Polym. Sci.* **1994**, *54* (6), 793–803.

Downloaded by OHIO STATE UNIV LIBRARIES on June 22, 2012 | http://pubs.acs.org
Publication Date (Web): November 10, 2010 | doi: 10.1021/bk-2010-1050.ch008

Chapter 8

Surface Characterization of Binary Graft Copolymers (PP-g-DMAEMA)-g-NIPAAm and (PP-g-4VP)-g-NIPAAm by Using SEM and AFM

H. I. Meléndez-Ortiz,[1] E. Bucio,[1,*] T. Isoshima,[2] and M. Hara[2]

[1]Departamento de Química de Radiaciones y Radioquímica, Instituto de Ciencias Nucleares, Universidad Nacional Autónoma de México, Circuito Exterior, Ciudad Universitaria, 04510 México D.F.
[2]Flucto-Order Functions Research Team, RIKEN-HYU Collaboration Research Center, RIKEN Advanced Science Institute Wako Lab : 2-1 Hirosawa, Wako, Saitama 351-0198, Japan Seoul Lab : Fusion Technology Center 5F, Hanyang University, Seoul 133-791, Korea
***ebucio@nucleares.unam.mx**

In the present work, thermal-pH dependent binary graft copolymers (PP-g-DMAEMA)-g-NIPAAm and (PP-g-4VP)-g-NIPAAm at different degree of grafting (DG, %) of N-isopropylacrylamide (NIPAAm) (DG of 30, 90, 200 and 400 %) were characterized by scanning electron microscope (SEM), atomic force microscope (AFM) and swelling studies. SEM images showed formation of NIPAAm crosslinked network at degree of grafting greater than 90 %. Also, when the graft reaction time is increased, NIPAAm crosslinking is increased. Higher NIPAAm crosslinking resulted in lower swelling ratio. In addition, the AFM technique was used in order to obtain information on the changes in surface topography and roughness under different degree of grafting. Both binary graft copolymers presented larger surface roughness than their precursor single graft copolymers, though surface roughness decreased at degree of grafting higher than 200 %. These results of SEM, AFM and swelling studies suggest that both binary graft copolymers, (PP-g-DMAEMA)-g-NIPAAm and (PP-g-4VP)-g-NIPAAm, have potential in biopplications and

In Smart Coatings III; Baghdachi, J., et al.;
ACS Symposium Series; American Chemical Society: Washington, DC, 2010.

that a relatively lower degree of grafting around 90 % is the optimal value.

Introduction

The selection of materials for applications in the biomedical and biotechnological fields, including controlled drug delivery agents, tissue engineering, gene transfection and tunable and stimuli-responsive polymeric sensors; requires proper considerations of their mechanical, physical and biological properties. Only rarely does one find a single natural material with good mechanical properties (no degradation and reusable materials) which shows responsiveness towards pH and temperature. For this reason, synthetic materials which can provide these properties are desirable for a number of applications such as, adhesion, friction, wetting, swelling, drug delivery systems, bio-interaction ability (cell adhesion and/or proliferation) and susceptibility to chemical reactions (*1–6*).

The development of these suitable synthetic materials by modifying the physical and chemical properties of common bulk polymers through grafting processes has been proved to be successful in producing materials with surface and bulk properties which are promising for bio-applications in fields such as health and environmental science (*7–11*). Particularly, surface modification of polymers is an important area for both applied (*12–14*) and basic research (*15*, *16*). The surface modification of polymer materials by graft copolymerization is an efficient method of imparting a number of functional properties to these materials (*17–20*).

Poly[2-(dimethylamino) ethyl methacrylate] (PDMAEMA) and poly(4-vinylpyridine) (P4VP) are pH-dependent polymers (critical pH point around 7.6 and 5 in pure water respectively which are retained even when they are copolymerized with other co-monomers) (*21–24*). Poly(N-isopropylacrylamide) (PNIPAAm) is a well-known thermal-dependent water-soluble polymers with a lower critical solution temperature (LCST) at 32-35 °C (*25–27*). Below the LCST the PNIPAAm chains have an extended coil shape and are hydrophilic while above the LCST the PNIPAAm chains are hydrophobic and have a globular shape. In fact, the hydrophobic, globular shaped PNIPAAm chains actively interact with biocompounds such as cells and proteins, or other hydrophobic compounds, while the hydrophilic hydrated and flexible PNIPAAm chains do not interact with them. There are several literature reports concerning applications for PNIPAAm-grafted surfaces which involve the hydrophilic-hydrophobic transition of PNIPAAm. An example of such applications is the growth and detachment of adherent cells (*3*, *5*, *27*). Once grafted with PNIPAAm a polymer surface such as PP may be used for growth and detachment of adherent cells. After being cultured on the surface below LCST, adherent cells can be transferred without damage by raising temperature above LCST.

Downloaded by OHIO STATE UNIV LIBRARIES on June 22, 2012 | http://pubs.acs.org
Publication Date (Web): November 10, 2010 | doi: 10.1021/bk-2010-1050.ch008

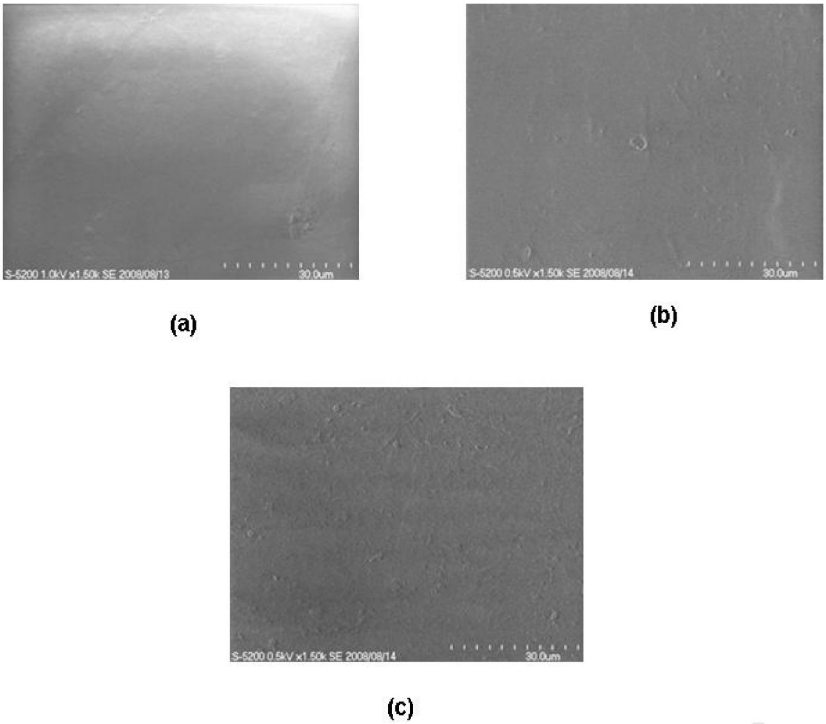
S-5200 1.0kV x1.50k SE 2008/08/13
30.0um
S-5200 0.5kV x1.50k SE 2008/08/14
30.0um
S-5200 0.5kV x1.50k SE 2008/08/14
30.0um

(a) **(b)** **(c)**

Figure 1. SEM micrographs of: (a) PP, (b) PP-g-DMAEMA and (c) PP-g-4VP.

We are aiming to develop new copolymers with combined features described above as novel biocompatible materials. In previous works, thermal-pH sensitive binary graft copolymers (PP-g-DMAEMA)-g-NIPAAm and (PP-g-4VP)-g-NIPAAm were synthesized by using gamma irradiation (*28*, *29*). However, before starting the studies of bioapplications, it is necessary to know morphology and topography of these materials, because combination of these results will reveal the actual surface behavior as the response to the applied external stimuli (pH and/or temperature change). In this work, (PP-g-DMAEMA)-g-NIPAAm and (PP-g-4VP)-g-NIPAAm films were analyzed using scanning electron microscope (SEM) and atomic force microscope (AFM) techniques in order to determine the influence of the content of grafted NIPAAm on the morphology, topography and surface roughness. SEM studies can show information on the morphology of graft copolymer systems (*17*, *19*, *30*, *31*). AFM and its application to the investigation of polymer structure and surface properties have continued to grow in recent years (*32–34*), including the investigation of topography, biodegradation, biomolecules interactions, and the mechanical properties of polymers (*4*, *8*, *11*, *35–37*). This information is very important because it can be used not only to predict the potential of these materials for bioapplications but also for optimizing the grafting process by using gamma irradiation.

Downloaded by OHIO STATE UNIV LIBRARIES on June 22, 2012 | http://pubs.acs.org
Publication Date (Web): November 10, 2010 | doi: 10.1021/bk-2010-1050.ch008

Downloaded by OHIO STATE UNIV LIBRARIES on June 22, 2012 | http://pubs.acs.org
Publication Date (Web): November 10, 2010 | doi: 10.1021/bk-2010-1050.ch008

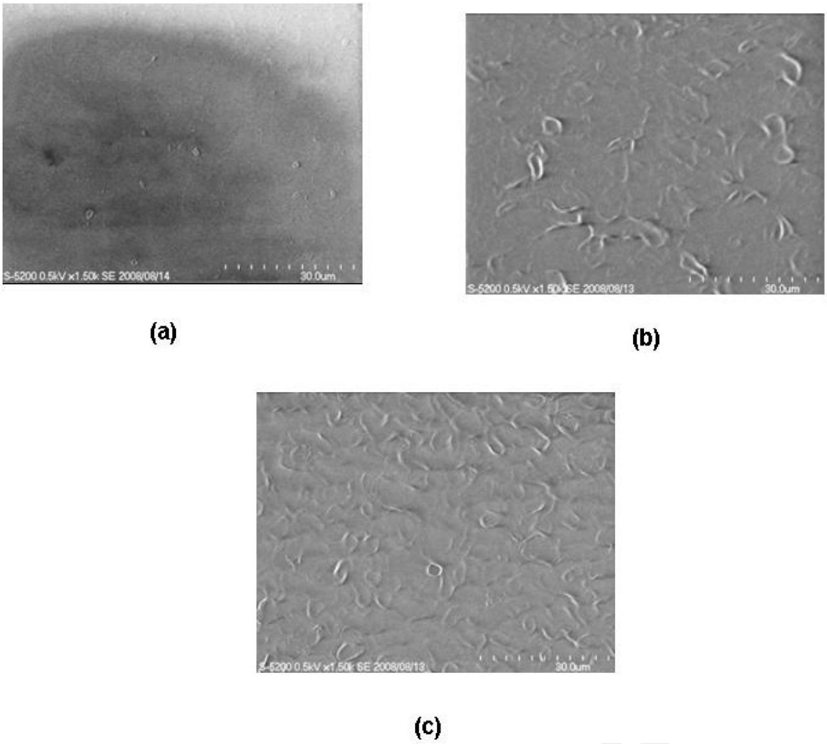
S-5200 0.5kV x1.50k SE 2008/08/14 30.0um
S-5200 0.5kV x1.50k SE 2008/08/13 30.0um
S-5200 0.5kV x1.50k SE 2008/08/13 30.0um

(a) (b) (c)

Figure 2. SEM micrographs of (PP-g-DMAEMA)-g-NIPAAm at different degree of grafting of NIPAAm: (a) 30 %, (b) 90 % and (c) 200 %.

Experimental Section

Materials

Isotactic polypropylene (PP) films (60 μm thickness and 1 x 5 cm in size, from PEMEX-Mexico), were first washed with methanol for 24 h and then dried under reduced pressure. 2-(Dimethylamino) ethyl methacrylate (DMAEMA), 4-vinylpyridine (4VP) and *N*-isopropylacrylamide (NIPAAm) were purchased from Aldrich Co. DMAEMA and 4VP were distilled under reduced pressure. NIPAAm was recrystallized from a solution of hexane / toluene (1/1, v/v).

PP-g-DMAEMA and PP-g-4VP with degree of grafting (DG) around 100 and 80 % respectively were synthesized as follows. A preweighed PP film was placed in a glass ampoule in a solution of DMAEMA/toluene (1/1, v/v) or 4VP/ dichlorometane (1/1, v/v). Each ampoule was degassed by repeated freeze-thaw cycles, sealed and then irradiated with a ^{60}Co γ source (Gamma Beam 651 PT, Nordion International) at an irradiation dose of 10 kGy, and a dose rate of 12 kGyh^{-1}. Grafted films of PP-g-DMAEMA and PP-g-4VP were extracted with a toluene and dimethylformamide (DMF) respectively, and then dried under reduced pressure. The DG was calculated from the following equation:

$$DG = [(Wg - Wo) / Wo]\, 100 \quad (1)$$

Downloaded by OHIO STATE UNIV LIBRARIES on June 22, 2012 | http://pubs.acs.org
Publication Date (Web): November 10, 2010 | doi: 10.1021/bk-2010-1050.ch008

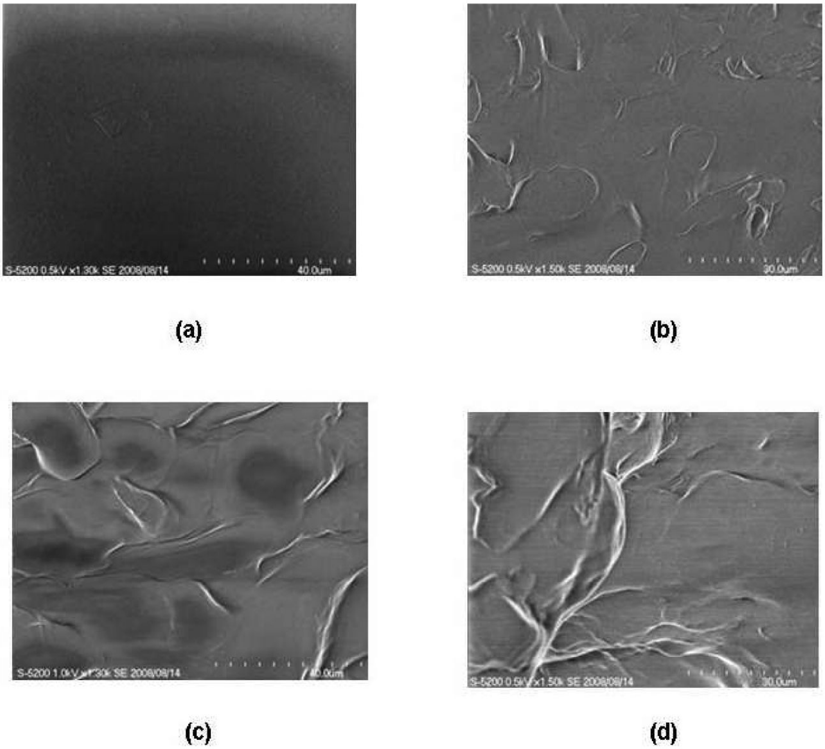
S-5200 0.5kV x1.30k SE 2008/08/14
40.0um
(a)
S-5200 0.5kV x1.50k SE 2008/08/14
30.0um
(b)
S-5200 1.0kV x1.30k SE 2008/08/14
40.0um
(c)
S-5200 0.5kV x1.50k SE 2008/08/14
30.0um
(d)

Figure 3. SEM micrographs for (PP-g-4VP)-g-NIPAAm at different degree of grafting of NIPAAm: (a) 30 %, (b) 90 %, (c) 200 % and (d) 340 %.

Where: Wg and Wo are the weights of the grafted and initial films, respectively.

Binary graft copolymers (PP-g-DMAEMA)-g-NIPAAm and (PP-g-4VP)-g-NIPAAm were prepared according to the methodology used in previous reports by our research team (*28*, *29*). In order to obtain binary graft copolymers, (PP-g-DMAEMA)-g-NIPAAm and (PP-g-4VP)-g-NIPAAm, with degrees of grafting around 30, 90, 200 and 400 % of NIPAAm the following procedure was carried out: preweighed films of PP-g-DMAEMA or PP-g-4VP were placed individually in glass ampoules and were then irradiated in the presence of air at an irradiation dose between 20 and 100 kGy, at a dose rate of 12 $kGyh^{-1}$. A NIPAAm aqueous solution (1 M) was added to each and then each solution was deaerated by bubbling argon during 15 min and sealed. They were then heated in a water bath at various reaction times at 60 °C. After heating, the grafted films were washed with water for 24 h to extract the residual monomer and PNIPAAm formed. The degree of grafting was calculated by using Eq. 1.

SEM Observation

The morphology of the graft copolymers was studied by using a SEM (S-5200, Hitachi) operating at an accelerating voltage of 0.5 kV and magnification of 1500x.

Downloaded by OHIO STATE UNIV LIBRARIES on June 22, 2012 | http://pubs.acs.org
Publication Date (Web): November 10, 2010 | doi: 10.1021/bk-2010-1050.ch008

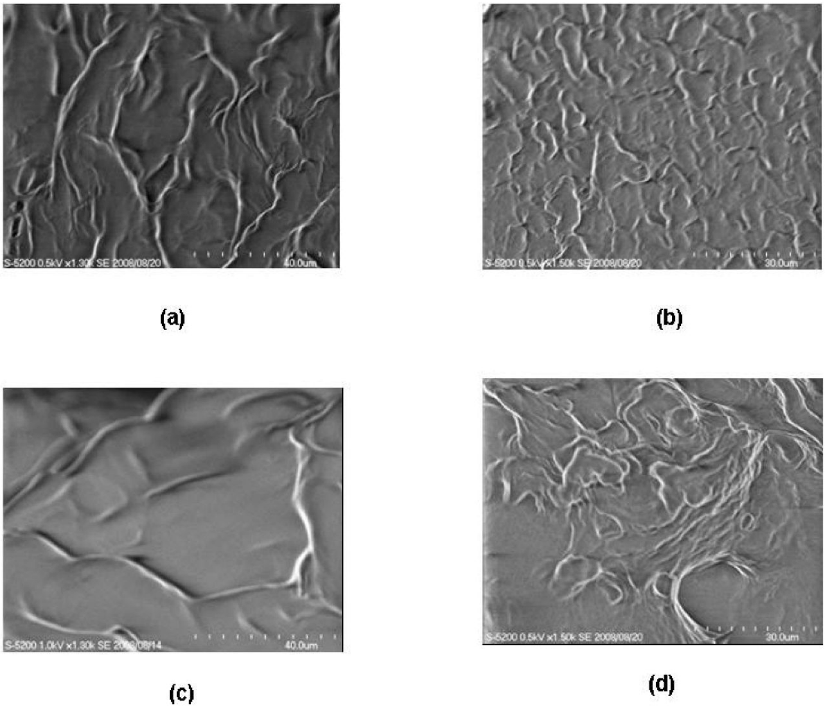
S-5200 0.5kV x1.30k SE 2008/08/20
40.0um
S-5200 0.5kV x1.50k SE 2008/08/20
30.0um
S-5200 1.0kV x1.30k SE 2008/08/14
40.0um
S-5200 0.5kV x1.50k SE 2008/08/20
30.0um

(a) (b) (c) (d)

Figure 4. SEM micrographs of binary graft copolymers at different reaction time for (PP-g-DMAEMA)-g-NIPAAm: (a) 5, and (b) 13 h; (PP-g-4VP)-g-NIPAAm: (c) 5, and (d) 10 h.

Before observation, graft copolymers samples were washed with ethanol and then dried during 48 h at 80 °C.

Swelling Studies

For determination of the equilibrium swelling ratio (SR, %), the graft copolymers (previously dried during 12 h at 100 °C) were immersed into distilled water for various periods of time until constant weight was attained (fully hydrated sample). To determinate the equilibrium swelling ratio gravimetrically, the surface of the copolymer film was wiped with filter paper in order to remove the free water. The swollen samples were then weighed. The equilibrium swelling ratio was determined by the following equation:

$$SR = [(Ws - Wd) / Wd]\ 100 \qquad (2)$$

Where: Ws and Wd are weights of the swollen and dried sample respectively.

The equilibrium swelling ratio (hydration capacity) of binary graft copolymers was determined as a function of the percentage of PNIPAAm grafted (DG, %) as well as PNIPAAm grafting reaction time at room temperature.

Downloaded by OHIO STATE UNIV LIBRARIES on June 22, 2012 | http://pubs.acs.org
Publication Date (Web): November 10, 2010 | doi: 10.1021/bk-2010-1050.ch008

AFM Measurement

The surface topography and roughness of graft copolymers were analyzed by using an AFM (SPI 3800 N Probe Station, Seiko Instruments Inc.). Imaging in air was performed in tapping mode. Cantilever with a nominal spring constant of 15 N/m and a drive frequency of approximately 130 kHz was used. In order to compare the topography of graft copolymers, the imagining parameters were kept constant for all samples. Before measurement, graft copolymer samples were previously washed with ethanol and then they were placed between two pieces of glass and dried during 48 h at 80 °C.

Results and Discussion

SEM Observation

SEM images for virgin PP, PP-g-DMAEMA and PP-g-4VP are shown in Fig. 1. The initial PP film has a flat and smooth surface (Fig. 1a). After the grafting of DMAEMA (DG 75 %) and 4VP (DG 100 %) onto the PP films, morphologic changes were not observed on the surfaces (Fig. 1b and 1c respectively), suggesting that the first graft (DG < 100 %) did not have any significant effect on the morphology of PP.

Figure 2 shows SEM images for (PP-g-DMAEMA)-g-NIPAAm at different DG of NIPAAm. The image for the binary graft copolymer with DG of 30 % (Fig. 2a) did not exhibit significant changes on the surface compared with those images for PP film and PP-g-DMAEMA (Fig. 1a and Fig. 1b respectively). However, when the DG is increased to 90%, it can be seen that NIPAAm networks start to form on the surface (Fig. 2b). The formation of these crosslinking networks is clearer at a DG of 200 % (Fig. 2c). This could be explained as follows: because of the higher degree of grafting, the denser layer of NIPAAm on the surface of the films, and resulted in the higher degree of crosslinking between grafted NIPAAm chains. A similar behavior was observed for (PP-g-4VP)-g-NIPAAm films with different DG of NIPAAm (Fig. 3). At low DG, the surface of the films did not show any significant morphological change (Figs. 3a and 3b), whereas at DG of 90 % and higher NIPAAm crosslinking networks on surface were observed (Figs. 3c and 3d).

In addition, the influence of the grafting reaction time of NIPAAm on morphology of the films was studied at a constant DG of 200 %. Figure 4 shows SEM images for both (PP-g-DMAEMA)-g-NIPAAm and (PP-g-4VP)-g-NIPAAm binary graft copolymers at different grafting reaction time. The images show that, when the grafting reaction time of NIPAAm is increased (Fig. 4b and 4d), the crosslinking between grafted PNIPAAm chains is increased. This suggests that, at long reaction times, NIPAAm grafted chains have more opportunity to form covalent bonds between them forming a denser layer of NIPAAm on the surface films.

Downloaded by OHIO STATE UNIV LIBRARIES on June 22, 2012 | http://pubs.acs.org
Publication Date (Web): November 10, 2010 | doi: 10.1021/bk-2010-1050.ch008

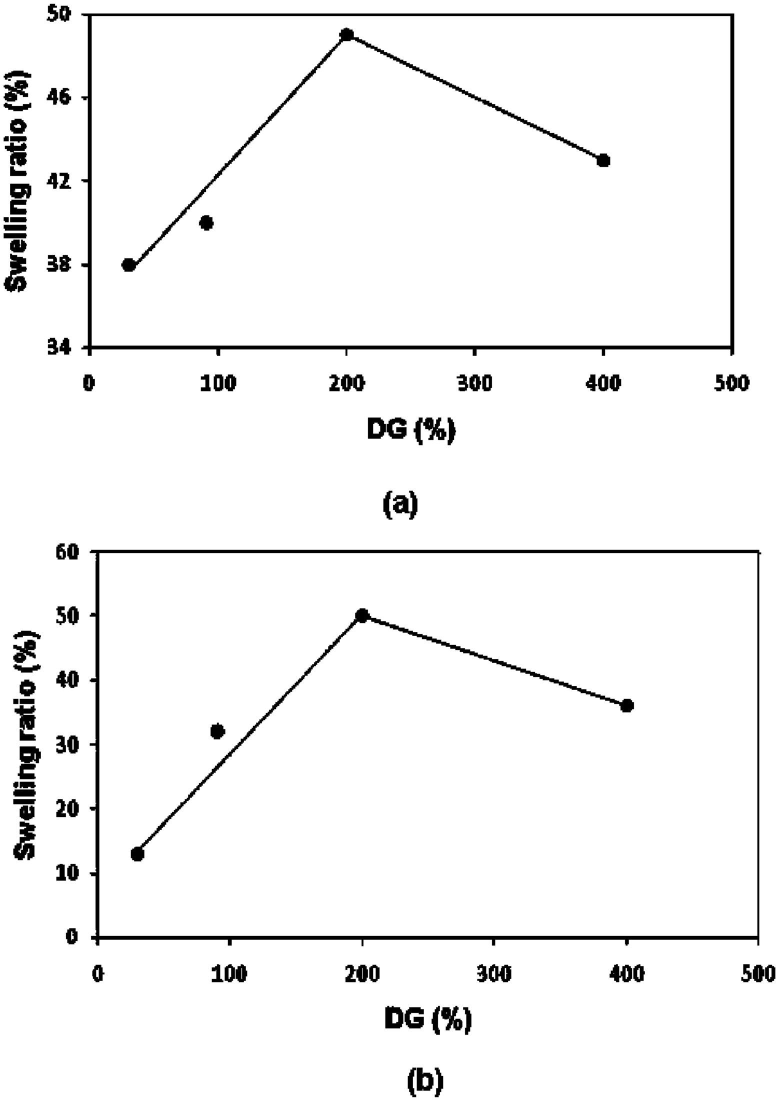

(a)

(b)

Figure 5. Swelling ratio (SR, %) at different degree of grafting of NIPAAm for: (PP-g-DMAEMA)-g-NIPAAm (Fig. 5a) and (PP-g-4VP)-g-NIPAAm (Fig. 5b).

Swelling Studies

Swelling studies in water were carried out for binary graft copolymers in order to obtain the dependence of hydration capacity with respect to DG and grafting reaction time of NIPAAm. Figure 5 illustrates swelling behavior for both (PP-g-DMAEMA)-g-NIPAAm (Fig. 5a) and (PP-g-4VP)-g-NIPAAm (Fig. 5b). It is shown that swelling ratio (hydration capacity) increased when DG is increased to 200 %. In spite of the fact that the maximum swelling ratio was observed for samples with DG of 200 %, the higher swelling ratio does not correlate to the

Downloaded by OHIO STATE UNIV LIBRARIES on June 22, 2012 | http://pubs.acs.org
Publication Date (Web): November 10, 2010 | doi: 10.1021/bk-2010-1050.ch008

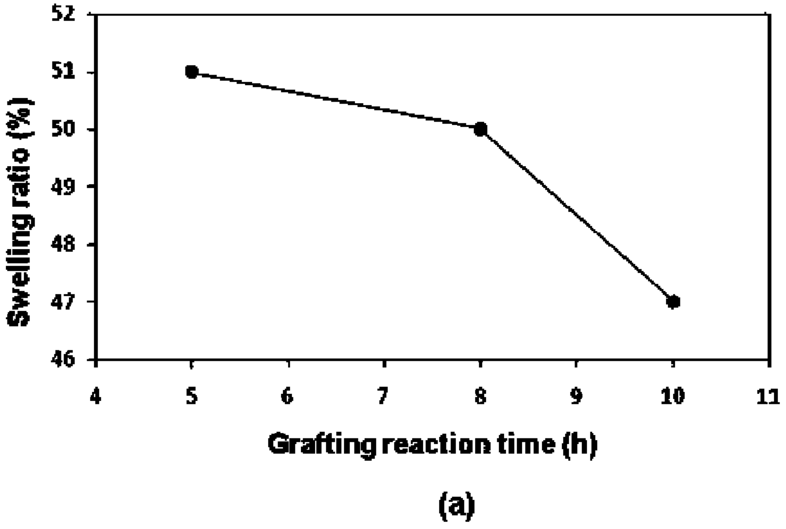

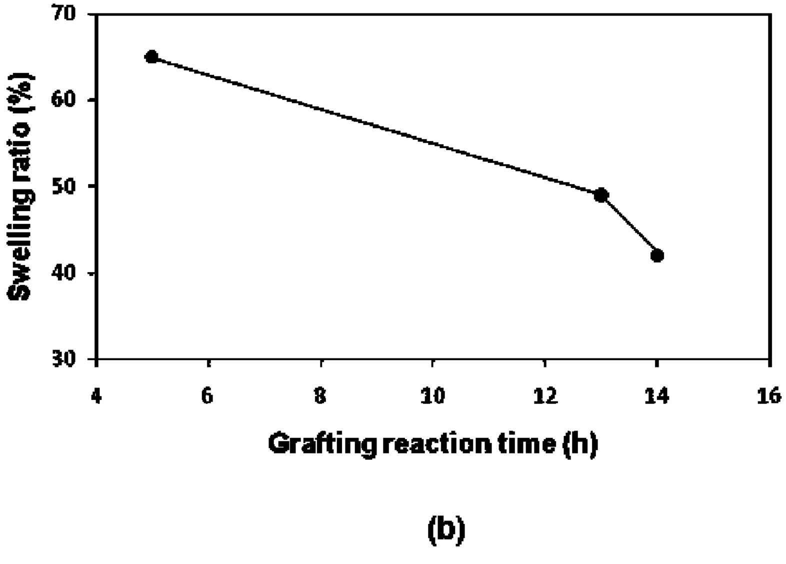

Figure 6. Swelling ratio (SR, %) at different NIPAAm graft reaction time for: (PP-g-DMAEMA)-g-NIPAAm films (Fig. 6a) and (PP-g-4VP)-g-NIPAAm (Fig. 6b).

higher DG. In fact, samples with DG greater than 200 % exhibited a lower swelling ratio.

In addition, swelling studies were carried out for binary graft copolymer samples at different grafting reaction times of NIPAAm (Fig. 6). The relevant graphs for (PP-g-DMAEMA)-g-NIPAAm (Fig. 6a) and (PP-g-4VP)-g-NIPAAm (Fig. 6b) showed that swelling ratio decreased when NIPAAm was grafted at long reaction times.

Downloaded by OHIO STATE UNIV LIBRARIES on June 22, 2012 | http://pubs.acs.org
Publication Date (Web): November 10, 2010 | doi: 10.1021/bk-2010-1050.ch008

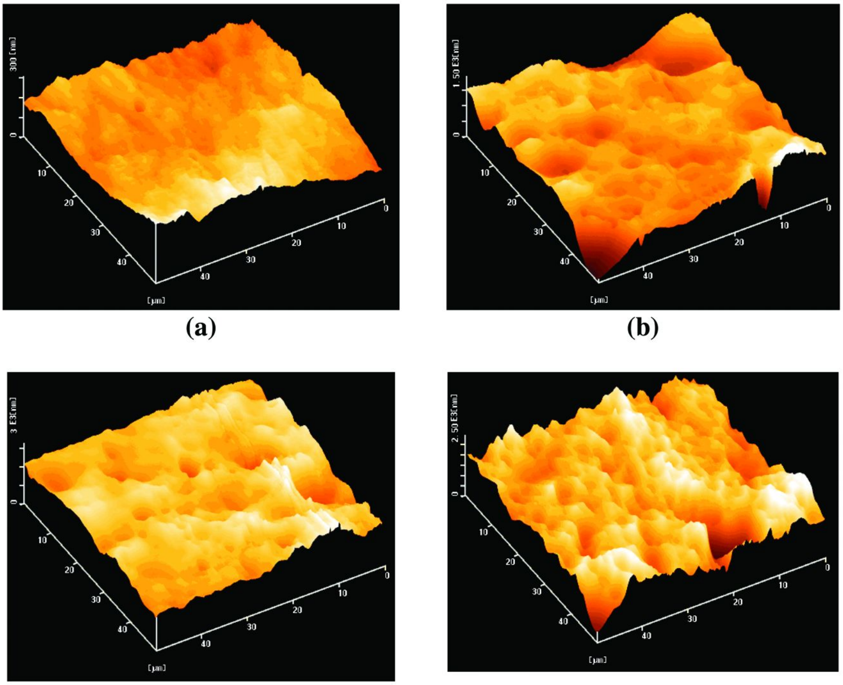

(a) **(b)**

(c) **(d)**

Figure 7. AFM images for: (a) PP, (b) PP-g-DMAEMA and (PP-g-DMAEMA)-g-NIPAAm with different degree of grafting of NIPAAm: (c) 30 %, (d) 90 %.

Combined with the SEM results, these results suggest that the higher cross-linking network in NIPAAm results in a decrease of swelling ratio.

AFM Measurement

AFM was used to examine the effect of the DG on surface topography. Images for PP, PP-g-DMAEMA and (PP-g-DMAEMA)-g-NIPAAm are shown in Figure 7. The PP film presented a flat and smooth surface (Fig. 7a) while PP-g-DMAEMA (Fig. 7b) and (PP-g-DMAEMA)-g-NIPAAm with a DG of 30 and 90 % (Fig. 7c and 7d respectively) presented a rough surface which increased as the DG was raised. However, at higher DG values (up 200 %), the estimated roughness (peaks-valleys) decreased significantly. This could be explained by the assumption that at higher DG, the surface is entirely covered by a homogeneous dense layer of PNIPAAm which would be in agreement with previous SEM and swelling studies in this work.

The root mean square (RMS) values of surface roughness obtained from the AFM analysis for PP and graft copolymers are shown in Table 1. Surface roughness of binary graft copolymers is larger than that of corresponding single graft copolymers, as expected from SEM results. Surface roughness of (PP-g-DMAEMA)-g-NIPAAm increased with DG, showing the highest value at

Downloaded by OHIO STATE UNIV LIBRARIES on June 22, 2012 | http://pubs.acs.org
Publication Date (Web): November 10, 2010 | doi: 10.1021/bk-2010-1050.ch008

Table 1. RMS surface roughness values obtained from the AFM analysis of PP virgin and grafted copolymers

Sample	*DG (%) of NIPAAm*	*RMS (nm)*
PP	---	32
PP-g-DMAEMA	---	218
(PP-g-DMAEMA)-g-NIPAAm	30	289
(PP-g-DMAEMA)-g-NIPAAm	90	397
(PP-g-DMAEMA)-g-NIPAAm	200	656
(PP-g-DMAEMA)-g-NIPAAm	440	397
PP-g-4VP	---	71
(PP-g-4VP)-g-NIPAAm	30	936
(PP-g-4VP)-g-NIPAAm	90	935
(PP-g-4VP)-g-NIPAAm	200	306
(PP-g-4VP)-g-NIPAAm	340	71

a DG of 200%. At higher DG, surface roughness decreased. Surface roughness of (PP-g-4VP)-g-NIPAAm was high at lower DG values of 30 and 90 % and then decreased drastically by a factor of 3 and 9 at DG values of 200 and 340 % respectively.

Large surface roughness of the binary graft copolymers (PP-g-DMAEMA)-g-NIPAAm and (PP-g-4VP)-g-NIPAAm at relatively lower DG around 90 % makes them very interesting and promising for bioapplications. Such "peaks and valleys" structure provides a surface adequate for bio-interaction for cell adhesion and/or proliferation, and physical or chemical immobilization of biomolecules such as enzymes, drugs, bacteria, and proteins (*8*, *11*, *19*, *34*).

Conclusions

Binary graft copolymer films, (PP-g-DMAEMA)-g-NIPAAm and (PP-g-4VP)-g-NIPAAm, were characterized by SEM and AFM. SEM results indicated that, at DG values greater than 90 %, a NIPAAm crosslinked layer was formed on the surface of the films. Also, SEM images exhibited that formation of crosslinking NIPAAm networks resulted from longer grafting reaction time. Swelling studies demonstrated not only that wettability increased when PNIPAAm is grafted, but also it is dependent of DG as well as grafting reaction time. AFM studies showed that the grafting process increases surface roughness of the films. According to SEM, AFM and swelling studies, both of the thermal-pH responsive binary graft copolymers, (PP-g-DMAEMA)-g-NIPAAm and (PP-g-4VP)-g-NIPAAm are indicated to have potential for multiple bioapplications such as drug delivery systems and immobilization of biomolecules, and the potential would be optimized at DG values of NIPAAm less than 90 % at short grafting and reaction time.

Downloaded by OHIO STATE UNIV LIBRARIES on June 22, 2012 | http://pubs.acs.org
Publication Date (Web): November 10, 2010 | doi: 10.1021/bk-2010-1050.ch008

Acknowledgments

The authors are grateful to H. Ito from RIKEN Advanced Science Institute for her help on the SEM and AFM studies. This work was financially supported by DGAPA-UNAM (Grant No. IN200208).

References

1. Okano, T.; Kikuchi, A.; Sakurai, Y.; Takei, Y.; Ogata, N. Temperature-responsive poly(N-isopropylacrylamide) as a modulator for alteration of hydrophilic/hydrophobic surface properties to control activation/inactivation of platelets. *J. Controlled Release* **1995**, *36*, 125–133.
2. Meyer, D. E.; Shin, B. C.; Kung, G. A.; Dewhirst, M. W.; Chilkoti, A. Drug targeting using thermally responsive polymers and local hyperthermia. *J. Controlled Release* **2001**, *74* (1), 213–224.
3. Chen, G. P.; Imanishi, Y.; Ito, Y. Effect of protein and cell behaviour on pattern-grafted thermoresponsive polymer. *J. Biomed. Mater. Res.* **1998**, *42* (1), 38–44.
4. Yamamoto, M.; Utsumi, M.; Kushida, A.; Konno, C.; Kikuchi, A.; Okano, T. Thermo-responsive culture dishes allow the intact harvest of multilayered keratinocyte sheets without dispase by reducing temperature. *Tissue Eng.* **2001**, *7* (4), 473–480.
5. Takezawa, T.; Mori, Y.; Yoshizato, K. Cell culture on a thermo-responsive polymer surface. *Biotechnology* **1990**, *8* (1), 854–856.
6. Lowman, A.; Morishita, M.; Kajita, M.; Nagai, T.; Peppas, N. Oral delivery of insulin using pH- responsive complexation gels. *J. Pharm. Sci.* **1999**, *88* (9), 933–937.
7. Pan, Y. V.; Wesley, R. A.; Luginbuhi, R.; Denton, D. D.; Ratner, B. D. Plasma polymerized N-isopropylacrylamide: Synthesis and characterization of a smart thermally responsive coating. *Biomacromolecules* **2001**, *2* (1), 32–36.
8. Cunliffe, D.; de las Heras, C.; Peters, V.; Smith, J. R.; Alexander, C. Thermoresponsive surface-grafted poly(N-isopropylacrylamide) copolymers: effect of phase transitions on protein and bacterial attachment. *Langmuir* **2003**, *19* (7), 2888–2899.
9. Curti, P. S.; de Moura, M. R.; Veiga, W.; Radovanovic, E.; Rubira, A. F.; Muniz, E. C. Characterization of PNIPAAm photografted on PET and PS surfaces. *Appl. Surf. Sci.* **2005**, *245* (1), 223–233.
10. Farquet, P.; Padeste, C.; Solak, H. H.; Gürsel, S. A.; Scherer, G. G.; Wokaun, A. EUV lithographic radiation grafting of thermo-responsive hydrogel nanostructures. *Nucl. Instrum. Methods B* **2007**, *265*, 187–192.
11. Stadler, V.; Kirmse, R.; Beyer, M.; Breitling, F.; Ludwig, T.; Bischoff, F. R. PEGMA/MMA copolymer graftings: generation, protein resistance, and a hydrophobic domain. *Langmuir* **2008**, *24* (15), 8151–8157.
12. Garbassi, F.; Morra, M.; Ochiello, E. *Polymer surfaces: from physics to technology*; Wiley: Chichester, U.K., 1994.

Downloaded by OHIO STATE UNIV LIBRARIES on June 22, 2012 | http://pubs.acs.org
Publication Date (Web): November 10, 2010 | doi: 10.1021/bk-2010-1050.ch008

13. Chan, C. M. *Polymer surface modification and characterization*; Hanser: Munich, 1994.
14. Harmer, M. A. Photomodification of surfaces using heterocyclic azides. *Langmuir* **1991**, *7* (10), 2010–2012.
15. Holmes-Farley, S. R.; Bain, C. D.; Whitesides, G. M. Wetting of functionalized polyethylene film having ionizable organic acids and bases at the polymer-water interface: relations between functional group polarity, extent of ionization, and contact angle with water. *Langmuir* **1988**, *4* (4), 921–937.
16. Ferguson, G. S.; Whitesides, G. M. In *Modern approaches to wettability: theory and applications*; Schrader, M. E., Loeb, G. I., Eds.; Plenum Press: New York, 1992; pp 143−177.
17. Adem, E.; Avalos-Borja, M.; Bucio, E.; Burillo, G.; Castillon, F. F.; Cota, L. Surface characterization of binary grafing of AAc/NIPAAm onto poly(tetrafluoroethylene) (PTFE). *Nucl. Instrum. Methods B* **2005**, *234*, 471–476.
18. El-Hag, A.; Said, A. Radiation synthesis of interpolymer polyelectrolyte complex and its application as a carrier for colon-specific drug delivery system. *Biomaterials* **2005**, *26*, 2733–2739.
19. Ferreira, L. M.; Falcao, A. N.; Gil, M. H. Elemental and topographic characterization of LDPE based copolymeric films obtained by gamma irradiation. *Nucl. Instrum. Methods B* **2007**, *265*, 193–197.
20. Ruiz, J. C.; Alvarez-Lorenzo, C.; Taboada, P.; Burillo, G.; Bucio, E.; De Prijck, K.; Nelis, H. J.; Coenye, T.; Concheiro, A. Polypropylene grafted with smart polymers (PNIPAAm/PAAc) for loading and controlled release of vancomycin. *Eur. J. Pharm. Biopharm.* **2008**, *70* (2), 467–477.
21. Liu, S.; Weaver, J. V. M.; Tang, Y.; Billingham, N. C.; Armes, S. P.; Tribe, K. Synthesis of shell cross-linked micelles with pH-responsive cores using ABC triblock copolymers. *Macromolecules* **2002**, *35* (16), 6121–6131.
22. Sen, M.; Sari, M. Radiation synthesis and characterization of poly(N,Ndimethylaminoethyl methacrylate-co-N-vinyl 2-pyrrolidone) hydrogels. *Eur. Polym. J.* **2005**, *41* (6), 1304–1314.
23. Xu, Y.; Shi, L.; Ma, R.; Zhang, W.; An, Y.; Zhu, X. Synthesis and micellization of thermo-and pH-responsive block copolymer of poly(N-isopropylacrylamide)-block-poly(4-vinylpyridine). *Polymer* **2007**, *48* (6), 1711–1717.
24. Özen, K.; Elmas, B.; Özsar, Ö.; Senel, S.; Tuncel, A. Thermoresponsive-fluorescent isopropylacrylamide–vinylpyridine–pyrenemethylacrylamide terpolymer and its complexation behaviour with DNA. *React. Funct. Polym.* **2008**, *68* (2), 623–633.
25. Schmaljohann, D.; Oswald, J.; Jorgensen, B.; Nitschke, M.; Beyerlein, D.; Werner, C. Thermo-responsive PNIPAAm-g-PEG films for controlled cell detachment. *Biomacromolecules* **2003**, *4* (6), 1733–1739.
26. Bergbreiter, D. E.; Case, B. L.; Liu, Y. S.; Caraway, J. W. Poly(N-isopropylacrylamide) soluble polymer supports in catalysis and synthesis. *Macromolecules* **1998**, *31* (18), 6053–6062.

27. Arenas, E.; Bucio, E.; Burillo, G.; López, G. Radiation grafting of N-isopropylacrylamide onto poly(vinyl chloride) tubes by gamma irradiation. *Polym. Bull.* **2007**, *58* (2), 401–409.
28. Meléndez-Ortiz, H. I.; Bucio, E. Radiation synthesis of a thermo-pH responsive binary graft copolymer (PP-g-DMAEMA)-g-NIPAAm by a two step method. *Polym. Bull.* **2008**, *61* (5), 619–629.
29. Meléndez-Ortiz, H. I.; Bucio, E.; Burillo, G. Radiation-grafting of 4-vinylpyridine and N-isopropylacrylamide onto polypropylene to give novel pH and thermo-sensitive films. *Radiat. Phys. Chem.* **2009**, *78* (1), 1–7.
30. Bucio, E.; Burillo, G.; Adem, E.; Coqueret, X. Temperature sensitive behavior of poly(N-isopropylacrylamide) grafted onto electron beam-irradiated poly(propylene). *Macromol. Mater. Eng.* **2005**, *290*, 745–752.
31. Zhai, G.; Kang, E. T.; Neoh, K. G. Poly(2-vinylpyridine)-and poly(4-vinylpyridine)-graft-poly(vinylidene fluoride) copolymers and their pH-sensitive microfiltration membranes. *J. Membr. Sci.* **2003**, *217*, 243–258.
32. Valsesia, A.; Manso-Silvan, M.; Ceccone, G.; Rossi, F. Surface topographic and structural characterization of plasma treated PMAA-PMMA copolymer films. *Surf. Sci.* **2004**, *560*, 121–129.
33. Krivykh, E. S.; Timofeeva, V. A.; Erina, N. A.; Ageeva, T. A.; Solov'eva, A. B.; Titov, V. A. An atomic-force microscopy study of the formation of vinyl and acryl graft polymers on a polypropylene film surface. *Russ. J. Phys. Chem.* **2007**, *81* (1), 91–95.
34. Kurkuri, M. D.; Nussio, M. R.; Deslandes, A.; Voelcker, N. H. Thermosensitive copolymer coatings with enhanced wettability switching. *Langmuir* **2008**, *24* (8), 4238–4244.
35. Campbell, P. A.; Rourke, B. O.; Dawson, P.; Turner, R. J.; Walmsley, D. G.; Spedding, P. L. Watters. *Appl. Phys. A.: Mater* **1998**, *66*, 867–871.
36. Pignataro, B.; Fragala, M. E.; Puglisi, O. AFM and XPS study of ion bombarded poly(methyl methacrylate). *Nucl. Instrum. Methods B* **1997**, *131*, 141–148.
37. Revenko, I.; Tang, Y.; Santerre, J. P. Surface structure of polycarbonate urethanes visualized by atomic force microscopy. *Surf. Sci.* **2001**, *491*, 346–354.

Downloaded by OHIO STATE UNIV LIBRARIES on June 22, 2012 | http://pubs.acs.org
Publication Date (Web): November 10, 2010 | doi: 10.1021/bk-2010-1050.ch008

Downloaded by CORNELL UNIV on June 22, 2012 | http://pubs.acs.org
Publication Date (Web): November 10, 2010 | doi: 10.1021/bk-2010-1050.ch009

Chapter 9

Surface Electrostatic Interactions: Effect of Protein Purification in a Thin Polysaccharide Film Adsorbed on a Solid Support

**Neoli Lucyszyn,[2] Adriana F. Lubambo,[1,2,*] Jorge J. Klein,[3]
Wido H. Schreiner,[1,3] Paulo C. de Camargo,[1]
and Maria R. Sierakowski[2]**

**[1]Departamento de Física, [2]BIOPOL/Departamento de Química, [3]Laboratório de Superfícies e Interfaces/LSI, Universidade Federal do Paraná/UFPR
Centro Politécnico Caixa Postal 19044, 81531-990 Curitiba-PR-Brasil
*af.lubambo@uol.com.br**

Thin films of xyloglucan purified (XGP), or not (XGNP), formed by spin-coating and drop incubation on mica under different pHvalues and with two degrees of residual protein content were investigated by AFM and XPS analysis. AFM images showed different states of aggregation depending on the pH and protein content. The aggregates were spherical-like at all pH values, irrespective of the purification, but under alkaline condition a network of aggregates linked by strands was observed only in XGNP. XPS spectra also showed that XGNP had a thicker layer at pH 5 compared to XGP, which had a lower protein content. Preferential protein adsorption at pH 3 was observed for XGNP, while the opposite was found at pH 12. Finally, at pH 5, the layer was estimated to be 64%

Carbohydrates are among the principal constituents of biological systems. As polysaccharides or oligosaccharides, they are present in plants (cellulose and derivatives), crabs and insects (chitin), animals (glycogen) and others (*1*). Their physico-chemical properties and interaction with proteins make them suitable for biotechnological applications (*2*). Furthermore, polysaccharides possess a high level of compatibility (*1*) with living organisms, making them advantageous

In Smart Coatings III; Baghdachi, J., et al.;
ACS Symposium Series; American Chemical Society: Washington, DC, 2010.

Downloaded by CORNELL UNIV on June 22, 2012 | http://pubs.acs.org
Publication Date (Web): November 10, 2010 | doi: 10.1021/bk-2010-1050.ch009

molecules to incorporate into a composite matrix for biological purposes (*3*). In particular, neutral hydrophilic polysaccharides are desirable coatings to apply on solid-phase diagnostics due to their ability to control the unspecific binding of proteins (*1*).

Many biosensors are built in the form of thin films of multifunctional coatings assembled on solid substrates. Polysaccharides often participate as either recognition elements or as scaffold components due to their stability and rigidity (*2*). However, the presence of the residual contaminants, which are left behind during polysaccharide extraction, may play an essential role in the interaction between the carbohydrates and the solid surface.

Carbohydrate-binding proteins such as lectins, agglutinins or hemagglutinins are natural proteins found as residues even after polysaccharide purification. They are compounds of non-immune origin with differences in molecular structure, biochemical properties and specificity that are able to agglutinate cells or precipitate glycoconjugates without altering their chemical structure (*4*).

Nonetheless, depending on the extraction and purification protocols, some contaminants such as sulfur, phosphorus, fluorine, chlorine found in alginate or carbohydrate-binding proteins generally present in polysaccharides such as xyloglucan, can drastically alter polysaccharide biocompatibility (*5*). In medical applications, like drug or nanoparticle encapsulation, biocompatibility is very important for drug therapy efficiency. The drugs or nanoparticles must be encapsulated in order to not be recognized by the immune system (*6*). Therefore, understanding the role of contaminants such as carbohydrate-binding proteins is crucial to successfully apply polysaccharides as functional coatings or for immobilization. Other consequences of protein purification processes are changes in viscosity and wetting due to the removal of molecules that participate in polymer inter-chain interactions (*5*).

This work investigates the behavior of a thin film of xyloglucan (XG), a polysaccharide extracted from *Guibourtia hymenifolia* seeds, a plant found in northeastern of Brazil,.formed by spin-coating and drop incubation on mica, with three different pH values and two levels of residual protein. The immobilization on mica was investigated by analyzing AFM and XPS results.

Xyloglucans are hemicellulosic polysaccharides that are found in the primary cell walls of non-graminaceous cells (monocotyledons) and in the cotyledon of some dicotyledonous seeds, where they are used for structural functions and as storage polysaccharides (reserves of energy), respectively (*7–9*). It is a neutral, branched, storage polysaccharide. The chemical structure has a cellulose-like backbone composed of β-glucosyl ring units with ribbon-like conformation, where units of xylose and galactose substituents are part of the branches (*8*). This biopolymer, like many other polysaccharides, has potentially important commercial and medical applications in the food industry as a texture modifier and for controlling drug release (*10–12*).

Downloaded by CORNELL UNIV on June 22, 2012 | http://pubs.acs.org
Publication Date (Web): November 10, 2010 | doi: 10.1021/bk-2010-1050.ch009

Experimental

Extraction and Purification of Xyloglucan

The isolation of xyloglucan from *G. hymenifolia* seeds (50 g) collected in Itatiba, São Paulo State, Brazil was performed as described by Lucyszyn et al. (*13*). The non purified XG (XGNP) obtained was filtered through cloth and dried at 25°C.

In order to purify the polysaccharide, it was resolubilized in water at 25°C and filtered under pressure through cellulose acetate membranes with 3.0, 0.8 and 0.22-μm pore diameters (Millipore®). Then, it was precipitated with excess ethanol to give the purified XG fraction (XGP).

Polysaccharide Adsorption Protocols

Polysaccharide solutions of purified xyloglucan (XGP, with 4.5% w/w of protein) and non-purified xyloglucan (XGNP, with 11.9% w/w of protein), at a final concentration of 10 nMol and different pH values were used. Hydrochloric acid (HCl, 0.1N) was used to decrease the pH to 3, and sodium hydroxide (NaOH, 1N) was used to increase the pH to 12. Solutions were prepared and stirred for 24 h.

The depositions of samples were performed in two different ways (see Table 1) on grade V-4 mica muscovite, bought from SPI supplies®. The support was cleaved using scotch tape and immediately used for the adsorption experiments.

In the first procedure, which was performed for both XGP and XGNP, a drop (20 μL) of solution was deposited without rinsing. Samples were allowed to dry at 24°C with humidity at 45% for 24 h.

In the second procedure, spin-coating deposition was used to obtain a homogeneous thin film of polysaccharide suitable for XPS analysis. A 10-μL drop of XGP solution was centrally pipetted onto the rotating substrate and then allowed to dry without rinsing. The same procedure was repeated for the XGNP.

AFM Measurements

AFM imaging was performed using a commercial microscope. Images were taken in the dynamic tapping mode (TM-AFM) with an oxide-sharpened micro-fabricated silicon μ-Masch cantilever, which had a nominal spring constant of 4.7 N/m and a tip radius of curvature measuring less than 10 nm. The scanning rate of the acquisition data was 1 Hz, and 256x256 data points were acquired. Piezoelectric movement was corrected by flattening the image data. The AFM operating point was always adjusted to minimize soft layer deformation. All images were acquired at room temperature (~24°C).

X-ray Photoelectron Spectroscopy (XPS) Measurements

XPS measurements were performed 48 h after XG deposition with an ESCA 3000 V.G. Microtech photoelectron spectrometer using Mg K_α radiation. The spectra were acquired with a 100-eV pass energy and a take-off angle of 45°

Table 1. Procedures adopted for xyloglucan (XG) deposition on mica as a thin film

Sample	*Protocol*	*XG (µL)*	*pH*	*Step 1 Deposition speed (rpm)*	*Step 2 Adsorption time*	*Step 3 Speed (rpm)*	*Step 4 Evaporation time*
1	Drop	20	3	-	24 h	-	24 h
2	Drop	20	5	-	24 h	-	24 h
3	Drop	20	12	-	24 h	-	24 h
4	Spinning	10	3	500	5 min	2000	24 h
5	Spinning	10	5	500	5 min	2000	24 h
6	Spinning	10	12	500	5 min	2000	24 h

Downloaded by CORNELL UNIV on June 22, 2012 | http://pubs.acs.org
Publication Date (Web): November 10, 2010 | doi: 10.1021/bk-2010-1050.ch009

for analysis for all samples. Element concentrations were evaluated from peak areas after Shirley background subtraction. The vacuum in the sample chamber was about 10^{-9} mbar during analysis. Charging effects were corrected using Si 2p (102.7 eV) as a reference for mica (*14*, *15*).

Results and Discussion

Atomic Force Microscopy Analysis

AFM images of XGNP and XGP in dynamic mode are shown in Figures 1 and 2, respectively. XGNP images presented a large number of spherical-like aggregates at all pH values. Furthermore, at alkaline pH, a network of aggregates linked by strands, which is not present in XGP at pH 12, is clearly observed. XGP, as shown in Figure 2 shows a rather compact superficial layer and does not present a significant number of spherical-like aggregates. These facts suggest that proteins, which are present in XGNP, favor the formation of a network of aggregates. An increase of 7.4% in protein amount, in fact, causes noticeable changes in the conformational aggregation of XG on the solid surface, especially for the situation where the solution is at alkaline pH.

X-ray Photoelectron Spectroscopy (XPS) Measurements

The XPS data in Figure 3A shows surface chemical compounds after polysaccharide XGNP adsorption on mica at pH 3, pH 5 and pH 12, using bare mica as a control and the XGP sample at pH 5 for comparison in Figure 3B. Table 2 details the relative elemental surface composition in all situations.

It is common to find organic impurities (C1s, E_b= 284.4-285.6 eV), which are always present in ambient conditions (*14*, *15*), on bare mica. It is shown in Table 2 and Figure 3A that the relative amount of carbon for bare mica is 3.5%. In addition, impurities like sodium in mica are often found replacing Al and K (Na 1s, E_b= 1072.35 eV).

The adsorption of the polysaccharide on the mica surface was detected by the presence of hemiacetal and acetal carbons bonds (O-C-O, E_b=287.8 eV) (*16*),

Downloaded by CORNELL UNIV on June 22, 2012 | http://pubs.acs.org
Publication Date (Web): November 10, 2010 | doi: 10.1021/bk-2010-1050.ch009

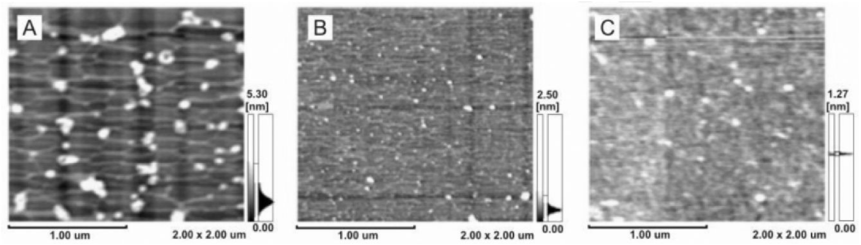

Figure 1. AFM dynamic mode (2.00 x 2.00) µm images of XGNP deposited under different pH values by drop incubation on mica: A - at pH 12; B - at pH 5; C - at pH 3.

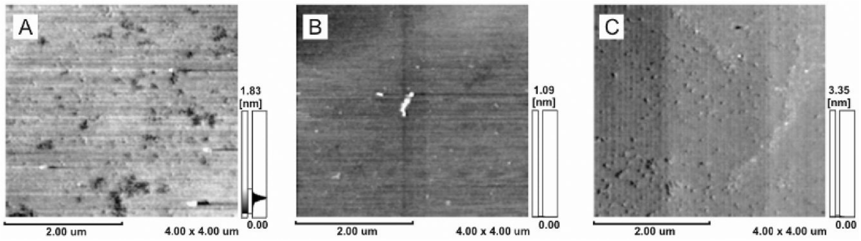

Figure 2. AFM dynamic mode (4.00 x 4.00) µm images of XGP deposited under different pH values by drop incubation on mica: A - at pH 12; B - at pH 5; C - at pH 3.

which are characteristic of the glycosidic linkage present in the chemical structure of the biopolymer. However, XG is a neutral polysaccharide and does not present a carboxylic (O=C-OH, E_b= 289.0 eV) (*16*) or carboxilate (O=C-O^-, E_b= 288.0 eV) (*16*) function in its polymeric structure. Thus, these functions were assigned to the protein content in the sample.

In order to compare the carbon and nitrogen contents of different samples, silicon from mica was taken as a reference, normalizing data to the ratios of carbon/silicon (C/Si) and nitrogen/silicon (N/Si). Silicon was chosen because its content is quite constant for mica substrates. The carbon adsorbed after XGNP deposition on mica was lowest at pH 3 (C/Si=0.58). It attained its highest value at pH 5 (C/Si =1.42) and, finally, decreased again at pH 12 (C/Si =0.64). Furthermore, if we compare the amount of carbon at pH 5 for XGP and XGNP, we see that the carbon ratio XGNP/XGP is doubled when the nominal protein content increases from 4.5% to 11.9%.

The nitrogen (N 1s) photoelectron peak signal revealed the presence of protein because XG does not contain nitrogen in its chemical composition. Results showed that the ratio (N/Si) was highest when XGNP was deposited at pH 3 (N/Si=0.072) and lowest when XGNP was deposited at pH 12 (N/Si=0.039). Nitrogen was not detected in XGP because the atomic content (at.%) expected was below the sensitivity of the spectrometer.

Downloaded by CORNELL UNIV on June 22, 2012 | http://pubs.acs.org
Publication Date (Web): November 10, 2010 | doi: 10.1021/bk-2010-1050.ch009

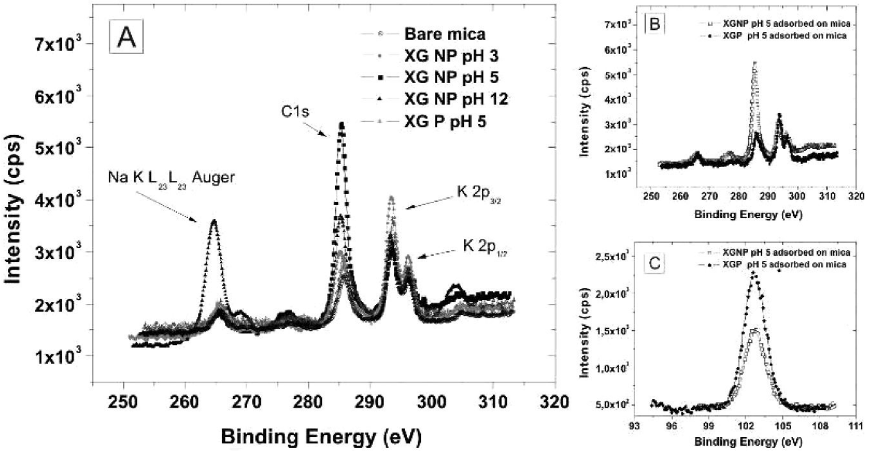

Figure 3. A - XPS of C1s, K 2p $_{3/2}$, K 2p $_{1/2}$ and Na $KL_{23}L_{23}$ Auger spectra obtained for XGNP at different pH values and XGP at pH 5 for comparison; B - Detail of C1s spectra for XGNP and XGP at pH 5; C - Si 2p spectra for XGP and XGNP at pH 5.

Finally, impurities like sulfur, phosphorus, fluorine and chlorine were not detected in the XPS spectra in any situation. See Figure 4 for the XGNP pH12 spectrum as an example.

Thus, XPS results showed that XGNP aggregates were less adsorbed when deposited at pH 3 than at pH 5. XGNP adsorbed more than XGP at pH 5, and protein was adsorbed at pH 3 for XGNP. These results can be understood if we assume that XGP and XGNP adsorption was driven by electrostatic and acid/base interactions, as described below.

Mica muscovite ($KAl_2Si_3AlO_{10}(OH)_{12}$) is a hydrous aluminosilicate with layers of $(Si,Al)_2O_5$ linked to a layer of Al_2OH_2 (*17*). In mica, one fourth of the tetravalent silicon is generally substituted by trivalent aluminum, creating a net negative charge. Normally, this charge imbalance is compensated by potassium ions (*17*). However, during cleavage, the layer is disrupted, exposing K^+ ions (*17–19*). As a consequence, in aqueous solutions, depending on electrolyte concentration (*20–22*), some of these ions dissociate easily, creating a net negative charge on the mica surface as the potassium ions are replaced to some extent by cations like H^+ and Na^+. Regarding the acidity/basicity of the surface of mica, the isoelectric point (iep), which is an indication of the acidity/basicity of hydroxyl groups, is around pH 3-3.5 (*23*).

At pH 5 the mica surface charge was negative, and the protein net charge was positive; therefore, a higher adsorption of XGNP was expected.

At pH 3, the mica surface is positively charged as well as the protein surface. The screening of protein surface charges probably gives rise to the higher N/Si ratio at pH 3 (N/Si=0.072) compared to pH 5 (N/Si=0.063), which was an apparently unexpected XPS result. This screening can be caused by HCl ions present in solution at pH 3 and not at pH 5.

Downloaded by CORNELL UNIV on June 22, 2012 | http://pubs.acs.org
Publication Date (Web): November 10, 2010 | doi: 10.1021/bk-2010-1050.ch009

Table 2. Elemental relative surface composition (at.%) detected by XPS analysis of the XGP and XGNP samples adsorbed on mica

Sample	*C%*	*O%*	*N%*	*Si%*	*Al%*	*K%*	*Na%*	**N/Si*	**C/Si*
Bare Mica	3.5	54.3	0	20.5	16.8	3.4	1.5	0	0.17
Mica/XGNP pH 3	9.6	52.5	1.2	16.6	15.0	3.7	1.4	0.072	0.58
Mica/XGNP pH 5	27.1	39.2	1.2	19.0	10.9	2.3	0.2	0.063	1.42
Mica/XGNP pH 12	11.5	46.5	0.7	17.7	14.2	3.2	6.2	0.039	0.64
Mica/XGP pH 5	11.2	50.9	0	16.5	15.9	4.1	1.3	0	0.68

* normalized peak taking stoichiometric Si on mica as reference

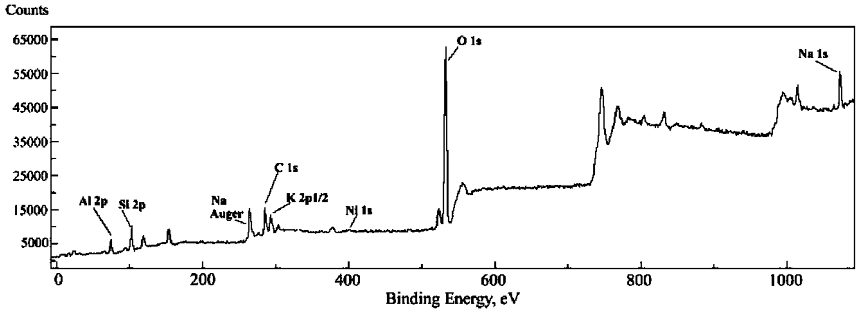

Figure 4. XPS survey spectrum of XGNP at pH 12 deposited on mica.

Comparing the carbon to nitrogen ratio for pH 3 (C/N=8) and for pH 12 (C/N=16.4), there was an increase of a factor of two. On the other hand, the protein content decreased by the same factor for pH 3 (N=0.072) compared to pH 12 (N=0.039). Therefore, at pH 12, half of the carbon content was from the polysaccharide. On the other hand, the carbon atomic percentage for hemiacetal function was low, considering the usual stoichiometry that showed 20% of polysaccharide carbons participating in an O-C-O bond and roughly 40% of polysaccharide carbons participating in a C-OH bond in a glucose ring. Thus, the relative carbon proportion detected in an hemiacetal bond was below the stoichiometric value. This result can be attributed to glycosyl linkages broken on the reducing end of the polymer by the action of two factors: the presence of hydroxide ions and the strong interaction with the mica surface (*24*).

The results in Table 3, line B, show the XGNP carbon chemical function components at pH 3, where 18% should be amide or hemiacetal functions and the N/Si ratio was the highest. XG is a neutral polysaccharide that protonates at acidic pH, making XG positively charged like mica. Therefore, the electrostatic repulsion should be higher between XG and mica than protein and mica at pH 3. This result can be interpreted as the preferential presence of amide instead of the hemiacetal function.

Downloaded by CORNELL UNIV on June 22, 2012 | http://pubs.acs.org
Publication Date (Web): November 10, 2010 | doi: 10.1021/bk-2010-1050.ch009

Table 3. C1s binding energy data obtained by XPS analysis (*16*) related to chemical function for XGNP at pH 12, pH 5 and pH 3 and XGP at pH 5 adsorbed on mica

Peak	*Chemical function C 1s*	*Component*	*Binding energy (eV)*	*C 1s Area %*
XGNP at pH 12 adsorbed on mica				
A	Carboxylate Amide	$O=C-O^-$ O=C-N	288.0	8.7
B	Hemiacetal, Acetal	O-C-O	287.0	3.2
C	Alcohol Amine, Amide	C-O C-N	285.5	42.7
D	Alkyl	C-(C,H)	284.8	45.4
XGNP at pH 5 adsorbed on mica				
A	Carboxilic acid	O=C-OH	288.67	3.0
B	Hemiacetal, Acetal Amide	O-C-O O=C-N	286.7	17.2
C	Alcohol Amine, Amide	C-O C-N	285.38	37.1
D	Alkyl	C-(C,H)	284.74	42.0
XGP at pH 5 adsorbed on mica				
A	Carboxilic acid	O=C-OH	289.1	1.6
B	Hemiacetal, Acetal Amide	O-C-O O=C-N	287.6	19.1
C	Alcohol Amine, Amide	C-O C-N	285.79	46.9
D	Alkyl	C-(C,H)	285.1	32.4
XGNP at pH 3 adsorbed on mica				
A	Carboxilic acid	O=C-OH	288.9	2.1
B	Hemiacetal, Acetal Amide	O-C-O O=C-N	286.82	18.5
C	Alcohol Amine, Amide	C-O C-N	285.19	38.4
D	Alkyl	C-(C,H)	284.55	40.9

Taking into account that protein in XGNP was essentially adsorbed at pH 3, the (C/N=8=0.58/0.072) proportion was roughly the measure of carbon from proteins. Keeping this proportion at pH 5, we observed that XPS results show that roughly that 64% of (C=1.42) the total carbon is from the polysaccharide, and 36% is from the protein. At this pH the polysaccharide had charges opposite that of mica, and the protein surface net charge must have been near its iep, which is a condition favorable to the electrostatic adsorption of polysaccharides.

Furthermore, the results of Table 3, line B, for carbon chemical function components at pH 5 for XGNP indicated that the stoichiometric O-C-O and C-O proportions related to the polysaccharide structure were preserved.

When the absorptions of XGNP and XGP at pH 5 are compared in Table 2, the carbon C1s, Figure 3B, photoemission peak is the highest for XGNP, and the Si 2p is the lowest, as shown in Figure 3C, for XGNP when compared to XGP photoemission peaks, indicating that the adsorption was more effective in the situation where the polysaccharide was not purified. Furthermore, carbon adsorption in XGNP was more than twice as large compared to that in XGP. The relative amount of carbon from the polysaccharide in XGNP was 64% of 1.42. Thus, 33% more polysaccharide was adsorbed in this case than for XGP.

Downloaded by CORNELL UNIV on June 22, 2012 | http://pubs.acs.org
Publication Date (Web): November 10, 2010 | doi: 10.1021/bk-2010-1050.ch009

Conclusions

Carbon adsorption was found to be high when the XGNP and the mica surface carried opposite charges at pH 5. On the other hand, carbon adsorption in alkaline pH is the lowest when mica and XGNP both carry a negative charge. Furthermore, at this pH, one peculiar mechanism takes place: Carbon 1s, indicative of the hemiacetal, acetal bond, which is characteristic of the polysaccharide structure, had a low relative content, indicating a polysaccharide mechanism of degradation by the action of hydroxide ions during adsorption on mica. These facts lead to the conclusion that the adsorption of non-purified xyloglucan (XGNP) on mica was driven mainly by electrostatic and acid/base interactions.

It was also observed that protein was preferentially adsorbed at pH 3 instead of pH 12 due to electrostatic interactions and the protein surface charge screening by HCl anions. Finally, comparing the performance of XGNP and XGP at pH 5, we noticed that 33% more polysaccharide was adsorbed in the presence of protein. Thus, the presence of protein favors polysaccharide adsorption.

Acknowledgments

The authors thank CNPQ/Nanoglicobiotec, CAPES/Nanobiotec and the Fundação Araucária for funding; and BIOPOL, MFA and LORXI Laboratories of UFPR for material support.

References

1. Claesson, P. M. In *Biopolymers at Interfaces*, 2nd ed.; Malmsten, M., Ed.; Surfactant Science Series 110; Marcel Dekker, Inc: New York, 2003; pp 165−193.
2. Jelinek, R.; Kolusheva, S. *Chem. Rev.* **2004**, *104*, 5987–6015.
3. Bratskaya, S. Y.; Avramenko, V. A. *Colloid J.* **2001**, *63*, 137–141.
4. Santi-Gadelha, T.; Gadelha, C. A. A.; Aragão, K. S.; Oliveira, C. C.; Mota, M. R. L.; Gomes, R. C.; Pires, A. F.; Toyama, M. H.; Toyama, D.

O.; Alencar, N. M. N.; Criddle, D. N.; Assreuy, A. M. S.; Cavada, B. S. *Biochem. Biophys. Res. Commun.* **2006**, *350*, 1050–1055.

5. Tam, S. K.; Dusseault, J.; Polizu, S.; Ménard, M.; Hallé, J.-P.; Yahia, L. *Biomaterials* **2006**, *27*, 1296–1305.
6. Rabinow, B.; Chaubal, M. V. In *Nanoparticle Technology for Drug Delivery*; Gupta, R. B., Kompella, U. B., Eds.; Drug and pharmaceutical Science 159; Taylor & Francis, Inc.: New York, 2006; pp 199−221.
7. Reid, J. S. G. *Adv. Bot. Res.* **1985**, *11*, 125–155.
8. Hayashi, T. *Annu. Rev. Plant Phys.* **1989**, *40*, 139–168.
9. Fry, S. C. *J. Exp. Bot.* **1989**, *40*, 1–11.
10. Miyazaki, S.; Kawasaki, N.; Kubo, W.; Endo, K.; Attwood, D. *Int. J. Pharm.* **2001**, *220*, 161–168.
11. Miyazaki, S.; Suisha, F.; Kawasaki, N.; Shirakawa, M.; Yamatoya, K.; Attwood, D. *J. Controlled Release* **1998**, *56*, 75–83.
12. Bhattacharya, S.; Bal, S.; Mukherjee, R. K.; Bhattacharya, S. *J. Food Eng.* **1991**, *13*, 151–158.
13. Lucyszyn, N.; Lubambo, A. F.; Matos, K. F.; Marvilla, I.; Souza, C. F.; Sierakowski, M.-R. *Mater. Sci. Eng. C* **2009**, *29*, 552–558.
14. Bhattacharyya, K. *Langmuir* **1989**, *5*, 1155–1162.
15. Liu, Z. H.; Brown, N. M. D. *J. Phys D: Appl. Phys.* **1998**, *31*, 1771–1781.
16. Gerin, P. A.; Dengis, P. B.; Rouxhet, P. G. *J. Chim. Phys.* **1995**, *92*, 1043.
17. Muller, D. J.; Amrein, M.; Engel, A. *J. Struct. Biol.* **1997**, *118*, 172–188.
18. Bhattacharyya, K. *J. Electron Spectrosc.* **1993**, *63*, 289–306.
19. Campbell, P. A.; Sinnamon, L. J.; Thompson, C. E.; Walmsley, D. G. *Surf. Sci.* **1998**, *410*, 768–772.
20. Pashley, R. M. *J. Colloid Interface Sci.* **1981**, *83*, 531–546.
21. Claesson, P. M.; Herder, P.; Stenius, P.; Eriksson, J. C.; Pashle, R. M. *J. Colloid Interface Sci.* **1986**, *109*, 31–39.
22. Pashley, R. M. *J. Colloid Interface Sci.* **1981**, *80*, 153–162.
23. Ta, T. C.; Sykes, M. T.; McDermott, M. T. *Langmuir* **1998**, *14*, 2435–2443.
24. Lubambo, A. F.; Lucyszyn, N.; Klein, J. J.; Schreiner, W. H.; de Camargo, P. C; Sierakowski, M.-R. *Colloids Surf., B* **2009**, *70*, 174–180.

Downloaded by CORNELL UNIV on June 22, 2012 | http://pubs.acs.org
Publication Date (Web): November 10, 2010 | doi: 10.1021/bk-2010-1050.ch009

Downloaded by PENNSYLVANIA STATE UNIV on June 22, 2012 | http://pubs.acs.org
Publication Date (Web): November 10, 2010 | doi: 10.1021/bk-2010-1050.ch010

Chapter 10

Multi-Functional Electroactive Polymers (EAPs) as Alternatives for Cadmium Based Coatings

**P. Zarras,[1,*] A. Guenthner,[1] D. J. Irvin,[1] J. D. Stenger-Smith,[1]
S. Hawkins,[1] L. Baldwin,[1] R. Quintana,[1] M. Baronowski,[2]
J. Baronowski,[2] J. Hibbs,[2] and C. P. Waltz[3]**

[1]NAWCWD (Code 4L4200D), 1900 N. Knox Road (Stop 6303), China Lake, CA, 93555-6106
[2]NAWCWD (Code 434100D), 1900 N. Knox Road (Stop 6213), China Lake, CA 93555-6106
[3]NAWCWD (Code 476400D), 1900 N. Knox Road (Stop 6622), China Lake, CA 93555-6106
[*]Peter.zarras@navy.mil

The Naval Air Warfare Center Weapons Division (NAWCWD) has investigated electroactive polymers (EAPs) as alternative cadmium pretreatment coatings. EAP coatings (polypyrrole derivatives) were synthesized with adhesion promoting groups and embedded with inorganic microparticles for both corrosion inhibition and lubricity. These polymers were coated onto high strength 4340 steel alloys. Several of these EAP coated high strength 4340 steel alloys failed at 24 hours exposure to neutral salt fog spray. However, a hexyl substituted polypyrrole coating showed improved corrosion inhibition as compared to poly(3-pyrrol-1-yl) propanoic acid. Lubricity studies were performed on several pyrrole compounds. These EAP coatings were tested against Cd plated high strength 4340 steel alloys as a control. Galling testing was performed in accordance with test method ASTM G98. Several of the polymer coatings provided little, if any, protection from steel on steel galling. Some of the coatings behaved like a grease and did not provide an accurate galling resistance measurement. The addition of graphite particles resulted in a slight improvement in the

In Smart Coatings III; Baghdachi, J., et al.;
ACS Symposium Series; American Chemical Society: Washington, DC, 2010.

galling performance of the poly(3-pyrrol-1-yl) propanoic acid coating, while adding SiO_2 particles led to a more pronounced improvement.

Introduction

The extensive use of cadmium (Cd) in industrial operations such as smelting and refining of zinc (Zn), lead, copper ores, electroplating, welding, manufacture of pigments, plastic stabilizers and nickel-cadmium batteries has resulted in worker exposure to Cd and this exposure can result in pulmonary carcinogenesis, tumors of the prostate, testes and hematopoietic system (*1–3*). Cadmium can leach through soils into the groundwater where it can bind to river sediment and bioaccumulate. It is a known carcinogen which is highly regulated by the Environmental Protection Agency (*4*).

Despite these environmental hazards, Cd is still widely used in the plating industry (especially for fasteners) because of its unique combination of properties. Cadmium plating has several properties that make it highly attractive for military use (*5*). Several high-strength steels used by the military that are Cd-plated for fastener applications include: AISI 4340, Hy-Tuf™ (an AISI 4340 derivative created by Crucible Specialty Metals), Aermet® 100, E4340, M50, 300M, PH 13-8Mo stainless steel and maraging Grades 200-250. The most common method of electroplating Cd onto high strength steel is the alkaline cyanide bath. While this technology ranks as one of the oldest for Cd-plating, it is also the most forgiving and reliable plating solution and proposed replacements have difficulty in matching its performance (*6–12*). Studies of replacements of Cd-plated high-strength steels include the Dacromet, Geomet and Magni families of coatings. These coatings, which have shown initial promise, consist of commercial Zn and aluminum (Al)-filled polymers deposited by the dip-spin coating technique, and are often used for automotive applications. Although they are quite effective, the coatings tend to clog fastener threads, creating installation problems. In addition, their torque characteristics tend to change over the course of multiple assemblies. This is not a problem for cars but it is a serious drawback for aerospace and other Department of Defense applications where weapon systems require periodic strip-down and maintenance.

Recent developments in using EAPs coated onto various metal substrates have demonstrated corrosion inhibition (*13*). EAPs, specifically polyaniline (PANI) have been shown to provide corrosion protection for steel alloys and testing at the Los Alamos National Laboratory (LANL) and the John F. Kennedy Space Center (KSC) have demonstrated that doped PANI coatings inhibited corrosion on carbon steel (*14*, *15*). EAPs other than PANI have also been demonstrated to protect steel alloys in harsh environments. Poly(3-methylthiophene) (P3MT) films coated onto platinum and 430 stainless steel (430SS) showed effective stabilization of the steel in a passive state (*16*). P3MT films coated onto a 430SS rotating disk electrode (RDE) in 1N sulfuric acid solution showed galvanic protection. This protection was described by DeBerry, whereby, the P3MT film stabilized the passive layer

Downloaded by PENNSYLVANIA STATE UNIV on June 22, 2012 | http://pubs.acs.org
Publication Date (Web): November 10, 2010 | doi: 10.1021/bk-2010-1050.ch010

by providing a transient current to heal small defects inside the passive film before they could expand (*17*).

Constant current (galvanostatic) and constant potential (potentiostatic) measurements on poly(2,5-bis-N-methyl-N-hexylamino)phenylene vinylenes (BAM-PPV) on aluminum alloy (AA) 2024-T3 panels in simulated seawater provided evidence for corrosion inhibition (*18*, *19*). The military requirement for an alternative pretreatment for chromate conversion coating (CCC) states that the unpainted coating must pass 336 hours of neutral salt fog exposure. The accept/reject criteria for this military requirement (MIL-DTL-81706B) is no corrosion of the underlying aluminum. Any staining of the coating is not considered a failure and the coating must not show blistering, delamination or evidence of corrosion (*20*, *21*). BAM-PPV coated onto AA 2024-T3 panels showed acceptable neutral salt fog exposure performance when compared to chromate conversion coated AA 2024-T3 panels (as controls) (*20*). The BAM-PPV coatings were able to pass the 336 hour neutral salt fog exposure test (ASTM B117) without pitting, corrosion or delamination of the coating which met the MIL-DTL-81706B requirement.

Polyethylene coatings have also been investigated for their wear resistance and corrosion protecting properties using molybdenum disulphide fillers (*22*). By incorporating hard particles for lubricity into an EAP coating system one could potentially provide corrosion and wear resistance from a single coating system. The following paper will describe our work on achieving this effect.

Experimental

3-(Pyrrol-1-yl) proprionitrile (3PPN), 7-bromoheptanitrile (7-BHN), sodium hydroxide (NaOH), pyrrole and 3-aminopropyltrimethoxysilane were purchased from Aldrich and used as received. Iron (III) chloride ($FeCl_3$) and iron(III) chloride hexahydrate ($FeCl_3*6H_2O$), were purchased from Aldrich and used as received. Ferric nitrate nonahydrate ($Fe(NO_3)_3*9H_20$) was obtained from Baker Chemical and used as received.

^1H and ^{13}NMR spectra were acquired using a Bruker Advance 400 MHz NMR spectrometer. Mass spectra data were obtained using a JEOL thermal desorption mass spectrometer (TD-MS). The FTIR measurements were made using a Nicolet Nexus 870 FTIR spectrometer with a liquid nitrogen cooled MCT detector. Each spectrum is an average of 128-256 scans with 4 cm^{-1} resolution. The monomer and polymer bulk samples were analyzed using a "Thunder dome" attenuated total reflectance (ATR-FTIR) accessory with a germanium crystal. The samples adsorbed on a surface were analyzed using specular reflectance and the incoming radiation was at 80° with respect to the surface normal.

The particles used in the particle coating operation included 1) Monarch 900 carbon black (an organic pigment containing ~50% graphite, dispersed as ~1µm particles), 2) molybdenum sulfide (99%, supplied from Aldrich Chemical as particles of less than 2µm size), 3) fumed silica, supplied by Aldrich as particles significantly less than 1µm in average size and 4) boron carbide, supplied by Aldrich as particles approximately 10µm in average size. Since the inclusion of

Downloaded by PENNSYLVANIA STATE UNIV on June 22, 2012 | http://pubs.acs.org
Publication Date (Web): November 10, 2010 | doi: 10.1021/bk-2010-1050.ch010

small, hard particles is intended to modify only the surface characteristics of the coating, an attempt was made to introduce the particles only at the outermost regions of the coated article. To do so, a quick method of hot pressing at low pressure was developed. The carbon black and molybdenum sulfide were chosen because of their enhanced lubricity, the carbon black and the silica were chosen because of their small particle size and ease of dispersion, and the boron carbide was chosen for its hardness and contrasting particle size. The procedure for hot pressing the particles was as follows. The particles were first suspended at a low volume fraction in deionizer water (DI water) by ultrasonication for one hour. The suspension was then transferred onto the surface to be tested via pipette and spread via shearing with compressed air to form a coating layer about 0.5 mm thick. For the larger particles (boron carbide), the suspended particle concentrations were about 0.5 wt%, while for the smaller particles (all others), they were about 0.1 wt%. The concentration used was scaled approximately to the particle size in order to provide fairly similar coverage (roughly 20-70% of a theoretical close-packed monolayer) on all surfaces upon drying. After spreading, the wet surfaces were gently dried in a stream of compressed air for about 1 minute to reduce the thickness of the wet layer to a thinner layer without de-wetting the edges of the surface. To press the samples, a clean thin sheet of Teflon, backed by sheets of aluminum arranged so as to constitute a total weight (including Teflon) equal to 106 g/button, was heated to 100°C. The sheets were then placed directly on to the wet surfaces and allowed to remain for 15 minutes while cooling. Assuming full contact between the sheet and the button faces, the pressure applied to the surfaces was about 8 kPa, or 1.2 psi. During the holding time, the temperature of the outer sheets was observed to decrease to about 50°C. After holding, the sheets were then removed from the surfaces, and allowed to dry completely at room temperature. The operation achieved the deposition of a uniform thin coating of particles over the entire target area. In many cases, however, an excess of particles was observed to deposit around the sample edges. Thus, while the method as developed is suitable for deposition of the particles to test specimens, more work would be needed to develop a deposition method (such as an electrostatic method similar to powder coating) that would be suitable for articles of arbitrary shape and surface characteristics.

Galling testing was then performed in accordance with test method ASTM G98, which required button and block specimens. These specimens were manufactured from AISI 4340 steel hardened to 50-55 HRC, representing high-strength steel. A group of button specimens was plated with cadmium (in accordance with SAE-AMS-QQ-P-416, Type II, Class 2), while others were coated with ion-vapor deposited (IVD) aluminum (in accordance with MIL-DTL-83488, Type II, Class 2) for comparison to the polymer samples. A high strength steel support cylinder and plate support fixture conforming to the dimensions listed in ASTM G98 for galling testing were fabricated.

EAP deposited onto high strength 4340 steels alloys was measured for morphology, chemical composition and corrosion performance using a combination of scanning electron microscopy/energy dispersive x-ray analysis (SEM/EDXA). The measurements were done with a Zeiss SEM Model EVO-50

Downloaded by PENNSYLVANIA STATE UNIV on June 22, 2012 | http://pubs.acs.org
Publication Date (Web): November 10, 2010 | doi: 10.1021/bk-2010-1050.ch010

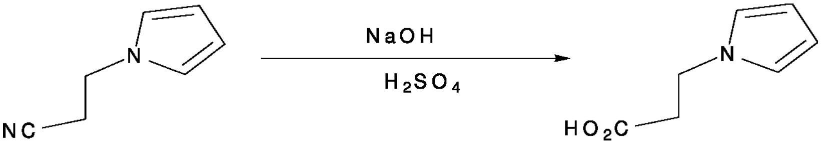

Figure 1. Synthesis of 3-(pyrrol-1-yl) propanoic acid (3PPA)

and EDXA Model LEO-EVO-50EP. Neutral salt fog exposure testing (ASTM B117) were performed on EAP films without hard particle additives.

Downloaded by PENNSYLVANIA STATE UNIV on June 22, 2012 | http://pubs.acs.org
Publication Date (Web): November 10, 2010 | doi: 10.1021/bk-2010-1050.ch010

Preparation of 3-(Pyrrol-1-yl) Propanoic Acid (3PPA) (see Figure 1) (*23*)

A 250 mL round bottom flask was equipped with a reflux condenser and nitrogen inlet/outlet valve. The round bottom flask was charged with 50 mL DI water and 13.3 g NaOH pellets. After addition of the NaOH pellets the solution became turbid. After 5 minutes, the solution was clear and homogenous. The 3-(pyrrol-1-yl) proprionitrile (10.0 g, 83.2 mmol) was added to the reaction flask and the solution refluxed for 12 hours under a positive nitrogen pressure. After 12 hours the solution was homogenous and orange colored. There was no ammonia evolution from the top of the condenser as determined by moist pH paper. Cold DI water (25 mL) was added and the solution was cooled to ambient temperature. The reaction flask was cooled in an ice/water bath and 14 mL of a 50% aqueous sulfuric acid solution (1:1, v/v) was added slowly. The solution was stirred and a semi-solid formed immediately. The contents of the reaction flask were extracted 3X with ether and the ether layer separated from the aqueous phase. The ether layer was dried over magnesium sulfate ($MgSO_4$) and the solution filtered through a medium porosity glass frit. The filtrate was rotovapped to a semi-solid residue and dried in a vacuum dessicator (0.05 Torr, 25°C) for 12 hours. An off-white tan product was obtained in 35% yield (4.0 g), m.p = 45-47°C (uncorrected, literature value = 59-60°C) (*23*, *24*). ^{1}H NMR (DMSO-d_6): 2.67 (t, 2H); 4.09 (t, 2H); 5.95 (t, 2H) and 6.73 (t, 2H), ^{13}C NMR (DMSO-d_6): 36.05, 44.40, 107.5, 120.4 and 172.3. FTIR: 3000 cm^{-1} broad (OH stretch), 1710 cm^{-1} (C=O stretch). The 3PPA compound was identified with thermal desorption-MS: molecular peak at 138.9 amu.

Electropolymerization of 3PPA

3PPA polymerizes quite well electrochemically, as can be seen in Figure 2. 3PPA undergoes a very well-behaved, reproducible electropolymerization which shows a linear increase in peak current as a function of scan rate for the poly(3(pyrrol-1-yl) propanoic acid), (P3PPA) compound, indicating that the film is electrode supported and electroactive.

Downloaded by PENNSYLVANIA STATE UNIV on June 22, 2012 | http://pubs.acs.org
Publication Date (Web): November 10, 2010 | doi: 10.1021/bk-2010-1050.ch010

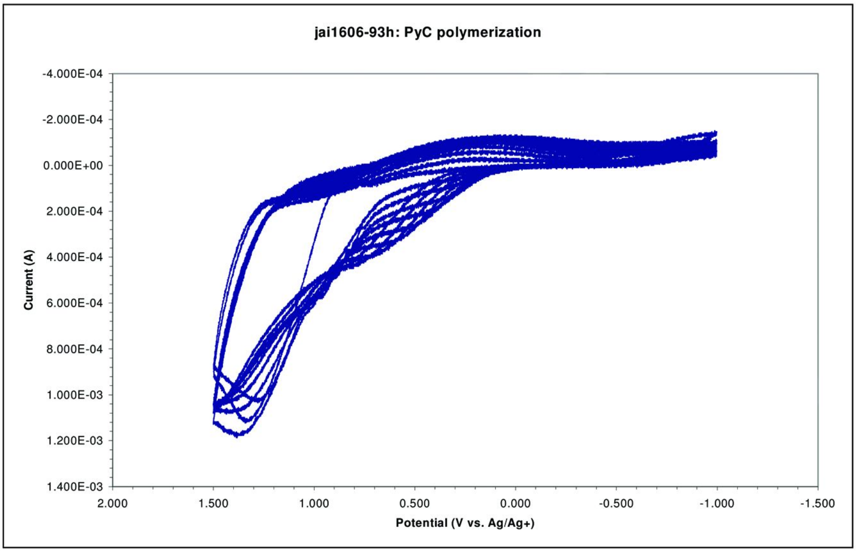

Figure 2. Electropolymerization of 3PPA

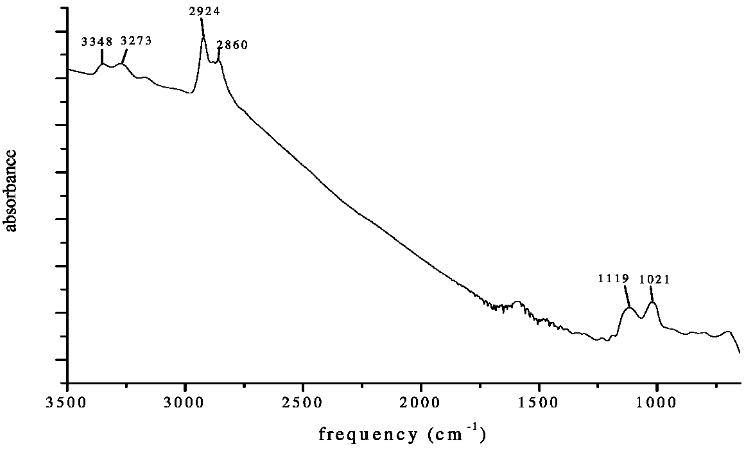

Figure 3. 3-aminopropyl trimethoxysilane on high strength 4340 steel alloy button

Electroless Deposition of 3PPA (24)

The electroless deposition (non line-of-sight) of 3PPA and 7-PHA used in this study was based on a prescreening process using the electropolymerization results described previously, based on the principle that the monomers with the lowest oxidation potential would undergo facile electroless polymerization. Since 3PPA does undergo electropolymerization at a low potential, it is a candidate for electroless deposition. The electroless deposition consisted of 3 steps using the 3PPA and 7-PHA monomers.

Downloaded by PENNSYLVANIA STATE UNIV on June 22, 2012 | http://pubs.acs.org
Publication Date (Web): November 10, 2010 | doi: 10.1021/bk-2010-1050.ch010

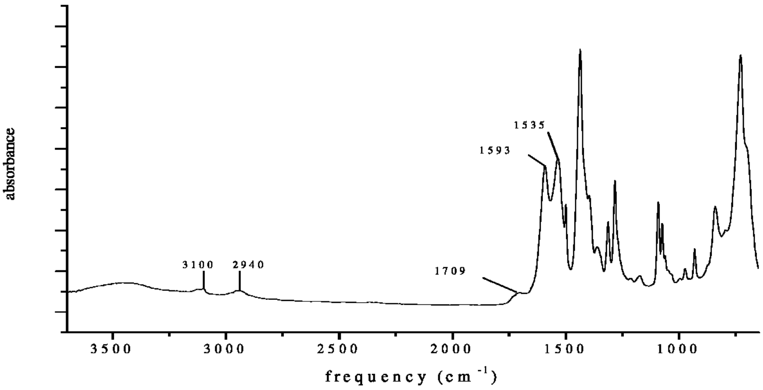

Figure 4. P(3PPA) deposited on high strength 4340 steel alloy substrate

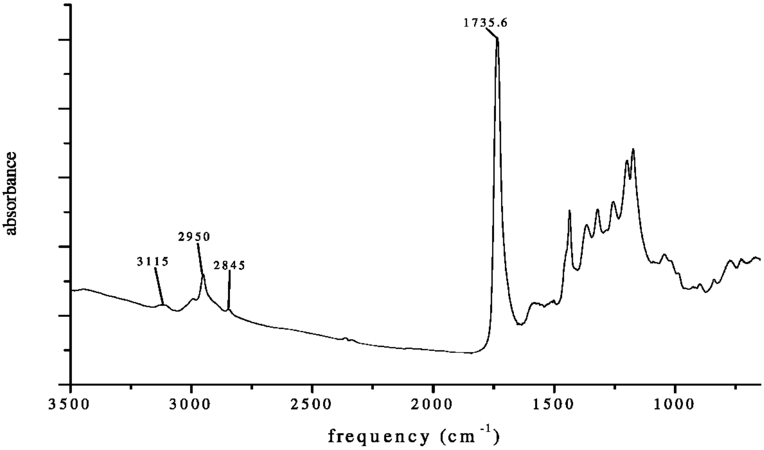

Figure 5. Bulk P(3PPA)

Step I: The high strength 4340 steel alloy substrate [3x3x0.25”; 3x6x0.25”, galling and defect tolerance specimens] were cleaned using toluene, acetone, methanol and isopropanol to remove grease, dirt and any other debris that may be present on the sample. The samples were then air dried for 15 minutes prior to deposition. No evidence of corrosion was visible during this stage of the electroless deposition process.

Step II: The cleaned sample was placed in a Pyrex glass dish (size depended on sample dimensions) and a 0.5 wt %/vol. of 3-aminopropyltrimethoxy silane solution was added to the samples. The samples were allowed to stand in the silane solution for 5 minutes after which time the samples were removed and dried in a vacuum oven (25 mm Hg, 100°C). After one hour, the samples were removed from the oven and allowed to cool in a dessicator for one hour. The steel samples were measured with FTIR to determine if the silane had reacted with the substrate. A thin layer of 3-aminopropyltrimethoxysilane was deposited on a high strength

Downloaded by PENNSYLVANIA STATE UNIV on June 22, 2012 | http://pubs.acs.org
Publication Date (Web): November 10, 2010 | doi: 10.1021/bk-2010-1050.ch010

4340 steel alloy surface which is shown in Figure 3, confirming the presence of the silane on the surface before the polymer deposition.

Step III: The silanated sample was then placed back into the Pyrex glass dish for the polymerization deposition process. Numerous attempts using a variety of solvents, (e.g. DI water, methanol) and oxidants ($FeCl_3$, $FeCl_3*6H_2O$) were tried. The oxidants $FeCl_3$ and $FeCl_3*6H_2O$ performed the best during the polymerization. Several different molar concentrations of the monomer in DI water were examined during the deposition (0.03M, 0.25M, and 057M). The 0.25M solution of 3PPA and oxidant $FeCl_3$ at a concentration of 0.67M were found to be the optimum conditions for the electroless deposition process. Both the monomer solution and oxidant solution were added simultaneously to the Pyrex dish containing the high strength 4340 steel alloy samples. The solution was briefly agitated (<5 minutes) and covered and allowed to react at ambient temperature for 6 hours. After 6 hours a black film was present on the substrate. The substrate was dried in a vacuum oven (25 mm Hg, 70°C) for 6 hours. After 6 hours of drying time, the substrate was removed from the oven and cooled to room temperature in a dessicator. The identification that the polymer (P(3PPA)) had reacted with the silane coated substrate was confirmed by FTIR. The polymer deposited on a silanated surface is shown in Figure 4. It is different from the bulk polymer sample (as prepared using $FeCl_3$ in DI water and purified after polymerization) (Figure 5). In Figure 4, peaks at ~ 3440, 1593, and 1539 cm^{-1} are indicative of the N-H stretch, amide I and amide II bonds, respectively, of a secondary amide. The carbonyl peak of the carboxylic acid group at 1710 cm^{-1} decreased in intensity, indicating that its concentration decreased significantly. This shows evidence of the polymer reacting to form an amide at the surface. The polymer was deposited on the surface as a non-uniform film, exhibiting brittleness with some flaking of the material.

Preparation of 7-Pyrrol-1-yl-heptanitrile (7-PHN) (see Figure 6) (*25–27*)

A 250 mL 3-neck round bottom flask was equipped with a reflux condenser, nitrogen inlet/outlet and 50 mL constant pressure addition funnel. The reaction flask was flushed with nitrogen and 50 mL dry THF, 2.0 grams pyrrole (29.8 mmol) and 3.34 g potassium tert-butoxide (K-*t*-OBu) (29.8 mmol) were added to the reaction flask. The addition funnel was charged with 6.80 grams 7-BHN (35.8 mmol, 5.4 mL). After addition complete, the contents were refluxed at 80°C overnight under a positive nitrogen blanket. The reaction was cooled to ambient temperature and quenched with 50 mL DI water. The aqueous solution was extracted 3x with chloroform (3 x 35 mL), the organic layers combined and dried over $MgSO_4$. The solution was filtered through a medium porosity glass frit and the filtrate rotovapped to an orange oil which was dried under vacuum (0.05 Torr, 25°C) overnight in a vacuum dessicator. The orange oil was obtained in 5.70 g (91%). ^1H, ^{13}C NMR and FTIR were used to identify the product. The proton and carbon NMR assignments are: ^1H NMR (δ, DMSO-d_6, 400 MHz, 300K): 6.72 (t, J = 2.1 Hz, 2H, pyrrole), 5.99 (t, J = 2.1 Hz, 2H, pyrrole), 3.85 (t, J = 7.1 Hz, 2H, CH_2), 2.44 (t, J = 7.1 Hz, 2H, CH_2), 1.68 (p, J = 7.3 Hz, 2H, CH_2), 1.53 (p, J = 7.3 Hz, 2H, CH_2), 1.39 (m, 2H, CH_2), 1.22 (m, 2H, CH2) and

^{13}C NMR (δ, DMSO-d_6, 400MHz, 300K): 120.42 (CN), 120.25 (pyrrole), 107.30 (pyrrole), 48.41 (NCH_2), 30.78 (CH_2), 27.56 (CH_2), 24.63 (CH_2), 24.57 (CH_2), 16.03 (CH_2). The FTIR peak assignments are as follows: 3095 cm^{-1} sp^2 C-H stretch, 2934 and 2861 cm^{-1} C-H stretch, 2245 cm^{-1} C≡N stretch, 1550 cm^{-1} out of phase C=C stretch, 1501 cm^{-1} in phase C=C stretch, 1462 cm^{-1} CH_2 scissor, 1425 cm^{-1} pyrrole anti-symmetric ring mode, 1280 cm^{-1} N-CH_2 stretch of 1-substituted pyrrole, 1089 and 1061 cm^{-1} in plane C-H deformation of pyrrole, 725 cm^{-1} in phase out of plane cis CH wag of pyrrole HC=CH.

Hydrolysis of 7-PHN (see Figure 6) (*28*)

A 100 mL 3-neck round bottom flask was equipped with a reflux condenser, nitrogen inlet/outlet. The reaction flask was charged with 20 ml DI water and 2.72 grams of NaOH pellets (68.1 mmol). After 5 minutes the pellets had dissolved forming a homogenous solution and 3.0 g 7-PHN (17.0 mmol) was added to the reaction flask. The solution was refluxed for 9 hours under a positive nitrogen blanket and completion of the reaction was determined with moist pH paper until no evolution of ammonia was evident. The reaction flask was quenched with 7 mL cold DI water poured down the condenser and the solution was acidified with a 50 wt % concentrated HCl: DI water (1:1, v/v). The pH was monitored during the addition changing from pH = 12 to pH = 2. After acidification, the solution was extracted with ethyl ether (3 x 25 mL). The ether layers were combined, and dried with $MgSO_4$, filtered through a medium porosity glass frit and the filtrate rotovapped to a red-brown oil. The oil was dried for 6 hours in a vacuum dessicator (0.05 Torr, 25°C) to give in quantitative yield a deep-red oil in 3.35 grams. ^1H, ^{13}C NMR and FTIR were used to identify the product. The proton and carbon NMR assignments are: ^1H NMR (δ, $CDCl_3$, 400 MHz, 300K): 10.42 (bs, -OH), 6.69 (t, J = 2.1 Hz, 2H, pyrrole), 6.19 (t, J = 2.1 Hz, 2H, pyrrole), 3.91 (t, J = 7.2 Hz, 2H, CH_2), 2.39 (t, J = 7.2 Hz, 2H, CH_2), 1.81 (m, 2H, CH_2), 1.68 (m, 2H, CH_2), 1.39 (bm, 4H, CH2) and ^{13}C NMR (δ, $CDCl_3$, 400MHz, 300K): 179.98 (C=O), 120.47 (pyrrole), 107.88 (pyrrole), 49.47 (NCH_2), 33.98 (CH_2), 31.36 (CH_2), 28.60 (CH_2), 26.40 (CH_2), 24.52 (CH_2). The FTIR peak assignments are as follows: 3096 cm^{-1} sp^2 hybridized C-H stretch, 2933 and 2862 cm^{-1} sp^3 hybridized C-H stretch, 1702 cm^{-1} C=O stretch, 1502 cm^{-1} C=C stretch, 1467, 1411, 1335 cm^{-1} C-H deformation modes, 1279 cm-1 N-CH_2 stretch of 1-substituted pyrrole, 1200 cm^{-1} C-O stretch, 1090 and 1060 cm^{-1} in plane C-H deformation of pyrrole ring carbons and 727 cm^{-1} in phase out of plane cis C-H wag of pyrrole.

Results and Discussion

Galling Measurements

The galling studies focused on depositing EAP materials on high strtength 4340 steel alloy buttons containing hard particles using the electroless deposition technique. The uncoated button and plate were tested first in order to determine an approximate threshold galling stress for uncoated high strength 4340 steel alloy (see Figure 7 for galling test set-up).

Downloaded by PENNSYLVANIA STATE UNIV on June 22, 2012 | http://pubs.acs.org
Publication Date (Web): November 10, 2010 | doi: 10.1021/bk-2010-1050.ch010

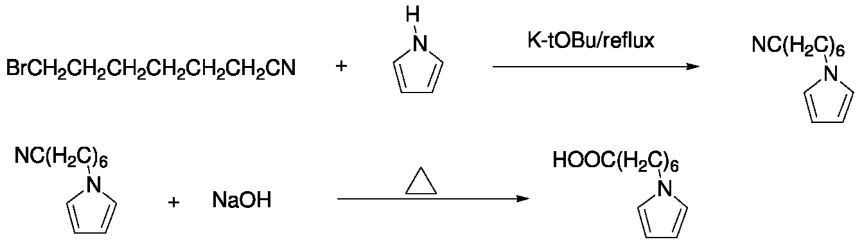

Figure 6. Synthesis Scheme for7-pyrrol-1-yl-heptanoic acid (7-PHA)

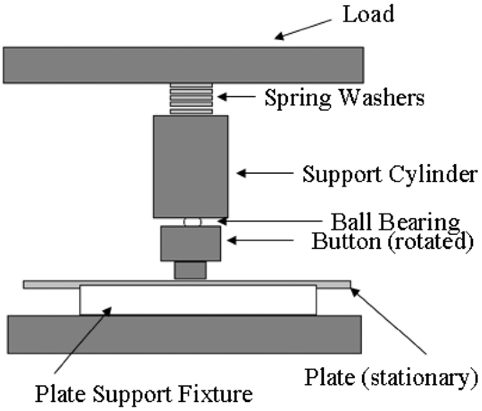

Figure 7. Schematic of galling test setup

Once the threshold was established, the various coatings were tested to see how much galling protection each provided. The load frame used for this test had a maximum load of 10,000-lbs, which equates to a stress of 51 ksi on the button. If galling did not occur at the maximum load, a value of 51+ ksi was recorded as the threshold galling stress. The galling stress values for all samples were determined from the following equation: stress = load/area (where: area = Πr^2 and r = 0.25 inches).

The uncoated high strength 4340 steel alloy began to gall at a stress of approximately 10 ksi. The Cd plated buttons were tested for galling resistance against the bare high strength 4340 steel alloy. Cadmium is considered a gall resistant coating; therefore, Cd on steel was tested at a starting stress of 10 ksi (2,000-lbs). After each test, the load was raised incrementally by 1,000-lbs until galling was noted. After each test, smearing and transfer of the Cd was noted, but no galling was observed. At the maximum load of 10,000-lbs, no galling was noted and a maximum threshold galling stress of 51+ ksi was recorded. The IVD aluminum coating was tested in the same manner as the Cd coated steel. The testing was started at 2,000-lbs, and was raised by 2,000-lbs until galling was noted. During testing it was noted that it was much more difficult to rotate the aluminum samples at low loads than the Cd samples at higher loads. At 8,000-lbs, the aluminum-coated sample was unable to be rotated using two 8-inch lever arms. After approximately 1/8 (~45°) of a rotation, the test was stopped and the

Downloaded by PENNSYLVANIA STATE UNIV on June 22, 2012 | http://pubs.acs.org
Publication Date (Web): November 10, 2010 | doi: 10.1021/bk-2010-1050.ch010

Downloaded by PENNSYLVANIA STATE UNIV on June 22, 2012 | http://pubs.acs.org
Publication Date (Web): November 10, 2010 | doi: 10.1021/bk-2010-1050.ch010

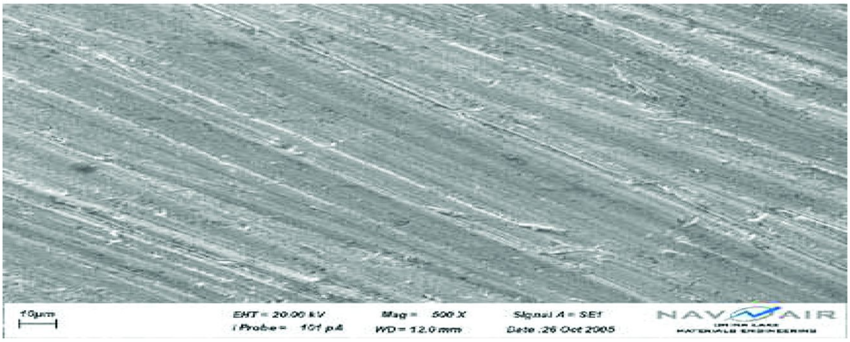
10µm
EHT = 20.00 kV
I Probe = 101 pA
Mag = 500 X
WD = 12.0 mm
Signal A = SE1
Date :26 Oct 2005
NAVAIR
CHINA LAKE
MATERIALS ENGINEERING

Figure 8. Cd-coated buttons tested on high strength 4340 steel alloy plate at 10,000-lbs (51ksi). Coating smearing was noticed, but no evidence of coating or base metal galling at 500X

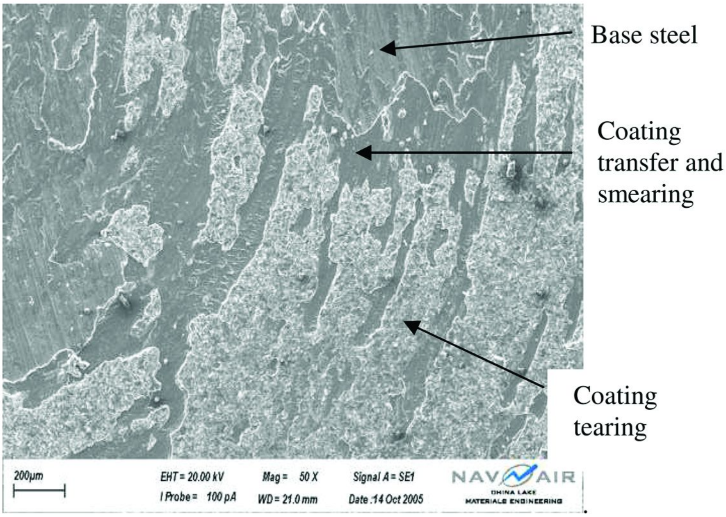
Base steel
Coating transfer and smearing
Coating tearing
200µm
EHT = 20.00 kV
I Probe = 100 pA
Mag = 50 X
WD = 21.0 mm
Signal A = SE1
Date :14 Oct 2005
NAVAIR
CHINA LAKE
MATERIALS ENGINEERING

Figure 9. High strength 4340 steel alloy plate tested for galling with IVD Aluminum coated button at 6,000-lbs. Coating transfer and tearing was noticed at 50X.

sample was removed and visually inspected. No galling was noted on the base metal, however it was assumed that the onset of cold welding was occurring and if the sample could have been rotated, metal would have been galled. A galling stress of 31 ksi was calculated for the IVD aluminum sample.

Polymer sample P(3PPA) was tested with both embedded MoS_2 and SiO_2 particles. The P(3PPA) MoS_2 samples were tested at 2,000 and 4,000-lbs. At 4,000-lbs galling of the coating was observed. The button and plate were fused together after testing and when they were broken apart, torn coating was seen. The P(3PPA) SiO_2 samples were tested in a similar manner, starting at 2,000-lbs. These samples were difficult to turn, showing poor lubricity, but no visible galling was noted. At 8,000-lbs the samples were unable to turn, and a galling stress of 41 ksi was calculated as described above.

ASTM G98 states that only the unaided eye shall be used to determine whether or not a system exhibited signs of galling. However, for the purpose of more thoroughly ranking coating galling resistance, SEM was used to identify signs of galling at high magnification. Cadmium exhibited coating smearing, which accounts for its lubricity when examined under the SEM. Figure 8 shows the Cd coating tested at 10,000-lbs at a magnification of 500x. IVD aluminum was also examined with the SEM for comparison purposes. Figure 9 shows the plate tested at 6,000-lbs, showing metal transfer and tearing of the aluminum coating. The various EAP coatings were examined with SEM to see if the same desired metal smearing could be observed. Figure 10 shows an SEM image of coating P(3PPA) with SiO_2 on a button tested at 6,000-lbs. This sample shows metal smearing and some tearing, but the tearing seems to be less than IVD aluminum tearing at 6,000-lbs.

Downloaded by PENNSYLVANIA STATE UNIV on June 22, 2012 | http://pubs.acs.org
Publication Date (Web): November 10, 2010 | doi: 10.1021/bk-2010-1050.ch010

Neutral Salt Fog Exposure Testing

The 3PPA monomer was electrodeposited onto several high strength steel alloys. The coated samples were placed in a neutral salt fog chamber and documented over 12 hour intervals vs. the Cd plated high strength 4340 steel alloy coupons as control. After 12 hours, rusting was present throughout the EAP film and this was due to the poor film quality. The film forming properties of the P(3PPA) were unsatisfactory. In contrast, the Cd plated high strength 4340 steel alloy coupons survived over 96 hours neutral salt fog exposure.

A new monomer was synthesized containing a hexyl group attached to the pyrrole monomer. This compound 7-pyrrol-1-yl-heptanoic acid (7-PHA) would potentially provide better film forming properties based on its lower thermal glass transition temperature. A high strength 4340 steel alloy (1x3x0.25”) panel coated with poly(7-pyrrol-1-yl-heptanoic acid), (P(7-PHA)) over the silane-based adhesion promoter was subjected to a neutral salt fog environment for a period of 96 hours. The formation of the (P(7-PHA) coating on the high strength 4340 steel alloy substrate was via the electroless deposition process. The panel was scribed and placed in a neutral salt fog chamber. The panels were photographed before and after 96 hours neutral salt fog exposure (see Figure 11 below).

The panel was also examined using SEM and EDXA for signs of corrosion at 24, 48, and 96 hours of neutral salt fog exposure. Figures 12, 13 and 14 include SEM images of different parts of the EAP coating surface at different inspection intervals. Figure 12 shows the areas farthest from the edges of the test panel. There was no catastrophic damage after exposure over time in the neutral salt fog chamber. The craters in the images are a result of the electroless deposition process, all craters were completely filled by the polymer compound (P(7-PHA)). There was no exposed, uncovered metal found in these images.

Figures 13 and 14 show multiple cracks forming during exposure of the steel substrate in the neutral salt fog chamber. The cracks may have formed during testing as the result of the silane-based adhesion promoter dissolving away. The polymer layer was disrupted. The coating did change physically as

Downloaded by PENNSYLVANIA STATE UNIV on June 22, 2012 | http://pubs.acs.org
Publication Date (Web): November 10, 2010 | doi: 10.1021/bk-2010-1050.ch010

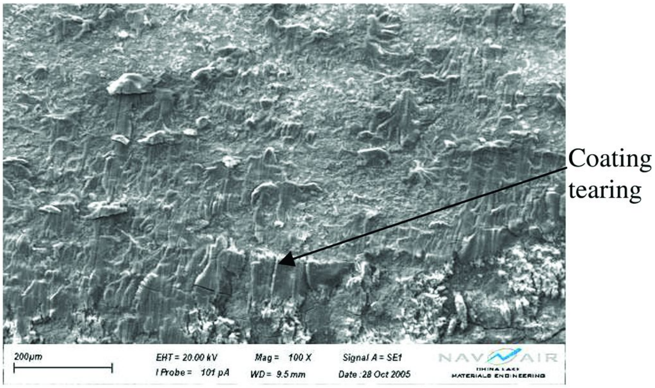

Figure 10. P(3PPA) with SiO_2 button galling tested at 6,000-lbs, showing significant metal transfer, but less tearing that observed with the IVD aluminum at100X.

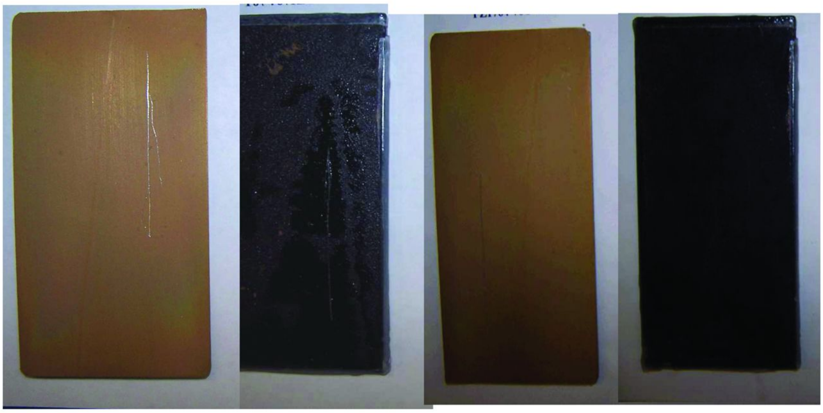

a) Cd and EAP coated coupons *b) Cd and EAP coated coupons*

Figure 11. a) Left side neutral salt fog exposure of scribed Cd and EAP(P-(7-PHA)) coated high strength 4340 steel alloy coupons at 0 hours and b) right side neutral salt fog exposure of scribed Cd and EAP coated high strength 4340 steel alloy coupons at 96 hours (see color insert)

time progressed. The center of the panel had the most uniform layer of polymer coating. By 48 hours of neutral salt fog exposure, the coating was beginning to crack, and the cracks expanded through 96 hours. However, the outer edges of the panel had defects in the coating. These areas showed signs of cracking at 24 hours of neutral salt fog exposure. These cracks expanded through 96 hours to the point that small flakes of polymer were disappearing. The cracking and flaking is possibly due to the adhesion promoter. In the defects where the adhesion promoter was exposed, the saline solution eroded and washed it away. As the adhesion promoter disappeared, the polymer had no foundation and cracked apart.

Downloaded by PENNSYLVANIA STATE UNIV on June 22, 2012 | http://pubs.acs.org
Publication Date (Web): November 10, 2010 | doi: 10.1021/bk-2010-1050.ch010

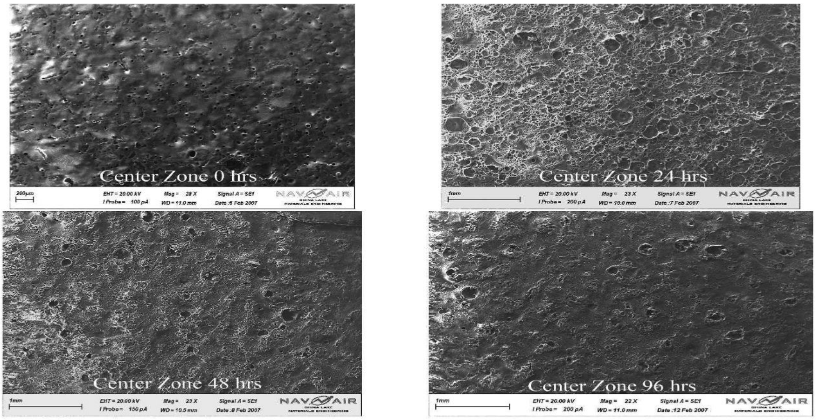

Figure 12. SEM Analysis of EAP (P(7-PHA)) onto High Strength 4340 Steel Alloy Substrate after Neutral Salt Fog Exposure.

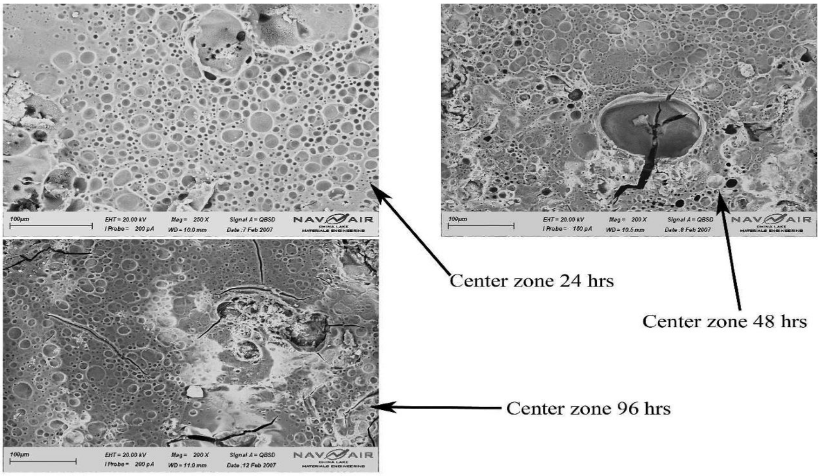

Figure 13. SEM Analysis of Coating Shows Crack Formation on Polymer Film.

After enough adhesion promoter had eroded, the polymer had nothing to hold it to the panel and flaked away.

EDXA spectra were taken at different locations on the coating at different inspection intervals. The overall trend was that the polymer itself did not corrode or decay in any significant amount. Between 0 and 24 hours of neutral salt fog exposure, the carbon peak dropped about 10 wt. % and the oxygen peak increased by about 8 wt. %. From 24 through to 96 hours exposure of neutral salt fog spray, the relative amounts of carbon, nitrogen, silicon, iron and oxygen observed from EDXA did not change significantly. The polymer may have some "limited throwing power" due to presence of nitrate ions in the film. This "throwing power" did provide limited corrosion protection to several areas without polymer coating.

Downloaded by PENNSYLVANIA STATE UNIV on June 22, 2012 | http://pubs.acs.org
Publication Date (Web): November 10, 2010 | doi: 10.1021/bk-2010-1050.ch010

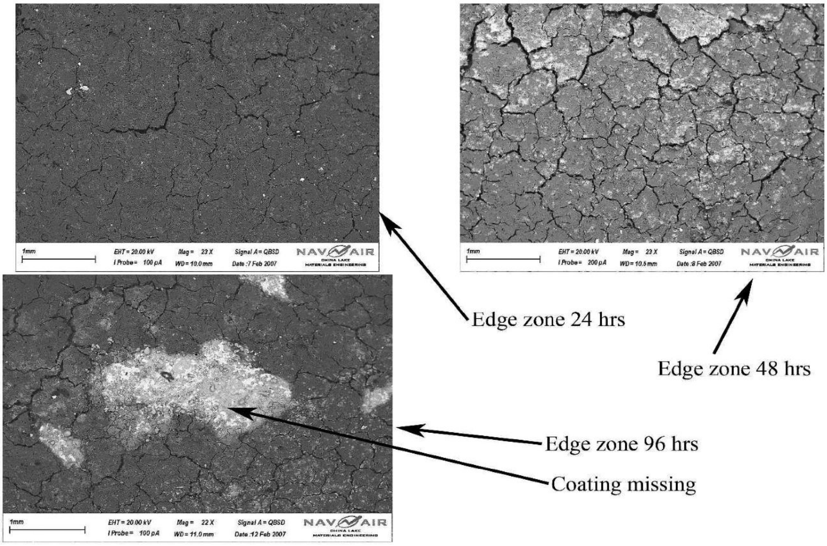

Figure 14. SEM Analysis of Outer Edges of Film After Neutral Salt Fog Exposure.

Discussion and Conclusions

The synthesis and characterization of novel polypyrrole compounds for corrosion inhibition and lubricity was investigated. A combination of NMR, IR, and cyclic voltametry was used to confirm that these materials were produced and attached onto the high strength 4340 steel alloy surface. The electroless deposition of the 3PPA and 7-PHA monomers onto high strength 4340 steel alloy substrates did not introduce toxic metals. The electroless deposition process has been shown to be an environmentally “green” method for deposition of EAPs on high strength 4340 steel alloy coupons.

Several tests were performed on the EAP coated high strength 4340 steel alloys, with comparisons to Cd-based coatings and other alternative coating materials, in order to elucidate key structure-property relationships. Galling measurements on the EAP systems showed that P(3PPA) containing hard particle additives (embedded fumed silica) showed no visible galling up to 8,000-lbs. The P(3PPA) with embedded fumed silica showed increased galling resistance comparable to IVD aluminum (though not Cd). One sample of the EAP pyrrole based system (P(7-PHA)) showed significant improvement in corrosion inhibition during neutral salt fog exposure.

The corrosion protection ability of the films was strongly correlated to film quality, with defects due to flaking or pin-holes limiting the corrosion inhibiting ability of the EAP-based systems. Improvements in film quality due to increased chain length on the pyrrole monomers produced films with significantly improved corrosion inhibition. However, the pretreatment silane compound appeared to slowly dissolve upon exposure to neutral salt fog spray. An improvement in the durability of the silane group combined with the long chain-alkyl pyrrole polymer system could potentially provide enhanced corrosion inhibition on high strength 4340 steel alloys.

Acknowledgments

The authors would like to acknowledge the financial support of the Strategic Environmental Research and Development Program (SERDP), Weapons Platforms, Program Manager, Mr. Charles Pellerin and the Office of the Director, Defense Research and Engineering.

References

1. IARC. Beryllium, Cadmium, Mercury and Exposures in the Glass Manufacturing Industry. *IARC Monogr. Eval. Carcinog. Risks Hum.* **1993**, *58*, 119–237.
2. Waalkes, M. P.; Infante, P.; Huff, J. The Scientific Fallacy of Route Specificity of Carcinogenesis with Particular Reference to Cadmium. *Regul. Toxicol. Pharmacol.* **1994**, *20*, 119–121.
3. Cherian, M. G.; Howell, S. B.; Imura, N.; Klaasaen, C. D.; Koropatnick, J.; Lazo, J. S.; Waakles, M. P. Role of Meallothionein in Carcinogenesis. *Toxicol. Appl. Pharmacol.* **1994**, *126*, 1–5.
4. NIOSH 1997 -Cadmium -NS. http://www.nsc.org/library/chemical/cadmium.htm.
5. Smith, C. J. E.; Baldwin, K. R. Some Cadmium Replacements for Use on Aircraft Components. *Prod. Finish. (London)* **1992**, *45* (6), 12–18.
6. FY98 Secretary of Defense Environmental Security Award, Award Category, Pollution Prevention–Weapons System Acquisition Team. https://www.denix.osd.mil/denix/public/news/earthday99/awards99/afaeronautical/aeronautical.html, referenced December 3, 2002.
7. *Guidance for Eliminating Cadmium from US Army Weapons Systems*, prepared by US Acquisition Pollution Prevention Support Office, April 1996.
8. *Alternative Surface Coatings and Surface Treatments for Hazardous Cadmium Plating of Small Parts*, prepared by Rosenblatt M. and Son, Inc., Arlington, VA, September 30, 1995.
9. *Active JTEG Project Summaries*, Depot Maintenance Technology Projects, Project 020303, Cadmium Alternatives for Fasteners. Updated March 2002. http://www.jdmag.wpafb.af.mil/projects2.htm, referenced December 3, 2002.
10. *The Pollution Prevention Pillar*, the Department of Defense Environmental Quality Technology Program (EQT). http://www.enviro.nfesc.navy.mil/p2library/cd/docs/dodoc/grnkpp.html, referenced December 3, 2002.
11. Shaw, G. *Long-Term Performance of Cadmium Alternatives*, US Army Tank Automotive and Armaments Command, Warren, MI, February 1999, pp 1−18.
12. Scheer, A. Tin-Zinc as a Replacement for Cadmium. Burbank Plating Service Corp., Pacoima, CA, January 2000, pp 1−2.
13. Tallman, D. E.; Bierwagon, G. P. Corrosion Protection Using Conducting Polymers. In *Handbook of Conducting Polymers: Conjugated Polymers:*

Downloaded by PENNSYLVANIA STATE UNIV on June 22, 2012 | http://pubs.acs.org
Publication Date (Web): November 10, 2010 | doi: 10.1021/bk-2010-1050.ch010

Downloaded by PENNSYLVANIA STATE UNIV on June 22, 2012 | http://pubs.acs.org
Publication Date (Web): November 10, 2010 | doi: 10.1021/bk-2010-1050.ch010

Processing and Applications, 3rd ed.; Skotheim, A., Reynolds, J. R., Eds.; CRC Press: New York, 2007; Chapter 15, p 15−1.

14. Thompson, K. G.; Byran, C. J.; Benicewicz, B. C.; Wrobleski, D. A. Los Alamos National Laboratory Report, LA-UR-92-360, 1991.
15. Wrobleski, D. A.; Benicewicz, B. C.; Thompson, K. G.; Byran, B. J. *ACS Polym. Prepr.* **1994**, *35* (1), 265–266.
16. Ren, S.; Barkey, D. *J. Electrochem. Soc.* **1992**, *139* (4), 1021–1026.
17. DeBerry, D. W. *J. Electrochem. Soc.: Electrochemical Science and Technology* **1985**, *132* (5), 1022–1026.
18. Zarras, P.; Anderson, N.; Webber, C.; Guenthner, A.; Prokopuk, N.; Stenger-Smith, J. D. Novel Conjugated Polymers Based on Derivatives of Poly(phenylene vinylene)s as Corrosion Protective Coatings in Marine Environments. *PACE Conference Proceedings*; Chapter 14, pp 175−182, September 8−9, 2004, Cologne, Germany.
19. Stenger-Smith, J. D.; Zarras, P.; Miles, M. H.; Nelson, J. G. *Intrinsically Electrically Conducting Polymers as Inhibiting Coatings*; NAWCPNS TP 8364, Unclassified, 1997.
20. Zarras, P.; He, J.; Tallman, D. E.; Anderson, N.; Guenthner, A.; Webber, C.; Stenger-Smith, J. D.; Pentony, J. M. Electroactive Polymer Coatings as Replacements for Chromate Conversion Coatings. In *Smart Coatings*; Provder, T., Baghdachi, J.; ACS Symposium Series 957; American Chemical Society: Washington, DC, 2007; Chapter 10, pp 135−151.
21. Military Specification, MIL-DTL-81706B Chemical Conversion Materials for Coating Aluminum and Aluminum Alloys, October 25, 2004.
22. Zarras, P.; Prokopuk, N.; Anderson, N.; Stenger-Smith, J. D. Investigation of Electroactive Polymers and Other Pretreatments as Replacements for Chromate Conversion Coatings: A Neutral Salt Fog and Electrochemical Impedance Spectroscopy Study. In *New Developments in Coatings Technology*; Zarras, P., Wood, T., Richey, B., Benicewicz, B. C., Eds.; ACS Symposium Series 962; American Chemical Society: Washington, DC, 2007; Chapter 4, p 40.
23. Barinov, V. Y.; Panasyuk, V. E.; Prots, S. R. Control of the Protective Properties of Polyethylene Coatings Using Molybdenum Disulphide Filling. In *Organic Coatings for Corrosion Control*; Bierwagen, G. P., Ed.; ACS Symposium Series 689; American Chemical Society: Washington, DC, 1998; Chapter 24, p 302.
24. Pickett, C. J.; Ryder, K. S. *J. Chem. Soc., Dalton Trans.* **1994**, *14*, 2181.
25. Kuhn, H. H.; Child, A. D.; Kimbrell, W. C. *Synth. Met.* **1995**, *71*, 2139.
26. Willicut, R. J.; McCarley, R. L. *Langmuir* **1995**, *11*, 296.
27. McCarley, R. L.; Willicut, R. J. *J. Am. Chem. Soc.* **1998**, *120*, 9296.
28. Friedman, L.; Shechter, H. *J. Org. Chem.* **1960**, *25* (6), 877.

Downloaded by CORNELL UNIV on June 22, 2012 | http://pubs.acs.org
Publication Date (Web): November 10, 2010 | doi: 10.1021/bk-2010-1050.ch011

Chapter 11

Polypyrrole/Aluminum Flake Hybrids as Corrosion Inhibitors for Aluminum 2024-T3

Christopher Vetter,[1] Katherine Gohmann,[2] Alice C. Harper,[2] and Victoria Johnston Gelling[1],*

[1]Department of Coatings and Polymeric Materials, North Dakota State University, 1765 NDSU Research Park Drive, Fargo, ND 58105 (USA)
[2]Department of Chemistry, Concordia College, 901 8th St S, Moorhead, MN 56562 (USA)
***V.J.Gelling@ndsu.edu**

The aluminum alloy 2024-T3 (AA 2024-T3) used in aircraft has localized corrosion issues such as pitting and intergranular corrosion. This susceptibility to localized corrosion is caused by the inherent nature of the copper-rich 2024-T3 aluminum alloy. Chromate surface treatments and chromate-containing epoxy primers are often used for the corrosion control of such aluminum alloys as 2024-T3. However, due to environmental concerns and adverse health effects surrounding such use of chromates, there is an intensive effort to find suitable replacements for chromate-based coatings. Electroactive conducting polymers (ECPs) continue to be of considerable interest as components of corrosion-resistant coating systems due to their conductivity and redox properties. One of the most studied of these conducting polymers is polypyrrole (PPy). PPy films have been shown to act as corrosion inhibitors for various metal substrates. Since the pyrrole monomer has moderate solubility in water (~1M), many groups have been investigating the aqueous electropolymerization of pyrrole onto surfaces. The use of an aqueous solution lowers the cost of waste disposal and the technique is able to be done under mild conditions.

In this paper, the synthesis of polypyrrole/aluminum flake hybrids under aqueous conditions is investigated. The polymer-coated flakes were then incorporated, at high pigment volume concentrations, into epoxy primers.

In Smart Coatings III; Baghdachi, J., et al.;
ACS Symposium Series; American Chemical Society: Washington, DC, 2010.

The resulting coatings were investigated for any corrosion inhibiting characteristics via long-term immersion in dilute Harrison's solution. This was accomplished by utilizing electrochemical impedance spectroscopy. Additionally, surface analysis and elemental analysis was performed utilizing scanning electron microscopy (SEM) and x-ray photoelectron spectroscopy (XPS). Density tests were also performed to determine the extent of polypyrrole attachment to the aluminum flake.

Downloaded by CORNELL UNIV on June 22, 2012 | http://pubs.acs.org
Publication Date (Web): November 10, 2010 | doi: 10.1021/bk-2010-1050.ch011

Introduction

Modern research in the area of organic conducting polymers, such as polypyrrole, began in 1977 with the paper "Synthesis of electrically conducting organic polymers: Halogen derivatives of polyacetylene $(CH)_x$." (*1*) The resulting doped polyacetylene was very conductive with a conductivity of 10^5 Siemens per meter, which is 10^9 times more conductive than that of the undoped polyacetylene and well into the range of conductivity seen for many metals (*2*). The key to the increased conductivity is the conjugated double bonds at the backbone of the conducting polymer. Additionally, doping of the polymer and the ability to easily oxidize the polymer enhance the conductivity of the polymer. Professor Alan J. Heeger, Professor Alan G. MacDiarmid, and Professor Hideki Shirakawa were awarded the 2000 Nobel Prize in Chemistry in part for the publication of this paper and the resulting research.

By 1980, many different conducting polymers were being studied throughout the world. In 1985, DeBerry published the result of his work on the use of polyaniline as a corrosion inhibitor for stainless steels. His work demonstrated that stainless steel electrodes coated with polyaniline thin films were passivated in acidic solutions while the same electrodes that were left untreated were rapidly corroded (*3*).

During the late 1990s, the amount of literature available on the production and uses for electroactive polymers lead to the writing of numerous review articles. McAndrew (*4*), Sitaram et al. (*5*), Yagova et al. (*6*), Lu et al. (*7*), Tallman et al. (*8*), and Spinks et al. (*9*) have all authored extensive reviews on the use of ECPs as corrosion inhibitors. Much of the research has been performed to increase the processability and, thus, the usefulness of ECPs. However, many simple polythiophenes, polyanilines, and polypyrroles are not soluble in most common solvents, making them difficult to scale up for industrial use. To make an ECP organic-soluble, many ECPs have alkyl substituents added to the polymeric backbone. The synthesis of alkyl-substituted pyrrole has yielded a polymer that is soluble in a range of organic solvents such as carbon tetrachloride, dichloromethane, and acetonitrile (*10–12*).

However, the use of an aqueous solution rather than an organic solution lowers the cost of waste disposal. The techniques employed are able to be done under mild conditions. With most governmental and industrial groups mandating the elimination of hazardous compounds, being able to polymerize pyrrole in water is desirable rather than an organic solvent. Since the pyrrole monomer has moderate solubility in water (~1M), many groups have been investigating the aqueous electropolymerization of pyrrole onto surfaces (*13–16*). Electropolymerization, however, is limiting as a technique as it is restricted to surfaces that are conducting (*15*). Chemical polymerization is a method that uses strong chemical oxidants, such as ammonium persulfate, that are able to oxidize the monomers to chemically active cation radicals. These radicals then react with the monomer molecules in solution, in this case water, yielding insoluble polymer. Conductive polymers formed in this method can deposit spontaneously onto the surface of materials that are immersed into the polymerization solution (*14*, *17*). The material does not have to be conductive as in the electrochemical deposition method. By adjusting the reaction conditions, a high yield of surface deposited conducting polymer can be deposited on to the surface of interest.

Downloaded by CORNELL UNIV on June 22, 2012 | http://pubs.acs.org
Publication Date (Web): November 10, 2010 | doi: 10.1021/bk-2010-1050.ch011

Experimental

Catechol (CAT) and pyrrole monomer (Py) were obtained from TCI America. Aluminum flake (Stapa Aloxal PM 2010) was obtained from Eckhart America; ammonium persulfate and ethanol (EtOH) were obtained from J.T. Baker. Acetone was obtained from E.M.D. and methyl ethyl ketone (MEK) from Alfa Aesar. Perchloroethylene was purchased from Sigma-Aldrich. All chemicals were used as received. Pacothane release film was obtained from Pacothane Technologies.

The polypyrrole/aluminum flake hybrids were prepared by combining the Al-flake paste with water and ammonium persulfate. The solution was stirred for fifteen minutes. Catechol was added and the solution was stirred for an hour. Pyrrole monomer was then added at which point the solution would turn black indicating the formation of polypyrrole. The polypyrrole/aluminum flake solution was then stirred overnight. To isolate the polypyrrole coated flakes, the solution was vacuum filtered and the resultant paste was placed on Pacothane release film and placed in an oven at 45°C overnight. The dried film was ground into a fine powder using mortar and pestle and passed through a 150 μm steel mesh sieve.

XPS measurements were performed on a PHI model 555 XPS instrument using Mg K-alpha x-ray excitation and a cylindrical mirror electron energy analyzer. Photoelectron spectra were obtained at 100 eV pass energy for survey and 25 eV pass energy for high resolution. During measurements, a low-energy electron flux (1.0 eV, 0.9 mA) was used to neutralize all samples. During curve fittings, charge compensations were done by setting the C 1s peaks for C-C/H at 285.0 eV, and a Gaussian-Lorentzian model with a 90:10 ratio was applied.

Samples were prepared for SEM by sprinkling onto carbon tape attached to aluminum mounts. Loose sample particles were removed by short bursts of compressed air. The sample was then coated with gold using a Balzers SCD 030 sputter coater. Images were obtained using a JEOL JSM-6300 Scanning Electron Microscope. Magnification, accelerating voltage values and micron bars are listed in each figure.

Downloaded by CORNELL UNIV on June 22, 2012 | http://pubs.acs.org
Publication Date (Web): November 10, 2010 | doi: 10.1021/bk-2010-1050.ch011

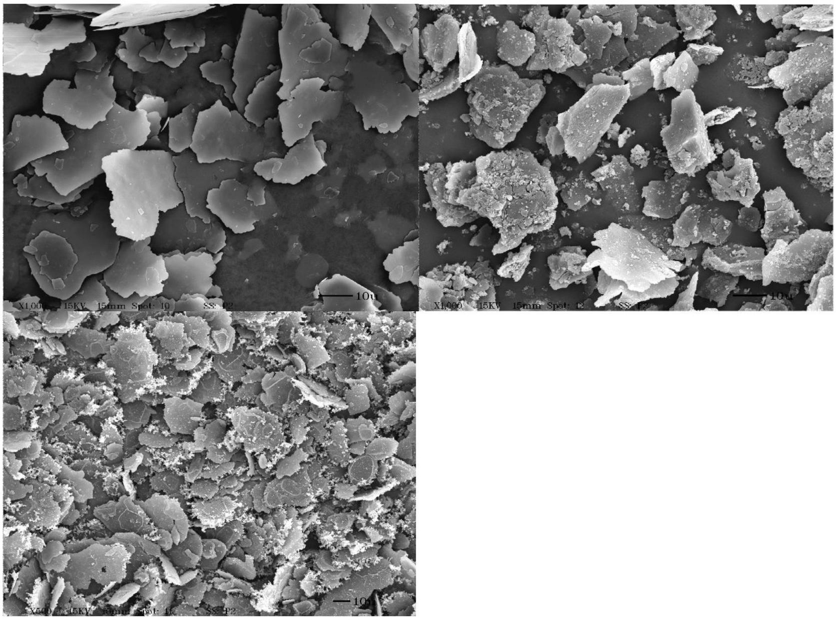
X1,000 15KV 15mm Spot: 10 SS: P2
10u
X1,000 15KV 15mm Spot: 12 SS: P2
10u
10u

Figure 1. SEM of as-received aluminum flake (left), flake coating with polypyrrole with Catechol present (middle), and flake coated with polypyrrole without Catechol present (right).

The epoxy primer was made using epon 828 and epicure 3175. Both were supplied by Hexion. The solvent used was methyl isobutyl ketone supplied by Aqua Solutions. The epon and epicure were mixed in a ratio of 1 equivalent of epoxy to 1.2 equivalents of polyamide (epicure). This was to ensure a maximum amount of crosslinking which would increase barrier properties as well as the hardness of the coating.

The pigment was then incorporated into an epoxy primer and applied to aluminum 2024 T3 panels using a drawdown bar. The primer was made in a wide range of pigment volume content. Films were formulated with pigment volume concentrations (PVC) ranging from 20% to 45%. This was used to determine what effect the PVC of a coating had on its corresponding corrosion inhibiting properties. The surface of the panels were prepared prior to coating using first 150 grit sandpaper and then 600 grit sandpaper. The panels were then degreased using ethanol. The films were applied used a drawn down bar at 8 mils wet thickness. The dry film thickness depended somewhat on the PVC of the films with most in the range of 5.5 mils to 7.5 mils.

Periodically during the immersion in dilute Harrison's solution (0.35% $(NH_4)_2SO_4$ and 0.05% NaCl), electrochemical impedance spectroscopy (EIS) was performed which provided detailed information regarding the condition of the coating. A minimum of three replicates was completed for each coating, with typical results presented in the figures below. All data is presented in raw impedance form and has not been adjusted for surface area of the setup. The electrochemical cell that was used for the EIS experiments consisted of a polyvinylchloride pipe with an inner diameter of 2.6 cm attached to the substrate using Marine Goop® adhesive. The setup included a platinum coated mesh counter electrode and saturated calomel reference electrode (SCE). The electrochemical cell had an exposed area of 5.3 cm^2. Gamry® Instrument's PC-4 or FAS1 was used to conduct the EIS experiments. An initial AC perturbation of 10 mV rms was applied to the samples. The frequency range studied was from 100,000 Hz to 0.01 Hz.

Downloaded by CORNELL UNIV on June 22, 2012 | http://pubs.acs.org
Publication Date (Web): November 10, 2010 | doi: 10.1021/bk-2010-1050.ch011

Results and Discussion

Before determining how well the coated flakes would perform in coatings, investigations were completed to determine the adherence of the polypyrrole to the aluminum flake. This was accomplished by performing a density test in perchloroethylene (density of 1.623 g/cm^3). The density of bare aluminum flake should be greater than that of the percholorethylene and the polypyrrole has a density of approximately 1.05 g/cm^3 (*18*, *19*). By using these values, the aluminum flake should sink in the presence of perchloroethylene and any un-adhered to the aluminum flake should float. The density test was performed for the polypyrrole coated flakes, synthesized both in the presence and absence of catechol. The density test showed that the majority of the polypyrrole was adhered to the flake, when catechol was present in the reaction, as there was very little free floating polypyrrole. The flake coated without catechol displayed significantly more free polypyrrole as determined visually. This would seem to indicate that while the catechol was not necessary to have polymerization of pyrrole under the conditions used in this investigation; the catechol did increase the adherence of the polypyrrole to the aluminum substrate. This is most likely due to the electron-transfer properties of catechol. Additionally, the catechol may allow for more initiation sites for polymerization on the surface of the aluminum flake.

Once it was established that the polypyrrole was coating the flake and not merely forming polymer in solution, SEM was performed to determine if any structural changes had taken place to the flake. As can be seen from Figure 1 below, the original flakes are on the order of 10-30 μm across. After performing the synthesis both in the presence and absence of catechol, both show that the flakes have not been damaged by the synthesis process, as the flake size appeared stable, yet there is a distinct coating on the flake as shown in Figure 1. Interestingly, micro/nano structures were observed on the aluminum flake when no Catechol was used during the synthesis as shown in Figure 2.

Downloaded by CORNELL UNIV on June 22, 2012 | http://pubs.acs.org
Publication Date (Web): November 10, 2010 | doi: 10.1021/bk-2010-1050.ch011

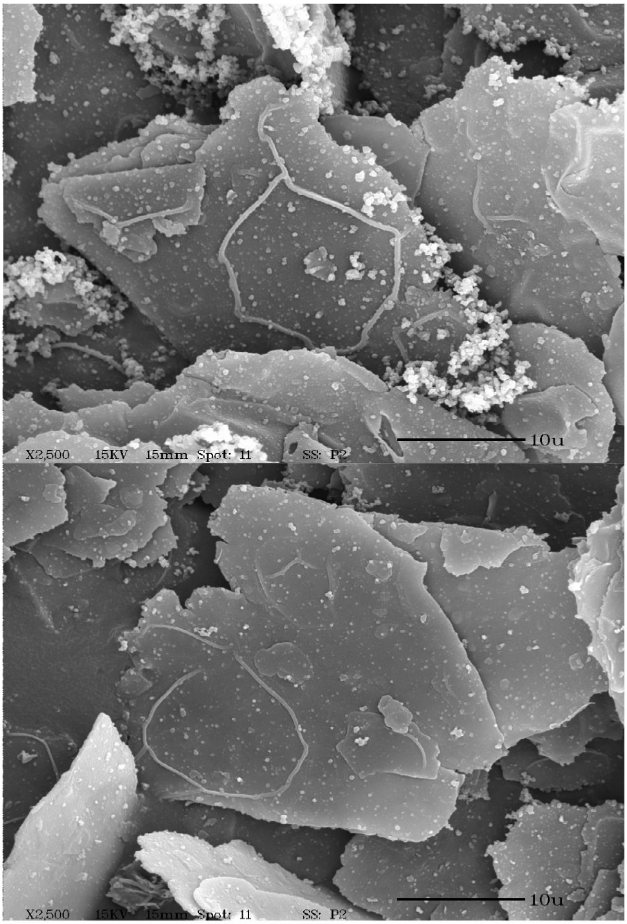
10u
X2,500 15KV 15mm Spot: 11 SS: P2
10u
X2,500 15KV 15mm Spot: 11 SS: P2

Figure 2. SEM images of structures on aluminum flake.

The cause of the structures is still unknown, however it is suggested that the structures could be due to the surfactant, 1-methoxy-2-propanol, used by the manufacturer of the aluminum flakes. There has been a recent report in the literature by Zhang et al. on the synthesis of polypyrrole nanostructures. Zhang was able to control the nature of the nanostructures by utilizing different surfactants with various oxidizing agents. Wire, ribbon, and sphere nanostructures of polypyrrole were formed during the study. Specifically, it was determined that ammonium persulfate was able to form ribbon-like or wire-like nanostructures in the presence of various surfactants (*20*).

Downloaded by CORNELL UNIV on June 22, 2012 | http://pubs.acs.org
Publication Date (Web): November 10, 2010 | doi: 10.1021/bk-2010-1050.ch011

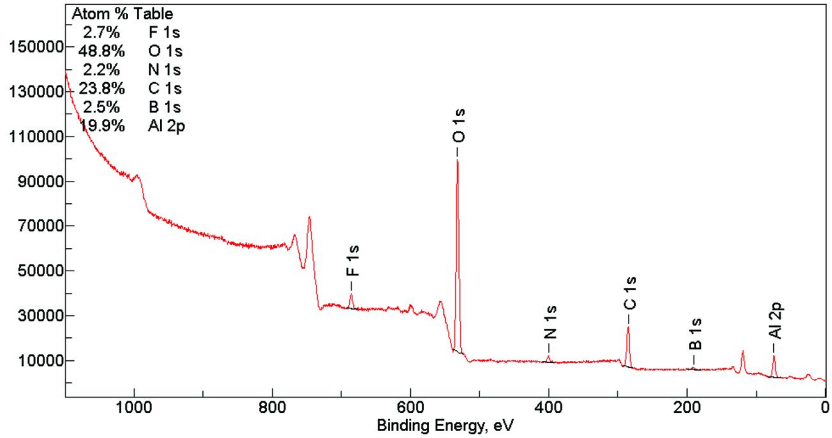

Figure 3. Aluminum flake as received from manufacturer.

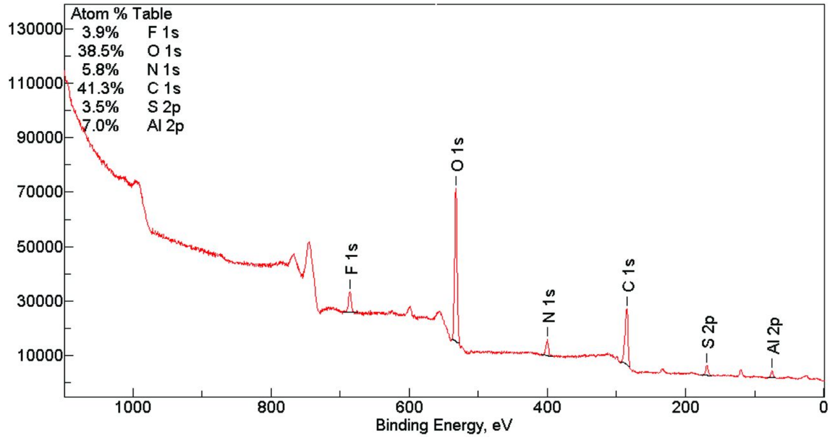

Figure 4. Aluminum Flake/ polypyrrole hybrid synthesized in the presence of catechol and ammonium persulfate.

X-ray photoelectron spectroscopy was performed on the samples to determine if the coated flakes did in fact have amine nitrogens that would be due to polypyrrole on the surface. As shown in Figure 3, the as-received flake displayed predominately aluminum, carbon, and oxygen. This is due to the native aluminum oxide layer which forms on the flakes as well as the 1-methoxy-2-propanol surfactant. In Figure 4, the results of the polypyrrole/aluminum flake hybrids synthesized in the presence of catechol are shown, the nitrogen and carbon atom percentage increases as compared to the uncoated flakes as would be expected as polypyrrole is now present on the surface. The N 1s spectrum has the major component at 401.82eV is attributable to the amine-like structure in polypyrrole (*21*, *22*). The shoulder at 399.49eV could be attributed to an imine nitrogen (*21*, *22*).

Downloaded by CORNELL UNIV on June 22, 2012 | http://pubs.acs.org
Publication Date (Web): November 10, 2010 | doi: 10.1021/bk-2010-1050.ch011

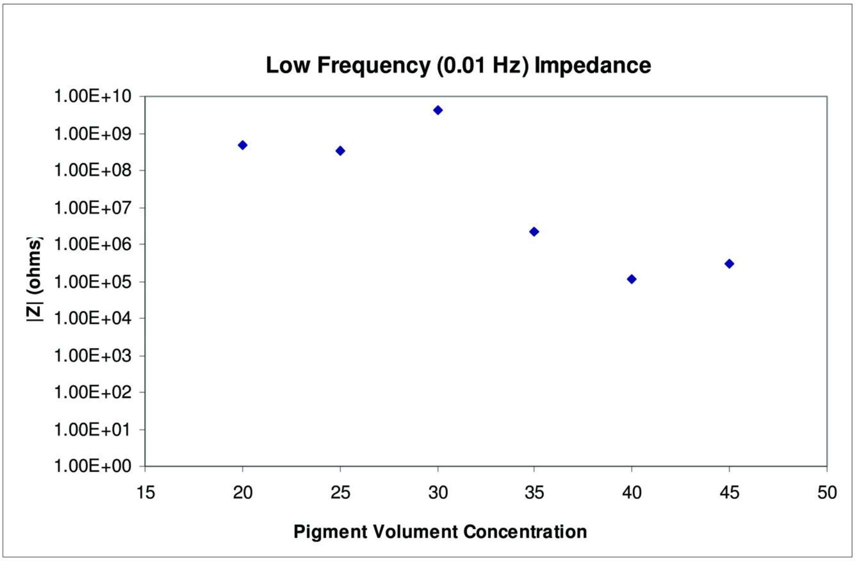

Figure 5. Low frequency impedance after 30 minutes exposure to dilute Harrison's solution.

As one can see in Figure 5, the low frequency impedance measured approximately 30 minutes after immersion in DHS depended greatly on the pigment volume concentration of the coatings; which was expected. The lower PVC coating displayed a higher impedance which would indicate that, indeed, the coating was below the critical pigment concentration therefore the coating is still displaying barrier properties indicative of the epoxy coating. Interestingly at a PVC of 30% an increase in low frequency impedance is observed possibly due to an aligning of the flake pigments at this concentration. However, as the pigment concentration is increased further, a decrease in impedance was observed indicating that the CPVC has been surpassed. Additionally this may suggest that there was conductivity in the coating due to the conductive polypyrrole coated flake. It appears that the lowest initial impedance is observed for the 40% PVC coating with a value of 1.18 x 10^5 ohms.

Samples were prepared using the as-received aluminum flake at 25%, 30%, and 35% PVC to allow for the determination of the affect of the polypyrrole on the resulting coating. Not only did the as-received aluminum flake containing coatings display a much higher initial impedance, the overall behavior during the immersion time is notably different between the samples as show in Figures 6−8. Arguably this could be due to an error involved in the CPV calculations as no contribution was included from any non-adhered polypyrrole particulates. This would cause the polypyrrole aluminum flake coatings to effectively have higher CPV than those calculated. An alternate conclusion would be that the polypyrrole coated aluminum flake would have a higher conductivity than the as-received aluminum flake due to the naturally high resistivity of aluminum oxide that would inherently form on the aluminum flake. When one takes into account the fact that even after significantly long immersions times, 1200 hours, with

Downloaded by CORNELL UNIV on June 22, 2012 | http://pubs.acs.org
Publication Date (Web): November 10, 2010 | doi: 10.1021/bk-2010-1050.ch011

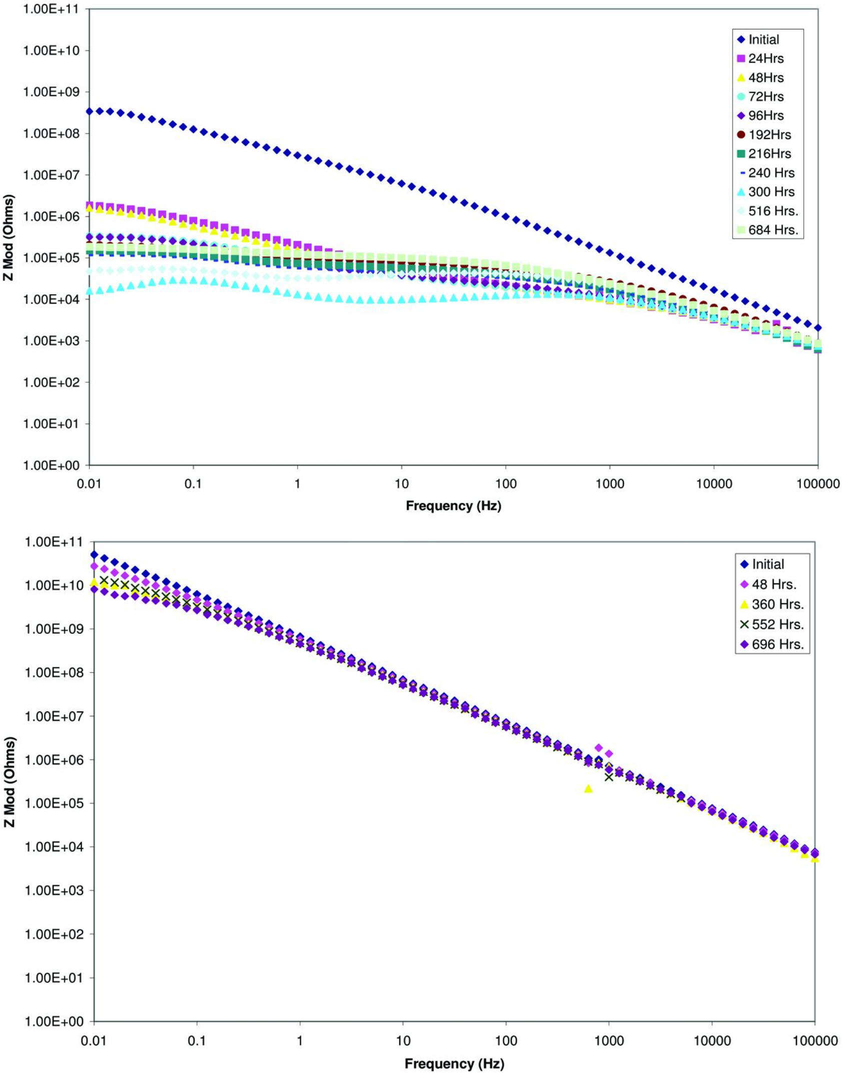

Figure 6. 25% CPV coatings made with polypyrrole coated aluminum flake (top) and as-received aluminum flake (bottom).

correspondingly low impedance values as those observed in Figure 7 one would assume that rampant corrosion would be detected visually. That is not the case. Coatings were removed from the substrate only to find a rather unaffected surface. It is, therefore, the authors' suggestion that the decrease in impedance is due to an increase in the conductivity of the coating due to hydration affects. Instead of the natural progression towards failure, the coating with the polypyrrole is able to maintain the integrity of the surface. Further experiments will be conducted to elucidate the mechanism behind the protection afforded by the polypyrrole/ aluminum flake hybrids.

Downloaded by CORNELL UNIV on June 22, 2012 | http://pubs.acs.org
Publication Date (Web): November 10, 2010 | doi: 10.1021/bk-2010-1050.ch011

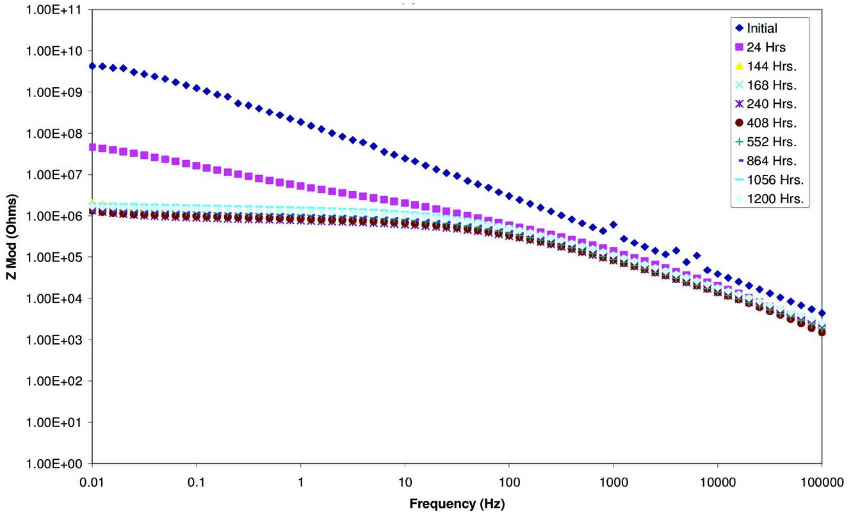

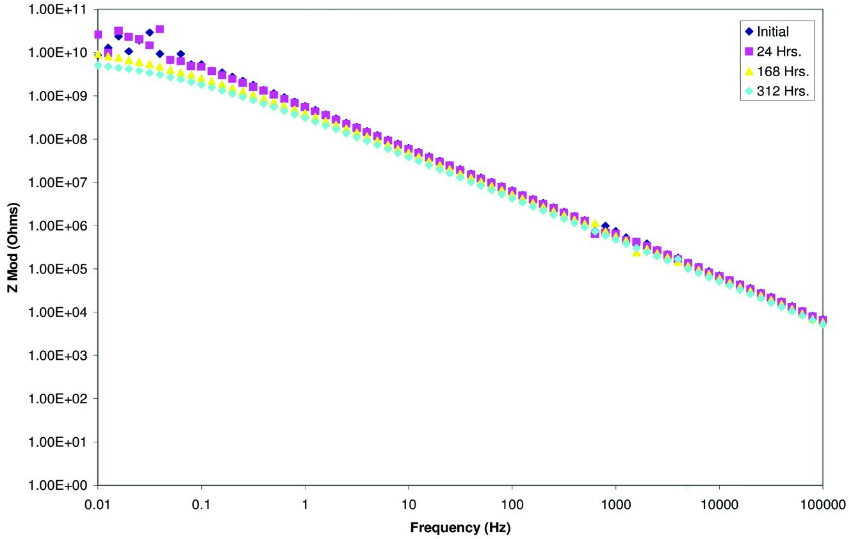

Figure 7. 30% PVC coatings made with polypyrrole coated aluminum flake (top) and as-received aluminum flake (bottom).

Conclusions

Aluminum flake was coated with polypyrrole under various synthesis conditions. It was determined that the polypyrrole was better adhered to the flake when catechol was included in the synthesis. This is most likely due to the electron-transfer properties of the catechol. Conductive films were able to be formulated using high pigment volume concentrations of the polypyrrole coated aluminum flake. The resulting films were exposed to dilute Harrison's solution and periodically monitored via electrochemical impedance spectroscopy. It was

Downloaded by CORNELL UNIV on June 22, 2012 | http://pubs.acs.org
Publication Date (Web): November 10, 2010 | doi: 10.1021/bk-2010-1050.ch011

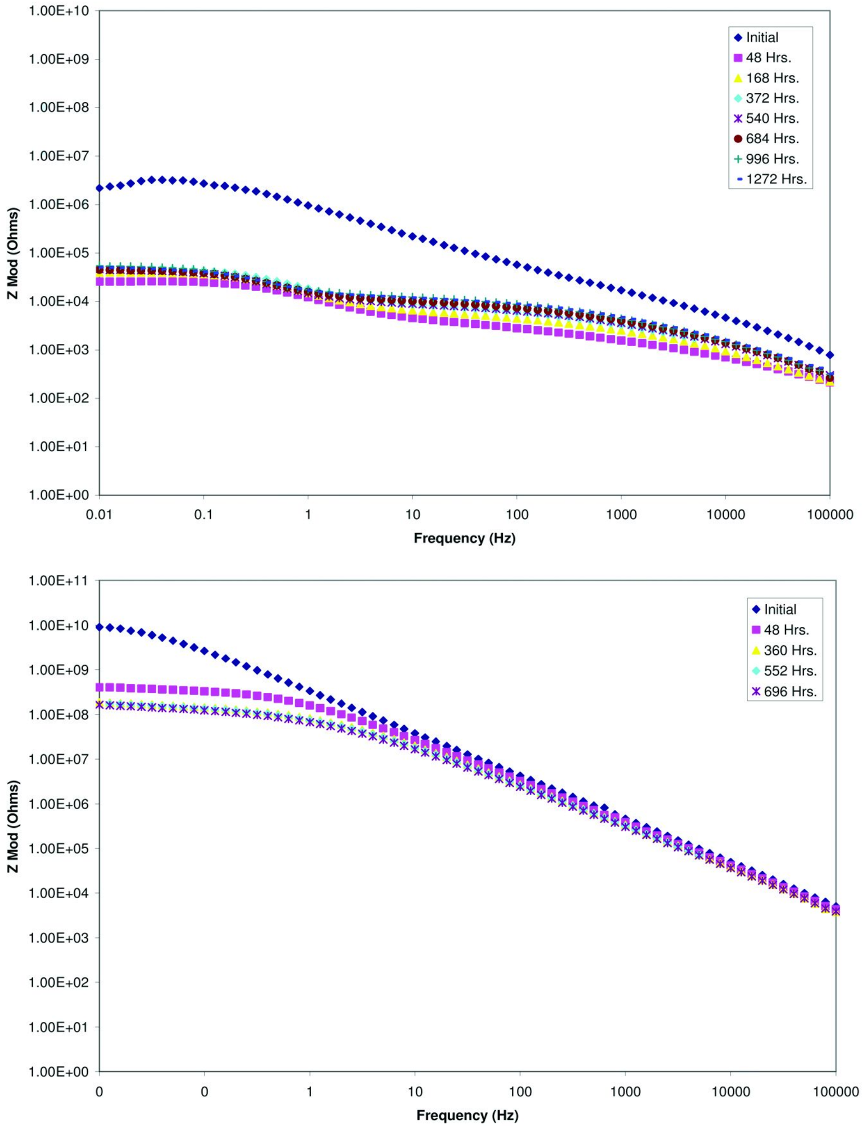

Figure 8. 35% PVC coatings made with polypyrrole coated aluminum flake (top) and as-received aluminum flake (bottom).

determined that the coatings formulated with the polypyrrole coated aluminum flake displayed a lower impedance than that of a similarly formulated coating with as-received flake. Additionally, it appears that the low impedance of the coating did not correspond with corrosion of the substrate. This was determined by physically removing the coating and visually monitoring the surface.

Acknowledgments

The authors would like to thank the Army Research Laboratory (Contract No. W911NF-04-2-0029) and Air Force Office of Scientific Research (Grant F49620-01-1-0333 Prime is U. of Minnesota (Ed Cussler)) for the generous financial support.

The authors would also like to thank Scott Payne, Assistant Director, of the NDSU Electron Microscopy Center for the SEM results and Bing Luo at the IT-Characterization Facility at University of Minnesota for the XPS results.

Downloaded by CORNELL UNIV on June 22, 2012 | http://pubs.acs.org
Publication Date (Web): November 10, 2010 | doi: 10.1021/bk-2010-1050.ch011

References

1. Shirakawa, H.; Louis, E. J.; MacDiarmid, A. G.; Chiang, C. K.; Heeger, A. H. *J. Chem. Soc., Chem. Comm.* **1977**, 578.
2. The Royal Swedish Academy of Sciences. Press release. 2000, pp 1−15.
3. DeBerry, D. W. *J. Electrochem. Soc.* **1985**, *132*, 1022–1026.
4. McAndrew, T. P.; Miller, S. A.; Gilicinshki, A. G.; Robeson, L. M. *Polym. Mater. Sci. Eng.* **1995**, *74*, 204–206.
5. Sitaram, S. P.; Stoffer, J. O.; O'Keefe, T. J. *J. Coat. Technol.* **1997**, *69*, 65–69.
6. Yagova, I. V.; Ivanov, S. S.; Bykov, I. V.; Yagov, V. V. *Prot. Met.* **1998**, *34*, 132–136.
7. Lu, W.-K.; Basak, S.; Elsenbaumer, R. L. In *Handbook of Conductive Polymers*; Skotheim, T. A., Elsenbaumer, R. L., Reynolds, J. R., Ed.; Marcel Dekker, Inc: New York, 1998; p 881−920.
8. Tallman, D. E.; et al. *J. Electrochem. Soc.* **2002**, *149*, C173.
9. Spinks, G. M.; et al. *J. Solid State Electrochem.* **2002**, *6*, 85–100.
10. Ruehe, J.; Ezquerra, T.; Wegner, G. *Makromol. Chem.* **1989**, *10*, 103–108.
11. Patil, A. O.; et al. *J. Am. Chem. Soc.* **1987**, *109*, 1858–1859.
12. Ashraf, S. A.; et al. *Polymer* **1996**, *37*, 2811–2819.
13. Prissanaroon, W.; et al. Electropolymerisation of pyrrole on copper in aqueous media. *Synth. Met.* **2004**, *142* (1−3), 25–34.
14. Tallman, D. E.; et al. Electroactive conducting polymers for corrosion control. Part 1. General introduction and a review of non-ferrous metals. *J. Solid State Electrochem.* **2002**, *6*, 73–84.
15. Malinauskas, A. Chemical deposition of conducting polymers. *Polymer* **2001**, *42*, 3957–3972.
16. Martins, J. I.; et al. Polypyrrole coatings as a treatment for zinc-coated steel surfaces against corrosion. *Corros. Sci.* **2004**, *46* (10), 2361–2381.
17. Jureviciute, I.; Bruckenstein, S. Electrochemical activity of chemically deposited polypyrrole films. *J. Solid State Electrochem.* **2003**, *7* (9), 554–560.
18. Eckart. *Technical Data Sheet*; Jan 2004.
19. Sigma-Aldrich. *Polypyrrole*; 2006.
20. Zhang, X.; et al. Controllable Synthesis of Conducting Polypyrrole Nanostructures. *J. Phys. Chem. B* **2006**, *110*, 1158–1165.

21. Neoh, K. G. Structure and Degradation Behavior of Polypyrrole Doped with Sulfonate Anions of Different Sizes Subjected to Undoping-Redoping Cycles. *Chem. Mater.* **1996**, 167–172.
22. Deng, S.; Advincula, R. Polymethacrylate Functionalized Polypyrrole Network Films on Indium Tin Oxide: Electropolymerization of a Precursor Polymer and Comonomer. *Chem. Mater.* **2002**, *14*, 4073–4080.

Downloaded by CORNELL UNIV on June 22, 2012 | http://pubs.acs.org
Publication Date (Web): November 10, 2010 | doi: 10.1021/bk-2010-1050.ch011

Chapter 12

Development of Corrosion Protection Coatings for AA2024-T3 Using Micro-Encapsulated Inhibitors

D. Raps,[1,3,*] T. Hack,[1] M. Kolb,[1] M. L. Zheludkevich,[2] and O. Nuyken[3]

[1]EADS Innovation Works, 81663 Munich, Germany
[2]University of Aveiro, CICECO, Dep. Ceramics and Glass Eng., 3810-193, Aveiro, Portugal
[3]Technical University Munich, Department of Macromolecular Chemistry, 85748 Garching, Germany
[*]Dominik.Raps@eads.net

The paper describes the development of a chromate-free self-healing corrosion protection coating for high strength aluminium alloys. The concept for this approach is based on using inhibitor loaded microcapsules incorporated in the paint film. The capsules are produced by means of interfacial polymerisation. The capsules and the loaded paints are characterised by Scanning Electron microscopy (SEM), Thermal Gravimetric Analysis and Differential Scanning calorimetry (TGA/DSC). The barrier properties and the active corrosion protection properties on AA2024-T3 are studied using Electrochemical Impedance Spectroscopy (EIS), Scanning Vibrating Electrode Technique (SVET) and standard corrosion tests. Encapsulation of inhibitors improves the effectiveness by increase of inhibition capacity and compatibility to organic paint primers.

Introduction

Lightweight and high strength materials are used in the aircraft industry for structural applications. Corrosion-induced degradation is the most important criterion in the determination of the service life and inspection intervals of an aircraft. The rate of corrosion is influenced by many factors, such as temperature,

In Smart Coatings III; Baghdachi, J., et al.;
ACS Symposium Series; American Chemical Society: Washington, DC, 2010.

moisture, chemical compounds and electrolytes. The stability of the structural material depends on the thermodynamic and kinetic behaviour of the system. Aluminium based materials are prone to the corrosion degradation because of their strong requisition to form more stable forms such as aluminium oxides. The corrosion kinetics of a given substrate can be influenced by the use of protective layers which can provide a physical barrier for the corrosive species. The protective coatings drastically reduce the rate of corrosion making metals resistant to corrosion in adverse environmental conditions and allowing them to be used in technological applications. The performance of a coating system is dependent on its barrier and adhesion properties as well as its ability to prohibit corrosion of exposed metal substrate at flaws and damaged sites. The adhesion properties of a coating help to prevent delamination initiated by a coating defect. The leachable corrosion inhibitor of a coating is essential for inhibiting initiation of delamination, preventing corrosion of exposed metal and protecting the substrate/coating interface. To date, corrosion protection of aluminium alloys has been achieved using hexavalent chromium based compounds in both surface pre-treatments and organic primers as potent corrosion inhibitors (*1*, *2*). The functionality of the chromate species in pre-treatments and coatings is unique. They are able to stabilise the aluminium oxide, when used as compounds in pre-treatment processes even at very low quantities. Furthermore, they protect active defect sites, where metallic surfaces are exposed to aggressive electrolytes. They dissolve fast enough to protect the aluminium before corrosion processes can be initiated and they leach slowly enough from the coating to provide long-term protection. Beyond that, they do not show negative impacts on the paint properties, such as curing conditions or susceptibility to operational fluids. However, the use of chromates will be restricted by the REACH (Registration, Evaluation and Authorisation of Chemicals) legislation due to their toxicity and carcinogenic properties (*3*). Furthermore, despite the increasing use of carbon fibre reinforced plastics as structural material, it is essential to extend the service life of aircrafts currently in service and to reduce maintenance costs associated with the ongoing use of aluminium alloys in the aircraft industry.

Need for Self-Healing Coatings

Polymer coatings in the aircraft industry provide superior properties, such as chemical and mechanical stability (*4*). The passive corrosion protection performance of coatings depends on adhesion to the metal, thickness and permeability. Because no technical coating is perfect, coating degradation due to cracks or imperfections occurs. As the degradation of protection systems develops faster after the protective barrier is broken, it is necessary to provide active corrosion protection based on self-healing of defects in order to provide a long-term effect (*5*). The term “self-healing” refers to the self-recovery of initial material properties, after detrimental impact from external factors. Smart coatings are materials, which are capable of adapting their properties dynamically to an external stimulus. In the case of protective coatings the main function is corrosion protection. Thus if coating is capable to keep a high level of corrosion protection after being damaged by any external mechanism it can be also considered as self-healing coating (*6*). One of the possible approaches is use of leachable inhibiting compounds which can be released from the coating to the defect site and stop propagation of the corrosion processes there. The release of ingredients from the coating can be controlled by chemical signals such as acid-base reactions, electrochemical reactions and photochemical reactions, pH, ionic strength or by physical signals such as temperature, pressure, mechanical influences, surface tension and electrical or magnetic fields.

The chromate based pre-treatments and coatings can be called smart self-healing coatings, because on the one hand they react on demand and on the other they show self-recovering properties by protection of the substrates after destructive impacts.

The desired new generation of smart self-healing anticorrosion coatings may be achieved using encapsulated inhibitors (*7*). The coatings loaded with encapsulated corrosion inhibitors are capable to provide an effective self-healing ability in the coating. The way of encapsulation of active matters will allow the incorporation of different inhibitors into the polymer matrices without the negative effect of inhibitors on the stability of the coating and without deactivation of the inhibitor resulting from strong interaction with the polymer (*8*, *9*). Encapsulation can also help to achieve a uniform distribution of the inhibitors in the coating as well as a higher filling degree. Because the environmentally benign inhibitors do not show the same grade of effectiveness as chromate based pigments, an intelligent application mode might compensate for the lack of inhibition activity.

Inhibition and Self-Healing Concepts

There are different approaches on immobilization of corrosion inhibiting compounds in micro-/nano-carriers reported in the literature. Plasma polymerisation was reported as a method to encapsulate triazole inhibitors to produce plasma polymerised pyrrole layers. The plasma treated triazole can be used in epoxy resins for slow and continuous release (*10*). Anionic inhibitors can be immobilised by anion-exchange pigments, as described on the example of Al-Zn-decavanadate hydrotalcite pigments. Corrosion protection is provided by release of vanadates or Zn^{2+}. Leaching of these inhibitors is reported to be sufficient to suppress corrosion in scribe areas. Inhibiting decavanadate is exchanged for chlorides, attacking ions are taken up and nucleate a new hydrotalcite phase (*11*). Inhibiting inorganic cations can also be incorporated as exchangeable ions associated with cation-exchange solids (*12*). Hollow cellular structures derived from zeolites provide a high loading capacity for organic or inorganic inhibitors (*13*).

Further approaches to develop loaded micro- and nanocontainers include the use of dendrimers or hyper branched polymers (*14*), suspension and emulsion polymerisation around latex particles (*15*), layer-by-layer assembly of oppositely charged species using polyelectrolytes, conductive polymers and nanoparticles as constituents of the nanocontainer shell (*16*), and the use of ultrasonic waves to fabricate inorganic and composite hollow nanospheres (*17*).

Self-healing by polymerisation was the first type of capsule containing coatings for the self-repair ability of polymers and polymer coatings. Healing is

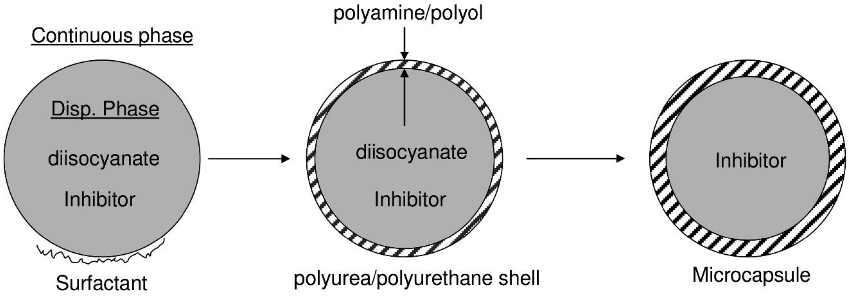

Figure 1. Formation of microcapsules by means of interfacial polyaddition

accomplished by incorporating a microencapsulated healing agent and a catalytic chemical trigger within an epoxy matrix. Different microcapsules measuring 50 to 100 µm are filled with monomers that are compliant to the coating matrix, and an appropriate catalyst that may initiate the polymerisation of the monomer. An approaching crack ruptures embedded microcapsules, releasing healing agent into the crack plane through capillary action. Polymerisation is triggered by contact with the embedded catalyst, bonding the crack faces (*18*, *19*).

Reviews on micro-encapsulation techniques and their applications can be found in references (*20*–*25*). Recent developments focus primarily on the fabrication of hollow spheres, which employ conventional emulsion/interfacial polymerisation processes as templating techniques (*26*–*29*). The concept of encapsulating a liquid polymer as a healing agent has also been proposed for one component paint systems. Microcapsules containing the one component paint can be encapsulated in micro-spheres and incorporated in the paint matrix. The corrosion resistance is improved by dispensing the encapsulated paint in the case of damage to the coating (*30*).

A new concept for the production of smart coating systems is the incorporation of nano-reservoirs produced by polyelectrolyte layer-by-layer (LbL) shells into conventional coating matrices. The nano-scale carriers can be loaded with inhibiting species and react as a “passive host” – “active guest” structure in the coating. The LbL assembled shells change their permeability depending on the pH and ionic strength. The inhibitors are encapsulated in the containers and are released when corrosion processes start at a defect site of the coating (*31*–*33*). Electrochemically active corrosion inhibitors can be absorbed onto a layer-by-layer assembled organic-inorganic multilayer coating to provide enhanced corrosion protection of metals (*34*).

The approach described in this paper covers the encapsulation of inhibitors into microcapsules and incorporation of the same into organic paint primers in order to attain a high loading degree of inhibitors in the coatings without having any influence on the primer chemistry. Interfacial oil-in-water microemulsion polymerization was used here to encapsulate oil-soluble corrosion inhibitors. The capsules provide a shelter for the inhibitors, meaning that they do not interact with the compounds of the paint matrix and are available when they are needed, so to speak, in the event of chemical or mechanical damage to the coating. One of the

Table I. Overview of synthesized microcapsules

Sample name	*Inhibitor*	*Core material 150 ml*	*Cont. phase 600 ml*	*Mon. sol. 1 DVL [g]*	*Mon. sol.2 DETA [g]*
AV	--	Ardrox AV 15	H_2O	13.3	6.87
HCBD	--	hexachlorobutadiene	H_2O	13.3	6.87
NA_1	--	diisopropylnaphth.	H_2O	13.3	6.87
NA	--	diisopropylnaphth.	H_2O	26.6	6.87
NA-MBT-16.7	30 g MBT	diisopropylnaphth.	H_2O	26.6	6.87
NA-MBT-28.6	60 g MBT	diisopropylnaphth.	H_2O	26.6	6.87
NA-MBI-16.7	30 g MBI	diisopropylnaphth.	H_2O	26.6	6.87
NA-8HQ-16.7	30 g 8-HQ	diisopropylnaphth.	H_2O	26.6	6.87

DVL: diphenylmethanediisocyanate
NA: diisopropylnaphthaline
AV: Ardrox AV 15 (Chemetall)
MBT: 2-mercaptobenzothiazole
PVA: polyvinyl alcohol
DETA: diethylenetriamine
HCBD: hexachloro butadiene
MBI: 2-mercaptobenzimidazole
8-HQ: 8-hydroxychinoline

primary concerns regarding organic inhibitors is the interaction of the inhibitors with the paint chemistry, e.g. disturbing the curing process or losing their activity and mobility due to chemical bonding with the paint. This drawback can be overcome using suggested encapsulated inhibitors. A beneficial property of the fluid used as oil in the capsules is the water displacing ability which can temporarily repel the electrolyte from the metal surface assisting absorption of the encapsulated inhibitor on the substrate. Combination of conventional accelerated weathering tests together with integral electrochemical techniques and localised methods were used in the present work to assess the corrosion protection performance and the self-healing ability of the developed coatings.

Experimental

Microcapsule Synthesis

The production of microcapsules by means of interfacial polyaddition is used widely due to its simple principle (*35–39*). Polyaddition is favoured compared to polycondensation because of the absence of interfering by-products. Figure 1 shows a schematic of the formation of microcapsules with an organic dispersive phase. Because only organic inhibitors are used in the microcapsules, the production of the microcapsules focuses on organic solvents as dispersive phase. For the synthesis, the respective inhibitor is dissolved or dispersed in the organic solvent (core material) containing one reaction partner (e.g. diisocyanate) of the

Table II. Paint configurations for self-healing coating system

Paint configurations	*Incorp. capsules*	*Inhibitor*	*Inhibitor content in capsule core [wt.-%]*	*Inhibitor amount in dry paint film [wt.-%]*
Cr (VI) ref.	--	Cr (VI) based	--	15
Non-inh.	--	non-inhibited	--	--
MBT-2.5	NA-MBT1	2-mercaptobenzothiazole	16.7	2.5
MBT-5	NA-MBT1	2-mercaptobenzothiazole	16.7	5.0
MBT-10	NA-MBT2	2-mercaptobenzothiazole	28.6	10.0
8-HQ-2.5	NA-8HQ	8-hydroxychinoline	16.7	2.5
8-HQ-5	NA-8HQ	8-hydroxychinoline	16.7	5.0
MBI-2.5	NA-MBI	2-mercaptobenzimidazole	16.7	2.5

polyaddition reaction. The organic phase is then dispersed in the aqueous phase by means of Ultra Turrax (Laboratory processing plant: Esco EL1). The resulting dispersion is stabilised by a dispersing agent. Then an aqueous solution containing the second reaction partner (e.g. polyamine) is poured into the dispersion. The polyaddition of the isocyanate with the amine takes place at the interface of both phases and the shell is formed. The wall thickness is limited by diffusion of the reactants through the wall.

The following example describes the synthesis of sample NA-MBT-16.7. Table I shows an overview of the different capsules produced in this work. A typical synthesis path, as example for polyurea wall material (with encapsulated corrosion inhibitors), is carried out in the following steps. The continuous phase is poured into the reactor and heated up to 40 °C. Then the monomer solution 1 (disperse phase) is poured into the continuous phase and dispersed by means of ultra turrax. The speed was set to the maximum speed of 15,000 rpm since previous tests have shown that this speed leads to the desired sizes of microcapsules. The dispersing time is set to 1 min. Then the turrax is turned off and the horseshoe mixer is set to 300 rpm. The monomer solution 2 is then added to the dispersion within 30 s. After 1 h, the thermostat is turned off and the speed of the horseshoe mixer is reduced to 300 rpm.

1. *Continuous Phase*

Polyvinyl alcohol (PVA) is used as a surfactant (2 wt.-% in the aqueous phase). 12 g polyvinyl alcohol (Mw = 10.000 g/mol, 80 % hydrolysed) are dissolved in 600 ml deionised water by heating the water bath to 80 °C.

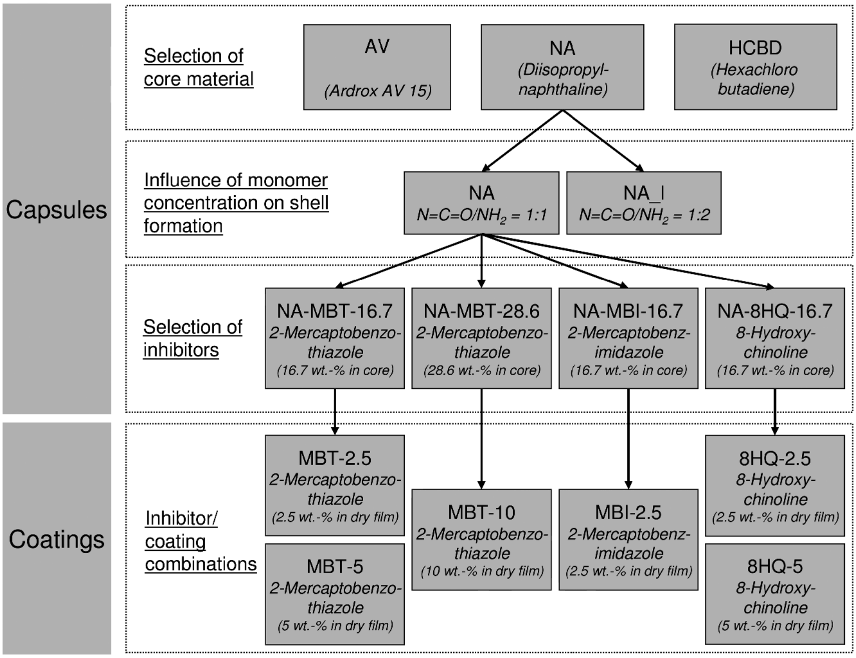
Capsules
Coatings
Selection of core material
AV
(Ardrox AV 15)
NA
(Diisopropyl-naphthaline)
HCBD
(Hexachloro butadiene)
Influence of monomer concentration on shell formation
NA
N=C=O/NH2 = 1:1
NA_I
N=C=O/NH2 = 1:2
Selection of inhibitors
NA-MBT-16.7
2-Mercaptobenzo-thiazole
(16.7 wt.-% in core)
NA-MBT-28.6
2-Mercaptobenzo-thiazole
(28.6 wt.-% in core)
NA-MBI-16.7
2-Mercaptobenz-imidazole
(16.7 wt.-% in core)
NA-8HQ-16.7
8-Hydroxy-chinoline
(16.7 wt.-% in core)
Inhibitor/ coating combinations
MBT-2.5
2-Mercaptobenzo-thiazole
(2.5 wt.-% in dry film)
MBT-5
2-Mercaptobenzo-thiazole
(5 wt.-% in dry film)
MBT-10
2-Mercaptobenzo-thiazole
(10 wt.-% in dry film)
MBI-2.5
2-Mercaptobenz-imidazole
(2.5 wt.-% in dry film)
8HQ-2.5
8-Hydroxy-chinoline
(2.5 wt.-% in dry film)
8HQ-5
8-Hydroxy-chinoline
(5 wt.-% in dry film)

Figure 2. Overview of the produced capsules and capsule/coating combinations

2. Monomer Solution 1

26.6 g (0.1 mol) Desmodur VL (diphenylmethanediisocyanate) are dissolved in 150 ml diisoproylnaphtaline. Additionally, 20 g mercaptobenzothiazole (MBT) are added to the solution and dispersed for 5 min by means of ultra sound (Dr. hielscher GmbH, UP 400s, cycle 0.5 pulsation, amplitude 70 %)

3. Monomer Solution 2

6.87 g (0.06 mol) DETA (diethylenetriamine) + 0.4 g diazabicyclo[2.2.2]-octane are dissolved in 150 ml deionised water.

Coating Application

The substrate under study was AA2024-T3 unclad. The coupons were cleaned in a standard procedure (solvent cleaning, alkaline degreasing, alkaline etching and acidic desmutting with rinsing in water after each cleaning step). Tartaric sulphuric acid (TSA) anodising was carried out after acidic pickling of the samples followed by a final rinse. The electrolyte comprised a mixture of tartaric and sulphuric acid. The anodising parameters were set to obtain a coating thickness of 3 µm. The concentration of tartaric acid and sulphuric acid in the electrolyte was 80 and 40 g/l, respectively. The anodising process was carried out at a voltage of 14 ± 1 V for 25 min in a temperature range of 37–43 °C. Alternatively, instead of anodization,

In Smart Coatings III; Baghdachi, J., et al.;
ACS Symposium Series; American Chemical Society: Washington, DC, 2010.

the AC131 sol-gel coating was applied as pre-treatment by dip coating using a single dip into the sol solution for 30 seconds followed by a withdrawal with a speed of 30 cm/min. The samples were dried at room temperature for 30 minutes and then cured at 120 °C for 1 hour.

The paint used in this study was a water-based epoxy primer (thickness 25 µm) over coated with a water-based epoxy topcoat (thickness 30 µm). Table II shows an overview of the tested paint films including the modifications by means of encapsulated inhibitors. Fig. 2 shows an overview of the produced capsules and capsule/coating combinations.

The primers and top coats were mixed with the curing agents according to the technical data sheets. The paint formulations were further diluted with water or an appropriate solvent depending on the spraying conditions. The primers containing microcapsules were prepared in the same way, however, the dilution of the paint was carried out by addition of the respective dispersion of microcapsules in a defined concentration. After applying the primer system by spraying, the top coat was applied within 24 hours.

Characterisation

Differential scanning calorimetry (DSC) was conducted in combination with thermogravimetric analysis (TGA) in a Netzsch STA 409 PC/PG. The sample was heated from 35 °C to 750 °C in synthetic air with a heating rate of 5 K/min. The XPS measurements were obtained with a Physical Electronics Quantum 2000 System. The spectra were taken with the electron emission angle at 45 ° to give a sampling depth of approximately 50 Å on a probe area of 100 µm diameter. The peak areas of the survey scan (energy range 0 – 1350 eV; low energy resolution (pass energy 117.4 eV) were used to determine the atomic concentration for the elements. High resolution scans were measured with a pass energy of 11.75 eV.

Particle size distribution measurements were performed by laser light scattering using a Malvern Mastersizer 2000 system. The capsule dispersion were washed twice with deionised water and poured into a beaker with 200 ml deionised water. Agglomerates were broken into individual particles by means of ultra sound.

A LEXT OLS3100 Confocal Laser Scanning Microscope from Olympus was used to determine the capsule/paint matrix interaction on fracture patterns. Electrochemical impedance spectroscopy (EIS) on coated test specimens was carried out with a EG&G Instruments potentiostat, Model 283. A three-electrode arrangement was used, consisting of a platinum counter electrode, a saturated calomel reference electrode and exposed sample (20 cm^2) as a working electrode. The frequency range of the applied AC potential was 10 mHz to 100 kHz with 10 steps per decade and the sinusoidal perturbations were 20 mV. The aqueous test solution was (0.5 g/l NaCl; 3.5 g/l NH_4SO_4) electrolyte in equilibrium with ambient air. The measurement was started after the open circuit potential was stable (OCP drift $\leq$ 0.1 mV/s).

SVET measurements were performed using Applicable Electronics Inc. equipment controlled by the ASET software from Sciencewares. Specimens of 1cm2 of metal substrates were glued to epoxy sleeves and adhesive tape around

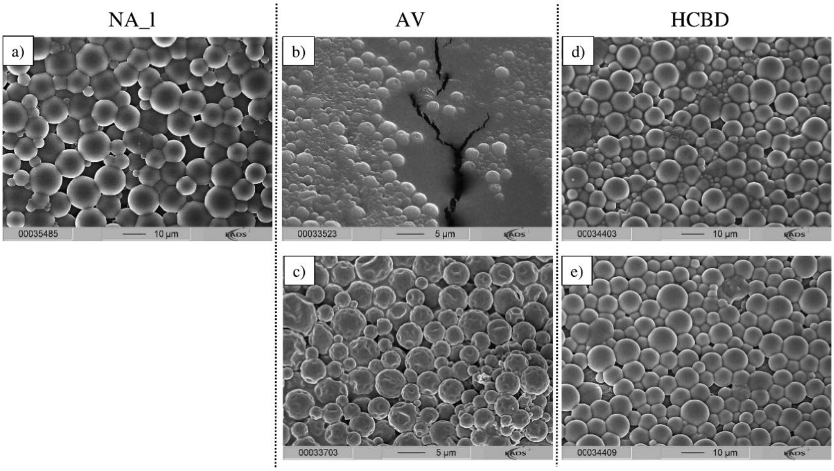

Figure 3. Influence of organic core material on capsule formation: a) uniform and isolated capsules with diisopropylnaphthalene (NA_l) core; b) Ardrox AV15: The capsules adhere together strongly and are covered by a film of dispersing agent, c) washing of the capsule dispersion helps to remove dispensable material; d) hexachlorobutadiene leads to the formation of uniform capsules exhibiting a narrow droplet size distribution; e) a prolonged reaction time (12 hours) seems to lead to more isolated and less agglomerated capsules.

the sample holders worked as solution reservoir. A mixture of beeswax and colophony delimited an exposed area of 2 x 2 mm^2. The test solution was aqueous 0.05 M NaCl. The microelectrode had a platinum tip with a diameter of 10 µm and was made to vibrate at an average distance of 100 µm above the surface, with 10 µm of amplitude. Each scan comprised 50 x 50 points.

The tensile test involves the attachment of a plunger with a defined surface area onto the test specimen and measurement of the maximum force that is necessary to pull off the stamp with the coating. The plunger was pulled off the test specimen vertically with a Zwick Z010 tensile testing machine while the maximum adhesion force was measured. The resulting adhesion strength was calculated by normalisation of the force by the surface area of the plunger.

The filiform corrosion test was performed according to ISO 3665. After initiation with concentrated hydrochloric acid, the scratched samples are placed in the test chamber at an angle of 6° from the vertical. The maximum length of filiform site is noted. Evaluation of inhibitor leaching performance from coatings was assessed by means of a droplet test on a scratch. A scratch (1 mm wide, 150 µm deep) is mechanically milled into the coated samples with a saw blade. Distilled water with 3 wt.-% NaCl is used as the electrolyte. A drop of the electrolyte is put on the scratch, covering the cut edges. Then the samples are stored in an exsiccator with high humidity (a water reservoir was placed inside the exsiccator to achieve a humidity >80 %) to avoid drying of the drop. After exposure times of 24 h, 48 h and 72 h the droplet was rinsed with additional pure water and the sample was dried with a bellow. A light microscope was

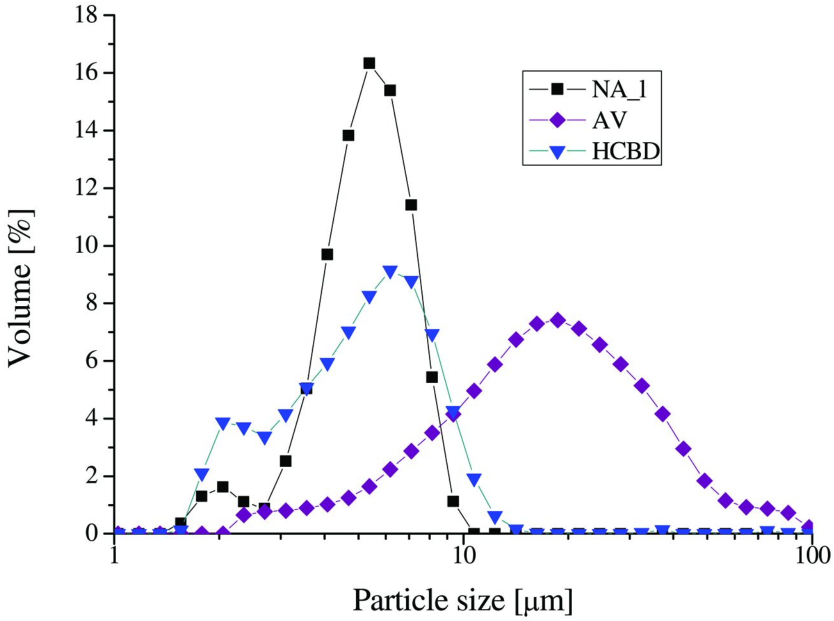

Figure 4. Capsule size distribution depending on the core material

used to determine the areal density of pits in the scratch. Furthermore, X-ray Photoelectron Spectroscopy (XPS) was used to quantify leached inhibitors.

Results and Discussion

Micro-Encapsulation of Inhibitors

The choice of organic phase as capsule core material is crucial since it serves as carrier for the corrosion inhibitors. The organic core material must not negatively influence the properties of the paint film in which they are incorporated. Therefore, the encapsulated organic phase should be more or less inert, it should not diffuse out of the capsules spontaneously and it must not destroy the barrier properties of the coatings. Various different organic solvents can be used as core materials. Three different materials are investigated in the present work for their applicability as liquid capsules cores. Figure 3 shows SEM images of the capsules produced with the same shell materials but different core materials.

The use of diisopropylnaphthalene (NA_l) as organic phase leads to uniform, dense and isolated capsules with a high stability. Furthermore, the capsule size distribution is uniform (Figure 3a). Ardrox AV15 (sample AV) as core material shows different behaviour. AV15 consists of naphthene derivates and other solvents and is used as a corrosion inhibiting compound in the aerospace industry. It is usually applied as a complementary surface protection measure on structural aluminium parts in order to creep into areas where the organic paint film is thin. The idea of encapsulating Ardrox AV15 is to implement the water displacing ability into the capsules. However, the picture shows that the encapsulation of AV15 is only partially successful. The capsules adhere together strongly and are covered by a film of dispersing agent and wall material that polymerised not around the solvent (Figure 3b). Washing of the capsule dispersion helps to remove dispensable material. The isolated capsules obtained by washing show dents on the entire surface area which indicates that lightly volatile compounds of the AV15 material evaporate after the polymerisation leaving a lack of core material (Figure 3c). The encapsulation of hexachloro butadiene (HCBD) leads to the formation of uniform capsules exhibiting a narrow droplet size distribution. It is shown that the there is almost no difference of the shape of the capsules in dependence of the reaction time, although a longer reaction time (Figure 3d shows the capsules after 3 hours and Figure 3e after 12 hours) seems to lead to more isolated and less agglomerated capsules.

The choice of core material influences also the distribution of the capsule size. Figure 4 reveals the capsule size distribution depending on the core material. The employment of diisopropylnaphthalene results in capsule sizes $d_{0.5}$ = 5.8 µm and $d_{0.9}$ = 10.1 µm (sample NA_l). As visible in the SEM images, the encapsulation of AV 15 (sample AV) is incomplete and wall material is polymerised without forming capsules. This is proven by the capsule size distribution measurement. The AV sample exhibits a wide distribution and a high degree of larger capsules ($d_{0.5}$ = 15.8 µm, $d_{0.9}$ = 38.0 µm), although it can be assumed that the larger detected “objects” do not have typical capsule-like appearance. The encapsulation of hexachloro-butadiene (HCBD) also leads to a wider distribution but mean amounts of the capsules are in the range of less than 10 µm ($d_{0.5}$ = 5.2 µm, $d_{0.9}$ = 9.8 µm).

The amount of isocyanate monomer employed for the polymerisation with amines in order to form a shell around the dispersant phase is important for the mechanical stability of the capsules. The capsules must be stable enough to sustain the dispersing in the primer matrix by high shear stresses. Furthermore, the application of the capsule loaded primer by means of spraying is another strong mechanical impact on the microcapsules. After paint application, the capsules must remain stable in the paint film, because the active ingredients of the capsule may affect the stability and the curing mechanism of the paint. If the capsules are broken prior to curing of the paint film, its advantages are obsolete. Therefore, strongly cured shells around the organic phase are favourable.

Figure 5 depicts SEM pictures of capsules containing the same organic phase (diisoproyplnaphthaline) with different N=C=O to NH_2 ratios. The pictures show that a 1:1 ratio leads to a slight buckling of the capsule surface (Figure 5b). However, comparison of both samples shows that the higher amount of monomer leads to more stable capsule walls. The capsules show a lower tendency of adhering to each other. Both samples have been washed once prior to SEM investigation so that an influence of remaining surfactant can be negated.

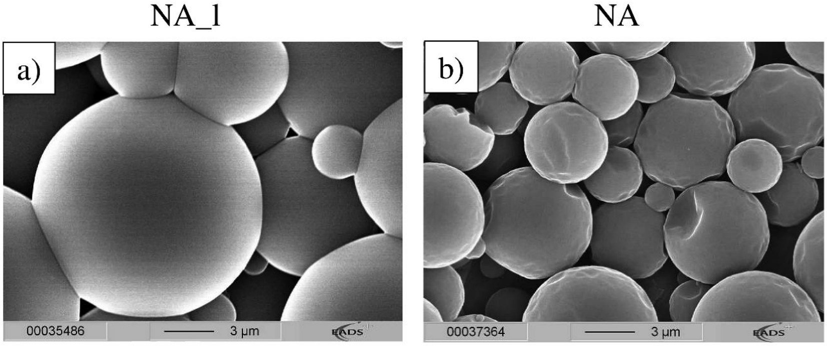

Figure 5. SEM micrographs of the micro-capsules obtained using different N=C=O to NH_2 ratios: a) sample NA_l: ratio N=C=O/NH_2 = 1:2; b) sample NA: ratio N=C=O/NH_2 = 1:1

Inhibitors are incorporated into microcapsules produced by using the optimal parameters described above. In each case the inhibitors are not completely soluble, hence a suspension of the inhibitors in the KMC solvent are produced using ultrasound. Fig. 6 reveals the influence of the incorporated inhibitors onto the formation of the capsule shell. The encapsulation of 2- mercaptobenzothiazole (MBT) (Fig. 6a) does not hinder the formation of the shell around the encapsulated suspension. The figures demonstrate the high rate of yield of the encapsulation process. In contrast, encapsulation of 2-mercaptobenzimidazole (Fig. 6b) significantly influences the polymerisation of the shell.

The SEM images show strong deformation of the capsules and a low yield. This behaviour is assigned to the imidazole group of the inhibitor which reacts with the isocyanate curing agent. The encapsulation of 8-hydroxychinoline (Fig. 6c) is more successful. The SEM image exhibits a high rate of yield and the formation of uniform capsules. The dependence of the capsule formation on the inhibitor employed is also emphasised by the capsule size distribution. Figure 7 shows the size distribution of the respective inhibitor-containing capsules.

The distribution of the capsules becomes slightly wider upon filling with inhibitors (samples NA-MBT-16.7, NA-MBT-28.6 and NA-8HQ-16.7). However, the mean capsule size decreases compared to sample NA_l due to a larger fraction of small capsules (NA-MBT-16.7: $d_{0.5}$ = 4.5 µm, $d_{0.9}$ = 7.5 µm, NA-MBT-28.6: $d_{0.5}$ = 4.8 µm, $d_{0.9}$ = 7.9 µm, and NA-8HQ-16.7: $d_{0.5}$ = 5.2 µm, $d_{0.9}$ = 7.9 µm). As observed by SEM, the incorporation of MBI significantly changes the capsule properties and therefore the capsule size distribution. The change of the shape and the occurrence of large particles lead to an increase in the capsule size (NA-MBI-16.7: $d_{0.5}$ = 8.3 µm, $d_{0.9}$ = 13.5 µm).

TGA/DSC was carried out for the estimation of the effective loading degree of inhibitors in the capsules and the quantity of capsules in a particular volume of paste-like capsule dispersion used as pigmentation for the organic paint primers. Therefore, the produced capsules are allowed to settle to the bottom of the storage container after washing. Then, excessive water is transfused and the obtained

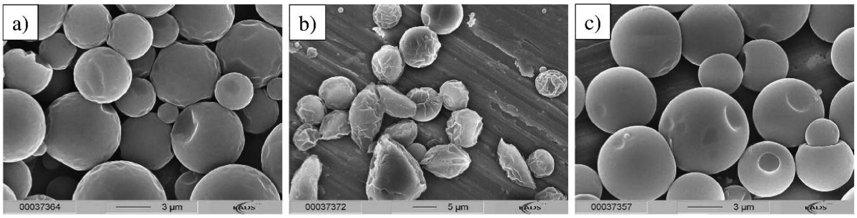

Figure 6. Influence of inhibitors on capsule formation: a) sample NA-MBT-16.7, b) sample NA-MBI-16.7, c) sample NA-8HQ-16.7

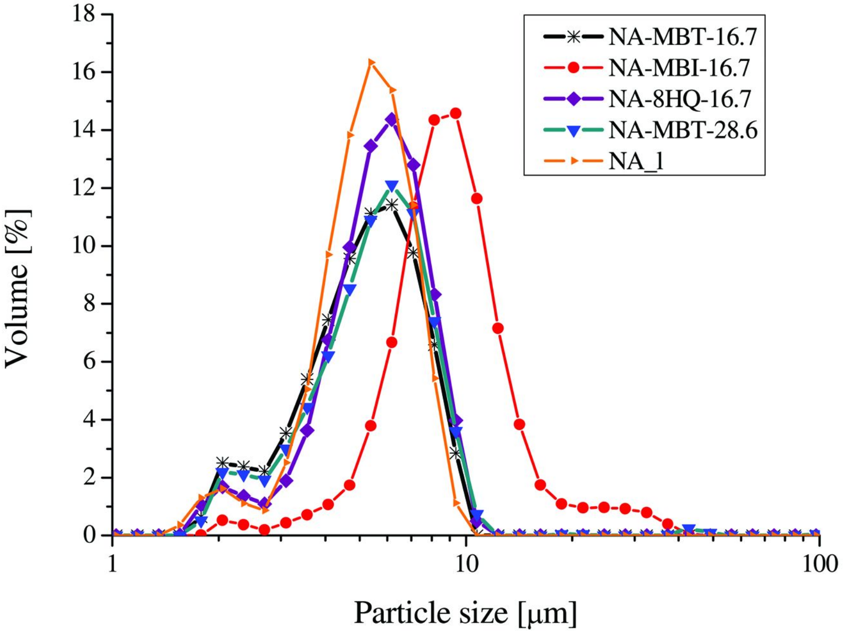

Figure 7. Capsule size distribution depending on incorporated inhibitor

capsule paste is measured by means of TGA/DSC. Figure 8 shows the TGA/DSC spectra of sample NA-MBT-16.7.

The graph shows that the capsule paste contains around 30 wt.-% water. The melting of the MBT inhibitor takes place at around 180 °C. The exothermic decomposition of the shell material at around 260 °C is superposed by the endothermic evaporation of the core material diisopropylnaphthaline. Both reactions lead to significant weight loss. Finally, the decomposition of MBT is detected at 315 °C. The information gained allows for the determination of the inhibitor content in a defined amount of the aqueous capsule “paste”. Most of the capsule shell material is released during decomposition at around 260 °C and the MBT remains in the tested material until higher temperatures than the evaporation temperature of diisopropylnaphthaline. Therefore, the 15 wt.-% remaining material after evaporation of diisopropylnaphthaline can be correlated to the calculated inhibitor content of 13.6 wt.-%.

Characterisation of the Self-Healing Coating System

Structure of the Coatings

Figure 9 shows SEM images of the conventional coating system and the developed coating system consisting with primer MBT-10.

Figure 9a shows the needle like strontium chromate pigments in the conventional primer. Figure 9b demonstrates the coating with primer MBT-10 with incorporated microcapsules. The capsules are uniformly distributed and adhere well to the primer matrix. No separation of primer and microcapsules is observed, which emphasises the excellent compatibility of the primer and the capsules (Figure 10). No physically trapped water (in between the capsules in the capsule paste) is released during the measurement because it is removed with the diluent water of the primer during drying.

Adhesion Properties

Measurement of the adhesion strength by means of the tensile test is sufficiently distinctive to compare different adhesion behaviours in a more meaningful manner than conventional cross-cut adhesive tape test.

Figure 11 shows the adhesive strength in dependence of pre-treatment and primers (mean value out of 5 samples). The adhesion strength depends on the applied paint film. The incorporation of microcapsules into the primer partly leads to lower paint adhesion of the primer to the pre-treatments. The decrease depends on the concentration of capsules in the primer. Typical cohesive fracture in the coating close to the aluminium substrate is observed in all paints, except MBT-10, 8-HQ-2.5 and MBI-2.5, were cohesive failure of the paint is detected. Only marginally different values are obtained for samples MBT-2.5 (e.g. 4.5 MPa) and MBT-5, both being higher than for paint MBT-10 (2.8 MPa). The high loading degree of capsules leads to the formation of predetermined breaking points in the paint film. The chromate loaded reference primer reveals only a minor decrease in the adhesion strength. Comparing the influence of the pre-treatments, the anodic film offer the highest adhesion strength (around 7 MPa), exhibiting a slightly better adhesion than the sol-gel film AC131. This observation clearly demonstrates that superior adhesion of sol-gel coatings on the aluminium alloy by formation of strong chemical bonds is also possible without mechanical anchoring as present in case of the anodic film. Figure 12 shows typical fracture behaviour of pigmented paint films. In case of the non-inhibited paint film, the fracture appears cohesively in the primer close to the aluminium substrate (Figure 12a). The capsule doped primer (MBT-2.5, Figure 12b) shows a planar fracture area with limited fracture leading through the capsules. The amount of visible capsule “dents” is lower than the amount of incorporated capsules. This shows, that there is not preferred “break” through the capsules in the paint film. In contrast, the high capsule loaded primer (MBT-10) shows cohesive fracture of the primer along high capsule concentration areas (Figure 12c). This clearly emphasizes, that a capsule loading degree close to the critical pigment volume concentration leads

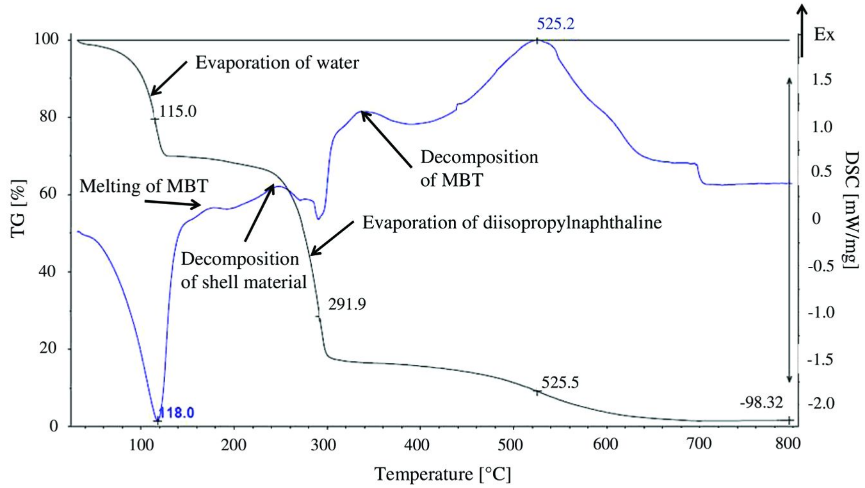

Figure 8. TGA/DSC spectrum of capsule sample NA-MBT-16.7

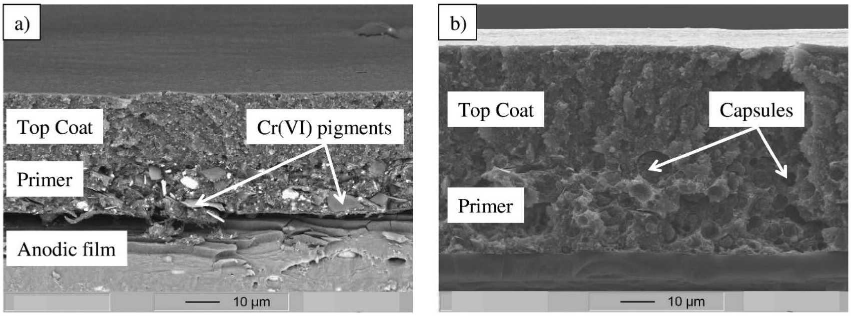
a)
Top Coat
Cr(VI) pigments
Primer
Anodic film
10 µm
b)
Top Coat
Capsules
Primer
10 µm

Figure 9. SEM pictures after cryo-fracture of conventional coating system (a) and the capsule containing coating system (b)

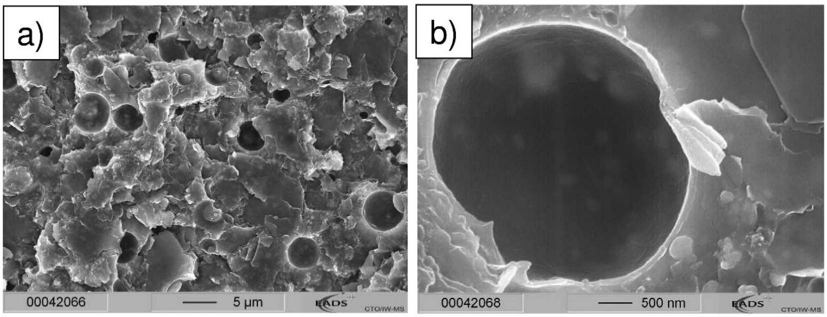
a)
00042066
5 µm
EADS
CTO/IW-MS
b)
00042068
500 nm
EADS
CTO/IW-MS

Figure 10. High resolution SEM picture of fracture area (a) of the primer 8HQ-5 with microcapsules showing enclosure of the capsules by the paint matrix (b).

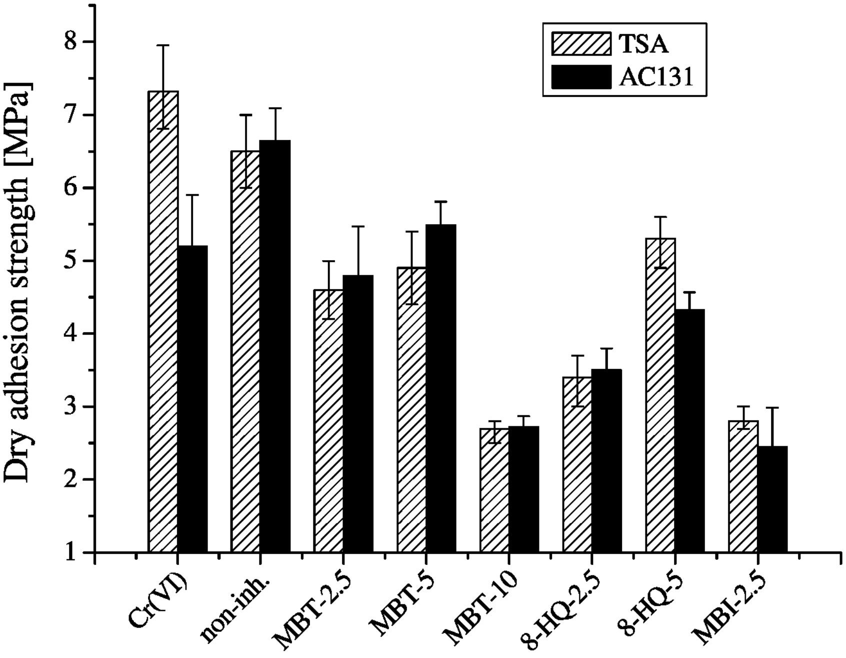

Figure 11. Dry adhesion strength [MPa] of paints with different incorporated capsules

to a decrease of the primer toughness. The cross-sections show the distinctive capsule "dents" of sample MBT-10 (Figure 12c) and the smoother section of the primer doped with the lower amount of capsules (MBT-2.5). The capsules break along their highest circumference. Typically, the cohesive toughness of the primer is significantly decreased in capsule agglomeration areas as due to a lack of reinforcing paint matrix stabilising the capsules.

Figure 13 shows a SEM image of the fracture area of tensile test specimens of primer MBT-10 and primer 8HQ-5. The image proves the excellent compatibility of the capsules with the epoxy paint matrix. No delamination of the paint from the capsules or enclosures of air are detected. Furthermore, it can be observed, that the fracture of the paint in all cases leads through the capsules. This shows that the paint adhesion to the capsules is good and that the fracture occurs in the most fragile areas of the capsule doped paint, namely the capsules themselves. Another interesting aspect is the impact of different inhibitor concentrations in the capsules. The images expose, that in case of primer 8HQ-5 (loaded with capsules NA-8HQ-16.7, Figure 13a and Figure 13b), the solvent core and the dissolved inhibitor evaporate in the vacuum after break of the capsules and no remnants can be found in the broken capsules. In contrast, residues of the dispersed inhibitor mercaptobenzothiazole can be detected in case of primer MBT-10 (bearing highly loaded capsules NA-MBT-28.6, Figure 13c and Figure 13d).

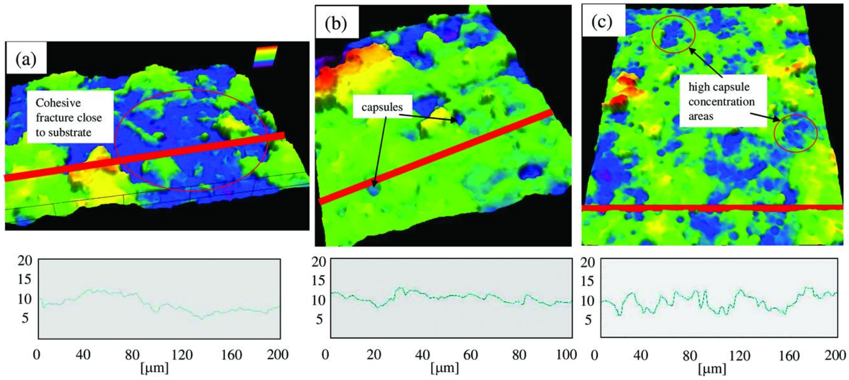

Figure 12. Confocal laser scanning microscopy pictures of the fracture area of tensile test specimens of different paints on TSA anodic film: (a) non-inhibited primer, (b) 2.5 wt.-% mercaptobenzothiazole in capsules (sample: MBT-2.5), (c) 10 wt.-% mercaptobenzothiazole in capsules (sample MBT-10). The profiles were recorded accross the red lines.

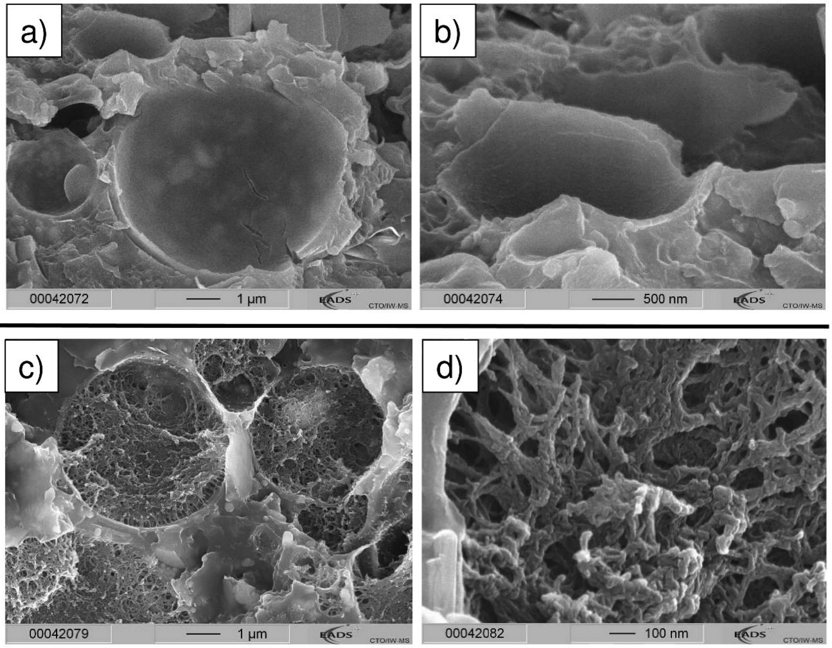
a)
00042072
1 µm
EADS
CTO/IW-MS
b)
00042074
500 nm
EADS
CTO/IW-MS
c)
00042079
1 µm
EADS
CTO/IW-MS
d)
00042082
100 nm
EADS
CTO/IW-MS

Figure 13. SEM pictures of fracture area of primer 8HQ-5 (figure a and b) and primer MBT-10 (figure c and d). No delamination of the paint from the capsules or enclosures of air are detected. The fracture of the paint in all cases leads through the capsules, showing that the paint adhesion on the capsules is good. The fracture occurs in the most fragile areas of the capsule doped paint, namely the capsules themselves. Figure 13c and Figure 13d show remnants of mercaptobenzothiazole after evaporation of the organic solvent core.

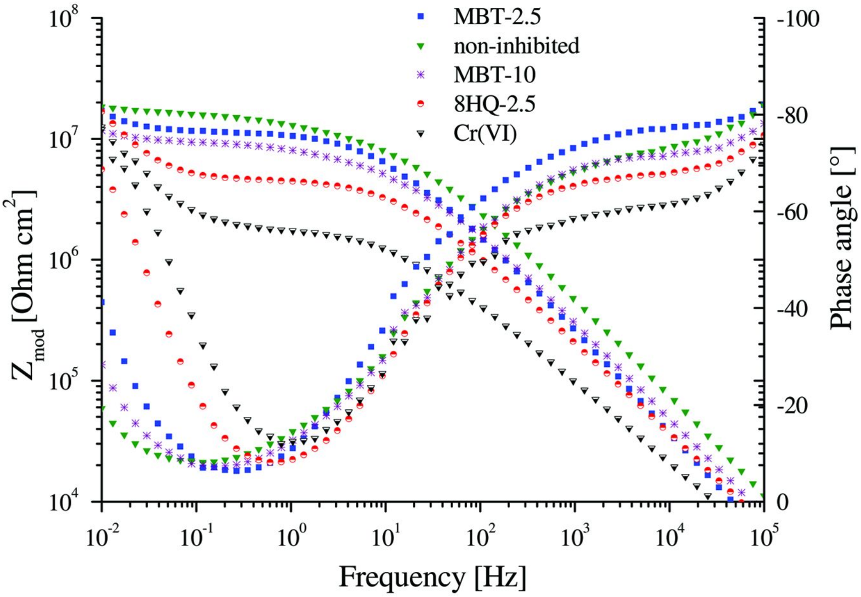

Figure 14. Impedance spectra of AA2024 unclad alloy coated with capsule doped primers and top coat on TSA anodic film after 42 days immersion in dilute Harrison solution

Corrosion Protection Properties

In addition to SEM, EIS measurements have been performed to prove the excellent compatibility of the capsules with the coating matrix and to demonstrate the enhancement of the passive (barrier properties) and active (self-healing) protective performance of the coatings in the case of microcapsule-containing systems. Figure 14 depicts impedance spectra taken from different primers and top coat on TSA anodic film after 42 days immersion in dilute Harrison solution. One relaxation process is well visible on the spectra of all coatings at high frequencies. This time constant is related to the barrier properties of the paints. The capacitive response, with respective phase angles close to -90, originates from capacitance of the coatings. The phase angle values not being equal to -90 can be explained by the non-ideal character of the film and normally is described with constant phase element. The resistive part of this high frequency time constant can be attributed to the pore resistance of the paints. The higher the pore resistance the less nano-/micro- pores and defects are present in the coating. The chromate-loaded primer has a pore resistance about one order of magnitude lower compared to the non-inhibited paint (1e6 compared to 1e7 Ohm cm^2).

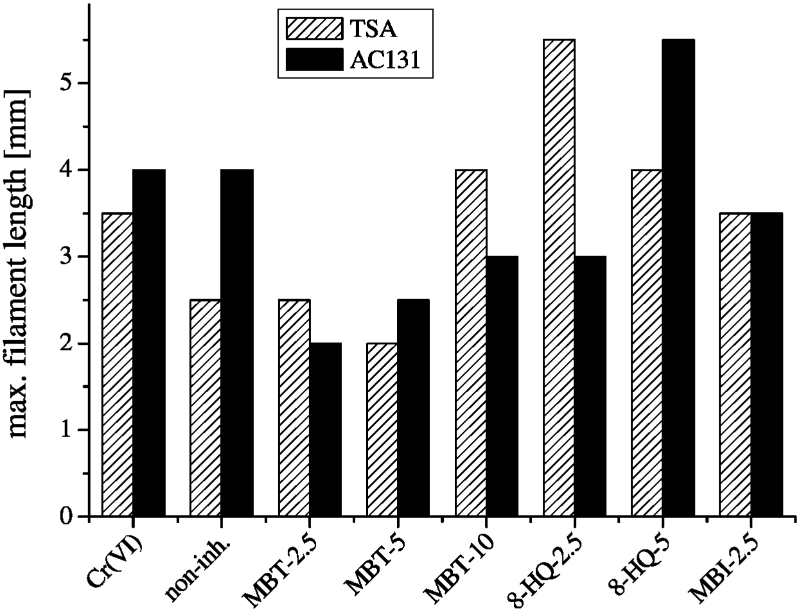

Figure 15. Maximum filament length in dependence of the employed microcapsules after 960 hours filiform corrosion test (FFC) test on AA2024 unclad alloy with anodic film or AC131 sol-gel film as pre-treatments

The capsule loaded paint films MBT-2.5 and MBT-10 show significantly higher resistance than the chromate-loaded primer. It is a clear sign that the capsules adhere well to the primer matrix such that no additional diffusion paths and voids occur in the film. Only the paint containing 8HQ-microcapsules demonstrate remarkable reduction of barrier properties showing lower compatibility. The analysis of capacitative part of high-frequency time constant can confer additional information on the rate of water uptake by the paint systems under study. The higher the water uptake, the more the spectra shifts towards lower impedance values in the paint capacitance region. Thus the chromate-loaded system demonstrates the highest amount of absorbed water. An additional important feature can be observed at low frequencies. The phase angles and change in slope in the impedance plot for both samples 8HQ-2.5 and Cr(VI) show a tendency towards the formation of an additional time constant in the low frequency region (1e-1 to 1e-2). This time constant can be attributed to the aluminium oxide underneath the paint film (*40*). This may only be observed in the plot after strong water uptake of the paint film.

Figure 15 shows the maximum filament length measured on filiform corrosion test specimens after 960 hours test duration in dependence on the pre-treatment and the applied organic primer and top coat.

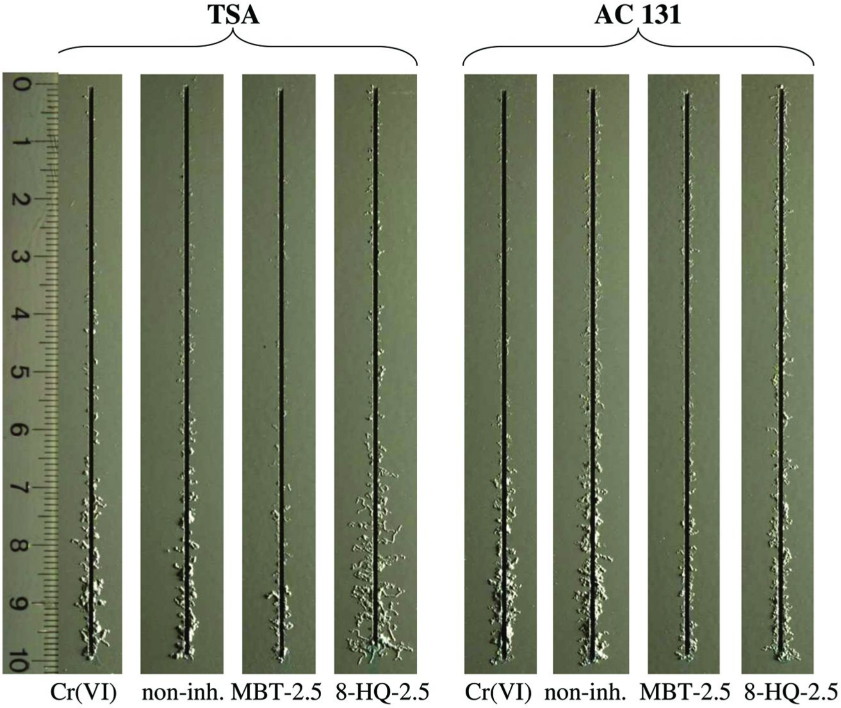

Figure 16. Photograph of the scratch area of fully painted test specimens (AA2024 unclad alloy) after 960 hours FFC test (scribe width: 1 mm), scale bar in centimetres.

The performance of the test specimens usually strongly depends on the pre-treatment, especially for thin sol-gel films such as the AC131 and anodic films. The graph shows, that the filament length depends on the inhibitor employed in the primer as well. In this case, it is evident that the inhibitors from the primer have an influence on the stabilisation of the interface, emphasising the self-healing effect. The primers doped with 2.5 wt.-% MBT and 5 wt.-% MBT improve the performance of the coating systems with AC131 and TSA pre-treatments. TSA test specimens with these primers show less than 2 mm maximum filament length after 960 hours test duration being superior to chromate loaded primer and the sol-gel thin film AC 131. The highly loaded primer MBT 10 does not have such a positive effect and allows a slight increase of the maximum filament length.

Figure 16 shows macroscopic pictures of the scratch area (1 mm scratch width) of the test specimens after 960 hours test duration.

The samples painted with the chromate loaded primer show typical behaviour of fewer initiation sites of filaments due to the inhibiting action of chromates. However, maximum filament length is observed to be lower on TSA anodic film than for sol-gel coating AC131. Concerning the filiform corrosion test, the low inhibitor content of MBT (MBT-2.5) is more beneficial than higher contents (MBT-10). Furthermore, substantial positive influence of the incorporated

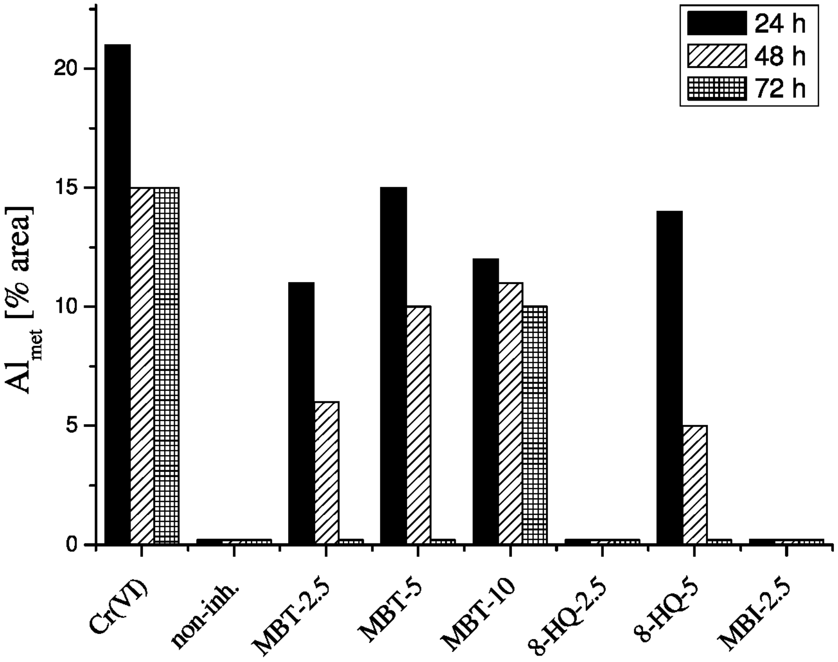

Figure 17. Surface area of metallic aluminium obtained by XPS high resolution scans on drop test samples after different exposure times to 3 wt.-% NaCl solution

microcapsules is detected on TSA and AC 131 pre-treatments with MBT-2.5 being far superior to 8-HQ-2.5.

The active corrosion protection potential of the coating system is compared to the conventional one by means of simple drop test (exposure of scratches down to the substrate with 3 wt.-% NaCl solution) and analysis of the exposed area by XPS. As expected, the active corrosion protection ability of the coating systems depends mainly on the primer. Figure 17 shows the amount of metallic aluminium area obtained by XPS on drop test samples on TSA painted with various primers after different exposure times (24 hours, 48 hours, 72 hours) to 3 wt.-% NaCl electrolyte.

Detection of metallic aluminium reveals good inhibition properties of the coating. In the case of the non-inhibited primer, only aluminium oxide and therefore no metallic aluminium can be detected by means of XPS. A survey scan made on the tested area reveals the presence of copper and magnesium from dissolved S-phase particles giving evidence to corrosion processes on the sample. Chromate loaded primer shows the highest average amount of metallic aluminium. Aluminium oxide is always present due to the natural oxide film. For this investigation, test specimens have been examined immediately after scratch preparation to avoid growth of a thicker oxide film. The figure enforces the concentration tendency of the MBT doped primers. Higher amounts of MBT lead to a higher amount of metallic aluminium in the scratch. The evolution of the area of metallic aluminium with immersion time reveals deceleration of corrosion processes in the presence of the corrosion inhibitors (including chromates) but the inhibitors released from the coatings are not able to completely stop the attack.

SVET measurements of the localised corrosion activity in artificial micro-defects allow the detection of active corrosion protection ability of the coating and enforcement of the drop test results. Figure 18 shows corrosion current density maps of samples coated with the non-inhibited primer, MBT inhibited primer (MBT-10), 8-HQ inhibited primer (8-HQ-5) and Cr (VI) reference primer. After one month of exposure to 0.05 M NaCl the non-inhibited reference sample shows a strong local current density in the scratch area indicating cations produced in anodic places due to oxidation of aluminium in the defect.

The rather high current density indicates ongoing pitting corrosion. The sample with incorporated MBT (primer MBT-10) shows only marginal cathodic activity in the scribe area after 2 months exposure. The minute currents detected emphasise the strong corrosion inhibition ability of the MBT-10 primer. Almost no differentiation of cathodic and anodic areas is possible. Thus the coating evidently demonstrates the self-healing ability. In the case of the chromate loaded primer, anodic current density origins from pit formation and cathodic currents can be assigned to reduction of dissolved oxygen. Both primers show a significantly better performance than the primer inhibited with 8-HQ (8-HQ-5), where almost no difference to the non-inhibited test samples is observed. However, pigmentation of the chromate loaded primer and MBT-10 leads to blistering.

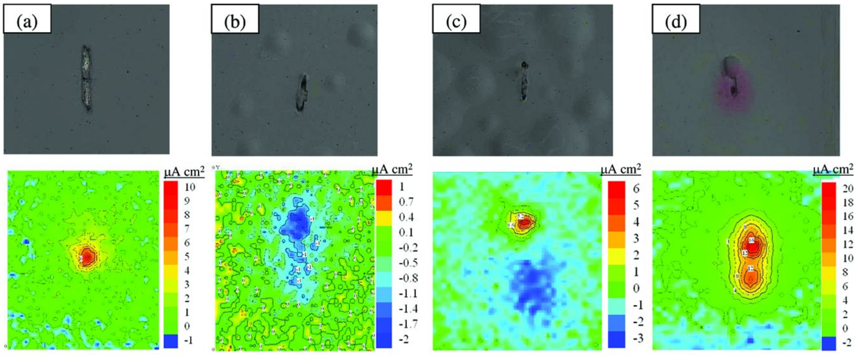

area:1250 x 1250 µm² 1 month / 0.05M NaCl

area:1250 x 1250 µm² 2 months / 0.05M NaCl

area:1560 x 1400 µm² 2 months / 0.05M NaCl

area:1560 x 1400 µm² 2 months / 0.05M NaCl

Figure 18. Optical pictures and SVET maps of AA2024 unclad alloy coated with: (a) non-inhibited primer, (b) mercaptobenzothiazole loaded primer (MBT-10), (c) chromate loaded primer and (d) 8-hydroxychinoline loaded primer (8-HQ-5). All samples have been treated with an artificial scratch.

Conclusion

Immobilization of corrosion inhibitors in polymer microcapsules is demonstrated as a feasible approach to combine effectiveness and compatibility of alternative corrosion inhibitors to organic paint primers. Micro-encapsulation by interfacial polymerisation permits increase of incorporation of organic inhibitors in paint matrices as well as the encapsulation of water-displacing fluids that include an additional corrosion preventing effect in the primer layer. The high compatibility of polyurea capsules with epoxy-based paint primers allows high loading degrees close to the critical pigment volume concentration without deteriorating the primer properties.

The active corrosion protection of large mechanical defects is accomplished by the capsule-doped primer. The best performance was reached by encapsulation of 2-mercapto-benzothiazole (10 wt.-% in dry paint film). It shows a performance level close to a chromate loaded primer under the given test conditions. The healing of the scratch area takes place instantly and corrosion initiation is prohibited by stabilisation of the aluminium oxide. SVET measurements confirm the self-healing ability of the coatings doped with encapsulated corrosion inhibitors.

The developed self-healing coating confers healing of small defects such as micro-cracks in coatings and the corrosion prevention of defects originating from mechanical impacts by release of inhibitors dispersed in a water displacing fluid. The protection relies on the fast release of inhibitors into the scratch area after rupture of the capsules incorporated in the polymer matrix. Further modification of the coating system by means of ion exchange pigments or layer-by-layer assemblies would probably allow providing protection in the case of smaller defects or minor mechanical impacts were the rupture of the microcapsules is not guaranteed. The combined inhibition mechanism, fast release from microcapsules in the case of a macroscopic defect and slower but steady release or release on demand in the case of smaller defects can further improve the long-term stability of the coating systems.

Acknowledgments

The authors gratefully acknowledge Dr. A.C. Bastos (University of Aveiro) for his assistance with SVET experiments and S. Zinz for the support with CLSM measurements.

References

1. Scholes, F. H.; Furman, S. A.; Hughes, A. E.; Nikpour, T.; Wright, N.; Curtis, P. R.; Macrae, C. M.; Intem, S.; Hill, A. J. *Prog. Org. Coat.* **2006**, *56*, 23.
2. Critchlow, G. W.; Brewis, D. M. *Int. J. Adhes. Adhes.* **1996**, *16*, 255.
3. Regulation (Ec) No 1907/2006 of the European Parliament and of the Council. *Official Journal of the European Union* **2006**, *L396*, 1−849.
4. Bierwagen, G. P. *Prog. Org. Coat.* **1996**, *28*, 43.
5. Sinko, J. *Prog. Org. Coat.* **2001**, *42*, 267.
6. Zheludkevich, M. L. Self-healing anticorrosion coatings. In *Self-healing materials*; Ghosh, S. K., Ed.; Wiley-VCH: 2008.

7. Kumar, A.; Stephenson, L. D.; Murray, J. N. *Prog. Org. Coat.* **2006**, *55*, 244.
8. Shchukin, D. G.; Zheludkevich, M. L.; Yasakau, K. A.; Lamaka, S. V.; Möhwald, H.; Ferreira, M. G. S. *Adv. Mater.* **2006**, *18*, 1672.
9. Wang, H.; Presuel, F.; Kelly, R. G. *Electrochim. Acta.* **2004**, *49*, 239.
10. Yang, H.; van Ooij, W. J. *Prog. Org. Coat.* **2004**, *50*, 149.
11. Buchheit, R. G.; Guan, H.; Mahajanam, S.; Wong, F. *Prog. Org. Coat.* **2003**, *47*, 174.
12. Buchheit, R. G.; Mamidipally, S. B.; Schmutz, P.; Guan, H. *Corrosion* **2002**, *58*, 3.
13. Schmidt, C. US 6383271, 2002; Daimler Chrysler AG, *Chem. Abstr. 133*, 136816.
14. Manna, A.; Imae, T.; Aoi, K.; Okada, M.; Yogo, T. *Chem. Mater.* **2001**, *13*, 1674.
15. Lu, X.; Xin, Z. *Colloid Polym. Sci.* **2006**, *284*, 1062.
16. Schneider, G.; Decher, G. *Nano Lett.* **2004**, *4*, 1833.
17. Shchukin, D. G.; Möhwald, H. *Phys. Chem. Chem. Phys.* **2006**, *8*, 3496.
18. Brown, E. N.; White, S. R.; Sottos, N. R. *J. Mater. Sci.* **2004**, *39*, 1703.
19. Cho, S. H.; Anderson, H. M.; White, S. R.; Sottos, N. R.; Braun, P. V. *Adv. Mater.* **2006**, *18*, 997.
20. Gutcho, M. M. *Microcapsules and Microencapsulation Techniques*; Noyes Data Co.: Park Ridge, NJ, 1976.
21. Vandegaer, J. E. *Microencapsulation: Processes and Applications*; Plenum Press: New York, 1973.
22. Benita, S. *Microencapsulation: Methods and Industrial Applications*; Marcel Dekker Inc.: New York, 1996.
23. Arshady, R. *Microspheres, Microcapsules and Liposomes*; Citrus Books: London, U.K., 1999.
24. Sliwka, W. *Angew. Chem., Int. Ed. Engl.* **1975**, *14*, 539.
25. Wu, D. Y.; Meure, S.; Solomon, D. *Prog. Polym. Sci.* **2008**, *33*, 479.
26. Zoldesi, C. I.; Imhof, A. *Adv. Mater.* **2005**, *7*, 924.
27. Chen, M.; Wu, L.; Zhou, S.; You, B. *Adv. Mater.* **2006**, *18*, 801.
28. Guan, G.; Zhang, Z.; Wang, Z.; Liu, B.; Gao, D.; Xie, C. *Adv. Mater.* **2007**, *19*, 2370.
29. Chen, T.; Colver, P. J.; Bon, S. A. F. *Adv. Mater.* **2007**, *19*, 2286.
30. Keeney, Ch.; Clements, M.; Hawkins, J.; Yollick, S.; Fader, J. US 6420052, 2002; Meritor LightVehicle Sys Ltd (US), *Chem. Abstr.* **2001**, *135*, 373074.
31. Zheludkevich, M. L.; Shchukin, D. G.; Yasakau, K. A.; Möhwald, H.; Ferreira, M. G. S. *Chem. Mater.* **2007**, *19*, 402.
32. Shchukin, D. G.; Zheludkevich, M. L.; Möhwald, H. *J. Mater. Chem.* **2006**, *16*, 4561.
33. Shchukin, D. G.; Möhwald, H. *Small* **2007**, *3*, 926.
34. Kotov, N.; Knobbe, E. T.; Kachurina, O.; Metroke, T. L. US 2003027011, 2003; Chem. Abstr. **2003**, *138*, 124031.
35. Arshady, R. *J. Microencapsulation* **1989**, *6*, 1.
36. Frère, Y.; Danicher, L.; Gramain, P. *Eur. Polym. J.* **1998**, *34*, 193.

37. Ramanathan, L. S.; Shukla, P. G.; Sivaram, S. *Pure Appl. Chem.* **1998**, *70*, 1295.
38. Ramanathan, L. S.; Baskaran, D.; Shukla, P. G.; Sivaram, S. *Macromol. Chem. Phys.* **2002**, *203*, 998.
39. Raps, D. Ph.D. Thesis, TU Munich, VDI Verlag, Nr. 736, 2008.
40. Raps, D.; Hack, T.; Wehr, J.; Zheludkevich, M. L.; Bastos, A. C.; Ferreira, M. G. S.; Nuyken, O. *Corros. Sci.* **2009**, *51*, 1012.

Chapter 13

Reversibly Porating Coatings – Pinned Spinodal Decompositions

Feng Yan,[1,2] Dustin England,[1] Hong Gu,[1] and John Texter[1,*]

[1]School of Engineering Technology, Eastern Michigan University, Ypsilanti, MI 48197
[2]Key Laboratory of Organic Synthesis of Jiangsu Province, School of Chemistry and Chemical Engineering, Soochow University, Suzhou 215123, China
[*]jtexter@emich.edu

A new class of hydrogel/solvogel copolymers have been derived by microemulsion polymerization of methacrylates and reactive ionic liquid surfactants in aqueous-methacrylate-surfactant microemulsions. Depending on the cross-linking density, the resulting gels (transparent or translucent) can be reversibly transformed into microporous or nanoporous materials with open cell structures via spinodal decomposition of the gel phases. Reversibility is aided by the cross-linking. The spinodal decomposition is induced by changing the solvent quality from good to poor for the copolymeric blocks containing the polymerized ionic liquid surfactant. These materials when coated on a supporting filter can provide automatic flow regulation or termination when solvent quality improves, as convection is blocked in the gel state. They also can provide solvent-reversible opacity as an overcoat to otherwise transparent materials.

Introduction

We present an approach for creating solvent-induced reversibly porous polymeric coatings, thin films, and bulk materials. We begin with microemulsion polymerization using microemulsions stabilized by polymerizable (ionic liquid) IL-based surfactants. A class of ionic liquids (ILs) comprising an imidazolium

In Smart Coatings III; Baghdachi, J., et al.;
ACS Symposium Series; American Chemical Society: Washington, DC, 2010.

polar group and a reactive and hydrophobic tail was chosen as a new class of surfactants for these investigations.

Ionic liquids are organic salts with melting points below or near-room temperature (*1*). They are of increasing interest because of their chemical stability, thermal stability, nonvolatility and high ionic conductivity (*2*, *3*). These properties qualify them as alternatives to traditional organic solvents, and ILs have already found use in organic/inorganic synthesis (*4*), catalysis (*5*, *6*), electrosynthesis (*7*, *8*), and polymer synthesis (*9*, *10*).

The incorporation of surfactants with and within ILs has been investigated by several groups in micelles and emulsions (*11–13*). Some nonionic surfactants, such as Brij-35, Tween-20, and Triton X-100 are able to form amphiphilic aggregates in a “conventional” IL, 1-ethyl-3-methylimidazolium bis(trifluoro methylsulfonyl) imide solution (*11*, *12*). It has also been demonstrated that ILs formulated from imidazole cations with appended perfluoro tails could act as surfactants in conventional imidazolium-based ILs, facilitating the emulsification of fluoroalkanes within IL continuous phases (*13*). Microemulsions composed of bmim-BF_4, cyclohexane and surfactant Triton X-100 have been recently prepared and characterized by Han (*14*), Eastoe et al. (*15*) and Chakrabarty et al. (*16*). A recent work presented by Gao et al. demonstrated that the bmim-PF_6-water-Triton X-100 system can also form microemulsions under suitable conditions (*17*).

We report (*18*) the synthesis of this new class of surfactant ILs that comprises an imidazolium polar group and an acryloyl hydrophobic tail (Fig. 1). We use these surfactant ILs to stabilize microemulsions of polymerizable monomers. These microemul-sions are then polymerized to produce useful copolymers. The resulting copolymer structure can be tuned between a solvogel and a porous structure by suitably modifying the solvent phase by modifying the amount of a suitable water-miscible organic solvent or by modifying the anion by ion exchange. After presenting the synthetic procedure we illustrate the formulation of the microemulsions. Example formulations subjected to polymeri-zation conditions are then presented and characterized.

Experimental

Materials

Chemicals

Acryloyl chloride (96%), 1-bromododecane (98%), 11-bromoundecanol (98%), triethylamine, 1-methylimidazole (99%), methyl methacrylate (MMA, 98%), 2,6-di-tert-butyl-4-methylphenol (98%), sodium tetrafluoroborate (98%), 2,2-azobisiso-butyronitrile (AIBN), tetrahydrofuran (THF), acetoni-trile, diethyl ether, ethyl acetate were purchased from Aldrich Chemical Co. MMA was purified by passing through an inhibitor column (Aldrich) to remove the inhibitor. Distilled deionized water was used for all experiments.

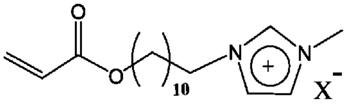

Figure 1. N-Acryloylundecyl-N'-methyl imidazolium IL reactive surfactant, where X^- is the counter anion.

Methods

Phase Diagrams

The single-phase domains of IL-BF_4-water-MMA microemulsions were determined visually on the basis of transparency and absence of phase separation in PTFE-lined, screw-capped culture tubes. These titrations were conducted at 24°C.

Surface Tension

Surface tension measurements were carried out using the pendant drop method in water on a Sigma 703 surface tensiometer at 24°C. The critical micelle concentrations (CMC) were determined from break points in plots of surface tension vs. log[C], where [C] is surfactant concentration in mM.

Polymerization

Polymerization of microemulsions was carried out in capped NMR tubes (or in 20 ml screw-capped culture tubes) at 60°C in an oil bath for 6 hr. AIBN was used as initiator at 0.5% (w/w) relative to MMA and IL-BF_4. No special attempt was made to remove dissolved oxygen. Conversion of final product was checked by analyzing the gels produced with 2% and 10% EGDMA. Small sections of gel slabs were cyclically soaked in the aqueous propanol solution and drained (three cycles) to try to remove unreacted IL-BF_4. The slab was then weighed and placed in a vacuum oven at 105°C overnight to remove solvent and volatile monomer. The samples were then weighed again and the percent solids determined: 2% EGDMA – 32.2% (calc. 30.8%); 10% EGDMA – 36.7% (calc. 32.2). The apparently > 100% conversion suggests solvent loss from the gel slabs after draining and before weighing.

Proton NMR

^1H NMR spectra were recorded on a JEOL 400 MHz spectrometer. The samples were dissolved in $CDCl_3$.

SEM

Scanning electron microscopy (SEM) images were recorded on a Hitachi S3400 SEM and a Philips XL30 FEG SEM. All of the samples were freeze-fractured in liquid nitrogen to expose the fresh fracture surfaces.

DSC

Melting points were measured on a TA Instruments SDT 2960 Simultaneous Differential Scanning Calorimetry (DSC), with the heating scans of 10°C/min.

TGA

Thermal stability of polymers was evaluated using a TA Instruments TGA Q500 thermogravimetric analyzer.

DMA

The DMA measurements of porous polymer rods (~3 mm diameter) were conducted with a TA Instruments (New Castle, Delaware, USA) DMA Q 800. Three-point bending tests were performed using a double cantilever clamp with 50 mN static force and 50 mN dynamic force applied at a frequency of 1.0 Hz. The samples were heated from -20°C to 100°C at a heating rate of 5.0°C/min. The sample chamber was purged with nitrogen at 20 mL/min throughout the test.

The storage modulus of the porous polymer ranges from about 54.5 MPa (2 wt % EGDMA) to 136.9 MPa (7 wt % EGDMA) and 236.6 MPa (10 wt% EGDMA) at 25 °C. Thermal analyses of the porous materials show that all the polymers have high decomposition temperatures ranging from 405 °C to 415 °C, indicating excellent thermal properties and likely ignition resistance.

Swelling Ratio

To measure the equilibrium swelling ratio (ESR) of the porous polymers, vacuum dried samples were immersed in water/DMSO solution (1:4 v/v) to equilibrate at room temperature. The excess surface solvent was removed by touching the sample surface with a filter paper. The ESR value was calculated using the following equation:

$$\mathbf{ESR = (Ws\text{-}Wd)/Wd}$$

where W_d is the dried sample weight and W_s is the weight of swollen sample.

For the purposes of drug delivery, the equilibrium swelling ratio (ESR) of the porous polymers has been characterized at room temperature. Porous polymer prepared with 1 wt% EGDMA shows an ESR value of 4.2, and decreases to 3.5 and 2.9 with the crosslinker content increased to 7 wt% and 10 wt%, respectively. These swelling results demonstrate that these materials can be effectively used for chemical and drug delivery.

Results and Discussion

Synthesis of 11-Bromoundecylacrylate (a)

11-Bromoundecanol (10.00 g, 40 mmol) was dissolved in 40 ml of dry tetrahydrofuran (THF) in a two-necked round bottom flask. The flask was cooled in an ice-bath and triethylamine (5.13 mL, 40 mmol) in THF (40 mL) was added to the stirring solution. Acryloyl chloride (3.65 g, 40 mmol) dissolved in 40 ml of THF was added dropwise to the stirring solution over a period of 15 min under N_2 atmosphere (Fig. 2). The mixture was further stirred for 2 days at room temperature and was filtered. The filtrate was washed with 2% sodium bicarbonate solution to remove any unreacted acid chloride and dried over anhydrous $MgSO_4$. The dried solution was filtered and the filtrate was passed through a short column of neutral alumina, using CH_2Cl_2 as the light yellow liquid (yield 10.58 g, 87%). ^{1}H NMR (400 MHz, $CDCl_3$): 6.37– 6.36 (1H, m, CH_2=CH), 6.15–6.12 (1H, m, CH_2=CH), 5.81–5.79 (1H, m, CH_2=CH), 4.16–4.12 (2H, t, –$OCOCH_2$), 1.85–1.82 (2H, m, $BrCH_2CH_2$–), 1.66–1.64 (2H, m, –$OCOCH_2CH_2$), 1.42–1.27 (14H, m, –$CH_2CH_2(CH_2)_7CH_2CH_2$–).

Synthesis of 1-(11-Acryloyloxyundecyl)-3-methylimidazolium Bromide (IL-Br)

Under N_2 atmosphere, a mixture of 11-bromoundecylacrylate (6.08g, 20 mmol) and 1-methylimidazole (1.64g, 20 mmol) and a small amount of 2,6-di-tert-butyl-4-methylphenol (inhibitor) was stirred at 40 °C for 48 h, and yielded a viscous liquid (Fig. 2). The viscous liquid was purified by the precipitation method with diethyl ether to obtain yellow viscous liquid 1-(2-acryloyloxyundecyl)-3-methylimidazolium bromide. The viscous liquid was dried under vacuum at room temperature as the white waxy solid (5.73g, 74 %). ^{1}H NMR (400 MHz, $CDCl_3$): 10.66 (1H, m, N–CH–N), 7.34–7.25 (2H, s, N–CH=CH–N), 6.36–6.35 (1H, m, CH_2=CH), 6.14–6.11 (1H, m, CH_2=CH), 5.81–5.79 (1H, m, CH_2=CH), 4.30–4.29 (2H, t, N–$CH_2(CH_2)_{10}$O–), 4.11 (3H, s, N–CH_3), 1.90–1.82 (2H, t, N–$CH_2(CH_2)_{10}$O–), 1.66–1.62 (2H, m, –$OCOCH_2CH_2$), 1.30–1.24 (14H, m, –$CH_2CH_2(CH_2)_7CH_2CH_2$–). Elemental analysis: Calculated: $C_{18}H_{32}BrN_2O_2$, C: 55.67 %; H, 8.31 %; N, 7.21 %. Found: C: 55.22 %, H: 7.79 %, N: 7.35 %.

Synthesis of 1-(11-Acryloyloxyundecyl)-3-methylimidazolium Tetrafluoroborate (IL-BF_4)

IL-Br (7.74 g, 20 mmol) was dissolved in 50 mL of dry acetonitrile and stirred with $NaBF_4$ (2.75 g, 25 mol) at room temperature. After the mixture

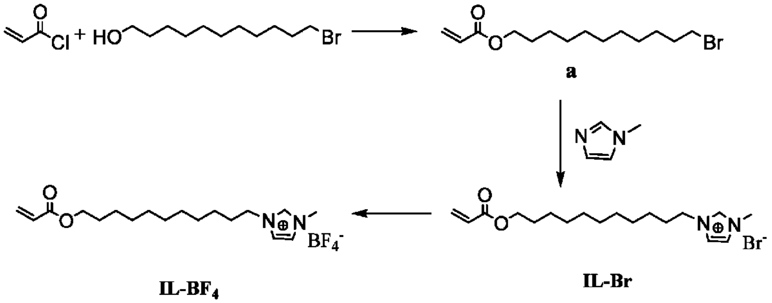

*Figure 2. Syntheses if **IL-Br** and **IL-BF$_4$** IL surfactants. 11-Bromoundecanol is first acrylated. The resulting bromoundecylacrylate **a** is then quaternarized with methylimidazole to give **IL-Br**. Ion exchange with NaBF$_4$ yields **IL-BF$_4$**.*

was stirred for 48 h under N_2 atmosphere, the sodium bromide precipitate was removed by filtration and the filtrate was concentrated. The concentrated filtrate was diluted with methylene chloride (300 mL) and filtered through a shrot column of silica gel. The Br^- concentration was checked qualitatively by the formation of AgCl after adding of silver nitrate ($AgNO_3$) into the decanted water. The resulting ionic liquid 1-(2-acryloyloxyundecyl)-3-methylimidazolium tetrafluoro-borate was dried under vacuum for 24 h as the white waxy solid. (6.24g, 79% yield). ^1H NMR (400 MHz, $CDCl_3$): 8.78 (1H, m, N–CH–N), 7.34–7.25 (2H, s, N–CH=CH–N), 6.36–6.35 (1H, m, CH_2=CH), 6.14–6.11 (1H, m, CH_2=CH), 5.81–5.79 (1H, m, CH_2=CH), 4.15–4.10 (2H, t, N–$CH_2(CH_2)_{10}O$–), 3.99 (3H, s, N–CH_3), 1.85–1.84 (2H, t, N–$CH_2(CH_2)_{10}O$–), 1.66–1.62 (2H, m, –$OCOCH_2CH_2$), 1.30–1.24 (14H, m, –$CH_2CH_2(CH_2)_7CH_2CH_2$–). Elemental Analysis: Calculated: $C_{18}H_{32}BF_4N_2O_2$, C: 54.70 %; H, 8.16 %; N, 7.09 %. Found: C: 54.22 %, H: 7.85 %, N: 7.35 %.

Hydrophobicity of Exchange Anions

The BF_4^- anion renders **IL-BF$_4$** more hydrophobic than **IL-Br**. Similarly, use of KPF_6 to produce an **IL-PF$_6$** moeity results in an even more hydrophobic IL surfactant. This series is illustrated in Fig. 3. This increase in hydrophobicity parallels an increase in the binding affinity for the respective anions and the imidazolium ring.

Surface Tension

Surface tension measurements at 24°C are illustrated in Fig. 4 for both IL-Br and IL-BF_4. The critical micelle concentration (CMC) of IL-Br is 13.8 mM and that of IL-BF_4 is 0.9 mM at 24°C. IL-Br is quite soluble, but it does pack effectively at the air/water interface, at high concentrations, to lower substantially the interfacial tension of water. IL-BF_4, however, being more hydrophobic has a substantially lower CMC. Its surface activity, however, appears only to be marginable, since it lowers the interfacial tension of water only about 4 mN/m at is CMC.

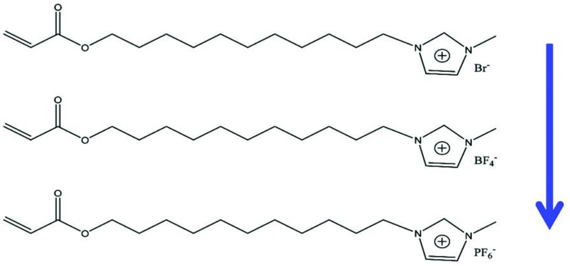

*Figure 3. **IL-Br, IL-BF$_4$**, and **IL-PF$_6$** reactive surfactant ionic liquids arranged in increasing order of hydrophobicity, due to increasing hydrophobitiy of the ions $Br^- < BF_4^- < PF_6^-$.*

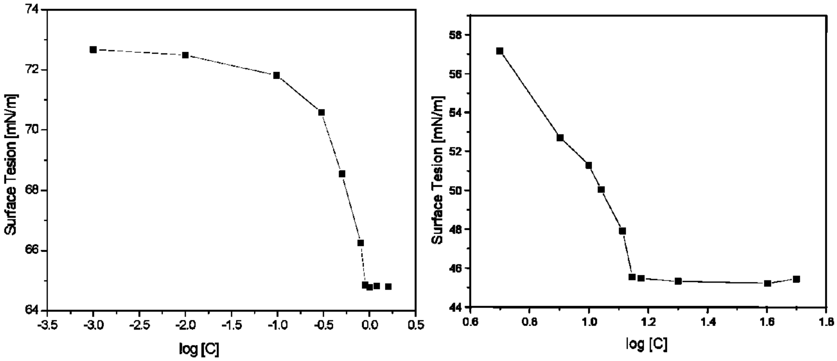

*Figure 4. Surface tension of ion liquid surfactants at the air/water interface at 24°C for (left) **IL-Br** and (right) **IL-BF$_4$**. Concentrations [C] are in mM.*

Phase Diagrams

Partial phase diagrams of the **IL-Br** -H_2O-methyl methacrylate (MMA) ternary system at 25 °C and 60 °C are illustrated in Fig. 5. Samples within the one-phase microemulsion region (to the left of the indicated boundaries) were transparent. Regions to the right and below the boundary are multiphase (emulsion) domains. The boundary line illustrated at 60°C shows that the single-phase microemulsion domain expands as temperature is raised to the polymerization temperature.

With 1-propanol as a cosurfactant, **IL-BF$_4$**-H_2O-1-propanol-methyl methacrylate (MMA) forms transparent and stable microemulsions at room temperature. A phase diagrams of the **IL-BF$_4$**-aqueous *n*-propanol-MMA pseudo-ternary system at 24°C is illustrated in Fig. 6. The shaded region represents a multiphase domain, and all of the remaining region at less than 50% by weight **IL-BF$_4$** is a single-phase microemulsion domain.

Polymerizations

Transparent gels can be produced by polymerization when surfactant and MMA concentrations are at the 25% level or higher (IL-Br-MMA-H_2O

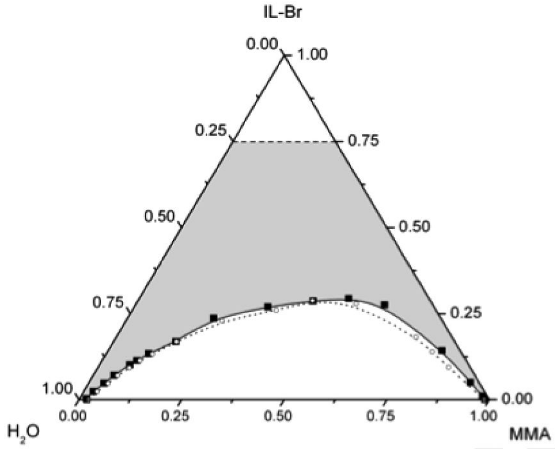

*Figure 5. Phase diagram (weight fraction) of **IL-Br**-water-MMA systems at 24°C, shadowed area shows the single phase microemulsion region.*

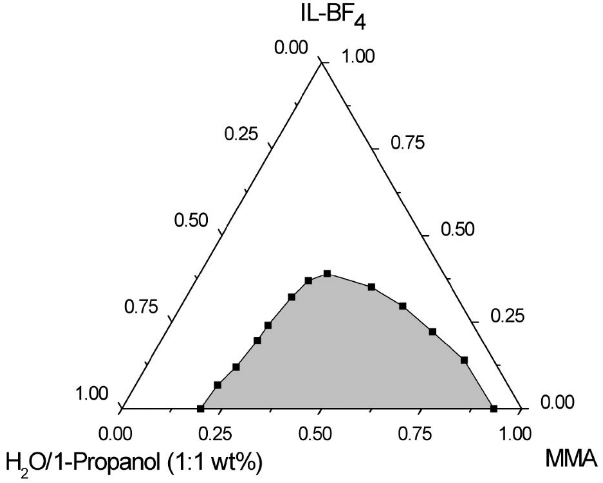

*Figure 6. Phase diagram (weight fraction) of **IL-BF$_4$**-aqueous propanol-MMA systems at 24°C, shadowed area shows two-phase region.*

(0.15/0.10/0.75)). Lower monomer levels yield uniform nanosized lattices upon polymerization. Such a transparent polymer gel shrinks and becomes opaque after being immersed in aqueous KPF$_6$ (Fig. 7(a) A, B). This opaque material can be converted back to a semi-transparent gel by further treatment with aqueous NaBr (Fig. 7(a) C). Scanning electron microscopy (SEM) images of the transparent gel (Fig. 7(b) A) show some weak stripes due to the shrinkage of the gel surface under the vacuum in the SEM. However, pores with diameters of ~3-8 μm can be observed in the opaque gel (Fig. 7(b) B). Most of these pores conect to others through small circular "windows", with diameters of ~ 1-3 μm.

These pores can be partially closed (self-healed) by further immersion in NaBr solution. The formation of the pores seen in the opaque gel is due to

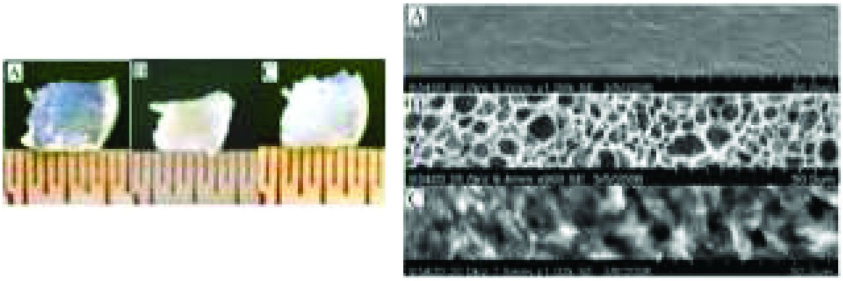

Figure 7. (a) Photographs of polymer gels: (A) after microemulsion polymerization; (B) gel in (A) treated with 0.1M KPF_6 solution; (C) gel in (B) treated with 0.1M NaBr solution. (b) SEM images of polymer gels (A) after microemulsion polymerization. (B) gel in (A) treated with aqueous 0.1M KPF_6. (C) gel in (B) treated with aqueous 0.1M NaBr solution. Reproduced by permission from Ref. (18). ©2006 Royal Society of Chemistry.

the shrinkage of the copolymer at the interfaces between aqueous and polymer domains. The polymerizable surfactant **IL-Br** molecules are situated along these interfaces between aqueous and MMA domains prior to polymerization. Once the vinyl groups of **IL-Br** and MMA are co-polymerized, the hydrophilic portions of **IL-Br** protrude into the aqueous domains or channels in the gel. The anion exchange from Br^- to PF_6^- changes the copolymer from being hydrophilic to being hydrophobic at these interfaces between aqueous and polymer domains, and thus causes shrinkage at the interface to make pores. This shrinkage results from condensation of surfactant IL chains on themselves and on the polymeric backbone as the polar imidazolium headgroups are transformed from being hydrophilic to being hydrophobic. The shrunken polymer domains at the interface can be converted back to hydrophilic and expanded in water again after anion exchange from PF_6^- to Br^-, and thus swell by imbibing water and partially healing or closing the pores.

The production of porous polymer membranes by non-solvent phase inversion (e.g., of PMMA) has been very thoroughly reported (*19–21*) However, in our approach we do not nucleate and grow porous membranes from polymer *solution*, but from polymer *solvogels*. These gels are the direct product of microemulsion polymerization, and it is not necessary to isolate the polymer and dissolve it, but to merely cast the solvogel precursor (microemulsion) on the surface you wish to be coated or in the shape of the object you wish to obtain.

In the **IL-BF$_4$**/aqueous propanol/MMA system, a microemulsion consisting of **IL-BF$_4$** (15 wt%), MMA (15 wt%), 1-propanol (35 wt%), and H_2O (35 wt%) was initiated with AIBN at 60°C. Ethylene glycol dimethacrylate (EGDMA) as crosslinker (1-10 wt % based on the weight of MMA and surfactant IL) was added to the formulation (*22*). All the transparent microemulsions were transformed into transparent or semi-transparent copolymer gels (depending on crosslinker content) after thermally initiated polymerization. Gravimetric analysis of the 2% and 10% EGDMA cross-linked samples indicated essentially complete conversion was obtained.

Figure 8A shows a transparent copolymer gel, polymerized with 2% EGDMA in an NMR tube. Such a transparent gel rod becomes opaque after being immersed in 0.1M KPF_6 solution (Figure 8B). This opaque material can be converted back to a semi- transparent polymer gel by imbibing a 1:4 v/v mixture of water and dimethylsulfoxide (aqueous DMSO) solution (Figure 8C). Such a recovered semi-transparent gel rod can be further converted back to an opaque rod by simply immersing into water (Figure 8D).

Figure 9A shows scanning electron microscopy (SEM) images of these polymer rods. The original transparent polymer gel shows some isolated pores with pore diameter of ~3 μm on the fractured surface (Figure 9A). These pores may be formed during the polymerization due to an earlier onset of phase separation, but most likely form due to the solvent evaporation under the vacuum during the SEM examination. However, as shown in Figure 9B, one observes close packed pores (both closed and open-cell pores) with diameters of 3-8 μm in the opaque gel shown in Figure 8B. The formation of theses pores is due to the shrinkage of the copolymer at the interfaces between aqueous and copolymer domains. Prior to the polymerization, the polymerizable surfactant **IL-BF_4** molecules are situated along these interfaces between aqueous and MMA liquid nanodomains with the hydrophilic imidazolium portions protruding into the aqueous domains or channels. The solvent exchange between the aqueous 1-propanol solution contained in the polymer gel and KPF_6 solution facilitates the anion exchange from BF_4^- to PF_6^- in the IL moiety. It is well-known that methylimidazolium-based ionic liquids containing PF_6^- are hydrophobic and immiscible with water (*23*). Therefore, the anion exchange from BF_4^- to PF_6^- changes the copolymer from being hydrophilic, a hydrogel, to being hydrophobic. This change causes shrinkage at the interface to make pores (see spinodal decomposition discussion below). The formation and distribution of closed-cell and open-cell pores are probably linked to how the net curvature evolves locally during polymerization and during ion exchange. Open-cell volumes have lower net curvature.

The shrunken polymer domains at the interface can be swollen in some organic solvents, such as aqueous DMSO, and thus partially heal or close the pores. Figure 9C shows the SEM images of a polymer gel recovered from DMSO. Most of polymer pores have been closed. DMSO is a poor solvent for PMMA, thus the pore healing is due to the swelling of IL surfactant containing copolymer blocks. In addition to DMSO solutions, these porous polymers have also been exposed to a representative range of organic solvents, such as dimethyl formamide (DMF), THF, acetonitrile, methanol, ethanol, 1-propanol, 1-buthanol, 1-pentanol, 1,2-buthandiol, hexane, benzene, toluene and cyclohexane. Interestingly, these polymer pores show a high selectivity, and can only be self-healed or closed after imbibing water-miscible solvents, such as DMF, THF, acetonitrile and alcohols (all of these solvents are good solvent for IL-PF_6). THF and acetonitrile are noteworthy since they are also good solvents for PMMA.

The most striking property of these copolymers is that the recovered gel can form porous polymer (with pore diameters of 3-7 μm) again by imbibing water (Figure 9D). The semi-transparent polymer gels are converted back to opaque and microporous materials as shown in Figure 8D. This transformation is due to the

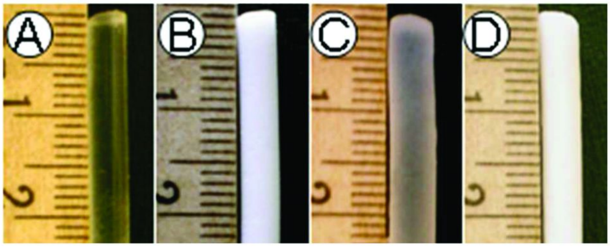

*Figure 8. Photographs of polymer rods: (A) after microemulsion polymerization (**IL-BF**$_4$, MMA, 1-propanol, H_2O at 15:15:35:35 weight ratio plus EGDMA at 2 wt% by weight with respect to other components); (B) gel in (A) treated with aqueous 0.1M KPF_6; (C) gel in (B) treated with water/DMSO solution (1:4 v/v); (D) recovered polymer gel in (C) treated with water. Reproduced by permission from Ref. (22). ©2007 Wiley InterScience.*

solvent exchange between the aqueous DMSO solution and water, which causes the surfactant IL chains to condense again and form pores.

The reversibility of pore formation has been verified by several aqueous DMSO/water cyclic treatments. Figure 9E shows the pore structure of the same polymer after 3 cycles of aqueous DMSO/water cyclic treatment. Compared with the structures shown in Figure 9B and 9D, most of the pores are close-packed and diameters of 3-7 μm are retained. However, some of the circular pores are deformed. Figure 9F suggests some loss of porosity with numerous cycles. We believe the reversibility of such a gel/pore formation can be improved by modification of the microemulsion formulations. Since DMSO, DMF and alcohols are widely used as drug solvents (*24*), these porous polymers have a demonstrable potential for controlled release applications in chemical delivery.

The pore size of the porous polymer can be tuned by adjusting the crosslinker content. Figures 10A and 10B show SEM images of the polymer prepared from a microemulsion containing 1 wt % of crosslinker EGDMA. One observes a honeycomb structured polymer with pores of 5-10 μm. With increasing crosslinker content, from 1 to 7 wt %, the pore size decreased to about 200 nm while the number of pores increased, as shown in Figure 10C.

Most of these pores connect to others through small circular “windows” with diameters of ~50 nm (see inset in Figure 10C). With the crosslinker content increased to 10 wt %, the size of open-cell pores decreased to ~100 nm (Figure 10D). Similarly, most of these pores are interconnected through ~ 20 nm diameter “windows”. This porous polymer exhibits a BET surface area of 36.6 m^2 g^{-1}. These results indicate that increasing the proportion of crosslinking agent present in the microemulsion not only affects the composition of the final monoliths but also decreases their average pore size as a result of early formation of highly cross-linked polymer domains with a reduced tendency to coalesce.

Thermal gravimetric analysis of this cross-linked EGDMA series and the 2% EGDMA gel is illustrated in Fig. 11. The results for the gel, run before substantial drying, show that the material is substantially solvent. The decomposition at about 400°C of the copolymer shows that the incorporation of the cationic imidazolium

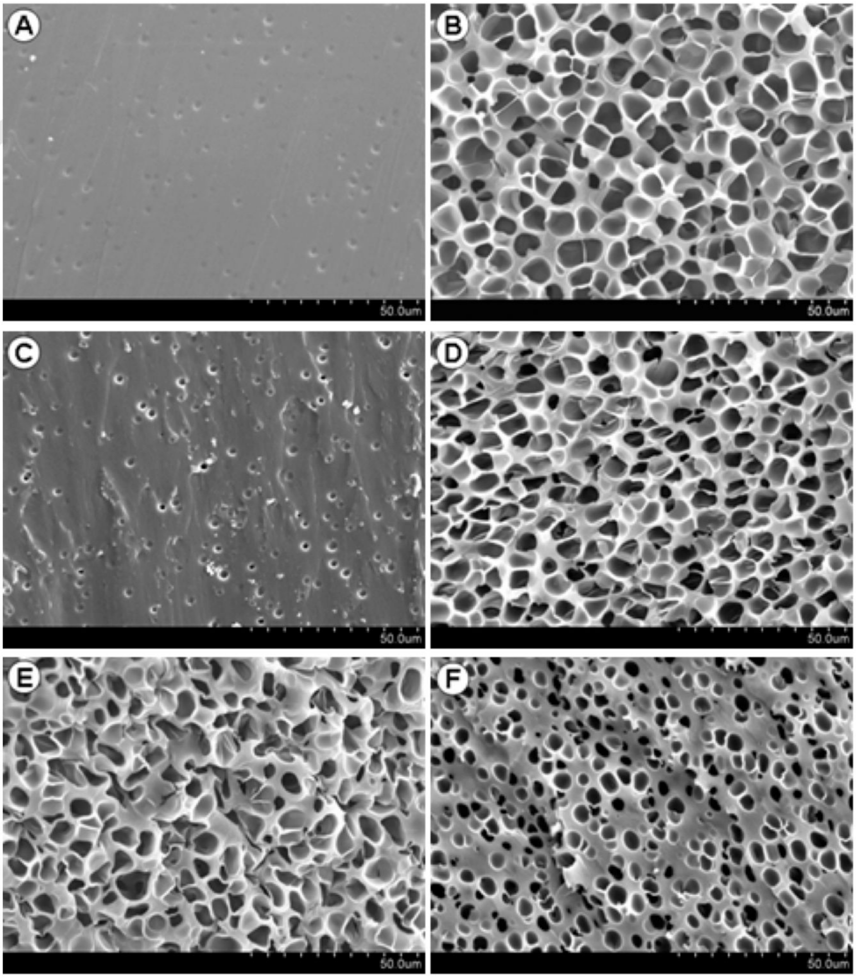

*Figure 9. SEM images of polymers: (A) after microemulsion polymerization (**IL-BF$_4$**, MMA, 1-propanol, H_2O at 15:15:35:35 weight ratio plus EGDMA at 2 wt% by weight with respect to other components); (B) gel in (A) treated with aqueous 0.1M KPF_6; (C) gel in (B) treated with aqueous DMSO; (D) gel in (C) treated with water; (E) after 3 cyclic treatments of aqueous DMSO/water; (F) after 7 cyclic treatments of aqueous DMSO/water. Reproduced by permission from Ref. (22). ©2007 Wiley InterScience.*

group into the comonomer substantially increases the thermal stability relative to PMMA by over 100°C.

It appears a physical explanation for this reversible solvogel-porous materials transition may be expressed in terms of (1) a three-dimensional phase space for the cross-linked copolymer, a polymer swelling solvent (e.g., DMSO), and a non-solvent (water), and (2) a spinodal decomposition of this three-component unstable solvogel phase, after addition of excess non-solvent, to give a small-pore condensed copolymer membrane in equilibrium with the non-solvent mixture.

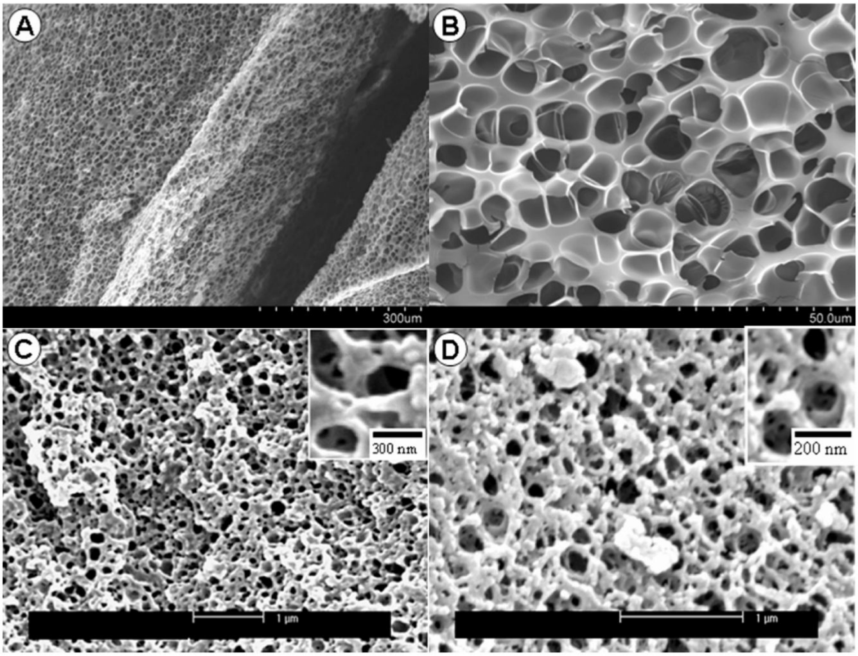

Figure 10. SEM images of porous polymers synthesized with different crosslinker contents (A) and (B) EGDMA 1 wt%; (C) EGDMA 7 wt%; (D) EGDMA 10 wt%. Reproduced by permission from Ref. (22). ©2007 Wiley InterScience.

The monomer sequences in the resulting copolymer strands (Fig. 12a-left) have not yet been identified, and detailed molecular weight and sequence analyses will be reported subsequently. However, from the cross-linking results presented below, it appears the final cell dimensions are controlled by the expanded chain length of the strands modeled in Fig. 12a-left. A solvogel phase exists when there is excess swelling solvent. The swelling solvent induces charge separation of the hexafluorphosphate anions from the imidazolium cations and thereby solvates the IL-surfactant blocks causing the copolymer to swell (Fig. 12a-left), and cause a significant decrease in light scattering, as the solvogel becomes translucent (Fig. 8C and Fig. 12b-left) or transparent. Immersion of the solvogel into excess non-solvent (water) induces “non-solvent phase inversion” to a totally collapsed and deswollen polymer having an open-cell porosity in equilibrium with the non-solvent/swelling solvent mixture (Figs. 8D and 12b-right). The non-solvent phase inversion process for producing microporous membranes from PMMA solutions put in contact with nonsolvents has been very well analyzed in terms of spinodal decompositions dynamics (*25*, *26*).

The spinodal nature and the reversibility of this transition is supported by the necessarily bicontinuous nature of the starting solvogel and resulting porous systems (Fig. 12b) (*27*, *28*). The solvogel comprises copolymer in swollen equilibrium with a preponderance of good solvent. The porous polymer comprises an open-cell highly scattering and condensed polymer in locally phase-separated

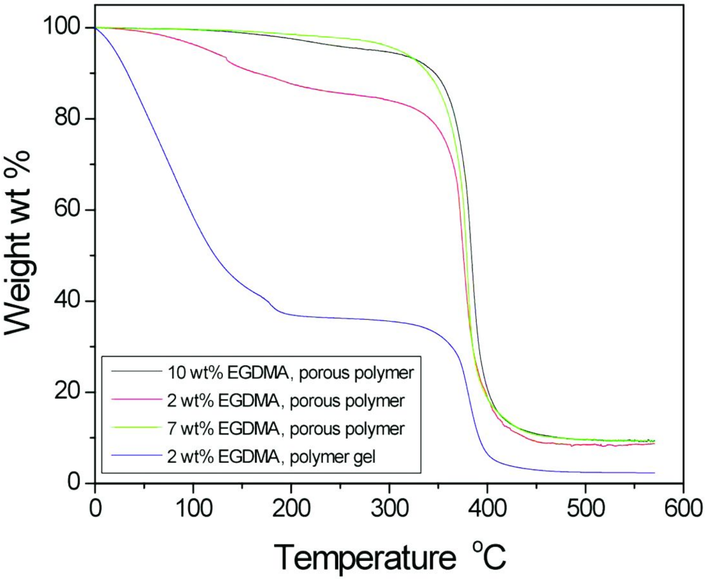

*Figure 11. TGA analysis of copoly(**IL-BF$_4$**/MMA) samples with different crosslinker (EGDMA) contents and of a precursor polymer gel.*

equilibrium with a preponderance of poor solvent. The solvogel is bicontinuous in cross-linked copolymer and solvent, and derives from the starting and opaque porous (random) block copolymer system, continuous in copolymer and continuous in non-solvent. As the open-cell porous materials is solvated by the swelling solvent, the IL-surfactant blocks solvate and the condensed copolymer film expands and becomes much less scattering because of its local solvation. The resulting solvogel, still inherently bicontinuous in cross-linked copolymer and solvent, then reversibly re-condenses to a highly light scattering bicontinuous system comprising an open-cell porous structure in equilibrium with the pore-filling solvent. The cross-linked nature of the copolymer necessarily precludes the possibility of this system undergoing a binodal decomposition, since macroscopic phase separation is precluded by the cross-linking. This lack o f access to binodal transitions tends to preserve the reversibility of the system, as demonstrated experimentally. The spinodal decompositional nature of this solvogel to porous material transition is “pinned due to elasticity arising from the crosslinkage” (*27*).

We have synthesized cross-linked polymer gels by polymerization of microemulsions stabilized by ionic liquid-based surfactants. The resulting polymer gels can be transformed to porous polymers by anion exchange of the IL moiety. These porous polymers can be recovered to polymer gels by imbibing organic solvents, such as DMSO and DMF or by ion-exchanging with a more hydrophilic anion, such as Br$^-$. These solvogels gels can be converted to porous polymers again by imbibing water. These striking properties present a new class of microporous polymers suitable for diverse applications, including tissue scaffolding, bicontinuous materials templating, antimicrobial filtration, and fire

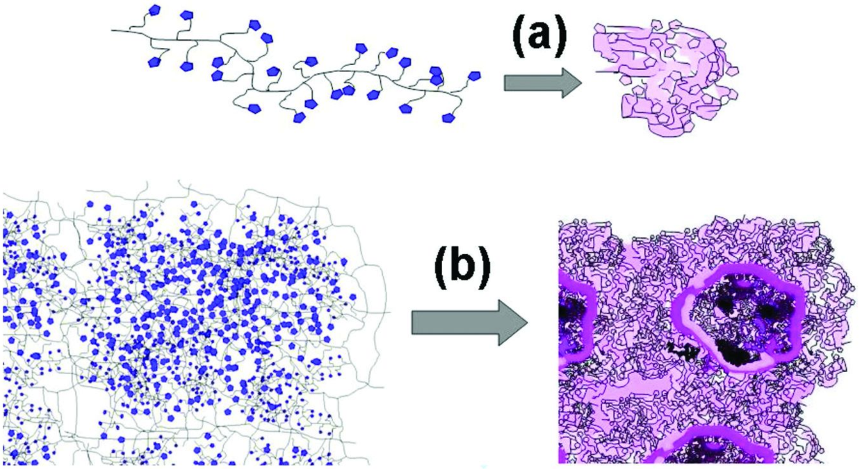

Figure 12. Cartoons illustrating (a) collapse of ionic liquid surfactant copolymer brush upon exposure to a poor solvent and (b) the corresponding spinodal decomposition of cross-linked bicontinuous gel to open cell porous material upon exposure to poor solvent. In (a) the individual brush hairs on the left represent the undecylimidazolium hexafluorophosphate species, with substantively dissociated hexafluorophosphate ions; these ions condense onto the imidazolium rings upon exposure to poor solvent (water), causing individual and proximal copolymeric chains to condense upon themselves (a-right). Reproduced by permission from Ref. (22). ©2007 Wiley InterScience.

resistant foams, in addition to controlled release chemical and drug delivery applications. Reversible poration in cell membranes has been reported as induced chemically (*29*) and physically (*30*, *31*). Reversible poration in synthetic systems has been recently reported in electrochemically active inorganic membranes (*32*) and in thermoreversibly porous systems (*33*–*35*).

This reversible poration provides means for fabricating useful and new classes of coating materials. One of these classes is based on the application of a low viscosity microemulsion to a solid or porous transparent support that cures to form a hydrogel. Ion exchange with a hydrophobic anion produces nano through microporous material that is highly light scattering and porous. Another of these class is based on application of a suitable microemulsion to a web to produce after polymerization and ion exchange an open cell porous material. This material is then imbibed with a suitable chemical or drug in liquid or dispersion form. Subsequent contact of this material to a suitable non-aqueous phase closes the pores in the periphery of the material to provide a loaded and controlled release web-supported chemical delivery system.

Acknowledgments

This work was supported by U.S. Army Tank-Automotive and Armaments Command Cooperative Agreement No. DAAD19-03-2-0013 and by the National Science Foundation grant award No. DMR-0414803 and award CHE-0443444.

References

1. Welton, T. *Chem. Rev.* **1999**, *99*, 2071.
2. Dupont, J.; de Souza, R. F.; Suarez, P. A. Z. *Chem. Rev.* **2002**, *102*, 3667.
3. Wasserscheid, P.; Keim, W. *Angew. Chem., Int. Ed.* **2000**, *39*, 3772.
4. Dyson, P. J. *Transition Met. Chem.* **2002**, *27*, 353.
5. Zhao, D.; Wu, M.; Kou, Y.; Min, E. *Catal. Today* **2002**, *74*, 157.
6. Sheldon, R. *Chem. Commun.* **2001**, *23*, 2399.
7. Fuller, J.; Carkin, R. T.; Osteryoung, R. A. *J. Electrochem. Soc.* **1997**, *144*, 3881.
8. Endres, F.; Bukowski, M.; Hempel-mann, R.; Natter, H. *Angew. Chem., Int. Ed.* **2003**, *42*, 3428.
9. Zhang, H.; Hong, K.; Mays, J. W. *Macromolecules* **2002**, *35*, 5738.
10. Ding, S.; Radosz, M.; Shen, Y. *Macromolecules* **2005**, *38*, 5921.
11. Anderson, J. L.; Pino, V.; Hagberg, E. C.; Sheares, V. V.; Armstrong, D. W. *Chem. Commun.* **2003**, 2444.
12. Fletcher, K. A.; Pandey, S. *Langmuir* **2004**, *20*, 33.
13. Anderson, J. L.; Pino, V.; Hagberg, E. C.; Sheares, V. V.; Armstrong, D. W. *Chem. Commun.* **2000**, 2051.
14. Gao, H.; Li, J.; Han, B.; Chen, W.; Zhang, J.; Zhang, R.; Yan, D. *Phys. Chem. Chem. Phys.* **2004**, *6*, 2914.
15. Eastoe, J.; Gold, S.; Rogers, S. E.; Paul, A.; Welton, T.; Heenan, R. K.; Grillo, I. *J. Am. Chem. Soc.* **2005**, *127*, 7302.
16. Chakrabarty, D.; Seth, D.; Chakraborty, A.; Sarkar, N. *J. Phys. Chem. B* **2005**, *109*, 5753.
17. Gao, Y.; Han, S.; Han, B.; Li, G.; Shen, D.; Li, Z.; Du, J.; Hou, W.; Zhang, G. *Langmuir* **2005**, *21*, 5681.
18. Yan, F.; Texter, J. *Chem. Commun.* **2006**, 2696.
19. Young, T.-H.; Chen, L.-W. *Desalination* **1995**, *103*, 233.
20. Barton, B. F.; Graham, P. D.; McHugh, A. J. *Macromolecules* **1997**, *31*, 1672.
21. Chun, K.-Y.; Jang, S.-H.; Kim, H.-S.; Kim, Y.-W.; Han, H.-S.; Joe, Y.-I. *J. Membr. Sci.* **2000**, *169*, 197.
22. Yan, F.; Texter, J. *Angew. Chem., Int. Ed.* **2007**, *119*, 2492.
23. (a) Cammarata, L.; Kazarian, S. G.; Salter, P. A.; Welton, T. *Phys. Chem. Chem. Phys.* **2001**, *3*, 5192. (b) Itoh, H.; Naka, K.; Chujo, Y. *J. Am. Chem. Soc.* **2004**, *126*, 3026.
24. Seedher, N.; Bhatia, S. *AAPS PharmSciTech* **2003**, *4*, 281.
25. Barton, B. F.; McHugh, A. J. *J. Membr. Sci.* **2000**, *166*, 119.
26. Di Luccio, M.; Norbega, R.; Borges, C. P. *Polymer* **2000**, *41*, 4309.
27. Onuki, A.; Puri, S. *Phys. Rev. E* **1999**, *59*, R1331.
28. Bastea, S.; Puri, S.; Lebowitz, J. *Phys. Rev. Lett.* **2001**, *63*, 041513-1.
29. Toner, M.; Russo, M.; Bieganski, R. WO 200001532 A1, March 23, 2000.
30. Chang, D. C. *Biophys. J.* **1989**, *56*, 641.
31. Fennell, D. F.; Whatley, R. E.; McIntyre, T. M.; Prscott, S. M.; Zimmerman, G. A. *Arterioscler. Thromb.* **1991**, *11*, 97.
32. Farrusseng, D.; Julbe, A.; Guizard, C. *J. Am. Chem. Soc.* **2000**, *122*, 12592.
33. Tsuji, T.; Konno, M.; Sato, S. *J. Chem. Eng. Jpn.* **2000**, *90*, 447.

34. Konno, M.; Tsuji, T.; Sato, S. In *Polymer Gels: Fundamental Biomedial Applications (Proc. Int. Symp. 1989)*; DeRossi, D., Ed.; Plenum Press: New York, 1992; pp 173−181.
35. Rama Rao, G. V.; Balamurugan, S.; Meyer, D. E.; Chilkoti, A.; López, G. P. *Langmuir* **2002**, *18*, 1819.

Downloaded by OHIO STATE UNIV LIBRARIES on June 22, 2012 | http://pubs.acs.org
Publication Date (Web): November 10, 2010 | doi: 10.1021/bk-2010-1050.ch014

Chapter 14

Washpermanent Nano-Structured Textiles

Surface Protection by Biomimicking the Lotus Leaves

Oihana Elizalde[*] and Michael Schmitt

BASF SE, 67056 Ludwigshafen, Germany
[*]oihana.elizalde@basf.com

The self-cleaning property of some plants and insects (such as the Lotus leaf) is the result of low surface energy and a unique dual-size surface topography. A large amount of work has been devoted to mimick the structure of the Lotus plant for producing water, oil and stain repellent textile finishes. The biggest challenges are to achieve a high wash fastness and a smooth touch, specially in the protection of everyday items, such as apparel, home textiles and industrial fabrics. To obtain a well-defined hydrophobic surface structure, a proper particle distribution, good particle adhesion onto the textile, and a hydrohobic surface are required. Following a newly developed concept, based on organic particles, we could produce nanostructured cotton fibres, with a high wash fastness. The finished textiles showed increased water and oil repellence, in comparison to other available finish systems. Nanotechnology plays a very important role in this application field, since thanks to the thin coating and the small size of the particles, the breathability and touch of the textiles are not affected.

There are many examples of water-repellent plants and insects in nature, of which probably the best known example is the Lotus plant (Nelumbo Nucifera). This plant is considered a symbol of purity in several Asian regions, and its leaves stay always perfectly clean even emerging from muddy waters. Many years it was believed that the water repellence and self-cleaning effect of the Lotus plant are

In Smart Coatings III; Baghdachi, J., et al.;
ACS Symposium Series; American Chemical Society: Washington, DC, 2010.

the result of a very flat and smooth surface that avoids water and dirt to adhere to it. In 1975 Barthlott and Neinhuis (*1*, *2*) (Botanical Institute of Bonn University) analyzed the Lotus leaf with a scanning electron microscope (SEM) and found out that the surface was actually rough, and that this surface roughness and its hydrophobicity were responsible for the water repellence and the self-cleaning properties. They named this effect the Lotus effect®.

There are two physical characteristics that explain this effect: on the one hand a combination of nano- and microstructures and on the other hand the hydrophobic character of the surface (the leaf surface is covered with microscopic wax particles). The hydrophobically structured surface minimizes the contact area between the surface and a water droplet. As a result, water cannot spread out and water droplets roll around removing dirt particles on the surface.

This effect opens the door to a large list of potential applications going from waterproof textiles to stain resistant paints. But despite all the interest and amount of work devoted to this research area very few commercial products offering water repellent surfaces/finishes are available. The main challenge is to build mechanically stable and robust nanostructures that provide long-term hydrophobicity and self-cleaning properties. The objective of this work is to obtain nanostructured textiles with good water, oil and stain resistance and high wash fastness. These textiles should be easy to clean and dirt particles should not adhere to the surface so that they can be easily cleansed off.

Downloaded by OHIO STATE UNIV LIBRARIES on June 22, 2012 | http://pubs.acs.org
Publication Date (Web): November 10, 2010 | doi: 10.1021/bk-2010-1050.ch014

The Role of Nanotechnology in Textile Finishing

Textile fabrics are usually finished, coated or laminated in order to provide them with different functions such as water resistance, vapor permeability, soil resistance, increased durability, wrinkle resistance, anti-bacteria, anti-static and UV-protection, flame retardation and optical appearance. In particular water, oil and stain repellent finishes are in very high demand for the protection of everyday items, such as apparel, home textiles and industrial fabrics. In the last years nanotechnology has been widely used to develop products with such performance. It is believed that the large surface area-to-volume ratio and high surface energy of nanoparticles provide better affinity to textiles, and therefore, an improved durability (important for the wash permanence). Nanoparticles can be coated onto fabrics using several methods like for example spraying, transfer printing, washing, rinsing and padding. To achieve a well-defined hydrophobic surface structure and a smooth touch is not an easy task and presents many challenges:

- A minimum load of chemicals is important for a smooth touch. This can be achieved thanks to nanoparticles, since a thin coating will not affect the breathability and touch of the fabrics (the particles are so small that they are not detectable by a human hand).
- The particles must be evenly distributed, to avoid agglomeration or migration, in order to provide high effectiveness.
- Good particle adhesion onto the textile is a key point to achieve a high wash fastness and mechanical resistance.

- Coating with nanoparticles has as additional advantage that the particles cannot be detected by the human eye, and therefore, no changes in the color of the textile are observable.
- In addition to all these points, the treatment with nanoparticles should be cost effective and have a better performance versus established fluorocarbon chemistry and be easy and safe to apply, with no health risk for the customers.

Hydrophobic surfaces are usually achieved by trifluoromethyl carbon (-CF_3) containing diblock polymers, surfactants, or coupling agents. They are able to self-assemble on the surface and form a monolayer. The state-of-the-art in textile applications are fluorocarbon (FC) resin finishes, which are applied as aqueous dispersions. The FC resins present superior and unique water, soil and oil repellent properties in comparison to other hydrophobic surface modifiers (such as silicones or alkanes) thanks to the extremely low surface energy of the perfluorinated side chains in the polymers.

FC resins form thin and smooth surfaces, where the perfluorocarbon chains on the surface provide hydrophobicity (as shown in Figure 1). The wetting behaviour of smooth surfaces is described by the equation of Young (*3*) (as displayed in Figure 2), who established the relation between the three surface tensions γ^{SV} (solid-vapor), γ^{SL} (solid-liquid), γ^{LV} (liquid-vapor) and the contact angle Θ.

$$\gamma^{SV} - \gamma^{SL} = \gamma^{LV} \cos\Theta \qquad (1)$$

The repellence of smooth surfaces is limited (the maximum contact angle achievable is around 120°) and many end users demand better systems with respect to properties like water, oil/fat and dirt repellence. In addition, it would be desirable to reduce the amount of FC due to price and ecological reasons. Introducing roughness into a smooth hydrophobic surface could exceed its limitations and provide a better performance. But Young´s equation is only valid in cases when the water/liquid droplet has complete contact with the rough surface. In reality this contact is never 100%, and thus an equation formulated by Cassie and Baxter (*4*, *5*) for microstructured surfaces should be applied. This equation describes the relation between the contact angle Θ of the smooth surface and the observed contact angle of the structured surface Θ_{com}.

$$\cos\Theta_{com} = a_S \cos\Theta - a_V \qquad (2)$$

where a_S is the surface area fraction in contact with the liquid and a_V the surface area fraction in contact with trapped air (see Figure 2). Contact angle values up to 150° - 160° and a decrease in the contact angle hysteresis can be reached when a_V is >> a_S (the more air trapped between the rough surface and the water, the larger the contact angle will be). This results in an easy roll-off of liquid drops (low roll-off angles) and therefore, in an enhanced hydrophobicity in comparison to smooth surfaces.

The main problem is that it is not easy to predict which is the required surface roughness to obtain a desired water, oil and stain repellence; it can vary from the order of nanometers to tens of microns depending on the application and surface.

Downloaded by OHIO STATE UNIV LIBRARIES on June 22, 2012 | http://pubs.acs.org
Publication Date (Web): November 10, 2010 | doi: 10.1021/bk-2010-1050.ch014

Downloaded by OHIO STATE UNIV LIBRARIES on June 22, 2012 | http://pubs.acs.org
Publication Date (Web): November 10, 2010 | doi: 10.1021/bk-2010-1050.ch014

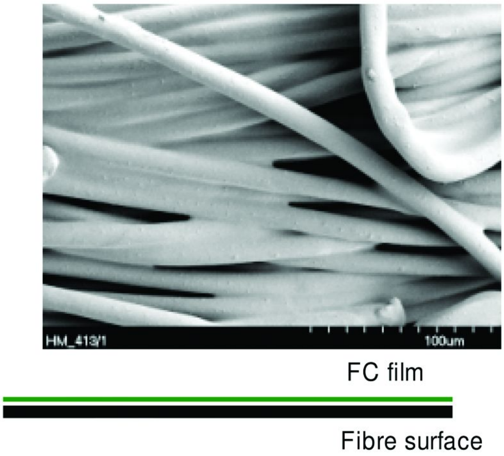

Figure 1. Fluorocarbon (FC) dispersions form smooth films, as shown in the upper microphotograph on polyester (PES) fibres.

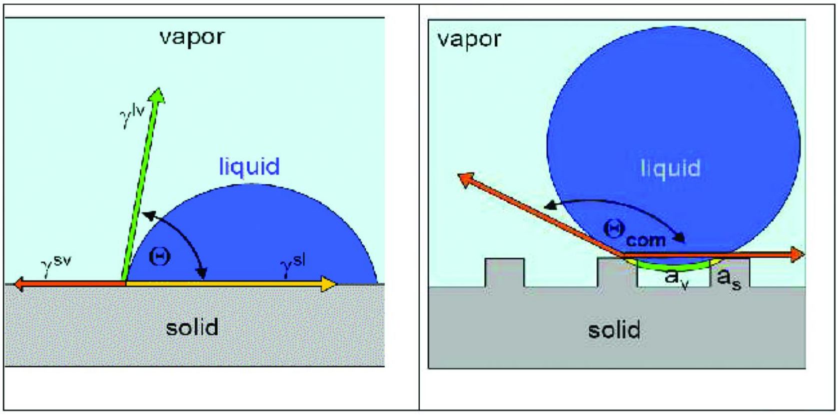

Figure 2. Wetting of a smooth hydrophobic surface and the four parameters contained in the Young equation (left). Wetting scheme of a rough hydrophobic surface (right), as described by the Cassie and Baxter equation.

There are different approaches to introduce the surface roughness, such as using sol-gel chemistry (*6–9*), silicon pilars (*10*), polyelectrolyte multilayers (*11*), or as shown in Figure 3, organic polymer nanoparticles. In the next sections the nature of these organic nanoparticles and their application onto textile substrates will be described.

Concept for Superhydrophobic Textile Finishes: Organic Polymer Nanoparticles

In this work we propose to introduce the required roughness onto the textile surface by means of organic polymer nanoparticles, and to provide

Downloaded by OHIO STATE UNIV LIBRARIES on June 22, 2012 | http://pubs.acs.org
Publication Date (Web): November 10, 2010 | doi: 10.1021/bk-2010-1050.ch014

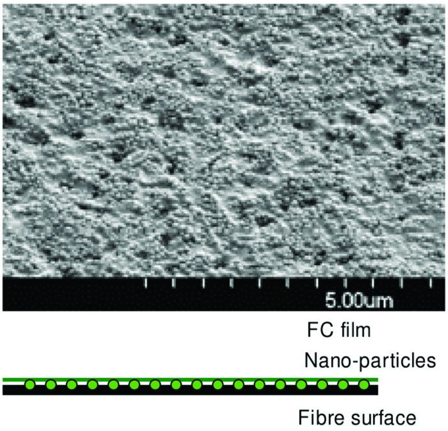

Figure 3. Nanostructured surface by applying organic nanoparticles onto a PES foil.

additional hydrophobicity by combining them with FC resins (although the use of other hydrophobizing agents is also possible). Shape retaining organic core shell particles synthesised via emulsion polymerization have been used in this work to obtain nanostructured surfaces onto cotton fabrics. The particles are directly synthesized in water via two stage emulsion polmerization, and they are compatible with commercially available FC emulsions. The core of the particles is formed of a highly crosslinked and high Tg polymer that does not form a film under the application conditions and thefore, retains its round shape providing a nanostructured surface. The shell is formed of a softer and film forming polymer fixes the particles onto the textile surface. The size of the structure forming core-shell particles and the core-to-shell ratio have a strong influence on the resulting surface nanostructure (even after the drying and curing steps). Figure 4 shows three different core-shell particles of different sizes applied onto a cotton fabric. The three examples show a very homogeneous distribution of particles onto the textile surface with practically no particle agglomeration.

The structure forming core-shell particles can be formulated together with a FC emulsion and applied onto the textile in one step, for example by padding (see Figure 5). Moderate drying and curing temperatures are required, and under these conditions the binder system must form a stable and structured layer on the textile.

Using this approach we obtain a double surface structure on the textile that combines micrometer (cotton fabrics as such are not smooth) and nanometer (through the shape retaining core-shell particles) scale (Figure 6). Several published works (*6*, *12–14*) showed as well the advantages and better performance of such dual structures. The amount of core-shell particles and FC resin must be optimized to get an optimal performance in terms of water, oil and stain repellence, mechanical stability of the nanostructure and wash fastness. When the amount of applied FC resin is too high in relation to the amount of particles, the spaces between the particles are filled with FC resin and the final roughness of the textile will decrease. This will result in worse water, oil and stain repellence,

Downloaded by OHIO STATE UNIV LIBRARIES on June 22, 2012 | http://pubs.acs.org
Publication Date (Web): November 10, 2010 | doi: 10.1021/bk-2010-1050.ch014

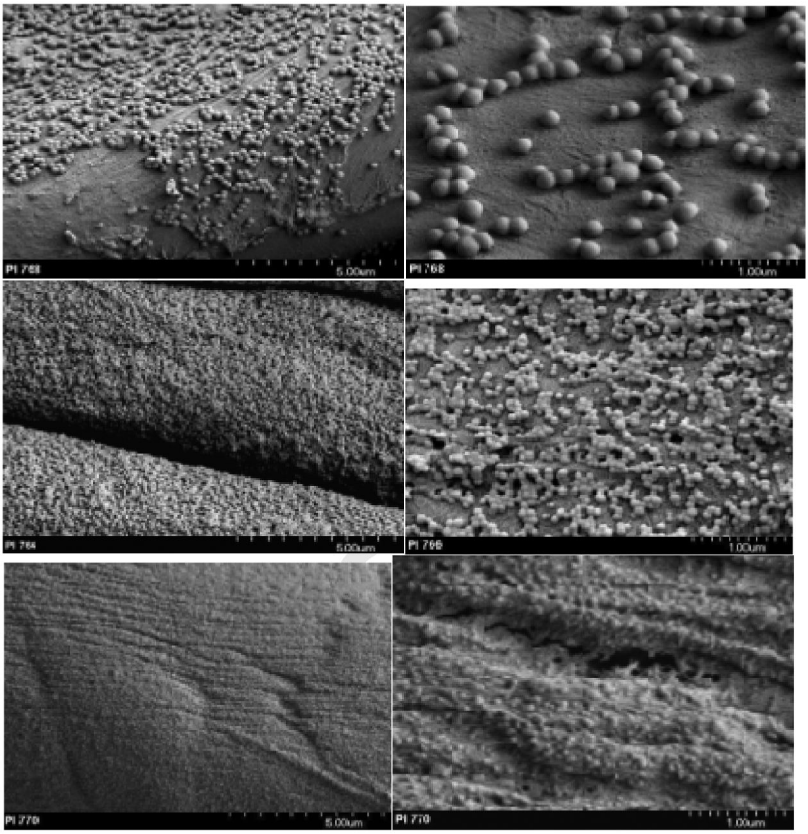

Figure 4. Core-shell particles of different sizes applied onto cotton. The 2 top figures show a fabric impregnated with 280nm size core-shell particles in two different magnifications; the two center figures show the textile surface impreganted with 120 nm particles; and the two bottom micrographs after treatment with 80 nm particles. The resulting surface nanostructure strongly depends on the size of the core-shell particles.

since the amount of air trapped between the water droplet and the surface will decrease.

In order to check the effect of the FC emulsion on the surface structure and the adhesion of the whole coating onto cotton fabrics different samples were prepared. Figure 7 shows a cotton fabric treated at first only with core-shell particles (top), and after coating it in a second step with a FC resin (bottom). As we can observe in Figure 7 (bottom) the FC resin forms a monolayer on top of the nanoparticles, keeping the surface roughness and providing additional hydrophobicity. Thanks to the soft shell and the FC resin, the coating is fixed onto the textile surface and even after washing the fabric, the nanostructure remains intact. As it will be shown later, even after washing, the water, oil and stain repellence are maintained at high levels.

Downloaded by OHIO STATE UNIV LIBRARIES on June 22, 2012 | http://pubs.acs.org
Publication Date (Web): November 10, 2010 | doi: 10.1021/bk-2010-1050.ch014

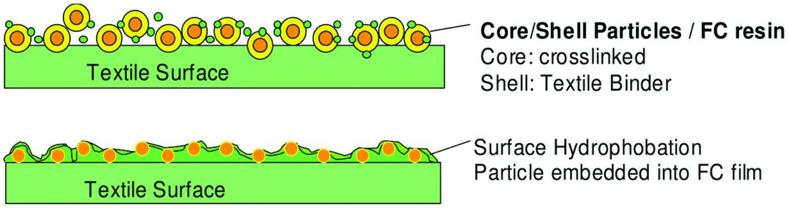

Figure 5. The top figure shows the one-step application of structure forming core-shell particles (yellow-orange) and a FC emulsion (green). The bottom scheme shows the nanostructured textile surface after drying and curing (typically at temperatures of around 160°C).

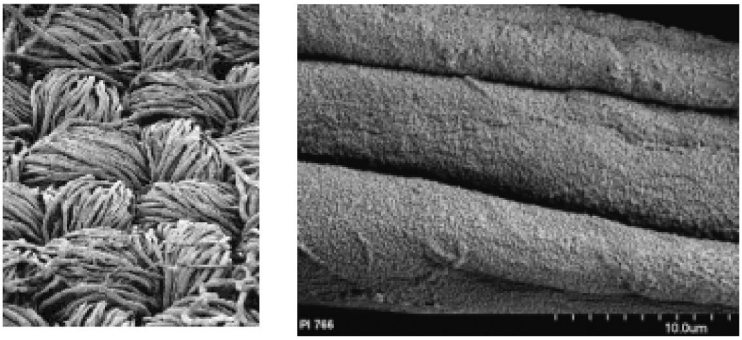

Figure 6. This figure shows the dual structure of the textile surface. Left: microstructure of cotton fabric. Right: detail of the additional nanostructure obtained through core-shell particles.

Experimental Results: Performance on Cotton Fabric

In order to test the performance of the described approach in comparison to pure FC finish a 100% cotton fabric (weight 114 g/m^2), normally employed for shirting applications, was used. The fabric was impregnated with two different formulations: formulation 1 (F1) contained only a FC resin (45 g/l) and formulation 2 (F2) contained the same FC amount, plus additionally a dispersion with core-shell particles. Both formulations were applied by padding, and after impregnation the fabrics were dryed and cured.

The oil repellence of the finished textiles was measured following the standard AATCC 118-2002, that uses test liquids of increasing polarity. The results are rated from 1 to 8; 1 being the worst oil repellence and 8 the best. The aqueous stain repellence is measured following the standard AATCC 193-2005, using water/isopropyl alcohol test liquids. In this case the rating goes from 1 to 10, 1 being the worst and 10 the best score. A very important test is the spray test (AATCC 22-2005) in which the water penetration through the textile is measured (as % of non-wetted surface). Until this moment no standards have been defined to measure the self-cleaning properties of the finished textiles. One possibility is to measure the sliding angle (see Figure 8). By measuring the sliding angle (α) and knowing

Downloaded by OHIO STATE UNIV LIBRARIES on June 22, 2012 | http://pubs.acs.org
Publication Date (Web): November 10, 2010 | doi: 10.1021/bk-2010-1050.ch014

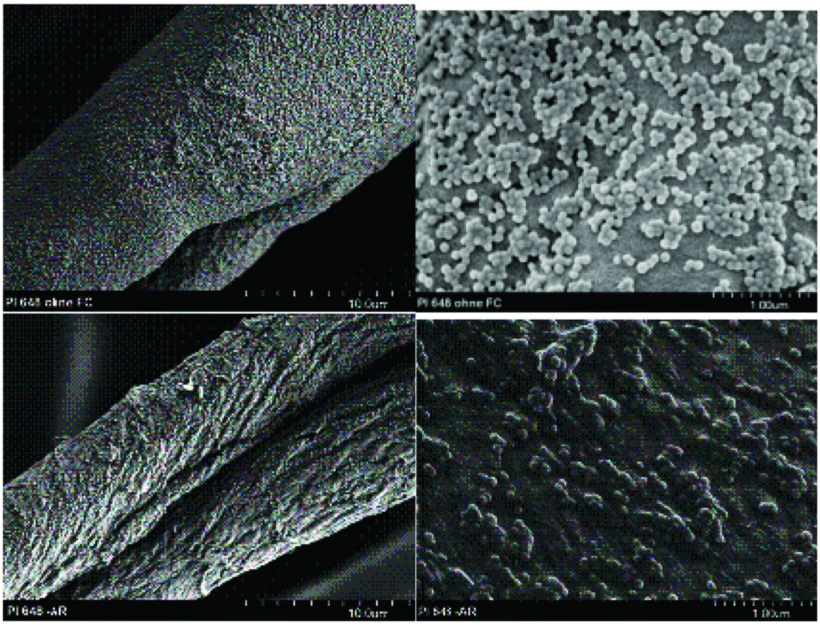

Figure 7. The two figures on the top show a cotton fabric coated only with core-shell particles; the two figures on the bottom shos the same fabric after a second coating with FC resin.

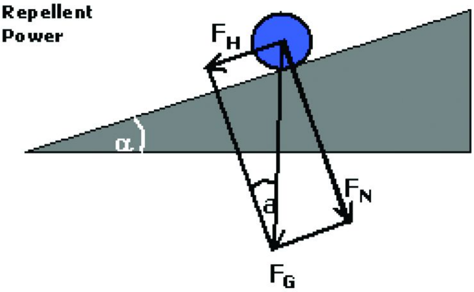

Figure 8. Schematic representation of the repellent power of a surface and the sliding angle.

the drop volume it is possible to have an exact determination of the repellence; the smaller the sliding angle, the higher the repellent power. A second possibility is to carry out tests where different soils are cleaned away (analoguously to the spray test), and the amount of water and time needed to clean the textile are measured.

Table I shows the results of the previously described tests for two cotton fabrics impregnated with formulations 1 and 2. As it can be observed in the table, the finished and unwashed nanostructured textile has superior performance in all the measured properties (note that the amount of FC was the same for both textiles).

Downloaded by OHIO STATE UNIV LIBRARIES on June 22, 2012 | http://pubs.acs.org
Publication Date (Web): November 10, 2010 | doi: 10.1021/bk-2010-1050.ch014

Table I. Water, oil and stain repellence tests of two cotton fabrics impregnated with formulations 1 and 2

Formulation	*F1* *(FC resin)*	*F2* *(Nanostructured finish)*
Finished cotton fabric, unwashed		
Spraytest	80	100
Oil repellence	1	7
Water repellence	2	9
Sliding angle	12	12
After 10 Home laundry washes (40°C, 15g detergent)		
Spraytest	50	95
Oil repellence	1	6
Water repellence	2	6

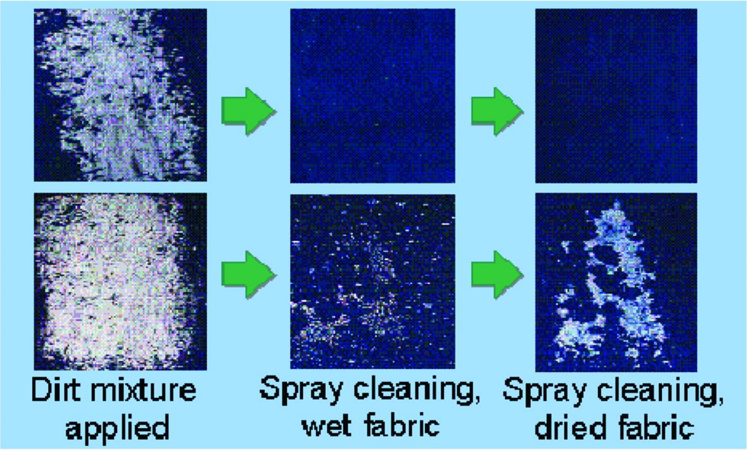

Figure 9. Self-cleaning behavior of the nanostructured finish (F2, top) in comparison to the FC-finish (F1, bottom). Employed dirt mixture: SiO_2 + olive oil + carbon black.

In order to measure the wash fastness of both finishes, each fabric was washed 10 times and the spray-test and oil and water repellence tests were repeated afterwards. Although there is a slight decrease in the general performance, the water, oil and stain repellencies of the nanostructured textile are still at a very high level and have superior results versus the pure FC finish.

In addition to the results shown in Table I, cleaning tests with different dirt mixtures were carried out. The objective of the measurements was to compare the self-cleaning behavior of the nanostructured finish (F2) in comparison to the FC-finish (F1). The test procedure employed was carried out according to EN 24920 (Figure 9). Important parameters to compare the self-cleaning behaviour of both textiles are the amount of time and water required to clean off the dirt from the textile. In all the tests, the nanostructured textile showed a superior self-cleaning effect.

Conclusions

Following a newly developed concept, based on shape-retaining organic core-shell nanoparticles, we could produce nanostructured cotton fabrics with high wash fastness. Thanks to this core-shell technology it is possible to expand into apparel applications, where the stability of the nanostructured surface is a critical issue. This approach allows to achieve a very good adhesion onto the textile thanks to the particle-shell (which is a key-point for the mechanical stability of the coating), and avoids particle agglomeration, providing a homogeneous and thin coating onto cotton (important for a high efficiency and the optical appearance, transparency, of the coating). The nanostructured textiles showed a significantly higher water and oil repellence, in comparison to other available textile finish systems (fluorocarbon resins). The aqueous stain repellence of the nanostructured textiles was also superior to the FC-finish and the self-cleaning properties of the textiles treated with this new concept could be demonstrated.

References

1. Neinhuis, C.; Barthlott, W. *Ann. Bot.* **1997**, *9*, 667.
2. Barthlott, W.; Neinhuis, C. *Planta* **1997**, *202*, 1.
3. Young, T. *Philos. Trans. R. Soc.* **1805**, *95*, 65.
4. Cassie, A. B. D.; Baxter, S. *Trans. Faraday Soc.* **1944**, *40*, 546.
5. Cassie, A. B. D. *Discuss. Faraday Soc.* **1948**, *3*, 11.
6. Ming, W.; Wu, D.; van Benthem, R.; de With, G. *Nano Lett.* **2005**, *5*, 2298.
7. Shirtcliffe, N. J.; McHale, G.; Newton, M. I.; Perry, C. C. *Langmuir* **2003**, *19*, 5626.
8. Shang, H. M.; Wang, Y.; Takahashi, K.; Cao, G. Z.; Li, D.; Xia, Y. N. *J. Mater. Sci.* **2005**, *40*, 3587.
9. Erbil, H. Y.; Demirel, A. L.; Avci, Y.; Mert, O. *Science* **2003**, *299*, 1377.
10. Bico, J.; Tordeux, C.; Quéré, D. *Europhys. Lett.* **2001**, *55*, 214.
11. Zhai, L.; Cebeci, F. C.; Cohen, R. E.; Rubner, M. F. *Nano Lett.* **2004**, *4*, 1349.
12. Pantakar, N. A. *Langmuir* **2004**, *20*, 8209.
13. Feng, L.; Li, S.; Li, Y.; Li, H.; Zhang, L.; Zhai, J.; Song, Y.; Liu, B.; Jiang, L.; Zhu, D. *Adv. Mater.* **2003**, *2*, 301.
14. Shirtcliffe, N. J.; McHale, G.; Newton, M. I.; Chabrol, G.; Perry, C. C. *Adv. Mater.* **2004**, *16*, 1929.

Downloaded by OHIO STATE UNIV LIBRARIES on June 22, 2012 | http://pubs.acs.org
Publication Date (Web): November 10, 2010 | doi: 10.1021/bk-2010-1050.ch014

Downloaded by 89.163.35.42 on June 22, 2012 | http://pubs.acs.org
Publication Date (Web): November 10, 2010 | doi: 10.1021/bk-2010-1050.ix002

Subject Index

A

- AA 2024-T3. *See* Aluminum alloy 2024-T3
- AA2024 unclad alloy
  - AC131 sol-gel film, 183*f*
  - capsule doped primers coating, 182*f*
  - chromate loaded primer, 186*f*
  - filiform corrosion test, 183*f*
  - 8-hydroxychinoline loaded primer, 186*f*
  - mercaptobenzothiazole loaded primer, 186*f*
  - non-inhibited primer, 186*f*
  - scratch area, 184*f*
  - SVET maps, 186*f*
  - TSA anodic film, 182*f*
- 1-(11-Acryloyloxyundecyl)-3-methylimidazolium bromide
  - hydrophobicity, 197*f*
  - surface tension, 196, 197*f*
  - synthesis, 195, 196*f*
  - water-MMA systems, 198*f*
- 1-(11-Acryloyloxyundecyl)-3-methylimidazolium tetrafluoroborate
  - aqueous propanol-MMA systems, 198*f*
  - hydrophobicity of exchange anions, 197*f*
  - surface tension, 197*f*
  - synthesis, 195, 196*f*
- AC131 sol-gel film, 183*f*
- AFM. *See* Atomic force microscopy
- $AlMe_3$. *See* Trimethylaluminum
- Aluminum alloy 2024-T3
  - corrosion
    - inhibitors, 151
    - protection coatings, 165
  - polypyrrole/aluminum flake hybrids, 151
- Aluminum flake
  - polypyrrole, 151
    - ammonium persulfate, 157*f*
    - catechol, 154*f*, 157*f*
    - CPV coatings, 159*f*
    - hybrid synthesized, 157*f*
    - PVC coatings, 160*f*, 161*f*
    - synthesis, 157*f*
  - as received, 154*f*, 157*f*
  - structures on, 156*f*
- Amine-terminated self-assembled monolayers
  - silicon wafers, 24
  - static water contact angle values, 26*t*
- 3-Aminopropyl trimethoxysilane and 4340 steel alloy button, 138*f*
- Ammonium persulfate and aluminum flake/polypyrrole hybrid synthesis, 157*f*
- Amphiphilic surfaces and Zonyl FSO-100 surfactant, 99
- Ardrox AV15, 173*f*, 174*f*
- As-received aluminum flake
  - CPV coatings, 159*f*
  - PVC coatings, 160*f*, 161*f*
- Atomic force microscopy
  - control PU surfaces CA & RMS roughness, 96*f*
  - MPEG-PU surfaces CA & RMS roughness, 97*f*
  - PFO-PU surfaces CA & RMS roughness, 98*f*
  - polymer brush 3b, 83*f*
  - PP, 116*f*
  - PP virgin and grafted copolymers, 117*t*
  - PP-g-DMAEMA, 116*f*
  - (PP-g-DMAEMA)-g-NIPAAm, 116*f*
  - roughness measurements, 94
  - XGNP, 125*f*
  - XGP, 125*f*
  - Zonyl-FSO PU surfaces CA & RMS roughness, 100*f*
- Atom transfer radical polymerization, 73
- ATRP. *See* Atom transfer radical polymerization

B

- Bending tests, 50*f*
- Binary graft copolymers, 107, 112*f*
- Boltorn H2004 dendritic polyol, 92*f*
- 11-Bromoundecylacrylate, 195, 196*f*
- Bulk P(3PPA), 139*f*

C

- Cadmium based coatings, alternatives, 133
- CA measurement. *See* Contact angle measurement
- Capsule
  - capsule/coating combinations, 171*f*
  - characterization and performance evaluation, 8
  - formation
    - inhibitors, 177*f*
    - organic core material, 173*f*

Downloaded by 89.163.35.42 on June 22, 2012 | http://pubs.acs.org
Publication Date (Web): November 10, 2010 | doi: 10.1021/bk-2010-1050.ix002

- size distribution
  - core material, 174*f*
  - incorporated inhibitor, 177*f*
- Carbon-fiber composite, 49, 56
- CA & RMS roughness
  - control PU surfaces, 96*f*, 97
  - MPEG-PU surfaces, 97*f*
  - PFO-PU surfaces, 98*f*
  - Zonyl-FSO PU surfaces, 100*f*
- Cassie and Baxter equation, 212*f*
- Catechol and aluminium flake, 154*f*, 157*f*
- Cd and EAP coated 4340 steel alloy coupons, 145*f*
- Cd-coated buttons tested and 4340 steel alloy plate, 143*f*
- Chain transfer agent, 64
- Chromate loaded primer, 186*f*
- Coating, healing
  - exposed, 12*f*
  - unexposed, 12*f*
- Contact angle measurement, 92
- Control PU surfaces CA & RMS roughness, 96*f*, 97
- Conventional coating system, 179*f*
- Copoly(IL-BF_4/MMA)
  - EGDMA, 204*f*
  - TGA analysis, 204*f*
- Copolymer brush, UV-visible spectra, 81*f*
- Core-shell particles
  - cotton, 214*f*, 216*f*
  - FC emulsion, 215*f*
- Corrosion inhibitors
  - aluminum alloy 2024-T3, 151, 165
  - polypyrrole/aluminum flake hybrids, 151
  - protection coatings, 165
- Corrosion test panels, 14, 16*f*
- Cotton
  - core-shell particles, 214*f*, 216*f*
  - FC resin, 216*f*
  - microstructure, 215*f*
  - oil repellence tests, 217*t*
  - performance, 215
  - stain repellence tests, 217*t*
  - water repellence tests, 217*t*
- CPV coatings
  - as-received aluminum flake, 159*f*
  - polypyrrole coated aluminum flake, 159*f*
- Crushed and vacant capsule, 9*f*
- Crushed microcapsule, 10*f*
- C1s binding energy data
  - XGNP, 128*t*
  - XGP, 128*t*
- CTA. *See* Chain transfer agent

D

- DCA. *See* Dynamic contact angle analyzer
- Dendritic polyols, 87
- Diamine conversion reactions, 26
- Diisopropylnaphthalene, 173*f*
- Dimethyethylenediamine, 27*f*
- Dimethylsulfoxide and polymers, 201*f*, 202*f*
- DMEDA. *See* Dimethyethylenediamine
- DMSO. *See* Dimethylsulfoxide
- Dry adhesion strength [MPa] of paints, 180*f*
- Dynamic contact angle analyzer, 96

E

- EAP. *See* Electroactive polymers
- EAP (P(7-PHA)) onto 4340 steel alloy substrate, 146*f*
- EGDMA. *See* Ethylene glycol dimethacrylate
- Electroactive polymers, 133
- Electrospun porous fibers, 38*f*
- Electrostatic deposition
  - methods, 34*f*
  - smart coating, delivery system, 31
- Empty shell, 9*f*
- End-functionalized PtBA, grafting, 24
- Ethylene glycol dimethacrylate
  - porous polymers, 203*f*
  - TGA analysis, 204*f*
- Exchange anions, hydrophobicity, 196

F

- FC. *See* Fluorocarbon
- FFC test. *See* Filiform corrosion test
- Filiform corrosion test, 183*f*, 184*f*
- Films and smart polyurethane surfaces, 91, 94*t*
- Finished textiles
  - repellent power, 216*f*
  - sliding angle, 216*f*
- First generation CTA
  - atomic percentages on surface, 68*t*
  - electro-grafted on gold, 66
    - CV curve, 66*f*
    - SI-RAFT polymerization of PEGMA, 69*f*
    - SI-RAFT polymerization of PMMA, 69*f*

Downloaded by 89.163.35.42 on June 22, 2012 | http://pubs.acs.org
Publication Date (Web): November 10, 2010 | doi: 10.1021/bk-2010-1050.ix002

- XPS data, 67*f*
  - expected atomic percentages, 68*t*
  - preparation, synthetic route, 65*s*
- Fluorocarbon
  - emulsion and core-shell particles, 215*f*
  - finish, self-cleaning behavior, 217*f*
  - polyester fibres, 212*f*
  - resin and cotton fabric, 216*f*
- FTIR spectra
  - neat PtBA, 25*f*
  - Si-g-PtBA, 25*f*
  - Si-NH_2, 25*f*

G

- Galling test setup, 141, 142*f*
- G1-CTA. *See* First generation CTA
- Gold and electro-grafted G1-CTA, 66*f*

H

- Harrison solution, 158*f*, 182*f*
- Hollow PLA polymer shell, 36*f*
  - filling and sealing, 35
  - interior, 36*f*
  - preparation, 34
- 8-HQ. *See* 8-Hydroxychinoline
- Hydrophilic surfaces
  - MPEG, 98
  - PFO, 99
- Hydrophobicity of exchange anions, 196
  - IL-BF_4, 197*f*
  - IL-Br, 197*f*
  - IL-PF_6, 197*f*
- 8-Hydroxychinoline, 179*f*, 186*f*

I

- IL-BF_4. *See* 1-(11-Acryloyloxyundecyl)-3-methylimidazolium tetrafluoroborate
- IL-Br. *See* 1-(11-Acryloyloxyundecyl)-3-methylimidazolium bromide
- IL-PF_6, hydrophobicity of exchange anions, 197*f*
- Ionic liquid surfactant copolymer brush, 205*f*
- Ionomer/carbon-fiber composite and resistive heating, 56, 57*f*
- Ionomer/iron oxide (nanoparticle) composite, 51*f*
- Ionomer/magnetic-particle composite, 50
- Ionomer/nickel magnetic nanoparticles, 53*f*, 54*f*, 55*f*, 56*f*
- Ion-vapor deposited aluminum and 4340 steel alloy plate, 143*f*
- IPDI. *See* Isophorone diisocyanate
- Isocyanate, 10*f*, 92*f*, 93*f*
- Isophorone diisocyanate, 90
- IVD aluminum. *See* Ion-vapor deposited aluminum

L

- Light-induced contact angle changes, photoresponsive surface, 80

M

- MBT-10. *See* Mercaptobenzothiazole loaded primer
- MC. *See* Merocyanine
- Mendomer-400, 58*t*
- Mendomer-401, 57*f*, 58*t*
- Mercaptobenzothiazole loaded primer, 186*f*
- Merocyanine
  - dimeric complex, 75*s*
  - spiropyran moiety, 75*s*
- Metal ion sensors, 73
- Metallic aluminium and drop test, 185*f*
- Methoxy terminated PEG
  - hydrophilic surfaces, 98
  - PU surfaces CA & RMS roughness, 97*f*
- Methyl methacrylate and surface initiated copolymerization, 80*s*
- Mica and xyloglucan deposition, 124*t*
- Microcapsules
  - broken with healing agent, 11*f*
  - encapsulation, 37*f*
  - formation, 168*f*
  - N=C=O to NH_2 ratios, 176*f*
  - reactive metal oxide, release, 37*f*
  - self-healing coating, 11*f*
  - synthesis, 168*f*
- Micro-encapsulated inhibitors, 165, 174
- MMA. *See* Methyl methacrylate
- MPEG. *See* Methoxy terminated PEG

N

- N-Acryloylundecyl-N′-methyl imidazolium IL reactive surfactant, 193*f*
- NA-8HQ-16.7 and capsule formation, 177*f*

Downloaded by 89.163.35.42 on June 22, 2012 | http://pubs.acs.org
Publication Date (Web): November 10, 2010 | doi: 10.1021/bk-2010-1050.ix002

- NA-MBI-16.7 and capsule formation, 177*f*
- NA-MBT-16.7 and capsule formation, 177*f*
  - TGA/DSC spectrum, 179*f*
- Nanostructured finish, self-cleaning behavior, 217*f*
- Nanotechnology and textile finishing, 210
- Neat PtBA and FTIR spectra, 25*f*
- Neutral salt fog exposure, 144
  - Cd and EAP (P(7-PHA)) onto 4340 steel alloy, 145*f*, 146*f*
  - film, outer edges, 147*f*
- NIPAAm. *See* N-isopropylacrylamide
- N-isopropylacrylamide, 107
  - grafting
    - PP-g-DMAEMA, 110*f*, 114*f*
    - PP-g-4VP, 111*f*, 114*f*
- Non-purified xyloglucan, 125*f*
  - C1s binding energy data, 128*t*
  - XPS, 126*f*, 127*f*, 127*t*

O

- Oil repellence tests and cotton fabrics, 217*t*
- Organic core material on capsule formation, 173*f*
- Organic polymer nanoparticles, 212
  - PES foil, 213*f*

P

- PAA. *See* Polyacrylic acid
- Paint
  - configurations for self-healing coating system, 170*t*
  - dry adhesion strength [MPa], 180*f*
- PDMAEMA. *See* Poly[2-(dimethylamino) ethyl methacrylate]
- PEG. *See* Polyethylene glycol
- PEGMA. *See* Poly(ethylene glycol) methyl ether methacrylate
- Perfluoro octanol, 91
  - hydrophilic surfaces, 99
  - PU surfaces CA & RMS roughness, 98*f*
- PES. *See* Polyester
- PFO. *See* Perfluoro octanol
- Phase diagrams
  - IL-BF_4-aqueous propanol-MMA, 198*f*
  - IL-Br-water-MMA systems, 198*f*
- 7-PHN. *See* 7-Pyrrol-1-yl-heptanitrile
- Photo-responsive surfaces, formation, 73
- Pigment volume concentrations coating
  - as-received aluminum flake, 161*f*
  - polypyrrole coated aluminum flake, 160*f*, 161*f*
- PLA. *See* Polylactic acid
- PMMA. *See* Poly(methyl methacrylate)
- Polyacrylic acid and Si-g-PtBA, 28*f*
- Polyalkyl acrylate, 8*f*
- Poly[2-(dimethylamino) ethyl methacrylate], 108
- Polyester
  - fibres, 212*f*
  - foil, 213*f*
- Polyethylene glycol, 91
- Poly(ethylene glycol) methyl ether methacrylate, 69*f*
- Polylactic acid, 36*f*
- Polymer
  - DMSO, 202*f*
  - film, crack formation, 146*f*
  - gels, 199*f*
  - microspheres and fibers, characterization, 35
  - rods, 201*f*
- Polymer brush 4 and reversible contact angle changes, 82*f*
- Polymer brush **3b** and UV light in DMF solvent, 83*f*
- Polymer brushes
  - metal ion sensors, 79
  - water contact angle measurements, 83*t*
- Polymer brushes (**3a**-**c**), 79*s*
- Polymerizations, 197
- Polymer 3-(pyrrol-1-yl) propanoic acid
  - IVD aluminum, 145*f*
  - SiO_2 button galling, 145*f*
  - 4340 steel alloy substrate, 139*f*
- Poly(methyl methacrylate), 69*f*
- Poly(poly(ethylene glycol) methyl ether methacrylate, 69*f*
- Polypropylene, 109*f*
  - AFM, 116*f*
  - SEM, 109*f*
  - virgin and grafted copolymers, 117*t*
- Polypyrrole
  - aluminum flake, 151
    - AA 2024-T3, 151
    - ammonium persulfate, 157*f*
    - catechol, 154*f*, 157*f*
    - corrosion inhibitors, 151
    - CPV coatings, 159*f*
    - hybrid synthesis, 157*f*
    - PVC coatings, 160*f*, 161*f*
- Poly(tert-butyl acrylate), grafting, 23
- Polyurethane, 16*f*
- Poly(4-vinylpyridine), 108
- Porous polymer fibers, 40
  - filling and sealing, 35

Downloaded by 89.163.35.42 on June 22, 2012 | http://pubs.acs.org
Publication Date (Web): November 10, 2010 | doi: 10.1021/bk-2010-1050.ix002

  preparation, 34
Porous polymers and EGDMA, 203*f*
PP. *See* Polypropylene
3PPA. *See* 3-(Pyrrol-1-yl) propanoic acid
PPEGMA. *See* Poly(poly(ethylene glycol) methyl ether methacrylate
PP-g-DMAEMA, 109*f*
  AFM, 116*f*
  SEM, 109*f*
(PP-g-DMAEMA)-g-NIPAAm, 107
  AFM, 116*f*
  SEM, 110*f*, 112*f*
  swelling ratio, 114*f*, 115*f*
PP-g-4VP, 109*f*
(PP-g-4VP)-g-NIPAAm, 107
  SEM, 111*f*, 112*f*
  swelling ratio, 114*f*, 115*f*
P(3PPA). *See* Polymer 3-(pyrrol-1-yl) propanoic acid
Primer
  8HQ-5, 181*f*
  MBT-10, 181*f*
Protein purification, 121
PtBA. *See* Poly(tert-butyl acrylate)
Pure shell polymer, 10*f*
Purified xyloglucan, 123, 125*f*
  C1s binding energy data, 128*t*
  XPS, 126*f*, 127*t*
PVC coating. *See* Pigment volume concentrations coating
P4VP. *See* Poly(4-vinylpyridine)
Py. *See* Pyrrole monomer
Pyrrole monomer, 153
7-Pyrrol-1-yl-heptanitrile
  hydrolysis, 141
  preparation, 140, 142*f*
3-(Pyrrol-1-yl) propanoic acid
  electroless deposition, 138
  electropolymerization, 138*f*
  synthesis, 137*f*

R

RAFT. *See* Reversible addition-fragmentation chain transfer
Resistive heating and ionomer/carbon-fiber composite, 57*f*
Reversible addition-fragmentation chain transfer, 64*s*
Reversible contact angle changes of film 4, 82*f*
Reversibly porating coatings, 191
RMS. *See* Root mean square roughness
Root mean square roughness, 96*f*, 97*f*, 98*f*, 100*f*, 117*t*
Rough hydrophobic surface, wetting, 212*f*
Roughness measurements, AFM, 94

S

Scanning electron microscopy
  binary graft copolymers, 112*f*
  PP, 109*f*
  PP-g-DMAEMA, 109*f*
  PP-g-DMAEMA)-g-NIPAAm, 110*f*
  (PP-g-DMAEMA)-g-NIPAAm, 112*f*
  PP-g-4VP, 109*f*
  PP-g-4VP)-g-NIPAAm, 111*f*
  (PP-g-4VP)-g-NIPAAm, 112*f*
Scanning vibrating electrode technique and AA2024 unclad alloy, 186*f*
Self-cleaning behavior
  FC-finish, 217*f*
  nanostructured finish, 217*f*
Self-healing coating, 10*f*, 166
  adhesion properties, 178
  BF fluorescence, 11*f*
  BF transmitted light, 11*f*
  coatings, structure, 178
  corrosion protection properties, 182
  corrosion testing, 14
  elongation, 13*t*
  mechanical properties, 11
  microcapsules, 11*f*
  optical microscopy, 11*f*
  paint configurations, 170*t*
  SEM image, 11*f*
  surface hardness, 13*t*
  tensile strength, 12, 13*t*
  water vapor permeability, 14*f*
Self-healing concepts, 167
Self-healing polyurethane coating, 14*f*, 16*f*
Si-g-PtBA
  conversion, 27*f*
  DMEDA, 28*f*
  FTIR spectra, 25*f*
  PAA, 28*f*
Silicon wafers, 24
Si-NH_2, FTIR spectra, 25*f*
SIP. *See* Surface initiated polymerization
SI-RAFT polymerization. *See* Surface-initiated RAFT
SI-ROMP. *See* Surface-initiated ring-opening metathesis polymerization
Smart coatings
  electrostatic deposition, 31
  fibers, 42, 43*f*

Downloaded by 89.163.35.42 on June 22, 2012 | http://pubs.acs.org
Publication Date (Web): November 10, 2010 | doi: 10.1021/bk-2010-1050.ix002

- self-healing delivery systems, 33*f*
Smart polyurethane surfaces, 87
  - design and synthesis, 95
  - films, 91, 94*t*
Smart self-healing material systems, 45
Smooth hydrophobic surface, wetting, 212*f*
Spinodal decompositions, 191
  - bicontinuous gel, 205*f*
Spiropyran
  - functionalized norbornyl derivatives (**2a-c**), 79*s*
  - moiety, 75*s*
  - polymer brushes, 79*s*, 82*f*
Spiropyran methacrylate derivative, 80*s*
SPMA. *See* Spiropyran methacrylate derivative
SR. *See* Swelling ratio
Stain repellence tests and cotton fabrics, 217*t*
4340 Steel alloy
  - button and 3-aminopropyl trimethoxysilane, 138*f*
  - EAP (P(7-PHA)), 146*f*
  - plate and Cd-coated buttons tested, 143*f*
  - plate and IVD aluminum coated button, 143*f*
  - P(3PPA), 139*f*
Superhydrophobic textile finishes, 212
Surface electrostatic interactions, 121
Surface initiated polymerization, 64
Surface-initiated RAFT, 68
  - PEGMA on gold, 69*f*
  - PMMA on gold, 69*f*
Surface-initiated ring-opening metathesis polymerization, 73, 79*s*
SVET. *See* Scanning vibrating electrode technique
Swelling ratio
  - (PP-g-DMAEMA)-g-NIPAAm, 114*f*, 115*f*
  - (PP-g-4VP)-g-NIPAAm, 114*f*, 115*f*
Synthesized microcapsules, 169*t*

T

Tartaric sulphuric acid, anodic film, 181*f*, 182*f*
Tert-butyl ester substitution, 23
Tethered dendritic polyols, 87
Tethered polymer films, 21
Tethered stimuli-responsive polymer films, 21
Textile finishing and nanotechnology, 210
Textile surface, structure, 215*f*
Thin polysaccharide film adsorbed on solid support, 121
$TiCl_4$. *See* Titanium (IV) chloride
Titanium (IV) Chloride, 40*f*
Trimethylaluminum, 41, 42*f*
TSA. *See* Tartaric sulphuric acid

W

Washpermanent nano-structured textiles, 209
Water repellence tests and cotton fabrics, 217*t*
Water vapor permeability, 13
  - self-healing coating films, 14*f*
  - self-healing polyurethane coating, 14*f*
Wetting scheme
  - rough hydrophobic surface, 212*f*
  - smooth hydrophobic surface, 212*f*
Wire insulation
  - composite
    - ionomer/carbon-fiber composite and resistive heating, 56
    - ionomer/iron oxide (nanoparticle) composite, 51*f*
    - ionomer/magnetic-particle composite, 50, 51
    - ionomer/nickel magnetic nanoparticles, 53*f*, 55*f*, 56*f*
    - material used, 49
  - failure, 48
  - solution, 48*f*

X

XG. *See* Xyloglucan
XGNP. *See* Non-purified xyloglucan
XGP. *See* Purified xyloglucan
XPS. *See* X-ray photoelectron spectroscopy
X-ray photoelectron spectroscopy
  - XGNP, 126*f*, 127*t*
  - XGP, 126*f*, 127*t*
Xyloglucan, 123, 124*t*

Y

Young equation, 212*f*

Z

Zonyl-FSO PU surfaces CA & RMS roughness, 100*f*

Downloaded by 89.163.35.42 on June 22, 2012 | http://pubs.acs.org
Publication Date (Web): November 10, 2010 | doi: 10.1021/bk-2010-1050.ix002